Testing models of galaxy formation and evolution with galaxy-galaxy-galaxy lensing

DISSERTATION

zur Erlangung des Doktorgrades (Dr. rer. nat.) der
Mathematisch-Naturwissenschaftlichen Fakultät der Rheinischen
Friedrich-Wilhelms-Universität Bonn

vorgelegt von
Laila Maria Linke
aus Frankenthal (Pfalz), Deutschland

Bonn, 2020

Angefertigt mit Genehmigung der Mathematisch-Naturwissenschaftlichen Fakultät der Rheinischen Friedrich-Wilhelms-Universität Bonn

1. Gutachter:	Prof. Dr. Peter Schneider
2. Gutachter:	Prof. Dr. Cristiano Porciani
Tag der Promotion:	11. März 2021
Erscheinungsjahr:	2021

For my grandparents

Abstract

Explaining the formation and evolution of galaxies is a fundamental issue in modern astronomy. Several competing models try to explain how galaxies form and predict the relationship between galaxies and dark matter. A prominent class of these models are semi-analytic models of galaxy formation and evolution (SAMs). They combine analytical prescriptions for small-scale physical effects with cosmological simulations of the dark matter. To test these models, their predictions, in particular for the correlation of dark and visible matter, need to be compared to observations.

The ideal tool to study the relationship between dark and visible matter is gravitational lensing. This effect describes how matter bends light rays and distorts the images of far-away objects. By comparing the position of nearby galaxies to this distortion, we can directly measure their correlation with the (predominantly dark) matter distribution.

In this thesis, we use gravitational lensing to test different models of galaxy formation and evolution. We concentrate on the correlation of galaxy pairs with the matter field. This correlation can be measured with galaxy-galaxy-galaxy lensing (G3L). Here, the position of galaxy pairs is correlated to the distortion by the matter field. This correlation effectively measures how much more dark matter exists around pairs of galaxies compared to single galaxies. We investigate how well different models predict this effect by comparing them to observations.

First, we improve the commonly-used estimator for G3L to enhance the precision and accuracy of the measurement. These improvements include a weighting of galaxy pairs according to their redshifts, an adaptive binning of the galaxy-galaxy-matter correlation function, and accounting for the magnification of galaxies by the cosmic large-scale-structure. We test the improvements with realistic simulated data based on the Millennium Run (MR) with the SAM by Henriques et al. (2015, H15). Our improvements increase the signal-to-noise ratio by 35% on average at angular scales between $0\overset{\prime}{.}1$ and $10'$ They also remove the bias of the G3L estimator at angular scales below $1'$, which was originally up to 40%. The signal due to lens magnification is approximately 10% of the total signal.

Next, we test the SAMs by H15 and Lagos et al. (2012, L12) by comparing their predictions for G3L to measurements in the overlap of the Kilo-Degree Survey (KiDS), VISTA Kilodegree Infrared Galaxy survey (VIKING), and Galaxy And Mass Assembly survey (GAMA) (KV450 × GAMA). Galaxies into two colour- and five stellar-mass samples. We measure G3L for 'mixed lens pairs' with galaxies from different samples, as well as for 'unmixed lens pairs' with galaxies from the same sample. Predictions by the H15 SAM for the G3L signal agree with the observations for all colour-selected samples and all but one stellar-mass-selected sample with 95% confidence.

Deviations occur for lenses with stellar masses below $9.5\,h^{-2}\,\mathrm{M}_\odot$ at scales below $0.2\,h^{-1}$ Mpc. Predictions by the L12 SAM for stellar-mass selected samples and red galaxies are significantly higher than observed, while the predicted signal for blue galaxy pairs is too low. We conclude that the L12 SAM predicts more pairs of low stellar mass and red galaxies than the H15 SAM and the observations, as well as fewer pairs of blue galaxies. This difference increases towards the centre of the galaxies' host halos. Likely explanations are different treatments of environmental effects by the SAMs and different models of the initial mass function (IMF).

Lastly, we propose an analytical model for G3L. We investigate the impact and physical meaning of the model parameters and find that G3L is sensitive to all but one of them. Then, we constrain the parameters by fitting the model to the observations in KV450 × GAMA with a multidimensional optimization routine. The resulting best fit agrees with the measurement at the 95% confidence level (CL). The parameter values indicate that red galaxies form in more massive dark matter halos than blue galaxies and that red and blue galaxies are positively correlated. We conclude that the halo model can describe G3L.

In conclusion, not all models of galaxy evolution and formation predict the correlation of galaxy pairs with the matter distribution accurately. The halo model can, despite its simple assumptions, reproduce the observed G3L with plausible parameters. SAMs, when tuned to the right parameters for the physical model, accurately predict the observed G3L signal. However, this is not the case for all SAMs. Consequently, G3L provides a stringent test for models of galaxy formation and evolution.

Contents

Abstract v

1 Introduction 1

2 Fundamentals of cosmology and gravitational lensing 5
- 2.1 Cosmology 5
  - 2.1.1 Friedmann equations and the cosmological standard model 5
  - 2.1.2 Cosmological structure formation 11
  - 2.1.3 Galaxy formation and evolution 14
  - 2.1.4 Random fields, correlation functions and polyspectra 16
- 2.2 Cosmological simulations 20
  - 2.2.1 N-Body simulations 20
  - 2.2.2 Semi-analytic models of galaxy formation and evolution 23
  - 2.2.3 Hydrodynamical simulations 25
- 2.3 Halo model 27
  - 2.3.1 Dark matter halo profile 28
  - 2.3.2 Halo mass function 29
  - 2.3.3 Halo bias 30
  - 2.3.4 Halo occupation distribution 31
- 2.4 Gravitational lensing 31
  - 2.4.1 Lens equation 32
  - 2.4.2 Weak gravitational lensing 34
  - 2.4.3 Projected spectra and Limber equation 35
  - 2.4.4 Galaxy-galaxy-lensing 36
  - 2.4.5 Galaxy-galaxy-galaxy-lensing 37
  - 2.4.6 Aperture Statistics 40
  - 2.4.7 Gravitational Lensing in N-body simulations 42

3 Improving the precision and accuracy of galaxy-galaxy-galaxy lensing 43
- 3.1 Motivation 43
- 3.2 Methods 44
  - 3.2.1 Redshift weighting 44
  - 3.2.2 New binning scheme 47
  - 3.2.3 Conversion into physical units 49
  - 3.2.4 Magnification of lens galaxies 50
- 3.3 Data 53
  - 3.3.1 Simulated data based on the Millennium Run 53

3.3.2 Simple mock data . . . 55
3.4 Results . . . 56
3.4.1 Effect of the new binning scheme . . . 56
3.4.2 Effect of lens magnification . . . 57
3.4.3 Effect of redshift weighting . . . 61
3.5 Discussion . . . 61

4 Testing semi-analytic galaxy models with galaxy-galaxy-galaxy lensing 65
4.1 Motivation . . . 65
4.2 Methods . . . 66
4.2.1 Estimating the three-point correlation function . . . 66
4.2.2 Computing aperture statistics . . . 67
4.3 Data . . . 68
4.3.1 Observational data . . . 68
4.3.2 Simulated data . . . 70
4.4 Results . . . 71
4.5 Discussion . . . 77

5 Modelling galaxy-galaxy-galaxy lensing with the halo model 81
5.1 Motivation . . . 81
5.2 Derivation of the halo model for galaxy-galaxy-galaxy-lensing . . . 82
5.2.1 Moments of the joint halo occupation distribution . . . 82
5.2.2 Modelling the galaxy-galaxy-matter bispectrum . . . 85
5.2.3 Projecting the bispectrum and obtaining the aperture statistics . . . 88
5.3 Fitting procedure . . . 88
5.3.1 Estimation of best-fitting parameters . . . 88
5.3.2 Estimation of parameter uncertainty . . . 89
5.4 Results . . . 91
5.4.1 Impact of model parameters . . . 91
5.4.2 Results of fitting halo model to observations . . . 93
5.5 Discussion . . . 96

6 Conclusion 99
6.1 Summary . . . 99
6.2 Outlook . . . 101

Bibliography 102

A Appendix to Chapter 3 119
A.1 Calculation of aperture statistics for mock data . . . 119
A.2 Computational implementation with graphics processing units . . . 123

B Appendix to Chapter 4 125
B.1 Results for aperture statistics in angular units . . . 125

C Appendix to Chapter 5 **129**
C.1 Calculation of galaxy-galaxy-matter bispectrum for galaxies from the same population 129
C.2 Calculation of galaxy-galaxy-matter bispectrum for different galaxy populations 133

List of Figures **137**

List of Tables **139**

List of Acronyms **141**

Acknowledgements **143**

1

Introduction

> *"There is a theory which states that if ever anyone discovers exactly what the Universe is for and why it is here, it will instantly disappear and be replaced by something even more bizarre and inexplicable.*
>
> *There is another theory which states that this has already happened."*
>
> Douglas Adams, *The Restaurant at the End of the Universe* (Adams, 1981).

We live in a dark universe. According to our best model for the Universe, the so-called ΛCDM cosmological model, only a small fraction of matter interacts with photons and follows the standard model of particle physics. This baryonic matter [1], such as stars, gas, or planets is only a tiny part ($\approx 5\%$) of the total energy-matter content of the Universe. Almost three-quarters of the energy-matter budget consists of the illusive and hardly understood dark energy, while most matter is not baryonic but dark and acts only gravitationally

There are several indications for the existence and abundance of dark matter. The first evidence was found in a study of galaxy clusters by Zwicky (1933). He measured the velocities of galaxies in the Coma cluster and estimated the mass of the cluster from the combined luminosity of the galaxies. To his surprise, the inferred mass was not enough to explain the high galaxy velocities. Zwicky concluded that the cluster must contain an additional invisible mass component, which he called *dark matter*.

Another sign for dark matter is the observation of galaxy rotation curves by Rubin et al. (1980). They measured the rotational velocities of stars in spiral galaxies. If the galaxies were composed only of their visible components, the rotational velocities should decrease with the distance of the stars from the centres of the galaxies outside the galaxies' bulges. However, the velocities stay almost constant up to the outskirts. Consequently, an additional invisible component contributes significantly to the masses of the galaxies. This component is dark matter.

The findings by Zwicky (1933) and Rubin et al. (1980), along with observations of the cosmic microwave background (CMB) and gravitational lensing, indicate that dark matter makes up most mass in the Universe. However, our observations are restricted to baryonic matter, in particular gas and stars. Their distribution and appearance are shaped by dark matter, because

---

[1] We follow here the cosmological convention, that matter consisting of neutrons, protons, and electrons is 'baryonic', even though electrons are strictly speaking leptons.

the gravitational potentials of dense dark matter halos attract gas and provide the breeding ground for stars and galaxies. Consequently, many galaxies form in regions with much dark matter and they interact frequently. These interactions change the gas content and morphology of the galaxies. Therefore, to explain our observed Universe, we need to understand how dark matter impacts the formation and evolution of galaxies.

There are several methods to model the formation, evolution and distribution of galaxies. They can be roughly categorized into purely analytical approaches (e.g. with the halo model; Cooray and Sheth, 2002), purely numerical approaches (e.g. with hydrodynamical simulations; Vogelsberger et al., 2020) and semi-analytic models of galaxy formation and evolution (SAMs). In SAMs, galaxies are inserted and evolved inside dark-matter-only numerical simulations with phenomenologically motivated analytical models of baryonic physics. A variety of SAMs with differing assumptions has been proposed (e.g., Bower et al., 2006; Guo et al., 2011; Lagos et al., 2012; Henriques et al., 2015).

We test models for galaxy formation by comparing their prediction to observations. The ideal tool for such comparisons is gravitational lensing (Bartelmann, 2010). Gravitational lensing describes how matter distorts the images of far away objects, for instance galaxies. Due to general relativity (GR), massive objects, such as dark matter halos, warp space-time. Light rays travelling near these objects are therefore bent, and images get distorted. By measuring the distortion, we can infer the mass of all matter between us and the light source, most of which is dark matter. Accordingly, with gravitational lensing, the distribution of dark matter can be estimated.

One form of gravitational lensing is galaxy-galaxy lensing (GGL). This effect causes correlations between the positions of foreground galaxies and the observed shapes of background galaxies. Measuring this correlation constrains the amount of matter around the foreground galaxies and has been used to test SAMs (e.g Saghiha et al., 2017; Renneby et al., 2020), as well as the halo model (e.g Mandelbaum et al., 2006). However, galaxy formation models can be better distinguished with galaxy-galaxy-galaxy lensing (G3L; Schneider and Watts, 2005). Here, observed galaxy shapes are correlated with the position of foreground galaxy pairs instead of individual galaxies. This measurement reveals how much more dark matter exists on average around galaxy pairs than around individual galaxies. Galaxy pairs are distributed differently than single galaxies, so galaxy formation models that predict the correct GGL signal do not necessarily predict the correct G3L signal. Therefore, studying G3L is a notable additional test for models of galaxy formation and evolution.

In this thesis, we use G3L to constrain and assess different galaxy formation and evolution models. We aim to answer the question: *How well do the different models for galaxy formation, evolution, and distribution reproduce the observed correlation of dark matter and galaxy pairs?* To answer this question, we consider three interconnected issues.

First, we improve the measurement of G3L. For this, we alter three aspects of the estimator for the G3L correlation function used in previous studies. We incorporate precise redshift information on the foreground galaxies, use a new binning scheme, and convert the signal from projected to physical scales. Then, we test these improvements on simulated data based on the Millennium Run (MR; Springel et al., 2005) and the SAM by Henriques et al. (2015).

Second, we test the SAMs by Henriques et al. (2015) and Lagos et al. (2012) by comparing their G3L predictions to observations. For this, we measure G3L with the improved estimator in the overlap of Kilo-Degree Survey (KiDS; Kuijken et al., 2015; de Jong et al., 2015), VISTA Kilodegree Infrared Galaxy survey (VIKING; Edge et al., 2013; Venemans et al., 2015), and Galaxy And Mass Assembly survey (GAMA; Driver et al., 2009, 2011; Liske et al., 2015). Then, we compare these observations to the predictions by the SAMs, obtained with the same improved estimator. By examining the differences between the predictions and the observations, we assess the assumptions of the SAMs.

Third, we determine whether an analytical model can accurately describe G3L. For this, we extend the halo model by Rödinger (2009) and Martin (2019) to galaxy pairs with galaxies from different populations. We qualitatively study the impact of its parameters on the predicted G3L signal. Finally, we determine the best-fitting parameter values for the observation in KiDS, VIKING, and GAMA.

This thesis is structured as follows.

- In Chapter 2, we review the theoretical foundation important for this work. We briefly introduce the cosmological standard model and cosmic structure formation. Then, we explain the concepts of cosmological simulations and the halo model. We also introduce the concepts of gravitational lensing, in particular of G3L.
- Chapter 3 describes our improvements to the standard G3L estimator. We show the results of testing these improvements in mock data and discuss their implications.
- In Chapter 4, we apply the improved estimator to the two SAMs and the observations. We describe our simulated and observed data sets, as well as our selection for different galaxy samples. We compare the SAMs predictions to the observations and discuss the accuracy of the SAMs.
- In Chapter 5, we analytically model the G3L signal. Our model is based on the halo model and contains several free parameters. We study the impact of these parameters and discuss their physical meaning. Lastly, we determine their best-fitting values based on the observed G3L signal.
- Chapter 6 concludes this thesis with a summary of our findings and an outlook to future research.

2

Fundamentals of cosmology and gravitational lensing

In this thesis, we explore the relationship of galaxies and the matter distribution of the Universe with the gravitational lensing effect. This relationship reveals how galaxies form and evolve inside the dark-matter dominated cosmic large-scale structure (LSS). The formation and evolution of galaxies depend primarily on three factors: The overall cosmological model describing the dynamics of the Universe, the formation of the dark-matter LSS, and physical processes affecting only baryons. We need to model all three factors to understand the galaxy-matter relationship. Therefore, we discuss their principles and current models in this chapter.

In Sect. 2.1 we outline the cosmological standard model, the formation of the LSS and our current general picture of galaxy formation. We present two approaches to model the connection of galaxies and dark matter, cosmological simulations in Sect. 2.2 and the halo model in Sect. 2.3. Finally, we introduce the effect with which we constrain these models in Sect. 2.4: Gravitational lensing, in particular, G3L.

2.1 Cosmology

Cosmology is the research of the origin, evolution and eventual fate of the Universe. Although this is a daunting task, humans have engaged in it for thousands of years by observing the skies and forming their models of the Universe. These models were often tightly connected to religious beliefs and mythology. However, since the last century, cosmology has evolved to a precise science, founded on astronomical observations and physical theories.

2.1.1 Friedmann equations and the cosmological standard model

Our modern understanding of cosmology relies on the theory of GR by Einstein (1915). The fundamental principle of GR is that space and time are not a rigid grid of coordinates, but instead form a topological manifold, distorted by mass and energy. This manifold can transform and change. Accordingly, the Universe does not need to be static but can expand and shrink depending on its energy content.

At the core of GR are Einstein's field equations,

$$R_{\mu\nu} - \frac{R}{2} g_{\mu\nu} = \frac{8\pi G}{c^4} T_{\mu\nu} + \Lambda g_{\mu\nu} \; . \tag{2.1}$$

Here, $R_{\mu\nu}$ is the Ricci tensor, which describes the curvature of space-time. Its trace is the Ricci scalar R. The metric of space-time is $g_{\mu\nu}$, while $T_{\mu\nu}$ is the energy-momentum tensor describing the energy content of the Universe. The cosmological constant Λ and the Newtonian gravitational constant G are two coupling constants. The field equations show that the curvature of space-time, represented by the Ricci tensor, is fundamentally linked to the energy and matter content, represented by the energy-momentum tensor. Accordingly, the amount and type of energy in the Universe determines its shape and dynamical evolution.

Solving the field equations is, in general, a difficult task, because they form a set of ten coupled non-linear differential equations. However, in cosmology, we use the *cosmological principle*, which significantly reduces the complexity of the problem (Einstein, 1917). It states that the Universe is spatially *isotropic* on scales above hundreds of Megaparsecs and that our position in space is not extraordinary in any way. The second condition implies that the large-scale Universe is isotropic around any point in space and consequently *homogeneous*.

Observations of the galaxy distribution or the CMB demonstrated the isotropy of the cosmic matter distribution (Eisenstein et al., 2011; Planck Collaboration: Aghanim et al., 2019). Homogeneity, though, has been notoriously difficult to test. We cannot probe the entire Universe at a fixed point in time or check the measurements of observers at other points in space. Nonetheless, there is no reason to assume our spatial position is in any way unique. Hence, it appears reasonable that all observers in the Universe observe the same statistical properties.

Due to the cosmological principle, the space-time of the Universe is described by the Robertson-Walker metric (Robertson, 1935; Walker, 1937). For this metric, the line element $\mathrm{d}s$, which is the arc length between two space-time points at (t, w, θ, ϕ) and $(t + \mathrm{d}t\,, w + \mathrm{d}w\,, \theta + \mathrm{d}\theta\,, \phi + \mathrm{d}\phi)$ is

$$\mathrm{d}s^2 = -c^2\,\mathrm{d}t^2 + a^2(t)\,\left[\mathrm{d}w^2 + f_K^2(w)\,\left(\mathrm{d}\theta^2 + \sin^2(\theta)\,\mathrm{d}\phi^2\right)\right] \; . \tag{2.2}$$

Here, t is the cosmic time, w is the comoving radial distance, θ and ϕ are angular coordinates, and $f_K(w)$ is the comoving angular diameter distance, given as

$$f_K(w) = \begin{cases} \frac{1}{\sqrt{K}}\,\sin\left(\sqrt{K}\,w\right) & \text{for } K > 0 \\ w & \text{for } K = 0 \\ \frac{1}{\sqrt{-K}}\,\sinh\left(\sqrt{-K}\,w\right) & \text{for } K < 0 \end{cases} \; . \tag{2.3}$$

The parameter K describes the spatial curvature of the Universe. A positive K corresponds to a positively curved universe, $K = 0$ to flat space and a negative K to a negatively curved space.

The line element also includes the scale factor $a(t)$, which may depend on time t. This factor describes the dynamics of the Universe. An increasing a corresponds to an expanding Universe, while a decreasing a means that the Universe is shrinking. The scale factor is normalised such that today, at t_0, $a(t_0) = 1$. With the scale factor each position in space can be assigned not only the comoving coordinate $\boldsymbol{w}$, but also the *proper coordinate* $\boldsymbol{r}$, which is

$$\boldsymbol{r}(t) = a(t)\, \boldsymbol{w} \ . \tag{2.4}$$

Inserting the metric from Eq. (2.2) into Eq. (2.1) and using the energy momentum tensor $T_{\mu\nu}$ of an ideal fluid with density ρ, pressure p and four-velocity u,

$$T_{\mu\nu} = \left(\rho + \frac{p}{c^2}\right) u_\mu\, u_\nu + p\, g_{\mu\nu} \ , \tag{2.5}$$

leads to the Friedmann equations for the scale factor a, which are (Friedmann, 1922)

$$\left(\frac{\dot{a}}{a}\right)^2 = \frac{8\pi\, \mathrm{G}}{3}\rho - \frac{k\, c^2}{a^2} + \frac{\Lambda\, c^2}{3} =: H^2(a) \ , \tag{2.6}$$

$$\frac{\ddot{a}}{a} = -\frac{4\pi\, \mathrm{G}}{3}\left(\rho + 3\,\frac{p}{c^2}\right) + \frac{\Lambda\, c^2}{3} \ . \tag{2.7}$$

The Friedmann equations describe the dynamics of the Universe and its expansion history. The expansion rate $H = \frac{\dot{a}}{a}$ is the Hubble parameter whose current value is the Hubble constant H_0. Frequently, one also uses the dimensionless Hubble constant $h = H_0/(100\,\mathrm{km\,s^{-1}\,Mpc^{-1}})$.

Equations (2.6) and (2.7) are solvable for a given equation of state $w = p/(\rho\, c^2)$. The equation of state varies for different types of energy-matter content in the Universe. For example, radiation and relativistic particles have $w = \frac{1}{3}$, while non-relativistic matter is approximately pressureless, so $w = 0$. Consequently, in a flat universe with vanishing Λ containing only radiation, the scale factor a is proportional to $t^{1/2}$, while the same Universe containing matter instead of radiation would have $a \propto t^{2/3}$. A universe without matter and a non-zero Λ would expand exponentially.

The Friedmann equations do not determine whether $a(t)$ increases or decreases with t. Therefore, the Universe could either expand or shrink. However, cosmologists are certain that the Universe is expanding, due to a famous discovery by Hubble (1929). He found that the observed frequency ν_obs of the light of distant galaxies is redshifted compared to the emitted frequency ν_em as

$$\nu_\mathrm{obs} = \frac{\nu_\mathrm{em}}{1+z} \ , \tag{2.8}$$

where z is the redshift. This redshift occurs, because in an expanding Universe time intervals between the arrival of two photons increase. This can be shown by considering two photons, one emitted at t_em and observed at t_obs and the other emitted at $t_\mathrm{em} + \Delta t_\mathrm{em}$ and observed at $t_\mathrm{obs} + \Delta t_\mathrm{obs}$. Photons travel on null geodesics with $\mathrm{d}s = 0$, so with Eq. (2.2),

$$c \ \mathrm{d}t = a(t) \ \mathrm{d}w \ . \tag{2.9}$$

Therefore,

$$\frac{\Delta t_\mathrm{em}}{\Delta t_\mathrm{obs}} = \frac{a(t_\mathrm{em})}{a(t_\mathrm{obs})} \ . \tag{2.10}$$

So the emitted and observed frequency of the light are

$$\frac{\nu_{\mathrm{em}}}{\nu_{\mathrm{obs}}} = \frac{\Delta t_{\mathrm{obs}}}{\Delta t_{\mathrm{em}}} = \frac{a(t_{\mathrm{obs}})}{a(t_{\mathrm{em}})} \,. \tag{2.11}$$

As $t_{\mathrm{obs}} > t_{\mathrm{em}}$, a must increase with time to explain the decreasing frequency. This implies an expanding Universe. With $a(t_0) = 1$, Eqs. (2.8) and (2.11) lead to the relation between the redshift z and the scale factor,

$$a(t) = \frac{1}{1 + z(t)} \,. \tag{2.12}$$

Lemaître (1931) was the first to describe the expansion of the Universe as an explanation of Hubble's findings and a natural implication of GR. He further inferred that the Universe must have originated from a tiny, dense region, which we now call the *Big Bang* [1].

Today, the favoured cosmological model is the so-called ΛCDM model. It assumes that the Universe contains not only baryonic matter but also dark matter. Dark matter is invisible, as it does not interact with electromagnetic radiation, but is detectable via its gravitational force. Together, baryonic and dark matter account for the total matter density ρ_{m}. The radiation content adds the density ρ_{r}. The ΛCDM model also assumes that the cosmological constant Λ is non-zero. Using the critical density ρ_{crit}, which is

$$\rho_{\mathrm{crit}} = \frac{3\,H_0^2}{8\pi G} \,, \tag{2.13}$$

we define the dimensionless densities

$$\Omega_{\mathrm{m}} = \frac{\rho_{\mathrm{m}}}{\rho_{\mathrm{crit}}} \,, \tag{2.14}$$

$$\Omega_{\mathrm{r}} = \frac{\rho_{\mathrm{r}}}{\rho_{\mathrm{crit}}} \,, \tag{2.15}$$

$$\Omega_{\mathrm{b}} = \frac{\rho_{\mathrm{b}}}{\rho_{\mathrm{crit}}} \,, \tag{2.16}$$

$$\Omega_{\Lambda} = \frac{\Lambda\, c^2}{8\pi G\, \rho_{\mathrm{crit}}} \,, \tag{2.17}$$

where ρ_{b} is the density of baryons. With these definitions, Eqs (2.6) and (2.7) can be cast into the more compact form

$$H(a)^2 = H_0^2 \left[\Omega_{\mathrm{r}}\, a^{-4} + \Omega_{\mathrm{m}}\, a^{-3} + (1 - \Omega_{\mathrm{r}} - \Omega_{\mathrm{m}} - \Omega_{\Lambda})\, a^{-2} + \Omega_{\Lambda}\right] \,. \tag{2.18}$$

Consequently, the density parameters and the Hubble constant fully determine the expansion history of the Universe. Eq. (2.18) reveals, that the Universe experienced three different expansion epochs. First, for small a at early times, the Universe was dominated by radiation. In

---

[1] Formally, the Big Bang is a point in space-time with infinite energy density. However, the description of cosmology with GR breaks down for such small, high-energy systems, so a physical model of the Big Bang would require a theory of quantum gravity

this epoch a grew proportional to $t^{1/2}$. With growing a, however, the term proportional to the matter density Ω_m took over, leading to the epoch of matter domination with $a \propto t^{2/3}$. The cross-over between the radiation and matter dominated epoch occured at the matter-radiation equality at scale factor a_eq. At this scale factor

$$\Omega_\mathrm{r}\, a_\mathrm{eq}^{-4} = \Omega_\mathrm{m}\, a_\mathrm{eq}^{-3}\ . \tag{2.19}$$

Today,

$$\Omega_\Lambda > \Omega_\mathrm{m}\, a^{-3}\ , \tag{2.20}$$

so the expansion of the Universe is dominated by the cosmological constant and a increases exponentially. The term proportional to a^{-2} vanishes, as measurements suggest that $\Omega_\mathrm{r} + \Omega_\mathrm{m} + \Omega_\Lambda = 1$.

Observations of various cosmological phenomena, such as the spatial galaxy distribution, the CMB, or distances to supernovae type Ia (SNIa) support the ΛCDM model (Eisenstein et al., 2011; Planck Collaboration: Aghanim et al., 2019; Riess et al., 2019). In particular, this model explains the observed accelerated expansion of the Universe (Riess et al., 1998; Perlmutter et al., 1999). Therefore, it is also frequently referred to as the *cosmological standard model.*

Even though the ΛCDM model is currently the best-fitting model for a wide range of observations, the values of its parameters are debated. Measurements of different observables do not yield the same values. The most prominent example is the so-called *H*0 *Tension*[2], which describes that the Hubble constant measured with SNIa distances in the local Universe is in tension with the value inferred from the CMB (Verde et al., 2019; Riess, 2019). For instance, Planck Collaboration: Aghanim et al. (2019) inferred $H_0 = (67.4 \pm 0.5)\,\mathrm{km\,s^{-1}\,Mpc^{-1}}$ from the CMB, while Riess et al. (2019) measured $H_0 = (74.03 \pm 1.42)\,\mathrm{km\,s^{-1}\,Mpc^{-1}}$ with SNIa. The difference between these measurements exceeds $4\,\sigma$. A similar tension, although with a lower significance, has been observed between the normalisation of the matter power spectrum σ_8 (see Sect. 2.1.4) in gravitational lensing surveys and CMB measurements (Hildebrandt et al., 2020; Joudaki et al., 2020). These tensions could indicate that measurements at high redshift are not directly comparable to measurements at low redshift. A wide range of cosmological models, which could solve this tension, are currently investigated (see Knox and Millea, 2020, for a review). Promising approaches are the addition of new relativistic particle species' (e.g. Kreisch et al., 2020) or an additional dark energy component in the early Universe before the release of the CMB (e.g. Poulin et al., 2019; Agrawal et al., 2019).

Here, however, we are not trying to solve this tension. Therefore, we work in the framework of the ΛCDM model, which is still the best description of our Universe. We adopt the parameter values listed in Table 2.1. These parameters were used in the creation of the numerical simulations that we use in this work, described in Sect. 2.2 and are based on the first year measurements by the CMB probe Wilkinson Microwave Anisotropy Probe (WMAP; Spergel et al., 2003). They differ from more recent constraints (e.g. Planck Collaboration: Aghanim et al., 2019). However, we use here weak gravitational lensing, which is most sensitive to the combination S_8 of the matter density Ω_m and the normalisation of the matter power spectrum σ_8, given by

---

[2] This tension has also been referred to as “Hubble Trouble”, for example by Sokol (2017).

Table 2.1: Parameters of the ΛCDM model used throughout this work.

Parameter	Value
Ω_m	0.25
Ω_Λ	0.75
Ω_b	0.045
H_0	$73\,\mathrm{km\,s^{-1}\,Mpc^{-1}}$
σ_8	0.9

$S_8 = \sigma_8\sqrt{\Omega_\mathrm{m}/0.3}$. This parameter is almost the same in our assumed cosmology and the most recent Planck measurements; it is $S_{8,\mathrm{MR}} = 0.822$ for our model and $S_{8,\mathrm{Planck}} = 0.825 \pm 0.011$ in Planck Collaboration: Aghanim et al. (2019).

With the Robertson-Walker metric, the distance to an object can be expressed. However, in GR distance measures are not unique. In Euclidean geometry, distance is the length of a line connecting two simultaneous events. The ambiguity of simultaneity in GR makes the definition of ‘distance’ more complicated. Therefore, different types of ‘distances’ are used in cosmology.

One of these is the radial comoving distance $D_\mathrm{com}(z_1, z_2)$ between an observer at z_1 and a source at z_2. This distance remains constant if both the source and the observer move with the Hubble expansion. It is defined as the spatial distance between the world lines of source and observer on the hypersurface with $t = t_0$ and corresponds to the coordinate distance w. To calculate it, we use Eq. 2.9, so

$$D_\mathrm{com}(z_1, z_2) = \int_{w(z_1)}^{w(z_2)} \mathrm{d}w = c\int_{a(z_2)}^{a(z_1)} \frac{\mathrm{d}a}{a^2\,H(a)}\;. \tag{2.21}$$

Another distance measure is the proper distance $D_\mathrm{prop}(z_1, z_2)$. This is the distance travelled by a photon from the source at z_1 to the observer at z_2 and is given by

$$D_\mathrm{prop}(z_1, z_2) = c\int_{t(z_1)}^{t(z_2)} \mathrm{d}t = c\int_{a(z_2)}^{a(z_1)} \frac{\mathrm{d}a}{a\,H(a)}\;. \tag{2.22}$$

The proper distance changes with the dynamics of the Universe, while the comoving distance is unaffected. Later, we also use the angular diameter distance D_A. This distance is defined such that the solid angle ω of an object at redshift z_2 that is observed at redshift z_1 relates to its area A by

$$D_\mathrm{A}(z_1, z_2) = \sqrt{\frac{A}{\omega}}\;, \tag{2.23}$$

which is the same relation as in Euclidean geometry. It can be calculated with

$$D_\mathrm{A}(z_1, z_2) = \frac{a(z_1)}{a(z_2)}\, f_K(D_\mathrm{com}(z_1, z_2))\;. \tag{2.24}$$

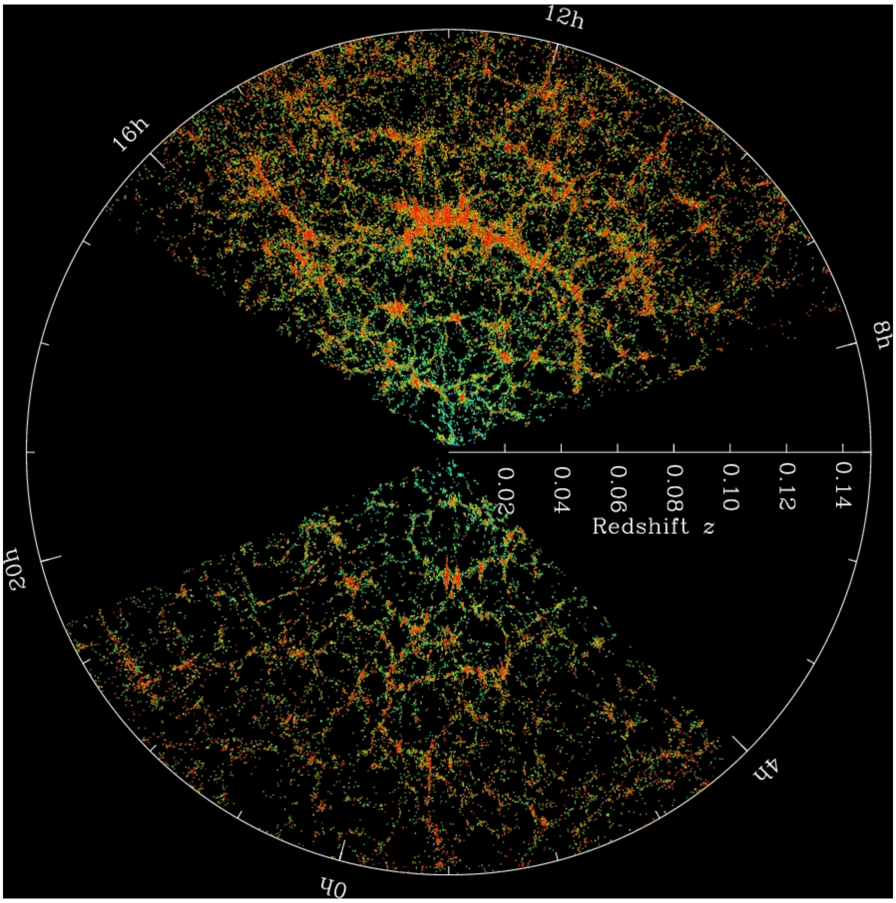

Figure 2.1: Map of all galaxies obtained by the Sloan Digital Sky Survey (SDSS). Each point is one galaxy and the colour correlates to the $g - r$ colour of the galaxies. Image from Blanton and SDSS (2014).

2.1.2 Cosmological structure formation

While the cosmological principle postulates that the Universe is homogeneous on large scales, this is certainly not true for smaller scales. Galaxies are not distributed homogeneously but instead assemble, in groups or galaxy clusters. These clusters are also not distributed uniformly on the sky but form the LSS. Due to its mesh-like appearance, illustrated in Fig. 2.1, with large voids separated by filaments, this structure is also called the *cosmic web*.

However, as the CMB is homogeneous with tiny Gaussian temperature variations on the order of 10^{-5}, the density variations in the early Universe had to be small and Gaussian as well. The process, by which the initially Gaussian density field with small fluctuations evolved into today's highly non-Gaussian LSS is the *cosmological structure formation*.

Structure formation can be summarised as follows. Small initial density fluctuations in the dark matter distribution grow denser, due to gravitational interaction. These fluctuations collapse as soon as they reach a threshold density and form dark matter halos. The halos merge to increasingly more massive halos. Consequently, small halos developed first, and the most massive structures in the Universe only arose later. This process is called bottom-up structure formation (Coles and Lucchin, 2002).

Baryons, such as gas or stars, follow the dark matter distribution, so they are dense in regions of high dark matter density. When the gas density is large enough, stars are formed. These stars eventually build galaxies, galaxy groups and galaxy clusters. However, the processes by which the galaxies form and evolve are complex and more challenging to model than the dark matter distribution (Cole et al., 2000).

The most promising mechanism to create the initial density fluctuations is cosmological inflation (Guth, 1981). This term describes a short time ($\simeq 10^{-32}$s) at around 10^{-34}s after the Big Bang during which the Universe expanded by a factor of at least $\mathrm{e}^{60} \simeq 10^{26}$. This massive expansion explains the observed flatness of the Universe and the homogeneity of the CMB. Additionally, it could inflate small quantum fluctuations to macroscopic scales, where they caused the initial density fluctuations (Mukhanov and Chibisov, 1981). However, the precise mechanisms of inflation and its end are unclear.

After inflation, the fluctuations evolved first during the radiation-dominated epoch of the Universe and then during the matter-dominated epoch. We can describe the growth of dark matter density fluctuations in the matter-dominated epoch with *linear perturbation theory* (see e.g. Peebles, 1980). This framework relies on the fluid approximation, which considers dark matter as a pressure-less fluid with density $\rho(\boldsymbol{r},t)$ and velocity $\mathrm{v}(\boldsymbol{r},t)$, as a function of the proper coordinate $\boldsymbol{r}$. Gravity is assumed to be weak and well-described by the Newtonian framework with the potential Φ and structure formation occurs on length scales much smaller than the *comoving horizon*

$$d_\mathrm{H}(a) = c \int_0^a \frac{\mathrm{d}a'}{a'^2\, H(a')} \; . \tag{2.25}$$

This assumption is valid as long as we consider the matter-dominated epoch of the Universe. We use the *pressureless hydrodynamical equations* (e.g. Coles and Lucchin, 2002),

$$\frac{\partial \rho}{\partial t} + \boldsymbol{\nabla}_r \cdot (\rho \mathbf{v}) = 0 \; , \tag{2.26}$$

$$\frac{\partial \mathbf{v}}{\partial t} + (\mathrm{v} \cdot \boldsymbol{\nabla}_r) \cdot \mathrm{v} = -\boldsymbol{\nabla}_r \Phi \; , \tag{2.27}$$

$$\nabla_r^2 \Phi = 4\pi\, G\, \rho - \Lambda \; . \tag{2.28}$$

The first equation is the *continuity equation* of the density field, the second is the *Euler equation*, which expresses momentum conservation, and the last is the *Poisson equation* for the gravitational field. The density, velocity and gravitational potential can also be expressed in terms of the comoving coordinate $\boldsymbol{x}$ as the comoving density

$$\varrho(\boldsymbol{x},t) = \rho\, [a(t)\, \boldsymbol{x}, t] =: \bar{\varrho}(t)\, [1 + \delta(\boldsymbol{x},t)] \; , \tag{2.29}$$

the comoving velocity

$$\boldsymbol{u}(\boldsymbol{x},t) = \mathrm{v}\, [a(t)\, \boldsymbol{x}, t] - H(t)\, a(t)\, \boldsymbol{x} \; , \tag{2.30}$$

and the comoving potential

$$\mathit{\Phi}(\boldsymbol{x},t) = \Phi\left[a(t)\,\boldsymbol{x},t\right] + \frac{\ddot{a}\,a}{2}\,|\boldsymbol{x}|^2\,, \tag{2.31}$$

where we used the mean density $\bar{\varrho}$ and defined the *density contrast* δ. Equations (2.26) - (2.28) also hold, when we replace ρ with $\bar{\rho}$, v with $H(t)\,a(t)\,\boldsymbol{x}$, and Φ with $\frac{\ddot{a}a}{2}\,|\boldsymbol{x}|^2$. From this follows, with

$$\boldsymbol{\nabla}_x = \frac{1}{a}\boldsymbol{\nabla}_r\,, \tag{2.32}$$

that

$$\frac{\partial\delta}{\partial t} + \frac{1}{a}\,\boldsymbol{\nabla}_x\cdot\left[(1+\delta)\,\boldsymbol{u}\right] = 0\,, \tag{2.33}$$

$$\frac{\partial\boldsymbol{u}}{\partial t} + H\,\boldsymbol{u} + \frac{1}{a}\,(\boldsymbol{u}\cdot\boldsymbol{\nabla}_x)\cdot\boldsymbol{u} = -\frac{1}{a}\boldsymbol{\nabla}_x\mathit{\Phi}\,, \tag{2.34}$$

$$\nabla_x^2\mathit{\Phi} = 4\pi G\bar{\varrho}\delta\,. \tag{2.35}$$

For small perturbations with $|\delta| \ll 1$ and $|\boldsymbol{u}| \ll H\,\boldsymbol{r}$, we can neglect terms of second or higher order in δ and $\boldsymbol{u}$, so we obtain the linear, pressureless hydrodynamic equations

$$\frac{\partial\delta}{\partial t} + \frac{1}{a}\,\boldsymbol{\nabla}_x\boldsymbol{u} = 0\,, \tag{2.36}$$

$$\frac{\partial\boldsymbol{u}}{\partial t} + H\,\boldsymbol{u} = -\frac{1}{a}\boldsymbol{\nabla}_x\mathit{\Phi}\,, \tag{2.37}$$

$$\nabla_x^2\mathit{\Phi} = 4\pi G\,\bar{\varrho}\,\delta\,, \tag{2.38}$$

which can be combined to the *linear growth equation* for the density fluctuations,

$$\frac{\partial^2\delta}{\partial t^2} + 2\frac{\dot{a}}{a}\frac{\partial\delta}{\partial t} = 4\pi\,G\,\bar{\varrho}\,\delta\,. \tag{2.39}$$

This equation has two solutions, a growing mode and a decaying mode. Both solutions can be split into a temporal part ($D_+(t)$ and $D_-(t)$, respectively) and a spatial part ($\Delta_+(\boldsymbol{x})$ and $\Delta_-(\boldsymbol{x})$, respectively), so Eq. (2.39) is solved by

$$\delta(\boldsymbol{x},t) = D_+(t)\,\Delta_+(\boldsymbol{x}) + D_-(t)\,\Delta_-(\boldsymbol{x})\,. \tag{2.40}$$

The decaying mode $D_-(t)\,\Delta_-(\boldsymbol{x})$ decreases with time, so it can be neglected for late-time cosmic structure formation. Consequently, the *linear growth function* $D_+(t)$, determines the growth of structures in the matter-dominated epoch. It is

$$D_+(t) = D\,H(t)\int_0^{a(t)}\mathrm{d}a'\left[\Omega_\mathrm{m}\,a'^{-1} + \Omega_\Lambda\,a'^2 - (\Omega_\mathrm{m} + \Omega_\Lambda - 1)\right]^{-3/2}, \tag{2.41}$$

where the normalisation constant D is given by requiring that today at t_0 $D_+(t_0) = 1$.

If δ and $\boldsymbol{u}$ are no longer small, the linearisation breaks down. Consequently, the formation of dark matter halos, which requires $\delta \gg 1$, cannot be described in this framework.

There are several analytical approaches to cosmic structure formation with larger δ involving the fluid approximation (Bernardeau et al., 2002). Some of these require a Lagrangian formulation of the hydrodynamical equations (e.g. Buchert, 1992; Bernardeau and Valageas, 2008), whereas others employ effective field theories reminiscent of particle physics (e.g. Carrasco et al., 2014). However, while these theories were successful at mildly non-linear scales (e.g. Buchert et al., 1994; Melott et al., 1995; Reid and White, 2011; d'Amico et al., 2020), the fluid approximation is, strictly speaking, not correct. Dark matter consists of collisionless particles, which only interact gravitationally. Streams of these particles can intersect and penetrate each other. Therefore, dark matter cannot form shocks or discontinuities that would arise in a 'proper' fluid. At stream crossings, where particles interact, a single dark matter 'fluid' element can have multiple assigned velocities. Hence, we cannot apply the hydrodynamical equations.

For small densities and low speeds, stream crossings are less likely; therefore, the hydrodynamical equations still hold for small δ. For large δ, though, different approaches are necessary to model the formation of the LSS. These approaches can be analytical, for example in the form of the Kinetic Field Theory by Bartelmann et al. (2019) or computational with numerical N-body simulations of the dark matter field (see Sect. 2.2)[3].

2.1.3 Galaxy formation and evolution

Galaxies form inside the densest regions of the dark matter large-scale structure (White and Rees, 1978). They are therefore often used as 'tracers' of the dark matter structure. However, they are not perfect tracers but rather biased. The galaxy number density contrast δ_g. defined as

$$\delta_\mathrm{g}(\boldsymbol{x},t) = \frac{n(\boldsymbol{x},t)}{\bar{n}} - 1 \,, \tag{2.42}$$

where n is the galaxy number density with mean $\bar{n}$, is not equal to the matter density contrast δ. The simplest model for the bias of the galaxy density with respect to the matter distribution is the *linear deterministic model* (Kaiser, 1984), where

$$\delta_\mathrm{g}(\boldsymbol{x},t) = b\,\delta(\boldsymbol{x},t) \,, \tag{2.43}$$

where the bias factor b is independent of scale and time. A larger bias factor b implies a higher galaxy number density for a given matter overdensity. The concrete value of the bias factor, as well as its possible scale- or time dependence, hinges on the evolution and formation of galaxies. We need to model these processes to understand how galaxies trace the dark matter distribution.

Even though the contribution of galaxies to the total energy budget of the Universe is tiny, accurately describing the formation and evolution of galaxies is much more complicated than

---

[3] Burchett et al. (2020) discuss an interesting (and amusing) third approach. They modelled the LSS by simulating the behaviour of a specific type of slime mould. Their virtual slime mould found an optimised network of connections between the positions of galaxies observed by the SDSS. This network is strikingly similar to the actual matter distribution. However, further applications of this 'slime mould approach' to cosmic structure formation are unclear.

of the dark matter structure. Any successful theory of galaxy evolution needs to explain the diversity of galaxies in terms of their colour, morphology, size and gas content. Galaxies can be divided roughly into two groups: early-type galaxies, which are typically red ellipticals with little star-formation and gas, and late-type galaxies, which are bluer spiral galaxies with active star-formation. Early-type galaxies are predominantly found in denser environments like the centres of galaxy clusters, while late-types are more often in 'the field' at regions with lower density (Kauffmann et al., 2004). To explain these observations, a general picture of galaxy formation and evolution has emerged, which we describe in the following, based on Mo et al. (2010).

Galaxies build from hot gas inside dark matter halos. In massive halos, this gas can have temperatures around 10^7 K and emit Bremsstrahlung from free electrons. Due to this radiation, as well as excitation and recombination processes, the gas cools. Its chemical composition determines its cooling rate. Once the gas is cold, it shrinks and accumulates at the centre of the halo in a flat disk. There it forms the dense, cold progenitor of the halos central galaxy.

As the gas accretes, pockets of high-density arise. These pockets collapse and form stars. The star-formation rate (SFR) gives the number of formed stars as a function of the gas density. The mass distribution of the newly-born stars is prescribed by the initial mass function (IMF). This function predicts how many stars of each mass form. Since most parameters of a stars' life, like luminosity, lifetime, and eventual remnant, are determined by its mass, the IMF is a crucial component of the galaxy evolution model. Together, the IMF, the SFR and the stellar population model predict the luminosities and spectra of all stars in a galaxy. The properties of the stars determine the luminosity and colour of the whole galaxy.

In the model described so far, most of the gas in a halo would eventually turn into stars. However, this does not agree with observations, that show that only a small fraction of baryons is in stars (Roberts et al., 1991; Mathews and Brighenti, 2003). Therefore 'feedback' processes must exist, which hinder the gas from cooling and reduce star-formation. Typically, two feedback processes are dominant: supernovae and Active Galactic Nuclei (AGN). Supernovae expel large amounts of energy on short time scales. This energy causes shock waves, which heat the gas and obstruct cooling. AGN are sources of intense radiation, which also heats the surrounding gas.

Once the galaxy has formed, it undergoes different types of evolutions. First, it evolves chemically. In general, elements heavier than Helium (referred to as 'metals' in astronomy), are almost not present in the initial gas. They are produced by stars or in supernovae. Therefore their amount in the interstellar medium (ISM), the *metallicity* increases with time. The metallicity of the ISM influences the colour and luminosity of the stars forming in it. It also affects the cooling rate and SFR. Therefore the chemical evolution impacts how galaxies appear over time.

Second, galaxies evolve dynamically. Due to their motion through the potential of the halo, they are affected by tidal forces. These forces can remove gas and stars in a process called *tidal stripping*. This process changes not only the structure of the galaxies but also its colour, as less new stars form. The galaxies become redder, as blue stars reach the end of their life earlier. Galaxies also interact with the hot gas surrounding them. This gas causes a drag force which can remove cold gas from the galaxy in a process called *ram pressure stripping* (Gunn and Gott, 1972). This process also creates more red galaxies with little star-formation. As massive halos contain more gas, ram pressure stripping could explain why galaxies in denser environments exhibit less star-formation. However, the precise mechanism is not entirely understood. In particular, the time scales at which the galaxies lose their gas are unclear. Some models assume that gas is stripped instantaneously (Kauffmann et al., 1993; Baugh, 2006; Bower et al., 2006; Lagos et al., 2012), while others argue that a gradual stripping better reproduces the observed colour distribution of galaxies (Font et al., 2008; Henriques et al., 2015).

Third, galaxies interact with each other. As their dark matter halos merge, several galaxies can find themselves in the same gravitational well. There, they become *satellites* moving around a central galaxy in the centre of the well. The satellites interact with each other and the central galaxy by *galaxy harassment* or *galactic cannibalism*.

In galaxy harassment, satellites encounter during their motion in the halo and disrupt each other. Since their velocities are large, galaxies typically do not merge in these encounters, but rather lose some of their gas and stars in the process. The tidal forces in these encounters can also destroy the disks of spiral galaxies (Farouki and Shapiro, 1981). This destruction causes shock-waves in the galaxies' remaining gas, which leads to a short period of intense star-formation, a so-called 'starburst'. Consequently, harassment has a strong effect on the morphology of galaxies.

Galactic cannibalism refers to the complete merger of two galaxies. Such a merger is unlikely between two satellites because of their high relative velocities. However, due to dynamical friction, satellites lose kinetic energy and 'fall' into the centre of the halo. There, they merge with the central galaxy. The merger of satellites explains the observed high masses of central galaxies in galaxy clusters (De Lucia and Blaizot, 2007).

This general picture of galaxy formation and evolution relies on several mechanisms, whose details are not fully understood. Observations are needed to constrain these models. One observable is the relation between the observed galaxy and the underlying matter distribution. This relation is defined, in a mathematical sense, by the correlation functions of the density field δ and the galaxy number density n.

2.1.4 Random fields, correlation functions and polyspectra

In cosmology, we are rarely interested in specific values of the density contrast $\delta(\boldsymbol{x}, t)$. Instead, our goal is to give statistical predictions on the density distribution. For this, we consider $\delta(\boldsymbol{x}, t)$ as *random field*, whose statistical properties we want to explore and model.

Like all other random fields, the probability distribution $P[\delta(\boldsymbol{x}_1, t), \delta(\boldsymbol{x}_2, t) \dots]$ of the density contrast at time t is fully characterized by its moments, the *n-point correlation functions* $\xi^{(n)}$

given by

$$\xi^{(n)}(\boldsymbol{x}_1,\ldots,\boldsymbol{x}_n,t) = \langle \delta(\boldsymbol{x}_1,t)\,\delta(\boldsymbol{x}_2,t)\ldots\delta(\boldsymbol{x}_n,t)\rangle \tag{2.44}$$

$$= \int \mathrm{d}\delta(\boldsymbol{x}_1,t)\ldots\mathrm{d}\delta(\boldsymbol{x}_n,t)\;\; \delta(\boldsymbol{x}_1,t)\ldots\delta(\boldsymbol{x}_n,t)\,P[\delta(\boldsymbol{x}_1,t),\delta(\boldsymbol{x}_2,t)\ldots]\;. \tag{2.45}$$

This equation employs an *ensemble average*, suggesting that we need to average over matter distributions in multiple, independent realizations of the Universe. However, since we can only explore the properties of a single universe, we usually assume that the density field is *ergodic* (Peebles, 1980). Ergodicity implies that ensemble averages can be replaced by spatial averages, so Eq. (2.45) can be transformed into

$$\xi^{(n)}(\boldsymbol{x}_1,\ldots,\boldsymbol{x}_n,t) = \frac{1}{V^n}\int_V \mathrm{d}^3x_1\cdots\int_V \mathrm{d}^3x_n\;\; \delta(\boldsymbol{x}_1,t)\ldots\delta(\boldsymbol{x}_n,t)\;, \tag{2.46}$$

where V is an arbitrary volume.

The correlation functions are frequently replaced by their Fourier transforms, the polyspectra $P^{(n)}$. These are averages of the Fourier transformed density contrast $\hat{\delta}(\boldsymbol{k},t)$, which is

$$\hat{\delta}(\boldsymbol{k},t) = \int \mathrm{d}^3x\;\; \delta(\boldsymbol{x},t)\;\exp(-\mathrm{i}\,\boldsymbol{k}\cdot\boldsymbol{x})\;, \tag{2.47}$$

where $\boldsymbol{k}$ is the comoving wavevector. The polyspectra are given by

$$(2\pi)^3\,\delta_\mathrm{D}\left(\boldsymbol{k}_1+\cdots+\boldsymbol{k}_n\right)\;P^{(n)}(\boldsymbol{k}_1,\ldots,\boldsymbol{k}_n,t) = \left\langle \hat{\delta}(\boldsymbol{k}_1,t),\ldots,\hat{\delta}(\boldsymbol{k}_n,t)\right\rangle\;, \tag{2.48}$$

with the Dirac delta ‘function’ δ_D.

The most studied polyspectra are the matter power spectrum $P(\boldsymbol{k}_1,\boldsymbol{k}_2,t) = P^{(2)}(\boldsymbol{k}_1,\boldsymbol{k}_2,t)$, and bispectrum $B(\boldsymbol{k}_1,\boldsymbol{k}_2,\boldsymbol{k}_3,t) = P^{(3)}(\boldsymbol{k}_1,\boldsymbol{k}_2,\boldsymbol{k}_3,t)$. Due to statistical homogeneity and isotropy, the power spectrum depends only on one, and the bispectrum on three parameters aside from the cosmic time t, so we can write them as

$$P(\boldsymbol{k},-\boldsymbol{k},t) =: P(k,t)\;, \tag{2.49}$$

$$B(\boldsymbol{k}_1,\boldsymbol{k}_2,-\boldsymbol{k}_1-\boldsymbol{k}_2,t) =: B(k_1,k_2,\phi,t)\;, \tag{2.50}$$

where k is the norm of $\boldsymbol{k}$ and ϕ is the angle between $\boldsymbol{k}_1$ and $\boldsymbol{k}_2$.

Linear perturbation theory predicts the power and bispectrum, given a primordial power spectrum $P_\mathrm{prim}(k)$, which characterizes the initial density fluctuations. For density fluctuations caused by inflation, the shape of this power spectrum is a power law, whose exponent is the scale index n_s,

$$P_\mathrm{prim}(k) \propto k^{n_\mathrm{s}}\;. \tag{2.51}$$

We choose $n_\mathrm{s} = 1$, which corresponds to the Harrison-Zeldovich spectrum (Harrison, 1970; Zeldovich, 1972), because this value was used in the MR, the cosmological simulation we use in this work and which we describe in Sect. 2.2.1. However, most popular inflation models predict a n_{s} slightly smaller than 1.

From $P_{\mathrm{prim}}(k)$ we can find the linear power spectrum $P_{\mathrm{lin}}(k,t)$ as

$$P_{\mathrm{lin}}(k,t) = A\, D_+^2(t)\, T^2(k)\, P_{\mathrm{prim}}(k)\ , \tag{2.52}$$

where A is a normalisation constant, D_+ is the growth function from Eq. (2.41), and T is the transfer function.

The transfer function describes how dark matter density fluctuations at different scales k evolved. During the matter-dominated epoch, fluctuations at all scales evolved the same: They grew proportional to the scale factor a. However, this was not the case during the radiation-dominated epoch. During this epoch, fluctuations at large scales without causal contact evolved proportionally to a^2. Fluctuations at scales smaller than the comoving horizon d_{H} were suppressed and did not grow at all. This suppression, the so-called Meszaros-Effect (Meszaros, 1974), occurs, because the rapid Hubble expansion counteracts the growth of the fluctuations. Therefore, as soon as d_{H} becomes larger than a fluctuation, the fluctuation stops growing until the matter-radiation equality at a_{eq}. Consequently, the power spectrum $P(k)$ is suppressed for $k \geq \frac{2\pi}{d_{\mathrm{H}}}$. The transfer function encodes this scale dependence. Throughout this work, we use the widely adopted transfer function by Eisenstein and Hu (1998).

The normalisation constant A in Eq. (2.52) is obtained by setting the constant σ_8. This parameter describes the variance of matter fluctuations within spheres of comoving radius 8 h^{-1} Mpc. It is defined as

$$\sigma_8^2 = \frac{1}{2\pi^2} \int_0^\infty \mathrm{d}k\ \ k^2\, P(k,t_0)\, |\hat{W}(k\, R)|^2\ , \tag{2.53}$$

with $R = 8\, h^{-1}$ Mpc, t_0 being today and the Fourier transform $\hat{W}$ of a tophat filter, given as

$$\hat{W}(x) = \frac{3}{x^2}(\sin x - x\ \cos x)\ . \tag{2.54}$$

We use $\sigma_8 = 0.9$, which was assumed for the cosmological simulations described in Sect 2.2.1.

The linear bispectrum B_{lin} can be derived from P_{lin} following the derivation by Cooray and Sheth (2002) as

$$\begin{aligned} B_{\mathrm{lin}}(\boldsymbol{k}_1, \boldsymbol{k}_2, \boldsymbol{k}_3, t) &= 2\, F(\boldsymbol{k}_1, \boldsymbol{k}_2)\, P(k_1,t)\, P(k_2,t) \\ &\quad + 2\, F(\boldsymbol{k}_1, \boldsymbol{k}_3)\, P(k_1,t)\, P(k_3,t) \\ &\quad + 2\, F(\boldsymbol{k}_2, \boldsymbol{k}_3)\, P(k_2,t)\, P(k_3,t)\ , \end{aligned} \tag{2.55}$$

with

$$F(\boldsymbol{k}_1, \boldsymbol{k}_2) = \frac{5}{7} + \frac{2}{7}\, \frac{(\boldsymbol{k}_1 \cdot \boldsymbol{k}_2)^2}{k_1^2\, k_2^2} + \frac{1}{2}\, \frac{\boldsymbol{k}_1 \cdot \boldsymbol{k}_2}{k_1\, k_2} \left(\frac{k_1}{k_2} + \frac{k_2}{k_1} \right)\ . \tag{2.56}$$

In principle, the non-zero polyspectra completely describe the density field. For a Gaussian density field, all $P^{(n)}$ with $n > 2$ are given by the power spectrum, so $P(k)$ captures all

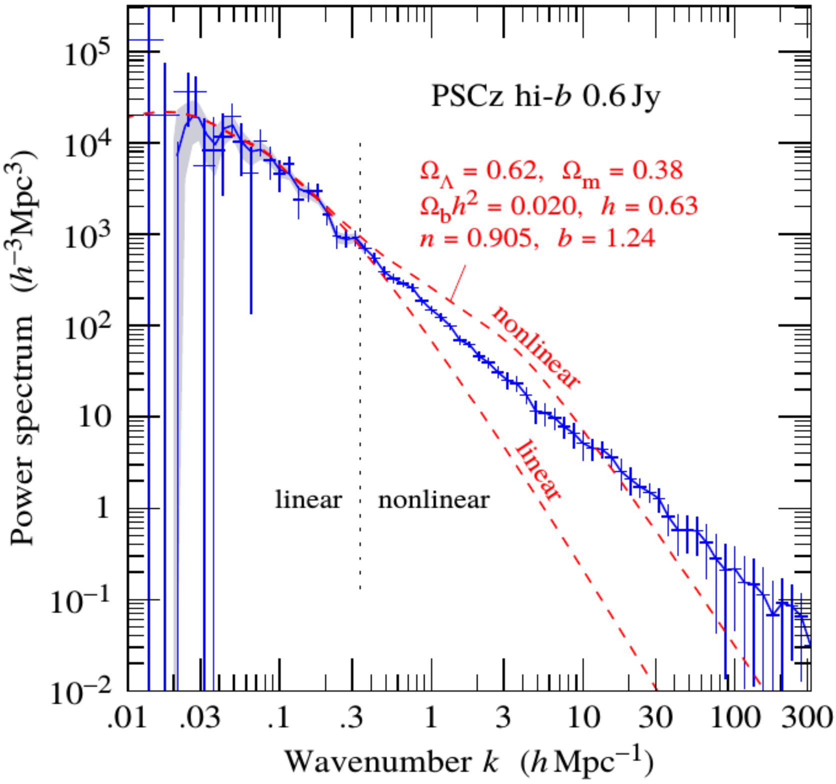

Figure 2.2: Power spectrum, measured in the IRAS Point Source Catalog (blue crosses). Also shown are the predictions of linear and non-linear perturbation theory (dashed red lines) with the cosmological parameters marked in the figure. From Hamilton and Tegmark (2002).

information of δ. Consequently, the power spectrum is the only relevant quantity for large scales and early cosmic times, for which linear perturbation theory holds. However, for smaller scales and at later times, when $\delta \gtrsim 1$, the density field is no longer Gaussian; therefore, higher-order polyspectra carry important information on the matter distribution.

The break-down of linear perturbation theory becomes apparent by comparing its prediction for the matter power spectrum to observations (Fig. 2.2). The linear theory can accurately predict the power spectrum for $k < 0.3\,h\,\mathrm{Mpc}^{-1}$ [4], which we consider the *linear regime*. For higher k, the linear theory is no longer accurate. We consider this the *non-linear regime*.

To study galaxy evolution and formation, more interesting than matter-matter correlations are correlations of δ with the galaxy number density n or the galaxy number density contrast δ_g. Examples of these galaxy-matter statistics are the two-point galaxy-matter correlation

$$\xi_{\mathrm{gm}}(\boldsymbol{x}_1, \boldsymbol{x}_2, t) = \left\langle \delta_{\mathrm{g}}(\boldsymbol{x}_1, t)\, \delta(\boldsymbol{x}_2, t) \right\rangle \,, \tag{2.57}$$

and the three-point galaxy-galaxy-matter correlation

$$\zeta_{\mathrm{ggm}}(\boldsymbol{x}_1, \boldsymbol{x}_2, \boldsymbol{x}_3, t) = \left\langle \delta_{\mathrm{g}}(\boldsymbol{x}_1, t)\, \delta_{\mathrm{g}}(\boldsymbol{x}_2, t)\, \delta(\boldsymbol{x}_3, t) \right\rangle \,, \tag{2.58}$$

---

[4] This corresponds roughly to spatial scales above $20\,h^{-1}$ Mpc.

Alternatively, we can consider the related polyspectra, the galaxy-matter power spectrum $P_{\mathrm{g}\delta}$, defined by

$$(2\pi)^3\, \delta_{\mathrm{D}}\, (\boldsymbol{k}_1 + \boldsymbol{k}_2)\; P_{\mathrm{g}\delta}(k_1, t) = \left\langle \hat{\delta}_{\mathrm{g}}(\boldsymbol{k}_1, t)\, \hat{\delta}(\boldsymbol{k}_2, t) \right\rangle \;, \tag{2.59}$$

and the galaxy-galaxy-matter bispectrum $B_{\mathrm{gg}\delta}$, defined by

$$(2\pi)^3\, \delta_{\mathrm{D}}\, (\boldsymbol{k}_1 + \boldsymbol{k}_2 + \boldsymbol{k}_3)\; B_{\mathrm{gg}\delta}(k_1, k_2, \phi, t) = \left\langle \hat{\delta}_{\mathrm{g}}(\boldsymbol{k}_1, t)\, \hat{\delta}_{\mathrm{g}}(\boldsymbol{k}_2, t)\, \hat{\delta}(\boldsymbol{k}_3, t) \right\rangle \;, \tag{2.60}$$

where $\hat{\delta}_{\mathrm{g}}(\boldsymbol{k}, t)$ is the Fourier transform of $\delta_{\mathrm{g}}(\boldsymbol{x}, t)$, and ϕ is the angle between $\boldsymbol{k}_1$ and $\boldsymbol{k}_2$.

These functions encode information on how galaxies form, evolve and interact inside the dark matter distribution (Simon, 2005; White et al., 2007). The galaxy-matter correlations are easier accessible in surveys than matter-matter correlations because the galaxy distribution is a direct observable. In contrast, we need to infer the dark matter distribution indirectly.

Modelling galaxy-matter correlations, though, is more complicated than matter-matter correlations, for three reasons. First, as discussed in Sect. 2.1.3, galaxy formation occurs inside dense dark matter halos at scales below a few Megaparsecs, which is in the non-linear regime (White and Rees, 1978). Accordingly, we cannot use linear perturbation theory to constrain the matter distribution. Second, galaxies are affected by more phenomena than dark matter, which only interacts gravitationally. These effects, such as star-formation, feedback by active galactic nuclei, and interactions with the intracluster medium, have to be carefully modelled to obtain accurate predictions for the galaxy-matter correlations (Vogelsberger et al., 2020). Third, galaxies come in different types, classified according to properties such as colour, SFR, or stellar mass. These types show separate physical properties and spatial distributions. Consequently, the galaxy-matter correlations depend sensitively on the studied galaxy population and selection function (Zehavi et al., 2005).

Nevertheless, theoretical models of galaxy-matter correlations are possible. An analytical way to derive them is the halo model, which we discuss in Sect. 2.3. They are also predicted by cosmological simulations, whose fundamental principles we describe in the next section.

2.2 Cosmological simulations

Cosmological simulations distinguish between dark and baryonic matter. The distribution of dark matter can be modelled accurately with N-body simulations, which we discuss in the following section. The evolution of baryons, including galaxies, can be either simulated with SAMs using the dark matter distribution from an N-body simulation (see Sect. 2.2.2) or with hydrodynamic simulations which directly calculate the dynamics of baryons (see Sect. 2.2.3).

2.2.1 N-Body simulations

Dark-matter-only N-body simulations have been used since the 1970s (e.g. Peebles, 1970; Press and Schechter, 1974). Since then, increased computational power and improved numerical techniques enabled larger simulated volumes and better resolution (Vogelsberger et al., 2020). Major successes of N-body simulations were the determination of the halo mass function (HMF), the dark matter halo profile, and the bottom-up structure formation (Sheth and Tormen, 1999; Navarro et al., 1996; Springel et al., 2005).

N-body simulations use that dark matter acts only gravitationally, and that structure formation occurs in the weak-field limit of GR. They model the dark matter distribution by individual macroscopic particles behaving according to Newtonian dynamics. These particles are placed into a cube with fixed comoving side length, in which they evolve due to the gravitational forces between them. The mass of an individual particle determines the mass resolution of the simulation.

Linear perturbation theory sets the initial distribution of dark matter particles. The probability distribution of their density is set to a Gaussian with power spectrum $P_{\rm lin}$ given in Eq. (2.52) at high redshift, typically $z \simeq 100$. The simulation then evolves this initial distribution of particles and outputs the positions and velocities of these particles at a set of redshifts. These outputs are also referred to as *snapshots*.

The force on the ith particle at proper position $\boldsymbol{r}_i$ with mass m_i is given by

$$\boldsymbol{F}_i = G \sum_{j \neq i} \frac{m_i \, m_j \, (\boldsymbol{r}_i - \boldsymbol{r}_j)}{|\boldsymbol{r}_i - \boldsymbol{r}_j|^3} \, , \tag{2.61}$$

where the $\boldsymbol{r}_j$ are the other positions of the particles. For N particles, the computational complexity of calculating the total force on each particle is $\mathcal{O}(N^2)$.Therefore, several numerical techniques reduce the complexity, such as the particle-mesh (PM) algorithm (Hockney and Eastwood, 1981). Here, particles are assigned positions on a regular mesh with approximately N cells, so the density distribution is defined on the mesh and can be converted to Fourier space with a Fast Fourier Transform. The Fourier transform $\hat{\Phi}$ of the gravitational potential is then given by the Fourier transformed Poisson equation

$$k^2 \, \hat{\Phi}(\boldsymbol{k}) = -4\pi G \, \hat{\rho}(\boldsymbol{k}) \, . \tag{2.62}$$

This approach reduces the numerical complexity to $\mathcal{O}(N \, \ln N)$.

However, the size of the mesh cells limits the spatial resolution of the simulation. Since the gravitational field is smoothed, the simulation is inaccurate at scales below a few mesh cells. Therefore, PM codes are often supplemented by corrections for nearby particles. The forces of these particles are summed and added to the contribution of the overall gravitational potential. Codes with this correction are referred to as particle-particle particle-mesh (P^{3}M) algorithms.

A different approach to reducing the computational complexity of N-body simulations are tree codes (Dehnen, 2000). In these codes, particles are grouped according to their position. The force of distant particles on a particular other particle is approximated by the contribution of a point mass at the centre of the particle group. In this way, not all particle-particle forces need to be computed. This method reduces the computational complexity to $\mathcal{O}(N \, \ln N)$.

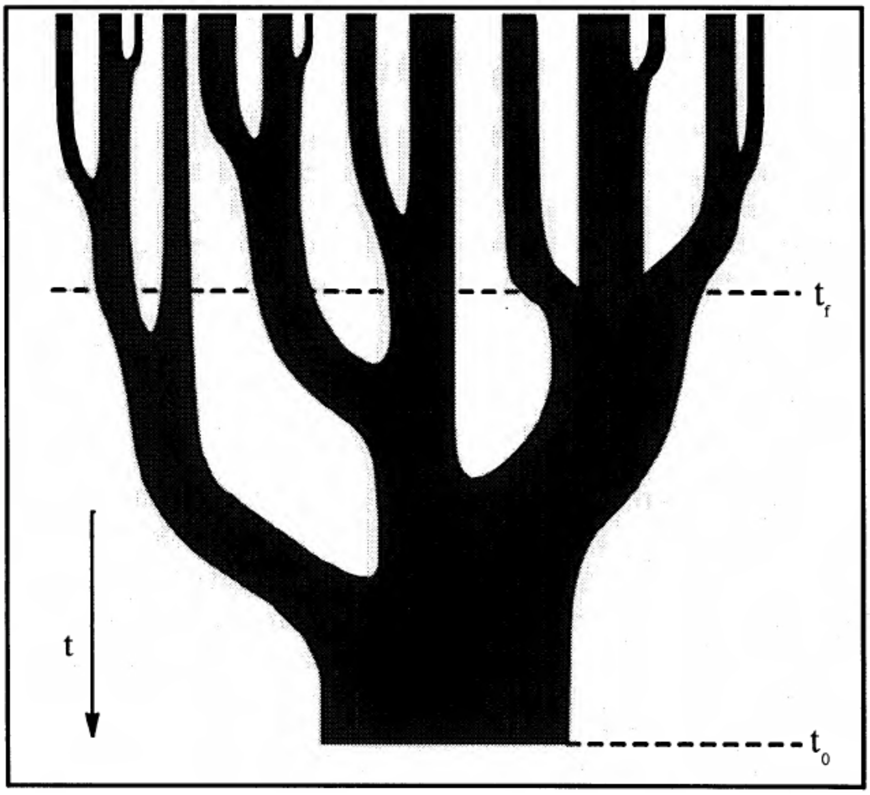

Figure 2.3: Schematic representation of a dark matter halo merger tree. Time increases on the vertical direction from top to bottom. Each "branch" represents a halo, whose width relates to the halos mass. From Lacey and Cole (1993)

Additionally, N-body simulations use a softening length, below which gravitational forces are reduced. This modification reduces unphysical scattering of nearby particles in the simulation. The softening length and size of mesh cells determine the spatial resolution of a simulation.

During the evolution, dark-matter particles attract each other and form larger overdensities and self-bound dark matter halos. These halos merge to increasingly massive halos. *Merger trees* (Fig. 2.3) record this halo growth and the formation of each halo from the merger of smaller parent halos. The merger history determines the distribution of galaxies and other baryons, as they follow the merging dark matter halos.

To find dark matter halos in simulations, two different approaches are possible: friends-of-friends (FOF)-finders or spherical-overdensity (SO)-finders. The SO approach defines a halo as a spherical region whose mean density is at least Δ_{thresh} higher than the background density $\bar{\rho}$ (Press and Schechter, 1974). The number of detected halos depends on Δ_{thresh}. Often $\Delta_{\mathrm{thresh}} = 180$ is chosen (Lacey and Cole, 1994; Sheth and Tormen, 1999), but other values, for example $\Delta_{\mathrm{thresh}} \in [200, 320]$ by Tinker et al. (2008), have also been used. The number and size of halos in the simulation is influenced by this choice.

SO-finders detect halos by centring a sphere on a particle and decreasing its radius until the overdensity inside the sphere exceeds Δ_{thresh}. The particles inside are then counted as part of a halo and removed. The process is repeated around other particles until all particles belong to halos. The main drawback of SO-finders is their assumption of spherical halos. Masses, as well as the total number of halos, are therefore biased.

FOF-finders (Davis et al., 1985) account for non-spherical halos by using a different halo definition. They define them as collections of particles, whose separations are smaller than a linking length b. The finder first selects a particle P_1. It then counts all particles P_2 with distances less than b from P_1 as part of a halo. Next, all particles, which are less than b away from the P_2, are assigned to the same halo. The FOF-finder repeats this process until no new particles are less than b away from halo members.

The choice of b is critical for the shape and number of the detected halos. Commonly, FOF-finders assume a linking length between $0.15\,n_\mathrm{p}^{-1/3}$ and $0.3\,n_\mathrm{p}^{-1/3}$, where n_p is the mean number density of simulated particles (Springel et al., 2005; Jenkins et al., 2001; Davis et al., 1985).

The softening length of an N-body simulation determines its spatial resolution, while the mass of its particles limits the mass resolution. Increasing the number of particles while decreasing their masses leads to higher resolutions but also increases the computational complexity of the simulation.

The resolution and size of a simulation determine its applications. Simulations with smaller volumes but higher resolution (e.g. Springel et al., 2008; Stadel et al., 2009) allow studies of individual dark matter (sub)halos. In contrast, larger simulations (e.g. Springel et al., 2005; Klypin et al., 2011) are useful to explore the statistical properties of the LSS.

In this work, we use the MR, which is a large-volume N-body simulation. It was computed with the GADGET2 code (Springel, 2005). This code uses a mixture of the tree-code and PM algorithms. The long-range particle interaction is calculated according to the PM approach. In contrast, the short-range interaction of nearby particles is calculated with a tree-code The MR has a comoving side length of $500\,h^{-1}$ Mpc and traces 2160^3 dark matter particles with mass $m = 8.76 \times 10^8\,h^{-1}\,\mathrm{M}_\odot$. It assumes the cosmological parameters in Table 2.1 and has a softening length of $5\,h^{-1}$ kpc.

2.2.2 Semi-analytic models of galaxy formation and evolution

One approach to simulating the formation and evolution of galaxies is through physically motivated analytic models for baryonic processes. These models are calibrated by observations, for instance of the fraction of satellite galaxies per halo, the stellar mass function of galaxies, or the stellar-mass-to-halo-mass ratio. They are implemented on baryons in dark matter halos from an N-body simulation. Combining analytical models and numerical simulations leads to SAMs (Baugh, 2006; Benson, 2010).

The evolution of galaxies in a SAM follows several steps that mimic the processes influencing real galaxies outlined in Sect. 2.1.3. Initially, each halo in the N-body simulation receives a fraction of baryons with mass $m_\mathrm{b} = \frac{\Omega_\mathrm{b}}{\Omega_\mathrm{m}}\,m$, where m is the halo mass. 75% of the baryon mass is ionised hydrogen and 25% ionised helium, which corresponds to the baryon composition after the initial nucleosynthesis in the early Universe. These baryons then cool down, according to an assumed cooling rate model. Cold gas accretes towards the halo centre and forms the central galaxy of the halo.

In the cold gas, stars are born. The SFR depends on the gas surface mass density according to the stellar population model of the SAM. The IMF assumed by the SAM gives the mass distribution of the newly-born stars. After a while, massive stars end their lives in supernovae. These inject metals and cold gas into the ISM, thereby changing its chemical composition. New stars form from this enriched ISM.

Galaxies in the SAM also interact with each other and the hot gas surrounding them. To calculate these interactions, SAMs model tidal and ram pressure stripping, galaxy harassment and mergers. The models include assumptions on the rate of interactions and the time scales on which galaxies are entirely stripped of their gas.

The main advantage of SAMs is their modest computational cost. Therefore, these models can be run on large cosmological volumes, leading to precise predictions of galaxy statistics. Their flexibility also allows for an exploration of their parameter space with a Monte Carlo Markov chain (Henriques et al., 2009) or emulators (Bower et al., 2010). Their principal drawback is that they idealise the thermal and spatial profiles of baryons, as well as the physical processes. Some of their assumptions might not be true, so their predictions can be biased. Furthermore, as they do not include individual baryonic particles, SAMs cannot predict detailed gas and stellar dynamics.

There exist a variety of SAMs (Bower et al., 2006; Lagos et al., 2012; Guo et al., 2011; Henriques et al., 2015), based on the same fundamental principles but using different assumptions on the physical processes. Some of the most important differences are the choice of halo finder in the underlying N-body simulation, the definition of central and satellite galaxies, the treatment of star-formation, and environmental interaction. The predictions of SAMs also vary due to the choice of IMF and stellar population model (Guo et al., 2016).

In this work, we use two different SAMs implemented in the MR. These are the Munich SAM by Henriques et al. (2015, H15) and the Durham SAM by Lagos et al. (2012, L12). Table 2.2 summarises some of the differences between these models. Aside from the choice of IMF and stellar population model, these are the treatment of satellite galaxies, star-formation and ram pressure stripping.

In the L12 SAM, satellite galaxies remain satellites unless they merge with a central galaxy. In the H15 SAM, though, satellite galaxies that have drifted far away from their host halo centres are reclassified as central galaxies. This effect reduces the fraction of satellites in H15 compared to L12.

The SFR in the L12 SAM is proportional to the cold gas mass of a galaxy. In contrast, in the H15 SAM, stars form only when the gas density exceeds a threshold. Therefore, galaxies with little gas show more star-formation in the L12 SAM.

Table 2.2: Differences of used SAMs

Property	Lagos et al. (2012)	Henriques et al. (2015)
IMF	Kennicutt (1983)	Chabrier (2003)
Stellar Population model	Bruzual and Charlot (2003)	Maraston (2005)
Evolution of satellites	Satellites become centrals only if they merge with a central galaxy	Satellites can become centrals when distant from their halo center
Star-formation	SFR is proportional to total cold gass mass	star-formation occurs only, if gas density exceeds threshold
Environmental processes	Instantaneous ram pressure stripping	Gradual ram pressure stripping

Environmental effects, such as ram pressure stripping, are also treated differently between the SAMs. L12 employs instantaneous ram pressure stripping, which quickly depletes satellites of their hot gas. This gas depletion rapidly quenches star-formation. H15 uses gradual ram pressure stripping that removes less of the gas reservoir.

2.2.3 Hydrodynamical simulations

A different approach to describing the evolution of galaxies is using hydrodynamic simulations (see Vogelsberger et al., 2020, for a review). These simulations directly solve the hydrodynamic equations for the baryon content of the Universe, simultaneously to evolving the dark matter distribution with an N-body simulation. Therefore, they predict the detailed distribution of gas in and around galaxies. In contrast to SAMs, they can predict gas dynamics and galaxy interactions.

However, this additional information comes at the cost of high numerical complexity. This complexity is due to the variety and broad dynamic range of baryonic effects. Consequently, hydrodynamic simulations with large volumes suitable for studies of galaxy statistics have been available only for the past few years (Dubois et al., 2014; Vogelsberger et al., 2014; Schaye et al., 2015).

In hydrodynamical simulations, baryons are modelled as inviscid ideal gases with density ρ_b, velocity field $\mathbf{v}$ and pressure P. Therefore, they follow the hydrodynamical equations

$$\frac{\partial \rho_\mathrm{b}}{\partial t} + \boldsymbol{\nabla}_r \cdot (\rho_\mathrm{b}\mathbf{v}) = 0 \,, \tag{2.63}$$

$$\frac{\partial \mathbf{v}}{\partial t} + (\mathbf{v}\cdot\boldsymbol{\nabla}_r)\cdot\mathbf{v} + \frac{\boldsymbol{\nabla}_r P}{\rho_\mathrm{b}} = -\boldsymbol{\nabla}_r \Phi \,, \tag{2.64}$$

$$\nabla_r^2 \Phi = 4\pi G \left(\rho_\mathrm{b} + \rho_\mathrm{cdm}\right) \,, \tag{2.65}$$

where ρ_{cdm} is the density of dark matter. These equations correspond to Eqs (2.26) – (2.28) with an added pressure term in the Euler equation. Several modern hydrodynamic simulations also account for magnetic fields around baryons by solving instead the equations of magnetohydrodynamics (see e.g., Bartelmann, 2013).

The simulations are initialised by inserting baryons consisting purely of hydrogen and helium gas into a simulation box, alongside dark matter particles. Dark matter is treated the same as in a regular N-body simulation. Meanwhile, baryons evolve according to the hydrodynamic equations in (2.63) – (2.65). Once the gas density is high enough, stars are formed, which eventually create galaxies. In this process, the formation and evolution of galaxies are replicated.

Three different approaches are used to solve the hydrodynamical equations: the Eulerian, the Lagrangian and the mixed Eulerian-Lagrangian framework. In the Eulerian framework (used for example in Horizon-AGN, Dubois et al., 2014), the simulation box is divided into a mesh. The density and velocity of the baryon fluid are calculated discretised for each mesh cell. Since the dynamical range of cosmological simulations is quite large, a regular mesh would lead to a too coarse binning in high-density regions in the simulations, while low-density areas would be covered by too many cells. Therefore, Eulerian simulations usually use adaptive mesh refinement algorithms, which create sub-meshes in regions of high density.

In the Lagrangian framework, used for instance, by Evolution and Assembly of GaLaxies and their Environments (EAGLE; Schaye et al., 2015), the calculation follows individual fluid elements through space and time. One example of such an approach is smoothed-particle hydrodynamics. Here, the continuous fluid is approximated by several sampling particles. These individual particles trace the overall baryon distribution. They are evolved according to equations of motion derived from the hydrodynamical equations and the gravitational forces between them and the dark matter field.

Mixed Eulerian-Lagrangian approaches combine the two frameworks by using a moving mesh (Springel, 2010). In this approach, similar to the Lagrangian framework, several sampling particles are chosen. However, instead of directly tracing the baryon distribution, these particles are used to define a mesh. This mesh is constructed such that its cells are small in high-density and large in low-density regions. Similarly to the Eulerian framework, the density and velocity field are discretised on this mesh. However, the sampling points evolve according to the hydrodynamical equations. Therefore, the mesh also changes, according to the dynamics of the baryon fluid. The moving-mesh formulation is used, for example, in the IllustrisTNG simulation (Springel et al., 2018).

Hydrodynamic simulations still require assumptions on several physical processes that occur on scales below the resolution limit of the simulation. Therefore, sub-resolution models need to complement them. These models describe, for example, the SFR, phase transitions of the ISM and the accretion rate of supermassive black holes. They are calibrated by adjusting their parameters, so that the simulation matches certain key observables, for example, the galaxy stellar mass function (Vogelsberger et al., 2020).

2.3 Halo model

The halo model is an analytical approach to model the cosmic galaxy and matter distribution. It is phenomenologically motivated by the observation that most dark matter concentrates in dense halos and galaxies form only within these dense regions (White and Rees, 1978). Dark matter halos form, when the density contrast in a region exceeds the critical value $\delta_\mathrm{c}(z)$. The region then collapses and virializes to a self-bound halo (Press and Schechter, 1974). After virialization, the halo reaches the density $\rho_\mathrm{vir} = \Delta\,\bar{\rho}$, where $\bar{\rho}$ is the mean density of the Universe. For a flat ΛCDM universe, the following fitting functions can be used (Bullock et al., 2001):

$$\delta_\mathrm{c}(z) = 1.686\,\left\{1 + 0.0123\log_{10}\left[\Omega_\mathrm{m}\,(1+z)^3\right]\right\}\;, \tag{2.66}$$

$$\Delta(z) = 178\left\{1 + 0.4093\left[\frac{(\Omega_\mathrm{m}^{-1} - 1)^{1/3}}{1+z}\right]^{2.71572}\right\}\;. \tag{2.67}$$

The halo model simplifies the matter distribution by assuming that all of dark matter is part of halos. The masses of these halos fully determine the physical properties of galaxies residing in them, including their number, population and spatial distribution.

With this assumption, the halo model gives an analytical framework for the calculation of galaxy-matter correlation functions. This framework is not limited to the linear regime, but also extends to highly non-linear scales. Cooray and Sheth (2002) give a review of the halo model in terms of galaxy-matter statistics.

Even though the halo model neglects environmental influences and the halo merger history on the galaxy distribution, its prediction for the galaxy-galaxy two-point correlation function agrees well with observations (Zehavi et al., 2011). Its forecast for the matter power spectrum also agrees with N-body simulations (Kravtsov et al., 2004; Zheng et al., 2005). Furthermore, the halo model can model the galaxy-matter power spectrum (Mandelbaum et al., 2006; Clampitt et al., 2016; Dvornik et al., 2018) and correlations between the matter distribution and the Sunyaev-Zel'dovich effect (Mead et al., 2020). It is therefore reasonable to also model third-order and higher galaxy-matter correlations with the halo model.

Rödinger (2009) proposed a halo model for higher-order galaxy-matter statistics, including the second-, third- and fourth-order galaxy-matter correlations. Martin (2019) used this model to predict the galaxy-galaxy-matter bispectrum. They found the model parameters by fitting it to observed galaxy-matter two-point correlation functions and then calculated the expected third-order signal. Their predictions agree well with measurements in Canada-France-Hawaii Telescope Lensing Survey (CFHTLenS; Heymans et al., 2012). However, their study was limited to auto-correlations with galaxies from the same population. They could not consider the galaxy-galaxy-matter cross-correlation, as this correlation depends on the joint distribution of galaxies from different populations inside a halo. This joint distribution cannot be predicted from the galaxy-matter two-point correlation.

In Chapter 5, we will instead model the galaxy-galaxy-matter bispectrum for both auto- and cross-correlations, based on the approaches by Rödinger (2009) and Martin (2019). For this, we require different ‘ingredients’ of the halo model, which we describe in the following. They are the spatial dark matter halo profile, the HMF, the halo bias and the halo occupation distribution (HOD).

2.3.1 Dark matter halo profile

The halo model assumes that all halos have the same density profile $\rho(\boldsymbol{r}|m)$, which depends only on the separation $\boldsymbol{r}$ from the halo centre and the halo mass m. It can also be expressed in terms of the normalised halo profile $u(\boldsymbol{r}|m)$ as

$$\rho(\boldsymbol{r}|m) = m\, u(\boldsymbol{r}|m) \;, \tag{2.68}$$

where

$$\int \mathrm{d}^3 r \;\; u(\boldsymbol{r}|m) = 1 \;. \tag{2.69}$$

N-body simulations suggest that most dark matter halos follow the same $\rho(\boldsymbol{r}|m)$, the Navarro-Frenk-White (NFW) profile (Navarro et al., 1996),

$$\rho(\boldsymbol{r}|m) = \rho_\mathrm{s} \left[\frac{r}{r_\mathrm{s}} \left(1 + \frac{r}{r_\mathrm{s}}\right)^2\right]^{-1} \;, \tag{2.70}$$

where r_s and ρ_s are the scale radius and -density, respectively. The total mass of the NFW profile diverges. However, the total halo mass can be replaced by the mass m_{200}. This is the mass enclosed by a sphere around the halo center with the radius r_{200}, inside which the mean density of the halo is exactly 200 times the mean density of the Universe [5],

$$m_{200} = \int_0^{r_{200}} \mathrm{d}r \;\; r^2\, \rho(r) = \frac{4\pi}{3} \;(200\,\bar{\rho})\; r_{200}^3 \;. \tag{2.71}$$

For the NFW-profile m_{200} is The mass m_{200} is

$$m_{200} = \frac{4\pi\rho_\mathrm{s}}{c^3} \left[\ln(1+c) - \frac{c}{1+c}\right] r_{200}^3 \;, \tag{2.72}$$

where $c = r_{200}/r_\mathrm{s}$ is called concentration parameter.

The concentration parameter c depends on the halo redshift and mass, as well as the underlying cosmology and details of the non-linear structure formation. Several models for $c(m, z)$ have been proposed (Dolag et al., 2004). We use the formula obtained in N-body simulations by Bullock et al. (2001) for a ΛCDM universe,

$$c(m, z) = \frac{c_0}{1+z} \left(\frac{m}{m^\star}\right)^{-\alpha} \;, \tag{2.73}$$

---

[5] In their original derivation Navarro et al. (1996) defined m_{200} as region, whose density is 200 times the critical density ρ_crit, given in Eq. (2.13). However, the fitting function for the concentration by Bullock et al. (2001) was found for m_{200} in terms of the mean density $\bar{\rho}$. Therefore, we use this definition in terms of the mean density.

with $c_0 = 9$ and $\alpha = 0.13$. The mass $m^\star$ is the mass enclosed by a sphere of radius $r_\star$,

$$m^\star = \frac{4\pi}{3} r_\star^3 \,, \tag{2.74}$$

where $r_\star$ is the scale at which the standard deviation of density fluctuations is equal to the critical density δ_{cr}. It is given by

$$\sigma^2(m^\star) := \int \mathrm{d}^3k \;\; P(k)\, \hat{W}^2(r_\star\, k) = \delta_{\mathrm{c}}^2 \,, \tag{2.75}$$

where $\hat{W}$ is the Fourier transformed tophat filter given in Eq. (2.54).

The Fourier transform of the NFW profile, a useful quantity for the calculation of polyspectra, is (Scoccimarro et al., 2001),

$$\hat{\rho}(k|m) = m\, \hat{u}(k|m) \tag{2.76}$$

$$\begin{aligned} &= m\, f(c) \left\{ \sin\!\left(\frac{kr_{200}}{c}\right) \left[\mathrm{Si}\left(\frac{kr_{200}(1+c)}{c}\right) - \mathrm{Si}\left(\frac{kr_{200}}{c}\right)\right] \right. \\ &\qquad + \cos\!\left(\frac{kr_{200}}{c}\right) \left[\mathrm{Ci}\left(\frac{kr_{200}(1+c)}{c}\right) - \mathrm{Ci}\left(\frac{kr_{200}}{c}\right)\right] \\ &\qquad \left. - \frac{\sin(kr_{200})}{kr_{200}} \, \frac{c}{1+c} \right\} , \end{aligned} \tag{2.77}$$

with

$$f(c) = \left[\ln(1+c) - \frac{c}{1+c}\right]^{-1} \,, \tag{2.78}$$

and

$$\mathrm{Si}(x) = \int_0^x \mathrm{d}y \;\; \frac{\sin(y)}{y} \,, \tag{2.79}$$

$$\mathrm{Ci}(x) = -\int_x^\infty \mathrm{d}y \;\; \frac{\cos(y)}{y} \,. \tag{2.80}$$

2.3.2 Halo mass function

The HMF $n(m)\,\mathrm{d}m$ describes the comoving number density of dark matter halos with mass between m and $m + \mathrm{d}m$. It depends not only on cosmic structure formation, but is also a sensitive probe of cosmology (e.g Eke et al., 1996; Vikhlinin et al., 2009).

Press and Schechter (1974) derived the first analytical model for the HMF under the assumption that dark matter halos collapse spherically. They further assumed that the spatial volume filled with halos of mass m is proportional to the probability of the initial matter field to exceed the critical density contrast in a sphere with radius $r = (3m/4\pi\bar{\rho})^{1/3}$. Their HMF, including a manually inserted factor of two to account for the cloud-in-cloud problem (Bond et al., 1991), is

$$n(m)\ \mathrm{d}m = \frac{1}{\sqrt{2\pi}}\,\frac{\bar{\rho}}{m^2}\,\nu\,\exp\left(-\frac{\nu^2}{2}\right)\frac{\mathrm{d}\ln\nu}{\mathrm{d}\ln m}\ \mathrm{d}m\ , \tag{2.81}$$

with $\nu = \delta_\mathrm{c}/\sigma(m)$ and the $\sigma(m)$ defined in Eq. (2.75).

However, N-body simulations show that the Press-Schechter HMF cannot fully describe the halo distribution, as dark matter halos generally collapse ellipsoidally and not spherically. Therefore, Sheth and Tormen (1999) proposed the fitting formula

$$n(m)\ \mathrm{d}m = \sqrt{\frac{2}{\pi}}\,A\left[1 + \frac{1}{(q\,\nu)^{2p}}\sqrt{\frac{(q\,\nu)^2}{2\pi}}\ \exp\left(-\frac{(q\,\nu)^2}{2}\right)\right]\frac{\bar{\rho}}{m^2}\,\frac{\mathrm{d}\ln\nu}{\mathrm{d}\ln m}\ \mathrm{d}m\ , \tag{2.82}$$

with $A = 0.322$, $p = 0.3$, and $q = 0.707$ found in N-body simulations. In contrast to the Press-Schechter formalism, this function also accounts for the collapse of non-spherical halos (Sheth et al., 2001). We use this HMF throughout the work.

Other N-body simulations yielded slightly different fitting formulas for the HMF (Jenkins et al., 2001; Tinker et al., 2008). However, the variations between the HMFs are small and mainly relevant for very high halo masses.

2.3.3 Halo bias

The polyspectra of dark matter halos are in general different from those of the overall dark matter distribution since halos only form if the initial density fluctuations in a region exceeded δ_c. The difference in the density contrast δ_H of halos to the overall density contrast δ can be modelled with the bias terms $b_{(n)}(m,z)$ (Mo et al., 1997),

$$\delta_\mathrm{H}(\boldsymbol{x},t|m) = b_1(m,z_t)\,\delta(\boldsymbol{x},t) + \frac{1}{2}\,b_2(m,z_t)\,\delta^2(\boldsymbol{x},t) + \frac{1}{6}\,b_3(m,z_t)\,\delta^3(\boldsymbol{x},t) + \dots\ , \tag{2.83}$$

where z_t is the redshift at cosmic time t. Here, we only take into account the first-order bias, which can be approximated with

$$b_1(m,z) = 1 + \frac{q\,\nu^2(z) - 2}{\delta_\mathrm{c}(z)} + \frac{2p}{1 + q^p\,\nu^{2p}(z)}\,\frac{1}{\delta_\mathrm{c}(z)}\ , \tag{2.84}$$

with $q = 0.707$ and $p = 0.3$ for a Sheth-Tormen HMF (Scoccimarro et al., 2001). With this bias, the halo power spectrum is

$$P_\mathrm{H}(\boldsymbol{k},-\boldsymbol{k},t|m_1,m_2) = b_1(m_1,z_t)\,b_1(m_2,z_t)\,P_\mathrm{lin}(k,t)\ , \tag{2.85}$$

where P_lin is the linear matter power spectrum, given by Eq. (2.51). The halo bispectrum is

$$B_\mathrm{H}(\boldsymbol{k}_1,\boldsymbol{k}_2,-\boldsymbol{k}_1-\boldsymbol{k}_2,t|m_1,m_2,m_3) = b_1(m_1,z_t)\,b_1(m_2,z_t)\,b_1(m_3,z_t)\,B_\mathrm{lin}(k_1,k_2,\phi,t)\ , \tag{2.86}$$

where ϕ is the angle between $\boldsymbol{k}_1$ and $\boldsymbol{k}_2$, and B_lin is the linear matter bispectrum, given by Eq. (2.53).

2.3.4 Halo occupation distribution

To predict the galaxy-matter correlation, the halo model requires two assumptions on the galaxy distribution: the spatial galaxy distribution inside a halo $n(\boldsymbol{x}|m) = \bar{n}\, u_\mathrm{g}(\boldsymbol{x}|m)$ and the HOD $N(m)$ which is the number of galaxies N in a halo with mass m.

Often, it is assumed that the spatial galaxy distribution follows the halo density profile. We also assume that both galaxies and dark matter follow NFW profiles. However, we allow the galaxy distribution to have a different concentration c_g than the dark matter distribution. For this, we introduce the parameter $f = \frac{c_\mathrm{g}}{c}$, where c is the dark matter concentration. So, if u is an NFW profile with concentration c, u_g is an NFW profile with concentration $c_\mathrm{g} = f\, c$. If $f = 1$, the galaxy distribution follows the matter distribution exactly.

Modelling the HOD is slightly more complicated. For the calculation of two- and three-point galaxy-matter statistics, we need models for the mean halo occupation number $\langle N|m\rangle$ and the mean number of galaxy pairs $\langle N\,(N-1)|m\rangle$ per halo mass m. If we calculate the galaxy-galaxy-matter bispectrum for galaxies from different populations 1 and 2, we further need the correlation $\langle N_1\, N_2|m\rangle$ of their HODs $N_1(m)$ and $N_2(m)$.

Using these assumptions, together with the other ingredients of the halo model, we can model the correlation functions of the galaxy and matter distribution. In particular, we can model the galaxy-galaxy-matter correlation function, as we show in Chapter 5. These correlation functions can be projected and transformed to observables from gravitational lensing, which is one of the best methods to explore the connection of baryonic and dark matter. We explain this method in the following section.

2.4 Gravitational lensing

Gravitational lensing is the method-of-choice to explore the matter distribution of the Universe, as its effects are well-understood, and it acts both on baryonic and dark matter. It describes that, as a consequence of GR, large masses warp space-time and thereby bend light rays similarly to optical lenses (Einstein, 1936). Accordingly, images of distant objects appear distorted.

Dyson et al. (1920) made the first detection of the gravitational lensing effect. Their expedition observed the apparent positions of stars in the Hyades cluster during the solar eclipse of 1919 and compared them to the position of the stars at night. The positions shifted during the solar eclipse because the Sun acted as a gravitational lens and its mass bent the light rays from the stars. The measured shift in the position of the stars was consistent with the predictions by GR and increased scientific and public support for Einstein's theory immensely.

Today, gravitational lensing is mostly observed by measuring the distortion of galaxy shapes by the matter content of the Universe, as first proposed by Zwicky (1937a,b). This measurement is an ideal tool for constraining the distribution of dark matter as well as galaxy-matter-correlations. A recent review of gravitational lensing can be found in Bartelmann (2010).

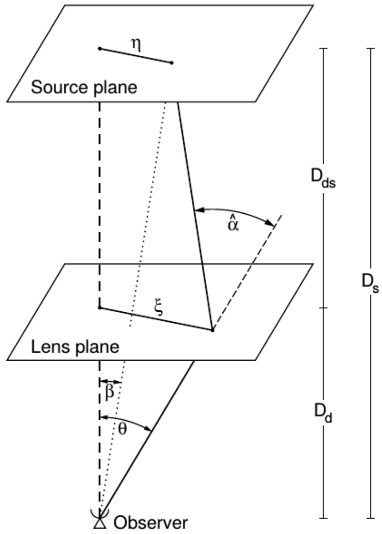

Figure 2.4: Sketch of a gravitational lensing system. The distances D_s, D_d, and D_ds are the angular diameter distances to the source, to the lens, and from the lens to source, respectively. From Bartelmann and Schneider (2001).

2.4.1 Lens equation

We consider gravitational lensing in the weak-field limit of GR, with the lensing systems embedded in Minkowskian space-time. For this, we assume that the lenses gravitational potential Φ, its typical scales L and intrinsic velocity $\mathbf{v}$ are all small, so,

$$|\Phi| \ll c^2 , \qquad L \ll \frac{c}{H_0} , \qquad |\mathbf{v}| \ll c . \tag{2.87}$$

Figure 2.4 shows a schematic sketch of a gravitational lens system. Light from a background object, the *source*, is bent by the gravitational potential of a foreground object, the *lens*. This deflection shifts the apparent position of the source. Using the distances and angles defined in Fig. 2.4 and the assumption that the gravitational potential of the lens lies on a single plane,

$$\boldsymbol{\beta} = \boldsymbol{\theta} - \frac{D_\mathrm{ds}}{D_\mathrm{s}} \hat{\boldsymbol{\alpha}} =: \boldsymbol{\theta} - \boldsymbol{\alpha} , \tag{2.88}$$

where we defined the *reduced deflection angle* $\boldsymbol{\alpha}$. The reduced deflection angle depends on the surface mass density Σ of the lens,

$$\Sigma(\boldsymbol{\theta}) = \int \mathrm{d}r_3 \, \rho(\boldsymbol{r}) , \tag{2.89}$$

with $\boldsymbol{r} = r_3 \, (\boldsymbol{\theta}, 1)$. With this surface mass density, we can define the lensing potential Ψ,

$$\Psi(\boldsymbol{\theta}) = \frac{4G}{c^2} \frac{D_\mathrm{d} D_\mathrm{ds}}{D_\mathrm{s}} \int \mathrm{d}^2\theta' \; \Sigma(\boldsymbol{\theta}') \, \ln(|\boldsymbol{\theta} - \boldsymbol{\theta}'|) . \tag{2.90}$$

The reduced deflection angle α is the gradient of this potential, so $\boldsymbol{\beta}$ is related to the lensing potential by

$$\boldsymbol{\beta} = \boldsymbol{\theta} - \nabla\Psi \, . \tag{2.91}$$

Taking the gradient of Eq. (2.91) and linearizing it, leads to

$$\partial_j \beta_i = \delta_{ij} - \partial_i \partial_j \Psi =: A_{ij}, \tag{2.92}$$

where A is the Jacobian of the lensing potential. It is given by

$$A(\boldsymbol{\theta}) = \begin{pmatrix} 1 - \partial_i^2 \Psi & -\partial_i \partial_j \Psi \\ -\partial_i \partial_j \Psi & 1 + \partial_j^2 \Psi \end{pmatrix} =: \begin{pmatrix} 1 - \kappa - \gamma_1 & -\gamma_2 \\ -\gamma_2 & 1 - \kappa + \gamma_1 \end{pmatrix} , \tag{2.93}$$

with the *convergence* κ and the *complex shear* $\gamma_\mathrm{c} = \gamma_1 + \mathrm{i}\,\gamma_2$.

The shear is often more conveniently expressed with respect to a given orientation ϕ. The rotated shear $\gamma(\boldsymbol{\vartheta}; \phi)$ is defined as

$$\gamma(\boldsymbol{\vartheta}; \phi) = -\mathrm{e}^{-2\mathrm{i}\phi}\, \gamma_\mathrm{c}(\boldsymbol{\vartheta}) =: \gamma_\mathrm{t}(\boldsymbol{\vartheta}; \phi) + \mathrm{i}\, \gamma_\times(\boldsymbol{\vartheta}; \phi) \, , \tag{2.94}$$

where γ_t is the *tangential shear* and $\gamma_\times$ is the *cross shear.*

The convergence is a normalised version of the surface mass density,

$$\kappa(\boldsymbol{\theta}) = \frac{4\pi G}{c^2} \frac{D_\mathrm{d} D_\mathrm{ds}}{D_\mathrm{s}} \Sigma(\boldsymbol{\theta}) =: \Sigma_\mathrm{crit}^{-1}(z_\mathrm{d}, z_\mathrm{s})\, \Sigma(\boldsymbol{\theta}) \, , \tag{2.95}$$

where Σ_crit is the critical surface mass density[6] and z_d and z_s are the redshifts of the lens and source respectively.

Shear and convergence are related to the reduced shear g,

$$g = \frac{\gamma_\mathrm{c}}{1+\kappa} = \frac{\gamma_1 + \mathrm{i}\,\gamma_2}{1+\kappa} \, . \tag{2.96}$$

Since κ and γ_c are both derivatives of the lensing potential, their Fourier transforms $\hat{\kappa}(\boldsymbol{\ell})$ and $\hat{\gamma}_\mathrm{c}(\boldsymbol{\ell})$ can be transformed into each other, using the Kaiser-Squires relation (Kaiser and Squires, 1993)

$$\hat{\gamma}_\mathrm{c}(\boldsymbol{\ell}) = \mathrm{e}^{2\mathrm{i}\,\phi_\ell}\, \hat{\kappa}(\boldsymbol{\ell}) \, , \tag{2.97}$$

where ϕ_ℓ is the polar angle of $\boldsymbol{\ell}$.

---

[6] This critical surface mass density is not the comoving critical surface mass density $\Sigma_\text{crit, com}$, defined by

$$\Sigma_\mathrm{crit,com}^{-1}(z_\mathrm{d}, z_\mathrm{s}) = \frac{4\pi G}{c^2} \frac{D_\mathrm{A}(z_\mathrm{d}, z_\mathrm{s})\, D_\mathrm{A}(z_\mathrm{d})}{(1+z_\mathrm{d})\, D_\mathrm{A}(z_\mathrm{s})} \, ,$$

and used in some gravitational lensing studies. Appendix C in Dvornik et al. (2018) discusses the implications of different definitions of the critical surface mass density.

Aside from the distortion of the source shape, gravitational lensing also magnifies images. This magnification μ affects the observed flux s of a source flux s_0 as

$$s = \mu \, s_0 \; , \tag{2.98}$$

and is given as

$$\mu = \frac{1}{(1-\kappa)^2 - |\gamma_\mathrm{c}|^2} \; . \tag{2.99}$$

Magnification by gravitational lenses can be used as a ‘natural telescope’ as it enables the observation of faint sources, which would be undetectable otherwise (see e.g. Richard et al., 2011; Schmidt et al., 2017). It also affects the observed number density of galaxies and therefore impacts measurements of GGL (see Sect. 2.4.4) and other weak gravitational lensing effects. We study its effect on G3L in Chapter 3.

2.4.2 Weak gravitational lensing

Equation (2.88) can be used in two different regimes. For $\kappa \gtrsim 1$, we are in the *strong lensing* regime, where source galaxy shapes are strongly distorted. Strongly lensed sources appear as arcs, complete rings, or even multiple images. However, for this work, we are concerned with *weak lensing*, where $\kappa \ll 1$ (see Bartelmann and Schneider, 2001, for a review). Weak lensing distorts galaxy shapes only slightly. Consequently, the images of weakly lensed galaxies look far less impressive for the casual observer than of strongly lensed galaxies. The shape distortion due to weak lensing is usually smaller than the intrinsic scatter of galaxy shapes, so it is not noticeable by observing individual galaxies. However, there are many more weakly lensed galaxies than strongly lensed sources. Therefore, weak lensing is ideal for measurements of the statistics of the matter distribution, while strong lensing gives mainly information on specific high-density objects such as galaxy clusters.

To first order, weak gravitational lensing only changes the apparent position and ellipticity of a source galaxy. The ellipticity of a galaxy with semi-major and semi-minor axes a and b is

$$\epsilon = \frac{a-b}{a+b} \mathrm{e}^{2\mathrm{i}\phi} \; , \tag{2.100}$$

where ϕ is the angle between the galaxies semi-major axis and the x-axis of the coordinate frame. Due to weak lensing, the observed ellipticity is composed of the intrinsic ellipticity ϵ_int and the reduced shear g,

$$\epsilon = \frac{\epsilon_\mathrm{int} + g}{1 + g^* \, \epsilon_\mathrm{int}} \; , \tag{2.101}$$

where the asterisk denotes complex conjugation. In the weak lensing regime $g \simeq \gamma_\mathrm{c}$, so we can in principle estimate the shear directly from the observed ellipticity.

However, for weak lensing, the shear is usually small compared to the intrinsic ellipticity of a galaxy. Moreover, as the intrinsic ellipticity is unknown, we cannot estimate the shear for any single galaxy. Therefore, instead of measuring the shear from a single galaxy, we average over the observed ellipticities of many sources. If the intrinsic ellipticities of the sources are uncorrelated to the shear, the average observed ellipticity is

$$\langle \epsilon \rangle = \langle \epsilon_{\mathrm{int}} \rangle + \langle g \rangle \simeq \langle \epsilon_{\mathrm{int}} \rangle + \langle \gamma_{\mathrm{c}} \rangle \ . \tag{2.102}$$

The first term vanishes, if galaxies are randomly orientated and have uncorrelated ellipticities, so we can find the shear with

$$\langle \gamma_{\mathrm{c}} \rangle \simeq \langle \epsilon \rangle \ . \tag{2.103}$$

The ellipticities of source galaxies are accordingly unbiased estimators of γ_{c}.

2.4.3 Projected spectra and Limber equation

In lensing, all observables are projections on the sky. The deflection angle alone only constrains the surface mass density and cannot directly yield the three-dimensional matter distribution. The three-dimensional density contrast δ is related to the lensing convergence by projecting it along the comoving distance w with

$$\kappa(\boldsymbol{\theta}) = \frac{3H_0^2\,\Omega_{\mathrm{m}}}{2c^2} \int_0^\infty \mathrm{d}w \ \ q(w)\ f_K(w)\ \frac{\delta[\vec{\mathrm{x}}(\boldsymbol{\theta}, w), t_w]}{a(w)} \ , \tag{2.104}$$

where f_K is defined by Eq. (2.3), t_w is the cosmic time at comoving distance w, $\boldsymbol{x}(\boldsymbol{\theta}, w) = (f_K(w)\,\boldsymbol{\theta}, w)$ and

$$q(w) = \int_w^\infty \mathrm{d}w' \ \ p_{\mathrm{s}}(w')\ \frac{f_K(w'-w)}{f_K(w')} \ , \tag{2.105}$$

with the distribution p_{s} of sources with comoving distance. With this relation for κ, we can infer the *projected matter power spetrum* $P_{\kappa\kappa}(\ell)$ which is defined by

$$(2\pi)^3\,\delta_{\mathrm{D}}(\boldsymbol{\ell}_1 + \boldsymbol{\ell}_2) P_{\kappa\kappa}(\ell_1) = \langle \hat{\kappa}(\boldsymbol{\ell}_1)\,\hat{\kappa}(\boldsymbol{\ell}_2) \rangle \ , \tag{2.106}$$

where $\hat{\kappa}$ is the Fourier transform of κ. This projected power spectrum can be derived from the three-dimensional power spectrum $P(k,t)$.

In general, this would require decomposing κ into spherical harmonics and evaluating the correlation between density fluctuations at different cosmic times. However, under two assumptions, the Limber approximation (Kaiser, 1992) can be used. These assumptions are, first, that the sky can be approximated by a plane (*flat-sky-approximation*), and second, that $q(w)$ varies little over the coherence length of the described structures. These assumptions hold if the angular scales on which $P_{\kappa\kappa}$ is evaluated are small, and the q are not too narrow. For example, Simon (2007) found, that for broad q, the Limber approximation is accurate at the 10% level for scales less than a few degrees. With these assumptions, the projected matter power spectrum is Universe is

$$P_{\kappa\kappa}(\ell) = \frac{9H_0^4\,\Omega_{\mathrm{m}}^2}{4c^4} \int \mathrm{d}w \ \ \frac{q^2(w)}{a(w)}\ P(\ell / f_K(w), t_w) \ . \tag{2.107}$$

We also define the projected galaxy number density $N(\boldsymbol{\theta})$, which is related to the three-dimensional number density $n[\boldsymbol{x}(\boldsymbol{\theta}, w), t_w]$ at comoving distance w by the selection function $\nu(w)$,

$$N(\boldsymbol{\theta}) = \int \mathrm{d}w \;\; \nu(w)\, n[\boldsymbol{x}(\boldsymbol{\theta}, w), t_w] \; . \tag{2.108}$$

The selection function gives the fraction of galaxies at comoving distance w included in the galaxy sample. For a flux-limited sample, this corresponds to the fraction of galaxies brighter than the magnitude limit. The selection function $\nu(w)$ is related to the distribution $p(w)$ of the galaxies with comoving distance, according to (Schneider, 2005)

$$\nu(w) = p(w)\, \frac{\int \mathrm{d}^2\theta \;\; N(\boldsymbol{\theta})}{\int \mathrm{d}^2\theta \;\; n[\boldsymbol{x}(\boldsymbol{\theta}, w), t_w]} \; . \tag{2.109}$$

With $N(\boldsymbol{\theta})$, we can define the galaxy convergence κ_g as

$$\kappa_\mathrm{g}(\boldsymbol{\theta}) = \frac{N(\boldsymbol{\theta})}{\bar{N}} - 1 \; , \tag{2.110}$$

where N is the mean projected galaxy number density. The galaxy convergence determines the *projected galaxy-matter power spectrum* $P_{\mathrm{g}\kappa}$, defined as

$$(2\pi)^3\, \delta_\mathrm{D}\left(\boldsymbol{\ell}_1 + \boldsymbol{\ell}_2\right)\; P_{\mathrm{g}\kappa}(\boldsymbol{\ell}_1) = \left\langle \hat{\kappa}(\boldsymbol{\ell}_1)\, \hat{\kappa}_\mathrm{g}(\boldsymbol{\ell}_2) \right\rangle \; , \tag{2.111}$$

and the *projected galaxy-galaxy-matter bispectrum* $B_{\mathrm{gg}\kappa}$, defined as

$$(2\pi)^3\, \delta_\mathrm{D}\left(\boldsymbol{\ell}_1 + \boldsymbol{\ell}_2 + \boldsymbol{\ell}_3\right)\; B_{\mathrm{gg}\kappa}(\ell_1, \ell_2, \phi) = \left\langle \hat{\kappa}(\boldsymbol{\ell}_1)\, \hat{\kappa}_\mathrm{g}(\boldsymbol{\ell}_2)\, \hat{\kappa}_\mathrm{g}(\boldsymbol{\ell}_3) \right\rangle \; . \tag{2.112}$$

These can be derived from their three-dimensional counterparts in a similar way as the projected matter power spectrum. Under the same assumptions as for the Limber approximation, that is a flat sky and a slowly varying $\nu(w)$, they are (Schneider and Watts, 2005)

$$P_{\mathrm{g}\kappa}(\ell) = \frac{3H_0^2\,\Omega_\mathrm{m}}{2c^2} \int \mathrm{d}w \;\; \frac{q(w)\, p(w)}{w\, a(w)}\, P_{\mathrm{g}\delta}(\ell / f_K(w), t_w) \; , \tag{2.113}$$

$$B_{\mathrm{gg}\kappa}(\ell_1, \ell_2, \phi) = \frac{3H_0^2\,\Omega_\mathrm{m}}{2c^2} \int \mathrm{d}w \;\; \frac{q(w)\, p^2(w)}{w^3\, a(w)}\, B_{\mathrm{gg}\delta}(\ell_1 / f_K(w), \ell_2 / f_K(w), \phi, t_w) \; . \tag{2.114}$$

2.4.4 Galaxy-galaxy-lensing

Weak gravitational lensing is an excellent tool to measure the galaxy-matter correlations. To estimate the galaxy-matter power spectrum $P_{\mathrm{g}\delta}(k)$, the method-of-choice is GGL. For GGL, we measure the ellipticity of background source galaxies and their angular separation from foreground lens galaxies. Then, we average the ellipticities of all sources with separation $\boldsymbol{\vartheta}$ to a lens to find an estimate of

$$\left\langle \gamma_\mathrm{t} \right\rangle (\boldsymbol{\vartheta}) = \frac{1}{\bar{N}} \left\langle N(\boldsymbol{\theta})\, \gamma_\mathrm{t}(\boldsymbol{\theta} + \boldsymbol{\vartheta}; \phi) \right\rangle \; , \tag{2.115}$$

where ϕ is the polar angle of $\boldsymbol{\vartheta}$. This quantity is related to the projected galaxy-matter power spectrum $P_{\mathrm{g}\kappa}$ by

$$\langle \gamma_{\mathrm{t}} \rangle \, (\boldsymbol{\vartheta}) = \int \frac{\mathrm{d}^2 l}{(2\pi)^2} \, \mathrm{e}^{\mathrm{i}\boldsymbol{\vartheta}\cdot\boldsymbol{\ell}} \, \mathrm{e}^{2\mathrm{i}(\phi_l - \phi)} \, P_{\mathrm{g}\kappa}(\ell) \; , \tag{2.116}$$

where ϕ_l is the polar angle of $\boldsymbol{\ell}$.

GGL is an established tool to constrain the galaxy-matter power spectrum (Mandelbaum et al., 2005, 2006), parameters of the halo model (Dvornik et al., 2018), or SAMs (Saghiha et al., 2017; Renneby et al., 2020). It can also be combined with other probes to constrain cosmological parameters (Abbott et al., 2018; van Uitert et al., 2018). However, higher-order statistics, such as the galaxy-galaxy-matter bispectrum are not accessible to GGL.

Magnification due to gravitational lensing affects GGL. In particular, due to lensing by the LSS, the number density of observed lens galaxies is affected. As detailed by Bartelmann and Schneider (2001), the number density of observed lens galaxies at angular position $\boldsymbol{\vartheta}$ and redshift z is changed from the intrinsic number density $n_0(\boldsymbol{\vartheta}, z)$ to

$$n(\boldsymbol{\vartheta}, z) = n_0(\boldsymbol{\vartheta}, z) + 2\left[\alpha(z) - 1\right] \bar{n}(z) \, \kappa(\boldsymbol{\vartheta}, z) \; , \tag{2.117}$$

where $\kappa(\boldsymbol{\vartheta}, z)$ is the convergence caused by all matter in front of redshift z, and $\alpha(z)$ is the negative slope of the luminosity function $\Phi(S, z)$ at the flux limit S_{lim} of lens galaxies. We define α by

$$\alpha = - \left. \frac{\mathrm{d}\log_{10}\Phi}{\mathrm{d}\log_{10} S} \right|_{S=S_{\mathrm{lim}}} \; . \tag{2.118}$$

This change in number density correlates with the shear of source galaxies and therefore causes an additional signal to $\langle \gamma_{\mathrm{t}} \rangle$. This effect, while often overlooked, has a significant impact on observed shear profiles, the overall GGL-signal and halo mass estimates (Simon et al., 2008; Unruh et al., 2019, 2020). In Chapter 3, we study how magnification of lens galaxies impacts observations of the galaxy-galaxy-matter bispectrum.

2.4.5 Galaxy-galaxy-galaxy-lensing

We can study the galaxy-galaxy-matter bispectrum with G3L (Schneider and Watts, 2005). This effect includes the lensing of source galaxies by lens galaxy pairs, which determines the lens-lens-shear correlation. Unlike GGL or galaxy clustering, G3L depends on the galaxy-matter three-point correlation and the HOD of galaxy pairs. In principle, it also depends on the ellipticity of dark matter halos as well as misalignments between the galaxy and matter distribution because the galaxy pair orientation introduces a preferred direction.

The lens-lens-shear correlation was measured for lens pairs separated by several Mpc to detect inter-cluster filaments (Mead et al., 2010; Clampitt et al., 2016; Epps and Hudson, 2017; Xia et al., 2020). However, for the assessment of SAMs, it is more suitable to study the correlation at smaller, sub-Mpc scales. At these scales, the G3L signal is more sensitive to the small-scale physics that vary between different SAMs, because it depends primarily on galaxy pairs with

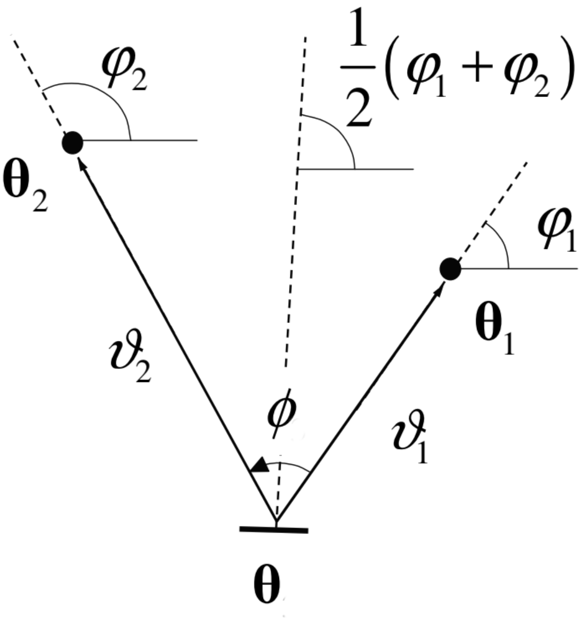

Figure 2.5: Geometry of a G3L system with one source and two lens galaxies. Adapted from Schneider and Watts (2005).

galaxies in the same dark matter halo. For lens pairs with galaxies of similar stellar mass or colour, the small-scale lens-lens-shear correlation was determined by Simon et al. (2008) in the Red-sequence Cluster Survey (RCS; Gladders and Yee, 2005) and Simon et al. (2013) in the CFHTLenS. The G3L measured in CFHTLenS was compared to predictions by multiple SAMs implemented in the MR by Saghiha et al. (2017) and Simon et al. (2019). They demonstrated that G3L is more effective in evaluating SAMs than GGL and that the H15 SAM agreed with the observations in CFHTLenS, while the L12 SAM predicts too large G3L signals.

For this work, we are concerned with the lensing of single sources around pairs of lens galaxies. Figure 2.5 depicts the corresponding geometric configuration of lens and source galaxies. The main observable of this type of G3L is the correlation function $\tilde{\mathcal{G}}$, defined as

$$\tilde{\mathcal{G}}(\boldsymbol{\vartheta}_1,\boldsymbol{\vartheta}_2) = \frac{1}{\overline{N}^2}\left\langle N(\boldsymbol{\theta}+\boldsymbol{\vartheta}_1)\,N(\boldsymbol{\theta}+\boldsymbol{\vartheta}_2)\,\gamma(\boldsymbol{\theta};\frac{\varphi_1+\varphi_2}{2})\right\rangle\,, \tag{2.119}$$

or $\mathcal{G}$, which is

$$\mathcal{G}(\boldsymbol{\vartheta}_1,\boldsymbol{\vartheta}_2) = \left\langle \kappa_{\mathrm{g}}(\boldsymbol{\theta}+\boldsymbol{\vartheta}_1)\,\kappa_{\mathrm{g}}(\boldsymbol{\theta}+\boldsymbol{\vartheta}_2)\,\gamma(\boldsymbol{\theta};\frac{\varphi_1+\varphi_2}{2})\right\rangle\,. \tag{2.120}$$

The two correlation functions are linked by

$$\begin{aligned}\mathcal{G}(\boldsymbol{\vartheta}_1,\boldsymbol{\vartheta}_2) =&\tilde{\mathcal{G}}(\boldsymbol{\vartheta}_1,\boldsymbol{\vartheta}_2) - \frac{1}{\overline{N}}\left\langle N(\boldsymbol{\theta}+\boldsymbol{\vartheta}_1)\gamma_{\mathrm{t}}(\boldsymbol{\theta};\varphi_1)\right\rangle \mathrm{e}^{-\mathrm{i}\phi} - \frac{1}{\overline{N}}\left\langle N(\boldsymbol{\theta}+\boldsymbol{\vartheta}_1)\gamma_{\mathrm{t}}(\boldsymbol{\theta};\varphi_2)\right\rangle \mathrm{e}^{\mathrm{i}\phi} && (2.121)\\ =&\tilde{\mathcal{G}}(\boldsymbol{\vartheta}_1,\boldsymbol{\vartheta}_2) - \langle\gamma_{\mathrm{t}}\rangle\,(\boldsymbol{\vartheta}_1)\mathrm{e}^{-\mathrm{i}\phi} - \langle\gamma_{\mathrm{t}}\rangle\,(\boldsymbol{\vartheta}_2)\mathrm{e}^{\mathrm{i}\phi}\,, && (2.122)\end{aligned}$$

so $\tilde{\mathcal{G}}$ contains terms arising from GGL, while $\mathcal{G}$ is only the third-order correlation due to G3L. The correlation functions are related to the projected galaxy-galaxy-matter bispectrum by

$$\mathcal{G}(\boldsymbol{\vartheta}_1, \boldsymbol{\vartheta}_2) = \int \frac{\mathrm{d}^2\ell_1}{(2\pi)^2} \int \frac{\mathrm{d}^2\ell_2}{(2\pi)^2}\, \mathrm{e}^{-\mathrm{i}(\boldsymbol{\ell}_1\cdot\boldsymbol{\vartheta}_1+\boldsymbol{\ell}_2\cdot\boldsymbol{\vartheta}_2)}\, \frac{1}{|\boldsymbol{\ell}_1+\boldsymbol{\ell}_2|^2} \left(\ell_1\,\mathrm{e}^{\mathrm{i}\phi_1} + \ell_2\,\mathrm{e}^{\mathrm{i}\phi_2}\right)^2 B_{\mathrm{gg}\kappa}(\ell_1, \ell_2, \phi_\ell)\ , \tag{2.123}$$

where ϕ_ℓ is the angle between $\boldsymbol{\ell}_1$ and $\boldsymbol{\ell}_2$.

Due to statistical homogeneity and isotropy, $\tilde{\mathcal{G}}$ and $\mathcal{G}$ only depend on the lens-source separations ϑ_1 and ϑ_2 and the angle ϕ between $\boldsymbol{\vartheta}_1$ and $\boldsymbol{\vartheta}_2$. Consequently, we write

$$\tilde{\mathcal{G}}(\boldsymbol{\vartheta}_1, \boldsymbol{\vartheta}_2) =: \tilde{\mathcal{G}}(\vartheta_1, \vartheta_2, \phi)\ , \tag{2.124}$$

$$\mathcal{G}(\boldsymbol{\vartheta}_1, \boldsymbol{\vartheta}_2) =: \mathcal{G}(\vartheta_1, \vartheta_2, \phi)\ . \tag{2.125}$$

Simon et al. (2008) showed how to estimate $\tilde{\mathcal{G}}(\vartheta_1, \vartheta_2, \phi)$ by averaging the ellipticities of source galaxies over all lens-lens-source triplets, where ϑ_1 (ϑ_2) is the separation between the first (second) lens and the source. Their estimator of $\tilde{\mathcal{G}}$ in a bin B of ϑ_1, ϑ_2 and ϕ for N_s source, and N_d lens galaxies is

$$\tilde{\mathcal{G}}_\mathrm{est}(B) = -\frac{\sum_{i,j=1}^{N_\mathrm{d}} \sum_{k=1}^{N_\mathrm{s}} w_k\, \epsilon_k\, \mathrm{e}^{-\mathrm{i}(\varphi_{ik}+\varphi_{jk})} \left[1+\omega(|\boldsymbol{\theta}_i-\boldsymbol{\theta}_j|)\right] \Delta_{ijk}(B)}{\sum_{i,j=1}^{N_\mathrm{d}} \sum_{k}^{N_\mathrm{s}} w_k\, \Delta_{ijk}(B)} \tag{2.126}$$

$$=: -\frac{\sum_{i,j,k} w_k\, \epsilon_k\, \mathrm{e}^{-\mathrm{i}(\varphi_{ik}+\varphi_{jk})} \left[1+\omega(|\boldsymbol{\theta}_i-\boldsymbol{\theta}_j|)\right] \Delta_{ijk}(B)}{\sum_{i,j,k} w_k\, \Delta_{ijk}(B)}\ , \tag{2.127}$$

with

$$\Delta_{ijk}(B) = \begin{cases} 1 & \text{for} \quad \left(|\boldsymbol{\theta}_k-\boldsymbol{\theta}_i|, |\boldsymbol{\theta}_k-\boldsymbol{\theta}_j|, \phi_{ijk}\right) \in B \\ 0 & \text{otherwise} \end{cases}\ . \tag{2.128}$$

The angle $\varphi_{ik}(\varphi_{jk})$ is the polar angle of $\boldsymbol{\theta}_k-\boldsymbol{\theta}_i$ ($\boldsymbol{\theta}_k-\boldsymbol{\theta}_j$) and ϕ_{ijk} is the opening angle between $\boldsymbol{\theta}_k-\boldsymbol{\theta}_i$ and $\boldsymbol{\theta}_k-\boldsymbol{\theta}_j$. The w_k are the weights of the measured ellipticities. Source galaxies with more precise shape measurements receive a higher ellipticity weight w_k. The weight, therefore, increases the contribution of source galaxies with more precise shapes to the estimator. For the simulated shear data in Chapters 3 and 4, we set the weights to $w_k = 1$ for all sources. This estimator also includes the angular two-point correlation function ω, which takes account of the clustering of lens galaxies. The two-point correlation can be estimated with the Landy-Szalay estimator (Landy and Szalay, 1993),

$$\omega(\theta) = \frac{N_\mathrm{r}^2\, DD(\theta)}{N_\mathrm{d}^2\, RR(\theta)} - 2\,\frac{N_\mathrm{r}\, DR(\theta)}{N_\mathrm{d}\, RR(\theta)} + 1\ . \tag{2.129}$$

Here, $DD(\theta)$ is the paircount of lens galaxies, $RR(\theta)$ is the paircount of randoms, which are unclustered galaxies, and $DR(\theta)$ is the cross paircount of lenses and randoms at separation θ. The total numbers of lenses and randoms are denoted by N_d and N_r.

This estimator does not take into account redshift information on the galaxies. Therefore, lens-lens-source triplets with lenses separated along the line-of-sight have the same weight in the estimator as triplets whose lens galaxies are physically close. These separated lens pairs decrease the signal-to-noise ratio (S/N), as shown by Simon et al. (2019). We, therefore, propose a new estimator that uses lens redshift information to improve the S/N in Chapter 3.

2.4.6 Aperture Statistics

Both the GGL and the G3L correlation functions can be converted to *aperture statistics*, first introduced by Schneider et al. (1998). These are expectation values of products of the aperture mass $\mathcal{M}_\theta(\boldsymbol{\vartheta})$ and the aperture number count $\mathcal{N}_\theta(\boldsymbol{\vartheta})$, which are defined as

$$\mathcal{M}_\theta(\boldsymbol{\vartheta}) = \int \mathrm{d}^2\vartheta' \, U_\theta(|\boldsymbol{\vartheta} - \boldsymbol{\vartheta}'|) \, \kappa(\boldsymbol{\vartheta}') \,, \tag{2.130}$$

and

$$\mathcal{N}_\theta(\boldsymbol{\vartheta}) = \frac{1}{\bar{N}} \int \mathrm{d}^2\vartheta' \, U_\theta(|\boldsymbol{\vartheta} - \boldsymbol{\vartheta}'|) \, N(\boldsymbol{\vartheta}') \,, \tag{2.131}$$

with the filter function U_θ with aperture scale radius θ,

$$U_\theta(\vartheta) = \frac{1}{\theta^2} \, u\left(\frac{\vartheta}{\theta}\right) . \tag{2.132}$$

As long as this filter function is compensated, that is $\int \mathrm{d}\vartheta \, \vartheta \, U_\theta(\vartheta) = 0$, the aperture mass can be easily calculated from the tangential shear γ_t. For this, a new filter Q_θ is derived from U_θ as

$$Q_\theta(\vartheta) = \frac{2}{\vartheta^2} \int_0^\vartheta \mathrm{d}\vartheta' \;\; \vartheta' \, U_\theta(\vartheta') - U_\theta(\vartheta) \,. \tag{2.133}$$

With this filter, the aperture mass is

$$\mathcal{M}_\theta(\boldsymbol{\vartheta}) = \int \mathrm{d}^2\vartheta' \, Q_\theta(|\boldsymbol{\vartheta} - \boldsymbol{\vartheta}'|) \, \gamma_\mathrm{t}(\boldsymbol{\vartheta}') \,. \tag{2.134}$$

Analogous to $\mathcal{M}$, we define the B-mode of the aperture mass as

$$\mathcal{M}_{\perp,\theta}(\boldsymbol{\vartheta}) = \int \mathrm{d}^2\vartheta' \, Q_\theta(|\boldsymbol{\vartheta} - \boldsymbol{\vartheta}'|) \, \gamma_\times(\boldsymbol{\vartheta}') \,, \tag{2.135}$$

with the cross shear $\gamma_\times$. Aperture statistics involving $\mathcal{M}_\perp$ should vanish, as the shear is caused by a scalar gravitational potential. Non-vanishing B-modes are an indicator of additional effects, such as systematic errors in the analysis, clustering of sources (Schneider et al., 2002) or intrinsic alignments (Heymans et al., 2006).

For GGL, the relevant aperture statistics is $\langle \mathcal{N}\mathcal{M} \rangle \, (\theta_1, \theta_2)$, given as

$$\langle \mathcal{N}\mathcal{M} \rangle \, (\theta_1, \theta_2) = \left\langle \mathcal{N}_{\theta_1}(\boldsymbol{\vartheta}_1) \, \mathcal{M}_{\theta_2}(\boldsymbol{\vartheta}_2) \right\rangle \tag{2.136}$$

$$= \frac{1}{\bar{N}} \int \mathrm{d}^2\vartheta_1 \int \mathrm{d}^2\vartheta_2 \, U_{\theta_1}(\boldsymbol{\vartheta}_1) U_{\theta_2}(\boldsymbol{\vartheta}_2) \, \langle N(\boldsymbol{\vartheta}_1) \, \kappa(\boldsymbol{\vartheta}_2) \rangle \,, \tag{2.137}$$

while for G3L the relevant aperture statistics is $\langle \mathcal{N}\mathcal{N}\mathcal{M} \rangle$,

$$\begin{aligned}
&\langle \mathcal{N}\mathcal{N}\mathcal{M}\rangle\,(\theta_1,\theta_2,\theta_3) && (2.138)\\
&= \left\langle \mathcal{N}_{\theta_1}(\boldsymbol{\vartheta}_1)\,\mathcal{N}_{\theta_2}(\boldsymbol{\vartheta}_2)\,\mathcal{M}_{\theta_3}(\boldsymbol{\vartheta}_3)\right\rangle\\
&= \frac{1}{\overline{N}^2}\int \mathrm{d}^2\vartheta_1 \int \mathrm{d}^2\vartheta_2 \int \mathrm{d}^2\vartheta_3\, U_{\theta_1}(\boldsymbol{\vartheta}_1) U_{\theta_2}(\boldsymbol{\vartheta}_2) U_{\theta_3}(\boldsymbol{\vartheta}_3)\,\langle N(\boldsymbol{\vartheta}_1)\,N(\boldsymbol{\vartheta}_2)\,\kappa(\boldsymbol{\vartheta}_3)\rangle\ . && (2.139)
\end{aligned}$$

The aperture statistics can be easier related to the projected galaxy-matter polyspectra than the direct GGL and G3L correlation functions. For GGL,

$$\langle \mathcal{N}\mathcal{M}\rangle\,(\theta_1,\theta_2) = \int \frac{\mathrm{d}^2\ell}{(2\pi)^2}\hat{U}_{\theta_1}(\ell)\,\hat{U}_{\theta_2}(\ell)\,P_{\mathrm{g}\kappa}(\ell)\ , \tag{2.140}$$

and for G3L

$$\langle \mathcal{N}\mathcal{N}\mathcal{M}\rangle\,(\theta_1,\theta_2) = \int \frac{\mathrm{d}^2\ell_1}{(2\pi)^2}\int \frac{\mathrm{d}^2\ell_2}{(2\pi)^2}\hat{U}_{\theta_1}(\ell_1)\,\hat{U}_{\theta_2}(\ell_2)\,\hat{U}_{\theta_3}(|\boldsymbol{\ell}_1+\boldsymbol{\ell}_2|)B_{\mathrm{gg}\kappa}(\ell_1,\ell_2,\phi)\ , \tag{2.141}$$

where $\hat{U}_\theta$ is the Fourier transform of U_θ.

Throughout this work, we use an exponential filter function,

$$u(x) = \frac{1}{2\pi}\left(1-\frac{x^2}{2}\right)\exp\!\left(-\frac{x^2}{2}\right)\ . \tag{2.142}$$

For this choice, the correlation function $\tilde{\mathcal{G}}$ can be connected to $\langle \mathcal{N}\mathcal{N}\mathcal{M}\rangle$ with an analytical expression,

$$\begin{aligned}
&\langle \mathcal{N}\mathcal{N}\mathcal{M}\rangle\,(\theta_1,\theta_2,\theta_3) + \mathrm{i}\,\langle \mathcal{N}\mathcal{N}\mathcal{M}_\perp\rangle\,(\theta_1,\theta_2,\theta_3) && (2.143)\\
&= \int_0^\infty \mathrm{d}\vartheta_1\ \vartheta_1 \int_0^\infty \mathrm{d}\vartheta_2\ \vartheta_2 \int_0^{2\pi} \mathrm{d}\phi\ \tilde{\mathcal{G}}(\vartheta_1,\vartheta_2,\phi)\,\mathcal{A}_{\mathcal{N}\mathcal{N}\mathcal{M}}(\vartheta_1,\vartheta_2,\phi\mid\theta_1,\theta_2,\theta_3)\ ,
\end{aligned}$$

with the kernel function $\mathcal{A}_{\mathcal{N}\mathcal{N}\mathcal{M}}(\vartheta_1,\vartheta_2,\phi\mid\theta_1,\theta_2,\theta_3)$ given in the appendix of Schneider and Watts (2005). We measure aperture statistics only for equal scale radii $\theta_1=\theta_2=\theta_3$. Therefore, we use the abbreviations

$$\langle \mathcal{N}\mathcal{N}\mathcal{M}\rangle\,(\theta) := \langle \mathcal{N}\mathcal{N}\mathcal{M}\rangle\,(\theta,\theta,\theta)\ , \tag{2.144}$$

and

$$\mathcal{A}_{\mathcal{N}\mathcal{N}\mathcal{M}}(\vartheta_1,\vartheta_2,\phi\mid\theta) := \mathcal{A}_{\mathcal{N}\mathcal{N}\mathcal{M}}(\vartheta_1,\vartheta_2,\phi\mid\theta_1,\theta_2,\theta_3)\ . \tag{2.145}$$

The aperture statistics can be used to constrain the galaxy bias factor, discussed in Sect. 2.1.3 (e.g Schneider and Watts, 2005). For two galaxy populations with linear deterministic bias factors b_1 and b_2 and aperture number counts $\mathcal{N}_1$ and $\mathcal{N}_2$, this simple model predicts for the aperture statistics

$$\langle \mathcal{N}_1\,\mathcal{N}_2\,\mathcal{M}\rangle \propto b_1\,b_2\ . \tag{2.146}$$

From this follows that

$$R(\theta) := \frac{\langle \mathcal{N}_1\, \mathcal{N}_2\, \mathcal{M}\rangle\,(\theta)}{\sqrt{\langle \mathcal{N}_1\, \mathcal{N}_1\, \mathcal{M}\rangle\,(\theta)\;\langle \mathcal{N}_2\, \mathcal{N}_2\, \mathcal{M}\rangle\,(\theta)}} = \frac{b_1\, b_2}{\sqrt{b_1^2\, b_2^2}} = 1\;. \tag{2.147}$$

In Chapter 4, we measure R in the observation and simulation to assess the assumption of linear deterministic bias.

2.4.7 Gravitational Lensing in N-body simulations

To study gravitational lensing with N-body simulations, the three-dimensional density contrast δ, which is given by these simulations, needs to be converted to the two-dimensional convergence κ. To obtain κ, one uses *ray-tracing algorithms*. There exist a variety of different ray-tracing methods, some of which were reviewed and compared by Hilbert et al. (2020).

These algorithms are usually applied to a simulation after it was fully calculated, that is in ‘post-processing’. This approach makes it easier to change source redshifts or observer orientations, as the simulation only needs to run once. However, the number of simulational snapshots limits the accuracy of the resulting convergence maps. If only a small number of snapshots are available, the convergence is averaged over a larger time interval, so the resulting maps can be biased. There are also approaches to compute the convergence ‘on the fly’ that is together with the full particle distribution, (e.g. Barreira et al., 2016), but these are computationally more expensive.

Post-processing ray-tracing algorithms all operate similarly. First, these algorithms project the matter in each snapshot, either on lens planes perpendicular to the line-of-sight (Hilbert et al., 2009; Giocoli et al., 2016) or on spheres centred on the observer (Fosalba et al., 2008; Fabbian et al., 2018). Then, light rays are traced backwards from the observer to the source plane. At each lens plane/sphere, the deflection angle of the rays is calculated from the lensing potential of all matter at the plane/sphere. Adding up the deflections of all planes up to the source plane gives the total deflection angle due to the matter distribution. The gradient of this deflection angle corresponds to the lensing Jacobian in Eq. (2.92). The Jacobian can be converted to maps of the shear γ and convergence κ.

While different ray-tracing algorithms differ in details, such as the choice of the projection method, Hilbert et al. (2020) found that the predicted convergence maps agree in general very well. Differences exist mainly in the predicted mean convergence. However, this quantity is not directly observable in weak lensing measurements, as the shear does not depend on it. After normalising the convergence maps of different ray-tracing algorithms, differences are only of the order of a few percents. Consequently, the choice of the ray-tracing algorithm is not particularly critical for the comparison of simulations to observations. We use the ray-tracing algorithm by Hilbert et al. (2009) on the MR to study G3L in the following chapters.

3

Improving the precision and accuracy of galaxy-galaxy-galaxy lensing

This chapter is based on Linke et al. (2020a), published in Astronomy & Astrophysics.

In this chapter, we discuss how to improve measurements of G3L by increasing both the accuracy and precision of the measured aperture statistics. These improvements use precise redshift estimates for the lens galaxies, as well as an adaptive binning scheme for the estimation of the three-point correlation function $\tilde{\mathcal{G}}$. We motivate our improvements in Sect. 3.1, and explain their application in Sect. 3.2. We apply the improved and original measurement schemes to two different types of catalogues described in Sect. 3.3, one based on simple, but unrealistic assumptions on the galaxy distribution and one based on the SAM by H15, implemented in the MR. The resulting aperture statistics are presented in Sect. 3.4 and discussed in Sect. 3.5.

3.1 Motivation

As explained in Sect. 2.4.4, G3L is a sensitive probe of galaxy formation. However, previous measurements of this effect used only photometric data without precise redshift estimates. Consequently, pairs of physically close lens galaxies, which are highly correlated, had the same weight as galaxy pairs separated along the line of sight with little to no correlation. These separated galaxies decrease the signal and lower the S/N.

Additionally, G3L is affected by the magnification of lens galaxies caused by the LSS in front of the lenses. This magnification affects the number density of lens galaxies in a survey. Because source galaxies are also lensed by the LSS, the shear of sources correlates with the lens magnification, and an additional correlation signal arises. This signal has not yet been quantified for G3L, but was found to affect GGL by up to 5 % in CFHTLenS (Simon and Hilbert, 2018).

Consequently, we introduce three improvements to the G3L estimator used by Simon et al. (2008, 2013) and given in Eq. (2.126). These are (i) weighting the lens galaxy pairs according to their redshift difference, (ii) using a new, adaptive binning method for the correlation function to reduce biases, and (iii) estimating the magnification bias with lens galaxies separated along the line of sight. We also show how to measure correlation in terms of physical instead of angular separation and weigh it by the critical surface mass density $\Sigma_{\rm crit}$, as is typical for GGL (e.g. Mandelbaum et al., 2006). Thereby, the signal no longer depends on the redshift distribution of source galaxies. The next section describes these improvements in detail. To test their effect, we apply the new estimator to simple mock data, for which we can directly calculate the expected aperture statistics, and to simulated data based on the MR (Springel et al., 2005) with the SAM by H15. We compare the resulting aperture statistics to those obtained with the original estimator.

3.2 Methods

3.2.1 Redshift weighting

To reduce the signal degradation by uncorrelated lens pairs, we define a redshift-weighted correlation function $\tilde{\mathcal{G}}_Z$, for which lens pairs are weighted according to their redshift difference δz. To this end, we introduce the redshift-weighting function $Z(\delta z)$, for which we choose a Gaussian,

$$Z(\delta z) = \exp\left(-\frac{\delta z^2}{2\sigma_Z^2}\right) . \tag{3.1}$$

The width σ_Z is a free parameter that should correspond to the typical redshift difference of correlated lens pairs. The weighting function is normalised such that it is unity if the galaxies have the same redshift. Averaging over the tangential ellipticities of lens-lens-source triplets weighted with Z leads to an estimate of

$$\begin{aligned}
&\frac{\int \mathrm{d}z_1 \int \mathrm{d}z_2 \;\; \nu_Z(z_1)\, \nu_Z(z_2)\, Z(\Delta z_{12}) \;\langle n(\boldsymbol{\vartheta}_1+\boldsymbol{\theta}, z_1)\, n(\boldsymbol{\vartheta}_2+\boldsymbol{\theta}, z_2)\, \gamma_{\rm t}(\boldsymbol{\vartheta}_3+\boldsymbol{\theta})\rangle}{\int \mathrm{d}z_1 \int \mathrm{d}z_2 \;\; \nu_Z(z_1)\, \nu_Z(z_2)\, Z(\Delta z_{12}) \;\langle n(\boldsymbol{\vartheta}_1+\boldsymbol{\theta}, z_1)\, n(\boldsymbol{\vartheta}_2+\boldsymbol{\theta}, z_2)\rangle} \\
&=: \frac{\tilde{\mathcal{G}}_Z(\vartheta_1, \vartheta_2, \phi)}{1+\omega_Z\left(|\boldsymbol{\vartheta}_1-\boldsymbol{\vartheta}_2|\right)} \,,
\end{aligned} \tag{3.2}$$

where $n(\boldsymbol{\vartheta}, z)$ is the number density of lens galaxies at angular position $\boldsymbol{\vartheta}$ and redshift z, $\Delta z_{12} = z_1 - z_2$, and $\nu_Z(z)$ is the lens selection function per redshift z. The selection function is defined by

$$\nu_Z(z) = p(z) \frac{\int \mathrm{d}^2\theta \;\; N(\boldsymbol{\theta})}{\int \mathrm{d}^2\theta \;\; n(\boldsymbol{\theta}, z)} \,, \tag{3.3}$$

with the lens redshift distribution $p(z)$. Equation (3.2) defines the redshift-weighted correlation function $\tilde{\mathcal{G}}_Z$ and uses the redshift-weighted two-point angular correlation function ω_Z. We estimate $\tilde{\mathcal{G}}_Z$ with

$$\tilde{\mathcal{G}}_{Z,\mathrm{est}}(B) = -\frac{\sum_{ijk}\, w_k\, \epsilon_k\, \mathrm{e}^{-\mathrm{i}(\varphi_{ik}+\varphi_{jk})}\, \left[1 + \omega_Z\left(|\boldsymbol{\theta}_i - \boldsymbol{\theta}_j|\right)\right]\, Z(\Delta z_{ij})\, \Delta_{ijk}(B)}{\sum_{ijk}\, w_k\, Z(\Delta z_{ij})\, \Delta_{ijk}(B)}\ . \tag{3.4}$$

To estimate the redshift-weighted two-point correlation ω_Z, we use the N_r randoms, located at $\boldsymbol{\theta}'_i$, the N_d lenses at the positions $\boldsymbol{\theta}_i$, and the estimator

$$\omega_Z(\theta) = \frac{N_\mathrm{r}^2\, DD_Z(\theta)}{N_\mathrm{d}^2\, RR_Z(\theta)} - 2\frac{N_\mathrm{r}\, DR_Z(\theta)}{N_\mathrm{d}\, RR_Z(\theta)} + 1\ , \tag{3.5}$$

with the modified pair-counts

$$DD_Z(\theta) = \sum_{i=1}^{N_\mathrm{d}}\sum_{j=1}^{N_\mathrm{d}} \Theta_\mathrm{H}\left(\theta + \Delta\theta/2 - |\boldsymbol{\theta}_i - \boldsymbol{\theta}_j|\right)\, \Theta_\mathrm{H}\left(-\theta + \Delta\theta/2 + |\boldsymbol{\theta}_i - \boldsymbol{\theta}_j|\right)\, Z(\Delta z_{ij})\ , \tag{3.6}$$

$$RR_Z(\theta) = \sum_{i=1}^{N_\mathrm{r}}\sum_{j=1}^{N_\mathrm{r}} \Theta_\mathrm{H}\left(\theta + \Delta\theta/2 - |\boldsymbol{\theta}_i - \boldsymbol{\theta}_j|\right) \Theta_\mathrm{H}\left(-\theta + \Delta\theta/2 + |\boldsymbol{\theta}'_i - \boldsymbol{\theta}'_j|\right)\, Z(\Delta z_{ij})\ , \tag{3.7}$$

and

$$DR_Z(\theta) = \sum_{i=1}^{N_\mathrm{d}}\sum_{j=1}^{N_\mathrm{r}} \Theta_\mathrm{H}\left(\theta + \Delta\theta/2 - |\boldsymbol{\theta}'_i - \boldsymbol{\theta}'_j|\right) \Theta_\mathrm{H}\left(-\theta + \Delta\theta/2 + |\boldsymbol{\theta}'_i - \boldsymbol{\theta}'_j|\right)\, Z(\Delta z_{ij})\ . \tag{3.8}$$

Here, Θ_H is the Heaviside step function and $\Delta\theta$ is the bin size for which ω_Z is estimated. For $Z \equiv 1$, this estimator reduces to the standard Landy-Szalay estimator in Eq. (2.129).

The aperture statistics from the redshift-weighted correlation function $\tilde{\mathcal{G}}_Z$ are expected to have a higher S/N than the aperture statistics from the original $\tilde{\mathcal{G}}$. This expected improvement can be estimated with simplified assumptions. For this, we assume that the N_tot lens-lens-source triplets can be split into N_true physical triplets, each carrying the signal s, and $N_\mathrm{tot} - N_\mathrm{true}$ triplets carrying no signal. We further assume that all triplets carry the same uncorrelated noise n. Then, the measured total signal S, noise N and S/N are

$$S = \frac{N_\mathrm{true}}{N_\mathrm{tot}} s, \qquad N = \frac{1}{\sqrt{N_\mathrm{tot}}} n, \qquad \text{and } S/N = \frac{N_\mathrm{true}}{\sqrt{N_\mathrm{tot}}}\frac{s}{n}\ . \tag{3.9}$$

With redshift weighting we decrease the effective number of triplets from N_tot to $\tilde{N}_\mathrm{tot}$, while retaining the same number of physical triplets N_true. The signal $\tilde{S}$, the noise $\tilde{N}$ and the new S/N $\tilde{S}/\tilde{N}$ are then

$$\tilde{S} = \frac{N_\mathrm{true}}{\tilde{N}_\mathrm{tot}} s, \qquad \tilde{N} = \frac{1}{\sqrt{\tilde{N}_\mathrm{tot}}} n, \qquad \text{and } \tilde{S}/\tilde{N} = \frac{N_\mathrm{true}}{\sqrt{\tilde{N}_\mathrm{tot}}}\frac{s}{n}\ . \tag{3.10}$$

Consequently, redshift weighting increases the noise by a factor of $\left(N_\mathrm{tot}/\tilde{N}_\mathrm{tot}\right)^{1/2}$. Nonetheless, the S/N improves by $\left(N_\mathrm{tot}/\tilde{N}_\mathrm{tot}\right)^{1/2}$ because the signal increases by $N_\mathrm{tot}/\tilde{N}_\mathrm{tot}$. Accordingly, we expect the S/N to increase approximately by the square root of the signal increase.

The critical parameter for the redshift weighting is the width σ_z of the weighting function. For our application on the observational and simulated data described in Sect. 3.3, we choose $\sigma_z = 0.01$. Because there is no clear division between lens pairs that carry signal and those that do not, the choice of this parameter needs to remain somewhat arbitrary. However, three arguments motivate our choice.

The first argument considers the galaxy correlation length. Farrow et al. (2015) measured the two-point correlation function of galaxies in GAMA and found correlation lengths between $3.28 \pm 0.42\,h^{-1}$ Mpc and $38.17 \pm 0.47\,h^{-1}$ Mpc, depending on the stellar masses of the galaxies. Zehavi et al. (2011) measured the same function in the SDSS and found similar correlation lengths between $4.2\,h^{-1}$ Mpc and $10.5\,h^{-1}$ Mpc. These correlation lengths correspond to redshift differences between 0.001 and 0.005 at the median redshift of GAMA of $z = 0.21$. We assume that galaxies separated by more than twice the correlation length are only weakly correlated. Therefore our choice of $\sigma_z = 0.01$ seems appropriate.

The second argument relates to the distribution of lens galaxy pairs with their redshift difference. The blue histogram in Fig. 3.1 shows the number of galaxy pairs per redshift difference δz with fixed angular separation between $4\overset{\prime}{.}5$ and $5\overset{\prime}{.}5$ in our lens sample from the MR (see Sect. 3.3). This distribution has a prominent peak for small δz and a broad background distribution. Thus, most galaxy pairs that appear close on the sky are also close in redshift space. These physical pairs make up the peak. However, the background distribution shows that there are also many galaxy pairs with small angular separation whose redshift difference is large. The optimal redshift weighting function should preserve pairs inside the peak but suppress the background.

The other histograms in Fig. 3.1 show different weighted distributions, where the number of galaxy pairs is multiplied by the redshift-weighting function from Eq. (3.1). These distributions correspond to the effective number of galaxy pairs per redshift difference bin considered for the improved $\tilde{\mathcal{G}}$ estimator. Here, the effect of different σ_z is visible. The weighting preserves the peak when we use $\sigma_z = 0.1$ and 0.05. However, a high percentage of the background is still present in the weighted distribution. Weighting with $\sigma_z = 0.005$ and $\sigma_z = 0.001$ removes the background but also suppresses parts of the peak. A middle ground is found for $\sigma_z = 0.01$. Here, the tails of the peak still contribute, whereas most of the background galaxy pairs are suppressed. Consequently, we adopt this value for the measurement of $\tilde{\mathcal{G}}$ and subsequently $\langle \mathcal{N}\mathcal{N}\mathcal{M} \rangle$.

The third argument for our choice of σ_z considers the peculiar velocities of galaxies in clusters, which can cause redshift differences of correlated galaxy pairs inside the same halo. The weighting function Z needs to be broad enough to avoid discarding galaxy pairs whose redshift differences are induced simply by their peculiar motion. Velocities of galaxies inside halos can reach up to $1000\,\mathrm{km\,s^{-1}}$, leading to redshift differences of up to 0.006. This value is a lower bound for σ_z, therefore choosing $\sigma_z = 0.01$ appears valid.

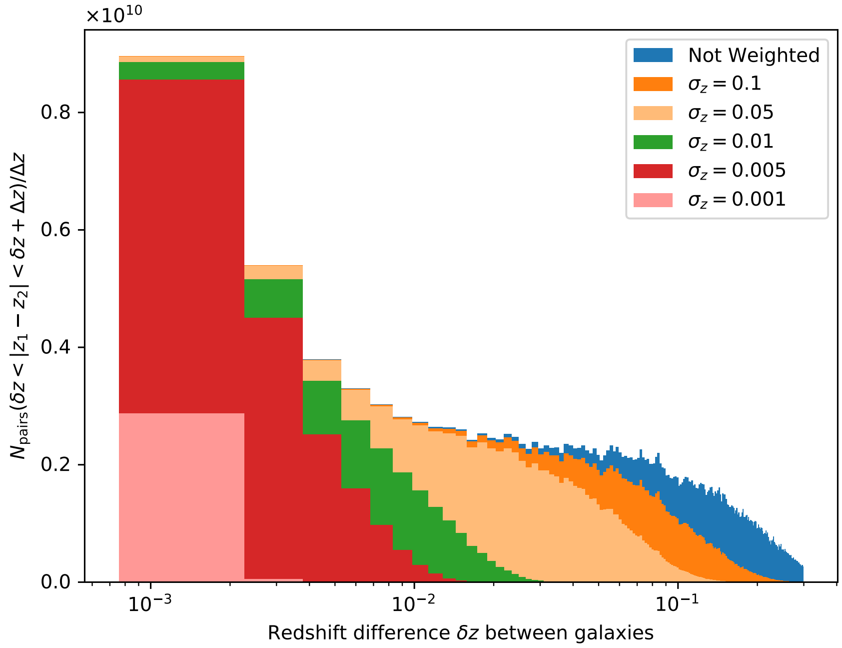

Figure 3.1: Weighted number of lens galaxy pairs in our sample from the MR with fixed angular separation between $4\overset{\prime}{.}5$ and $5\overset{\prime}{.}5$ per redshift difference between the pairs. Different colours indicate different widths of the Gaussian weighting function. The blue histogram shows the unweighed distribution, and the green histogram shows the distribution with the weighting chosen for the G3L measurements.

3.2.2 New binning scheme

In previous work (Simon et al., 2008, 2013), $\tilde{\mathcal{G}}$ was measured on a regular grid with logarithmic spacing in the lens-source separations ϑ_1 and ϑ_2 and linear spacing in the opening angle ϕ. The aperture statistics were then calculated by summing over this grid.

However, in this approach, the estimator for $\tilde{\mathcal{G}}$ is undefined in any bin without triplets. Previous works set $\tilde{\mathcal{G}}$ to zero in these empty bins. As a result, $\langle \mathcal{N}\mathcal{N}\mathcal{M}\rangle$, which is obtained by integrating over the estimated $\tilde{\mathcal{G}}$, was underestimated (Simon et al., 2008). This bias occurs for both small and large scales: At small scales, the bins for ϑ_1 and ϑ_2 are tiny because of the logarithmic binning. Therefore, many of them remain empty. At large scales, some bins are automatically empty because the opening angle ϕ cannot assume all values between 0 and 2π if ϑ_1 or ϑ_2 are larger than the side length of the field of view.

The bin sizes and the number of lens-lens-source triplets affect the severity of the bias. If the bins are smaller, more of them are empty, and the bias increases. If the number of triplets increases, there are fewer empty bins and the bias decreases.

To account for this effect, we introduce an adaptive binning scheme, illustrated in Fig. 3.2. In this new scheme, we define bins such that they contain at least one triplet, and therefore the estimator for $\tilde{\mathcal{G}}$ is always well defined. For this, $\tilde{\mathcal{G}}$ is first estimated on a regular grid, together with the average side lengths of the triplets in each bin. Then, in all bins with at least one

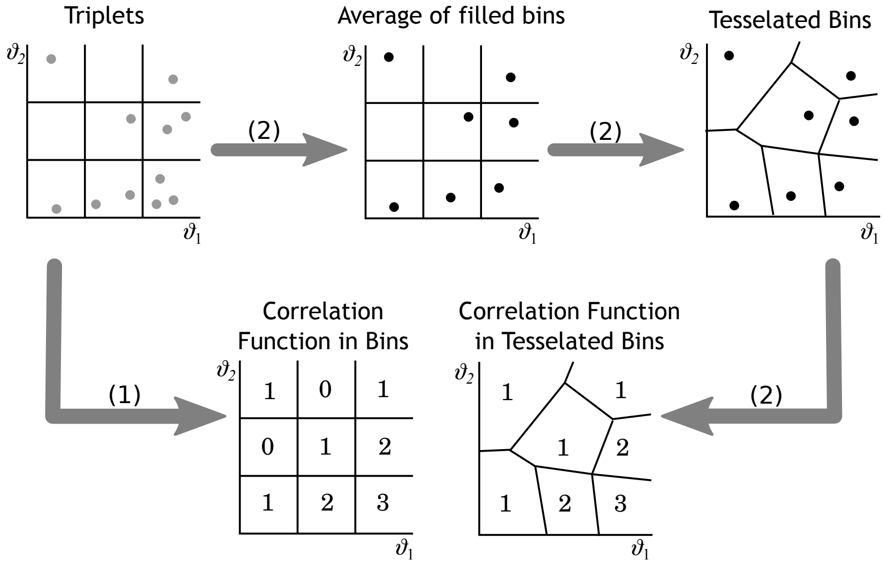

Figure 3.2: Illustration of the old (1) and new (2) binning scheme for the calculation of $\tilde{\mathcal{G}}$. In the old binning scheme, $\tilde{\mathcal{G}}$ was calculated directly from the lens-lens-source triplets inside a given bin. In the new binning scheme, at first, we calculate the average of the lens-lens-source triplets in a bin. We use these averages as seeds for a Voronoi tessellation of the parameter space. Then, we consider each Voronoi cell as a new bin for which we estimate $\tilde{\mathcal{G}}$. We obtain the aperture statistics by integrating over the new bins. We show only two dimensions here, but for the measurement, we also tesselated the third parameter ϕ.

triplets, the measured $\tilde{\mathcal{G}}$ is associated with the average ϑ_1, ϑ_2 and ϕ of the corresponding bin. We use the averages of the triplets in filled bins as seeds to divide the parameter space by a Voronoi tessellation, using the library `voro++` by Rycroft (2009). We consider each Voronoi cell as a new bin for $\tilde{\mathcal{G}}$. These bins, by definition, contain at least one triplet. We obtain the aperture statistics by integrating over the N_{bin} new bins, using the numerical approximation of Eq. (2.143),

$$\langle \mathcal{N}\mathcal{N}\mathcal{M} \rangle\,(\theta) + \mathrm{i}\,\langle \mathcal{N}\mathcal{N}\mathcal{M}_{\perp} \rangle\,(\theta) = \sum_{i=1}^{N_{\mathrm{bin}}} V(B_i)\,\tilde{\mathcal{G}}_{\mathrm{est}}(B_i)\,A_{\mathcal{N}\mathcal{N}\mathcal{M}}(B_i|\theta)\;, \tag{3.11}$$

where B_i is the ith bin, $V(B_i)$ is the volume of this bin, and $A_{\mathcal{N}\mathcal{N}\mathcal{M}}(B_i|\theta)$ is the kernel function of Eq. (2.143) evaluated at the seed of B_i. We estimate $\tilde{\mathcal{G}}$ on a grid with 128 × 128 × 128 bins with ϑ_1 and ϑ_2 between $0\overset{\prime}{.}15$ and $320'$ for the data based on the MR (see Sect. 3.3.1) and between $0\overset{\prime}{.}15$ and $200'$ for the simple mock data (see Sect. 3.3.2). The tessellation reduces the number of bins by approximately 3 % in both cases.

3.2.3 Conversion into physical units

With the lens redshifts z_1 and z_2, we can transform the projected angular separation vectors $\boldsymbol{\vartheta}_1$ and $\boldsymbol{\vartheta}_2$ into physical separations $\boldsymbol{r}_1$ and $\boldsymbol{r}_2$ on a plane midway between the two lenses, using

$$\boldsymbol{r}_{1,2} = D_{\mathrm{A}}\,(0, z_{12})\;\boldsymbol{\vartheta}_{1,2} =: D_{12}\,\boldsymbol{\vartheta}_{1,2}\;, \tag{3.12}$$

with the angular diameter distance $D_{\mathrm{A}}(z_a, z_b)$ between redshifts z_a and z_b and the average lens redshift $z_{12} = (z_1 + z_2)/2$.

The correlation function $\tilde{\mathcal{G}}_Z$ can therefore be estimated in physical scales in the bin B of r_1, r_2 and ϕ as

$$\tilde{\mathcal{G}}_{Z,\mathrm{est}}(B) = -\frac{\sum_{ijk} w_k\,\epsilon_k\,\mathrm{e}^{-\mathrm{i}(\varphi_{ik}+\varphi_{jk})}\,\left[1 + \omega\left(|\boldsymbol{\theta}_i - \boldsymbol{\theta}_j|\right)\right] Z(\Delta z_{ij})\Delta^{\mathrm{ph}}_{ijk}(B)}{\sum_{ijk} w_k\,Z(\Delta z_{ij})\,\Delta^{\mathrm{ph}}_{ijk}(B)}\;, \tag{3.13}$$

with

$$\Delta^{\mathrm{ph}}_{ijk}(B) = \begin{cases} 1 & \text{for } \left(D_A(0, z_{ij})\,|\boldsymbol{\theta}_k - \boldsymbol{\theta}_i|, D_A(0, z_{ij})\,|\boldsymbol{\theta}_k - \boldsymbol{\theta}_j|, \phi_{ijk}\right) \in B \\ 0 & \text{otherwise} \end{cases}\;, \tag{3.14}$$

This $\tilde{\mathcal{G}}_Z$ still depends on the redshift distribution of sources because the gravitational shear γ_{t} depends on the lensing efficiency, which in turn depends on the distances between observer and source and lens and source. To compare the measurements of different surveys with varying source redshift distributions, it is therefore useful to correlate the galaxy number density not with the tangential shear γ_{t}, but instead with the projected excess mass density $\Delta\Sigma$, given by

$$\Delta\Sigma(\boldsymbol{\theta}, z_{\mathrm{d}}, z_{\mathrm{s}}) = \begin{cases} \dfrac{\gamma_{\mathrm{t}}(\boldsymbol{\theta})}{\Sigma^{-1}_{\mathrm{crit}}(z_{\mathrm{d}}, z_{\mathrm{s}})} & \text{for } z_{\mathrm{d}} < z_{\mathrm{s}} \\ 0 & \text{else} \end{cases}\;, \tag{3.15}$$

with $\Sigma^{-1}_{\mathrm{crit}}$ defined in Eq. (2.95). Thus, we are interested in the correlation function $\tilde{\mathcal{G}}_{\mathrm{phys}}$, defined by

$$\begin{aligned}\tilde{\mathcal{G}}_{\mathrm{phys}}(\boldsymbol{r}_1, \boldsymbol{r}_2) = &\left[\int_0^\infty \mathrm{d}z_1 \int_0^\infty \mathrm{d}z_2 \;\; \nu_Z(z_1)\, \nu_Z(z_2)\, Z(\Delta z_{12})\, \bar{n}(z_1)\, \bar{n}(z_2)\right]^{-1} \quad (3.16)\\ &\times \int \mathrm{d}z_1 \int \mathrm{d}z_2 \;\; \nu_Z(z_1)\, \nu_Z(z_2)\, Z(\Delta z_{12})\\ &\times \left\langle n\left(\boldsymbol{\theta} + D_{12}^{-1}\, \boldsymbol{r}_1, z_1\right)\, n\left(\boldsymbol{\theta} + D_{12}^{-1}\, \boldsymbol{r}_2, z_2\right)\, \Delta\Sigma(\boldsymbol{\theta}, z_{12})\right\rangle\\ =:&\; \tilde{\mathcal{G}}_{\mathrm{phys}}(r_1, r_2, \phi)\ . \quad (3.17)\end{aligned}$$

To estimate this quantity with a maximum likelihood estimator, we need to multiply the weight w_k of each source galaxy with $\Sigma^{-2}_{\mathrm{crit}}$ (Sheldon et al., 2004). This leads to the estimator

$$\tilde{\mathcal{G}}_{\mathrm{est,phys}}(B) = \frac{\sum_{ijk} w_k\, \epsilon_k\, \mathrm{e}^{-\mathrm{i}(\varphi_{ik}+\varphi_{jk})} \left[1 + \omega\left(|\boldsymbol{\theta}_i - \boldsymbol{\theta}_j|\right)\right] Z(\Delta z_{ij})\, \Sigma^{-1}_{\mathrm{crit}}(z_{ij}, z_k)\, \Delta^{\mathrm{ph}}_{ijk}(B)}{\sum_{ijk} w_k\, \Sigma^{-2}_{\mathrm{crit}}(z_{ij}, z_k)\, Z(\Delta z_{ij})\, \Delta^{\mathrm{ph}}_{ijk}(B)}\ . \tag{3.18}$$

This estimator requires a precise knowledge of the source redshifts. For the application to real data, however, only photometric redshift estimates are often available for source galaxies. Therefore, we do not use the exact $\Sigma^{-1}_{\mathrm{crit}}$ for each triplet, but instead $\bar{\Sigma}^{-1}_{\mathrm{crit}}$, which is averaged over the source distribution $p_{\mathrm{s}}(z_{\mathrm{s}})$ as

$$\bar{\Sigma}^{-1}_{\mathrm{crit}}(z_{\mathrm{d}}) = \int \mathrm{d}z_{\mathrm{s}} \;\; p_{\mathrm{s}}(z_{\mathrm{s}})\, \Sigma^{-1}_{\mathrm{crit}}(z_{\mathrm{d}}, z_{\mathrm{s}})\ . \tag{3.19}$$

Consequently, we estimate $\tilde{\mathcal{G}}_{\mathrm{phys}}$ with

$$\tilde{\mathcal{G}}_{\mathrm{est,phys}}(B) = -\frac{\sum_{ijk} w_k\, \epsilon_k\, \mathrm{e}^{-\mathrm{i}(\varphi_{ik}+\varphi_{jk})} \left[1 + \omega\left(|\boldsymbol{\theta}_i - \boldsymbol{\theta}_j|\right)\right] Z(\Delta z_{ij})\, \bar{\Sigma}^{-1}_{\mathrm{crit}}(z_{ij})\, \Delta^{\mathrm{ph}}_{ijk}(B)}{\sum_{ijk} w_k\, \bar{\Sigma}^{-2}_{\mathrm{crit}}(z_{ij})\, Z(\Delta z_{ij})\, \Delta^{\mathrm{ph}}_{ijk}(B)}\ . \tag{3.20}$$

We convert this three-point correlation function into physical aperture statistics with

$$\begin{aligned}&\langle \mathcal{N}\mathcal{N}\mathcal{M}\rangle_{\mathrm{phys}}(R) + \mathrm{i}\,\langle \mathcal{N}\mathcal{N}\mathcal{M}_\perp\rangle_{\mathrm{phys}}(R)\\ &= \int_0^\infty \mathrm{d}r_1 \int_0^\infty \mathrm{d}r_2 \int_0^{2\pi} \mathrm{d}\phi \;\; r_1\, r_2\, \tilde{\mathcal{G}}_{\mathrm{phys}}(r_1, r_2, \phi)\\ &\times \mathcal{A}_{\mathcal{N}\mathcal{N}\mathcal{M}}\left(D_{12}^{-1}\, r_1, D_{12}^{-1}\, r_2, \phi \mid D_{12}^{-1}\, R\right)\ .\end{aligned} \tag{3.21}$$

These aperture statistics are in units of mass over area.

3.2.4 Magnification of lens galaxies

Magnification of lens galaxies by the LSS affects G3L because the apparent magnitude and number density of lenses is changed (see Sect. 2.4.4).

Using Eq. (2.117), the correlation function $\tilde{\mathcal{G}}_Z$ with the effect of lens magnification is

$$\begin{aligned}
&\tilde{\mathcal{G}}_Z(\vartheta_1, \vartheta_2, \phi) = \\
&\int \mathrm{d}z_1 \int \mathrm{d}z_2\ Z(z_1 - z_2) \\
&\times \left\{ \frac{1}{\bar{n}(z_1)\, \bar{n}(z_2)}\ \langle n_0(\boldsymbol{\vartheta}_1 + \boldsymbol{\theta}, z_1)\, n_0(\boldsymbol{\vartheta}_2 + \boldsymbol{\theta}, z_2)\, \gamma_\mathrm{t}(\boldsymbol{\theta}) \rangle \right. \\
&\quad + \frac{2[\alpha(z_2) - 1]}{\bar{n}(z_1)}\ \langle n_0(\boldsymbol{\vartheta}_1 + \boldsymbol{\theta}, z_1)\, \kappa(\boldsymbol{\vartheta}_2 + \boldsymbol{\theta}, z_2)\, \gamma_\mathrm{t}(\boldsymbol{\theta}) \rangle \\
&\quad + \frac{2[\alpha(z_1) - 1]}{\bar{n}(z_2)}\ \langle \kappa(\boldsymbol{\vartheta}_1 + \boldsymbol{\theta}, z_1)\, n_0(\boldsymbol{\vartheta}_2 + \boldsymbol{\theta}, z_2)\, \gamma_\mathrm{t}(\boldsymbol{\theta}) \rangle \\
&\quad \left. + 4[\alpha(z_1) - 1][\alpha(z_2) - 1]\ \langle \kappa(\boldsymbol{\vartheta}_1 + \boldsymbol{\theta}, z_1)\, \kappa(\boldsymbol{\vartheta}_2 + \boldsymbol{\theta}, z_2)\, \gamma_\mathrm{t}(\boldsymbol{\theta}) \rangle \right\} .
\end{aligned} \tag{3.22}$$

With the intrinsic aperture number count

$$\mathcal{N}_{0,\theta}(\boldsymbol{\vartheta}, z) = \frac{1}{\bar{n}(z)} \int \mathrm{d}^2\vartheta'\ U_\theta(|\boldsymbol{\vartheta} - \boldsymbol{\vartheta}'|)\, n_0\left(\boldsymbol{\vartheta}', z\right)\ , \tag{3.23}$$

and $\mathcal{M}_\theta$ as defined in Eq. (2.134), the aperture statistics are

$$\begin{aligned}
\langle \mathcal{N}\mathcal{N}\mathcal{M} \rangle(\theta) = &\int \mathrm{d}z_1 \int \mathrm{d}z_2\ Z(z_1 - z_2) \\
&\times \Big\{ \big\langle \mathcal{N}_{0,\theta}(\boldsymbol{\vartheta}, z_1)\, \mathcal{N}_{0,\theta}(\boldsymbol{\vartheta}, z_2)\, \mathcal{M}_\theta(\boldsymbol{\vartheta}) \big\rangle \\
&\quad + 2[\alpha(z_2) - 1]\ \big\langle \mathcal{N}_{0,\theta}(\boldsymbol{\vartheta}, z_1)\, \mathcal{M}_\theta(\boldsymbol{\vartheta}, z_2)\, \mathcal{M}_\theta(\boldsymbol{\vartheta}) \big\rangle \\
&\quad + 2[\alpha(z_1) - 1]\ \big\langle \mathcal{M}_\theta(\boldsymbol{\vartheta}, z_1)\, \mathcal{N}_{0,\theta}(\boldsymbol{\vartheta}, z_2)\, \mathcal{M}_\theta(\boldsymbol{\vartheta}) \big\rangle \\
&\quad + 4[\alpha(z_1) - 1][\alpha(z_2) - 1]\ \langle \mathcal{M}_\theta(\boldsymbol{\vartheta}, z_1)\, \mathcal{M}_\theta(\boldsymbol{\vartheta}, z_2)\, \mathcal{M}_\theta(\boldsymbol{\vartheta}) \rangle \Big\} .
\end{aligned} \tag{3.24}$$

Thus, the measured aperture statistics do not only include the intrinsic first term, but three additional terms that are due to lens magnification. These lens magnification terms, however, can be measured using as redshift-weighting function Z not a Gaussian, but a step function,

$$Z(z_1 - z_2) = \Theta_\mathrm{H}(z_2 - z_1 - \Delta z)\ . \tag{3.25}$$

This means that only lens pairs with a redshift difference larger than Δz and $z_2 > z_1$ are counted in the estimator in Eq. (3.4). As explained in Sect. 3.2.1, we expect lens pairs with redshift differences larger than 0.01 to be intrinsically uncorrelated. When we choose $\Delta z = 0.01$, the first term in Eq. (3.24), which contains only the correlation of intrinsic number densities, should vanish. The measured $\langle \mathcal{N}\mathcal{N}\mathcal{M} \rangle$ is then purely the correlation due to the lens magnification. We measure this $\langle \mathcal{N}\mathcal{N}\mathcal{M} \rangle$ with the estimator in Eq. (3.4), using the step function weighting. If this signal is then subtracted from the measured $\langle \mathcal{N}\mathcal{N}\mathcal{M} \rangle$ of all lenses, we obtain the intrinsic aperture statistics.

We tested our approach on simulated data from the MR, for which both the number density and convergence are available at different redshift planes. Hence, we can also use another approach to measure the terms due to lens magnification. In this approach we use the relation of the observed aperture number count $\mathcal{N}_\theta$ to the intrinsic aperture number count $\mathcal{N}_{0,\theta}$ and aperture mass $\mathcal{M}_\theta$ through

$$\begin{aligned} \mathcal{N}_\theta(\boldsymbol{\vartheta}, z) &= \frac{1}{\bar{n}(z)} \int \mathrm{d}^2\vartheta' \; U_\theta(\boldsymbol{\vartheta} - \boldsymbol{\vartheta}'|) \, n\left(\boldsymbol{\vartheta}', z\right) \qquad (3.26) \\ &= \mathcal{N}_{0,\theta}(\boldsymbol{\vartheta}, z) + 2\left[\alpha(z) - 1\right] \mathcal{M}_\theta(\boldsymbol{\vartheta}, z) \; . \qquad (3.27) \end{aligned}$$

Consequently, Eq. (3.24) with the step function weighting in Eq. (3.25) leads to

$$\begin{aligned} &\langle \mathcal{N}\mathcal{N}\mathcal{M}\rangle\,(\theta) \qquad (3.28) \\ &= \int_0^{z_\mathrm{max}} \mathrm{d}z_1 \int_{z_1+\Delta z}^{z_\mathrm{max}} \mathrm{d}z_2 \; \left\{\left\langle \mathcal{N}_{0,\theta}(\boldsymbol{\vartheta}, z_1)\, \mathcal{N}_{0,\theta}(\boldsymbol{\vartheta}, z_2)\, \mathcal{M}_\theta(\boldsymbol{\vartheta})\right\rangle\right. \\ &\quad +2\left[\alpha(z_2) - 1\right] \; \langle \mathcal{N}_\theta(\boldsymbol{\vartheta}, z_1)\, \mathcal{M}_\theta(\boldsymbol{\vartheta}, z_2)\, \mathcal{M}_\theta(\boldsymbol{\vartheta})\rangle \\ &\quad +2\left[\alpha(z_1) - 1\right] \; \langle \mathcal{M}_\theta(\boldsymbol{\vartheta}, z_1)\, \mathcal{N}_\theta(\boldsymbol{\vartheta}, z_2)\, \mathcal{M}_\theta(\boldsymbol{\vartheta})\rangle \\ &\quad \left. -4\left[\alpha(z_1) - 1\right]\left[\alpha(z_2) - 1\right] \langle \mathcal{M}_\theta(\boldsymbol{\vartheta}, z_1)\, \mathcal{M}_\theta(\boldsymbol{\vartheta}, z_2)\, \mathcal{M}_\theta(\boldsymbol{\vartheta})\rangle\right\} \; , \end{aligned}$$

where the terms due to lens magnification are given by the observed instead of by the intrinsic aperture number count. For a numerical evaluation, the integrals can be converted into sums over M redshift slices, so

$$\begin{aligned} &\langle \mathcal{N}\mathcal{N}\mathcal{M}\rangle\,(\theta) \\ &= \sum_{i=0}^{M} \sum_{j=i+1}^{M} \Delta z_i\, \Delta z_j \; \left\{\left\langle \mathcal{N}_{0,\theta}(\boldsymbol{\vartheta}, z_i)\, \mathcal{N}_{0,\theta}(\boldsymbol{\vartheta}, z_j)\, \mathcal{M}_\theta(\boldsymbol{\vartheta})\right\rangle\right. \qquad (3.29) \\ &\quad +2\left[\alpha(z_j) - 1\right] \; \left\langle \mathcal{N}_\theta(\boldsymbol{\vartheta}, z_i)\, \mathcal{M}_\theta(\boldsymbol{\vartheta}, z_j)\, \mathcal{M}_\theta(\boldsymbol{\vartheta})\right\rangle \\ &\quad +2\left[\alpha(z_i) - 1\right] \; \left\langle \mathcal{M}_\theta(\boldsymbol{\vartheta}, z_i)\, \mathcal{N}_\theta(\boldsymbol{\vartheta}, z_j)\, \mathcal{M}_\theta(\boldsymbol{\vartheta})\right\rangle \\ &\quad \left. -4\left[\alpha(z_i) - 1\right]\left[\alpha(z_j) - 1\right] \; \left\langle \mathcal{M}_\theta(\boldsymbol{\vartheta}, z_i)\mathcal{M}_\theta(\boldsymbol{\vartheta}, z_j)\, \mathcal{M}_\theta(\boldsymbol{\vartheta})\right\rangle\right\} \\ &=: \sum_{i=0}^{M} \sum_{j=i+1}^{M} \Delta z_i\, \Delta z_j \; \left\langle \mathcal{N}_{0,\theta}(\boldsymbol{\vartheta}, z_i)\, \mathcal{N}_{0,\theta}(\boldsymbol{\vartheta}, z_j)\, \mathcal{M}_\theta(\boldsymbol{\vartheta})\right\rangle \qquad (3.30) \\ &\quad + L_{\mathcal{N}\mathcal{M}\mathcal{M}}(\theta) + L_{\mathcal{M}\mathcal{N}\mathcal{M}}(\theta) + L_{\mathcal{M}\mathcal{M}\mathcal{M}}(\theta) \; . \end{aligned}$$

Using Eq. (3.30), we measure the lens magnification terms $L_{\mathcal{M}\mathcal{M}\mathcal{M}}$, $L_{\mathcal{M}\mathcal{N}\mathcal{M}}$ and $L_{\mathcal{N}\mathcal{M}\mathcal{M}}$ directly in the simulated data based on the MR for $z_j < 0.5$ and $z_i < z_j$.

For this, we first convolve the number density and convergence maps at each redshift plane with the filter function U_θ to obtain $\mathcal{N}_\theta(\boldsymbol{\vartheta}, z_i)$ and $\mathcal{M}_\theta(\boldsymbol{\vartheta}, z_j)$. We then multiply the aperture statistics for each combination of z_i and z_j and spatially average the products to obtain $\left\langle \mathcal{N}_\theta(\boldsymbol{\vartheta}, z_i)\, \mathcal{M}_\theta(\boldsymbol{\vartheta}, z_j)\, \mathcal{M}_\theta(\boldsymbol{\vartheta})\right\rangle$ and $\left\langle \mathcal{M}_\theta(\boldsymbol{\vartheta}, z_i)\, \mathcal{M}_\theta(\boldsymbol{\vartheta}, z_j)\, \mathcal{M}_\theta(\boldsymbol{\vartheta})\right\rangle$. These averages are then

Table 3.1: Slopes α of the luminosity function at different redshifts z in the MR. The limiting magnitude of galaxies is $r_{\mathrm{lim}} = 19.8\,\mathrm{mag}$.

z	0.46	0.41	0.36	0.32	0.28	0.24	0.21	0.17	0.14	0.12	0.06	0.04
α	2.51	2.38	2.01	1.80	1.36	1.15	0.91	0.78	0.49	0.48	0.47	0.17

multiplied by the appropriate α and summed over. We repeat this procedure for different aperture scale radii θ between $0\overset{\prime}{.}5$ and $8'$.

For this calculation, the slope $\alpha(z)$ of the lens luminosity function needs to be known. To obtain $\alpha(z)$, we extract the luminosity function $\Phi(S, z)$ at each redshift plane of the MR, with S measured in the r-band filter. We then fit a power law to $\Phi(S, z)$ in the proximity of the limiting flux. This flux is given in our case by the limiting r-band magnitude, chosen to be $r_{\mathrm{lim}} = 19.8\,\mathrm{mag}$. The slopes for each redshift z are the $\alpha(z)$ given in Table 3.1.

3.3 Data

3.3.1 Simulated data based on the Millennium Run

We tested our new estimator with simulated data sets from the MR, which we described in Sect. 2.2.1. Using the multiple-lens-plane ray-tracing algorithm by Hilbert et al. (2009), we created maps of the complex gravitational shear γ caused by the matter distribution for a set of source redshift planes. For each redshift, 64 maps of γ on a regular mesh with 4096^2 pixels, corresponding to $4 \times 4\,\mathrm{deg}^2$, were obtained. We combined the shear of nine different redshifts between $z = 0.5082$ and $z = 1.1734$ by summing γ weighted by an assumed source redshift distribution $p_{\mathrm{s}}(z)$. This redshift distribution, shown in Fig. 3.3, was modelled after the redshift distribution of galaxies in KiDS (Wright et al., 2019; Hildebrandt et al., 2020). To mimic the shape noise in observational data, we added a random number drawn from a Gaussian probability distribution with standard deviation 0.3 to both shear components at each pixel. With this procedure, we obtain 64 maps of mock source galaxies.

Lens galaxies in the simulation were created by using the SAM by H15 (see Sect. 2.2.2). It is one of various SAMs that have been implemented on the MR (see e.g. Guo et al., 2011; Bower et al., 2006), but as Saghiha et al. (2017) have shown, this model agrees particularly well with measurements of GGL and G3L in CFHTLenS. To simulate the selection function of observations, we applied a redshift and flux limit on our lens samples. We used lenses with $z \leq 0.5$ and SDSS r-band magnitude brighter than 19.8 mag. With these limits, we obtained a number density of lenses of $0.282\,\mathrm{arcmin}^{-2}$.

To mitigate possible biases induced by uneven galaxy pair numbers and matter distributions between the 64 lens galaxy maps, we subtracted the lensing signal around random points. This procedure is similar to methods for GGL (Singh et al., 2017, e.g.,). There, the shear around random positions is measured and subtracted from the original measurement. However, for

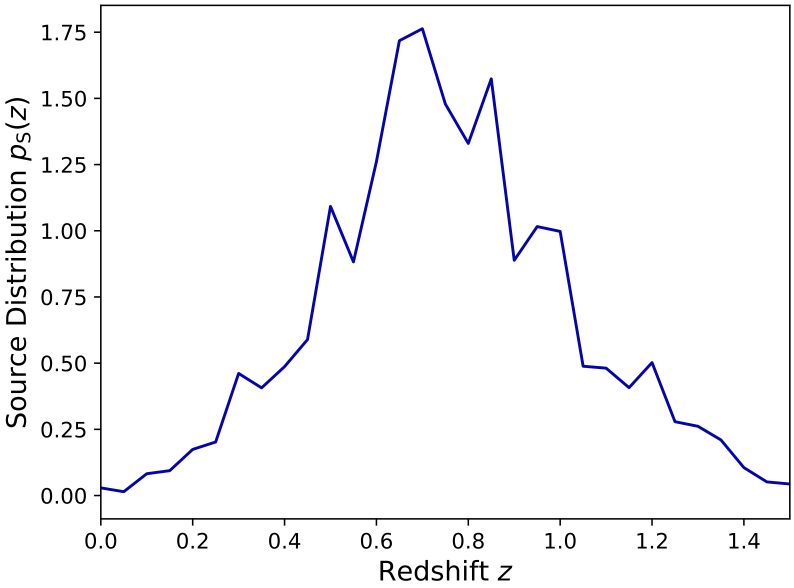

Figure 3.3: Assumed source redshift distribution. This distribution is used to weigh the shear maps at different redshifts in the MR. It is modelled after the redshift distribution of galaxies in Hildebrandt et al. (2020).

G3L, this task is in general more difficult because it requires a catalogue of unclustered galaxy pairs. Creating such a catalogue is in general non-trivial because the number of galaxy pairs depends on the selection function of individual galaxies in the survey. Nevertheless, we created a map of unclustered galaxies, similar to GGL, for each simulated lens map by distributing the same number of galaxies as on the lens map at random points on a $4 \times 4\,\mathrm{deg}^2$ area. We measured the correlation function $\tilde{\mathcal{G}}$ for each of these random maps. Afterwards, we subtracted it from the correlation function measured for the actual lens map.

The total number of triplets to consider for our measurement of $\tilde{\mathcal{G}}_Z$ and $\tilde{\mathcal{G}}_{\mathrm{phys}}$ is 5×10^{12}. This makes the evaluation of the sums in Eq. (3.4) and Eq. (3.20) computationally involved. Because of this computational complexity, computation of third-order correlation functions usually involves some approximation. One such approximation are kd-Tree codes (Simon et al., 2013), which average galaxy triplets with similar ϑ_1, ϑ_2 and ϕ. However, we implemented the estimator brute force and calculated it with a graphics processing unit (GPU). This approach has two advantages compared to the usual methods. First, it is exact, even at the smallest scales. Second, due to the highly parallelised execution on a GPU, which allows for several thousand simultaneous calculations, the computing time is drastically reduced. In our case, the computational time to process the MR decreased from 200 hours with a kd-Tree code executed on 8 CPU cores to just 9 hours with the brute-force code on a single GPU. Details for our computational implementation are given in Appendix A.2.

The covariance matrices of the measured $\langle \mathcal{N}\mathcal{N}\mathcal{M}\rangle$ and $\langle \mathcal{N}\mathcal{N}\mathcal{M}\rangle_{\mathrm{phys}}$ were computed with jackknifing. For this, we assumed that each of the 64 fields is an independent realisation and combined these fields to a total $\langle \mathcal{N}\mathcal{N}\mathcal{M} \rangle\,(\theta)$ and 64 jackknife samples $\langle \mathcal{N}\mathcal{N}\mathcal{M} \rangle_k\,(\theta)$, where all but the kth tile were combined. The covariance matrix is then

$$\begin{aligned} &C(\theta_i, \theta_j) \\ &= \frac{64}{64-1} \sum_{k=1}^{64} \left[\langle \mathcal{N}\mathcal{N}\mathcal{M} \rangle_k\,(\theta_i) - \overline{\langle \mathcal{N}\mathcal{N}\mathcal{M} \rangle_k}(\theta_i) \right] \left[\langle \mathcal{N}\mathcal{N}\mathcal{M} \rangle_k\,(\theta_j) - \overline{\langle \mathcal{N}\mathcal{N}\mathcal{M} \rangle_k}(\theta_j) \right]\,, \end{aligned} \tag{3.31}$$

where $\overline{\langle \mathcal{N}\mathcal{N}\mathcal{M} \rangle_k}(\theta_i)$ is the average of all $\langle \mathcal{N}\mathcal{N}\mathcal{M} \rangle_k\,(\theta_i)$. The statistical uncertainty of the aperture statistics $\langle \mathcal{N}\mathcal{N}\mathcal{M} \rangle\,(\theta_i)$ is $\sigma_i = \sqrt{C(\theta_i, \theta_i)}$. We define the S/N at each scale radius θ_i as

$$S/N(\theta_i) = \frac{\langle \mathcal{N}\mathcal{N}\mathcal{M} \rangle\,(\theta_i)}{\sigma_i}\,. \tag{3.32}$$

3.3.2 Simple mock data

Some of our tests also employed simple mock data. These were chosen such that it was easy to create them and to calculate their expected aperture statistics theoretically. For this, we used the following assumptions:

A. All matter and galaxies are distributed inside H halos over an area A.

B. All halos are situated on the same lens plane.

C. All halos have the same axisymmetric convergence profile $\kappa(\boldsymbol{\vartheta}) = K\,u(\vartheta)$ and the same number of galaxies N_{gal}, with $\int \mathrm{d}\vartheta\ \vartheta\,u(\vartheta) = 1$

D. There is no galaxy bias, so the discrete galaxy distribution follows the matter distribution up to Poisson shot-noise.

E. Halo centres are distributed randomly within A.

With these assumptions and the calculations in App. A.1, the theoretical expectation for the aperture statistics using the exponential filter function in Eq. (2.142) is

$$\begin{aligned} &\langle \mathcal{N}\mathcal{N}\mathcal{M} \rangle\,(\theta_1, \theta_2, \theta_3) \\ &= \frac{2\pi\,A\,K}{H} \int_0^\infty \mathrm{d}\vartheta\ \vartheta \prod_{i=1}^{3} \int_0^\infty \mathrm{d}y_i\ \frac{y_i\,u(y_i)}{\theta_i^2}\ \exp\left[-\frac{(y_i-\vartheta)^2}{2\theta_i^2}\right] \\ &\quad \times \left[\left(1 - \frac{y_i^2+\vartheta^2}{2\theta_i^2}\right) f_0\left(\frac{y_i\,\vartheta}{\theta_i^2}\right) + \frac{y_i\vartheta}{\theta_i^2}\,f_1\left(\frac{y_i\,\vartheta}{\theta_i^2}\right)\right]\,, \end{aligned} \tag{3.33}$$

with $f_n(x) = I_n(x)\,\mathrm{e}^{-x}$ and the modified Bessel functions of the first kind $I_n(x)$. We evaluated the integrals numerically with a Monte Carlo integration using the `monte-vegas`-routine of the GNU Scientific Library (GSL) (Gough, 2009).

We used the Brainerd-Blandford-Smail (BBS) profile (Brainerd et al., 1996) as halo convergence profile $\kappa(\boldsymbol{\vartheta})$, which is

$$\kappa(\boldsymbol{\vartheta}) = \frac{K}{2\pi\,\vartheta\,\theta_\mathrm{s}}\left(1 - \frac{\vartheta}{\sqrt{\vartheta^2 + \theta_\mathrm{s}^2}}\right) . \tag{3.34}$$

The BBS profile corresponds to a singular isothermal sphere (SIS) for ϑ much smaller than the scale radius θ_s that smoothly drops outside the sphere. In contrast to the SIS profile, it has a finite total mass. We chose $K = 1\,\mathrm{arcmin}^2$ and $\theta_\mathrm{s} = 5'$.

We created mock lens galaxies following assumptions A to E in a circular area with a radius of $700'$. We distributed the lens galaxies in 2170 halos with 200 galaxies each. These numbers were chosen such that the average number density of lens galaxies was $\overline{N}_\mathrm{d} = 0.287\,\mathrm{arcmin}^{-2}$, the lens number density in our lens sample from the MR. We distributed 3×10^6 source galaxies, whose shear we computed from the halo convergence profiles, in the central $750 \times 750\,\mathrm{arcmin}^2$ area. We only considered lens-lens-source triplets in this area to ensure that the shear of each source was affected by halos from all directions. No shape noise was added to the shears because our aim was not to create a realistic simulation, but only a simple test case. Because $\tilde{\mathcal{G}}$ is linear in the ellipticities, any shape noise would not bias its estimate and only lead to a larger uncertainty of the measurement. We cut the central area into quadratic tiles with a side length of $150'$, so that finally 25 maps of source and lens galaxies were used.

3.4 Results

3.4.1 Effect of the new binning scheme

Before measuring the aperture statistics in the data based on the MR, we estimated the effect of the new binning scheme by measuring the aperture statistics for equal-scale radii θ in the simple mock data, described in Sect 3.3.2. Figure 3.4 presents the aperture statistics measured in this mock data. The theoretically expected $\langle\mathcal{N}\mathcal{N}\mathcal{M}\rangle$ follows a power law for scale radii below $2'$ and steepens for larger scales. The $\langle\mathcal{N}\mathcal{N}\mathcal{M}\rangle$ measured with the old and the new binning scheme show the same steepening for θ larger than $2'$. However, the slope of the $\langle\mathcal{N}\mathcal{N}\mathcal{M}\rangle$ measured with the old binning scheme is considerably shallower for scales between $0\overset{'}{.}1$ and $0\overset{'}{.}6$ than the one measured with the new binning scheme. We confirm that the measurement with the new binning scheme agrees with the theoretical expectation within its statistical uncertainty. This agreement of the measured aperture statistics with the theoretical prediction validates our code for estimating $\tilde{\mathcal{G}}$ and for converting $\tilde{\mathcal{G}}$ to $\langle\mathcal{N}\mathcal{N}\mathcal{M}\rangle$.

To quantify the effect of the new binning scheme, Fig. 3.5 shows the difference of the measured $\langle\mathcal{N}\mathcal{N}\mathcal{M}\rangle$ to the theoretical prediction for both binning schemes, normalised by the theoretical prediction. The $\langle\mathcal{N}\mathcal{N}\mathcal{M}\rangle$ from the old method has no bias at scales between $1'$ and $5'$. However, it underestimates $\langle\mathcal{N}\mathcal{N}\mathcal{M}\rangle$ both above and below these scales. At large scales, this bias grows to 10 % at $\theta = 10'$, whereas at small scales, the bias increases with decreasing scale to 40 %

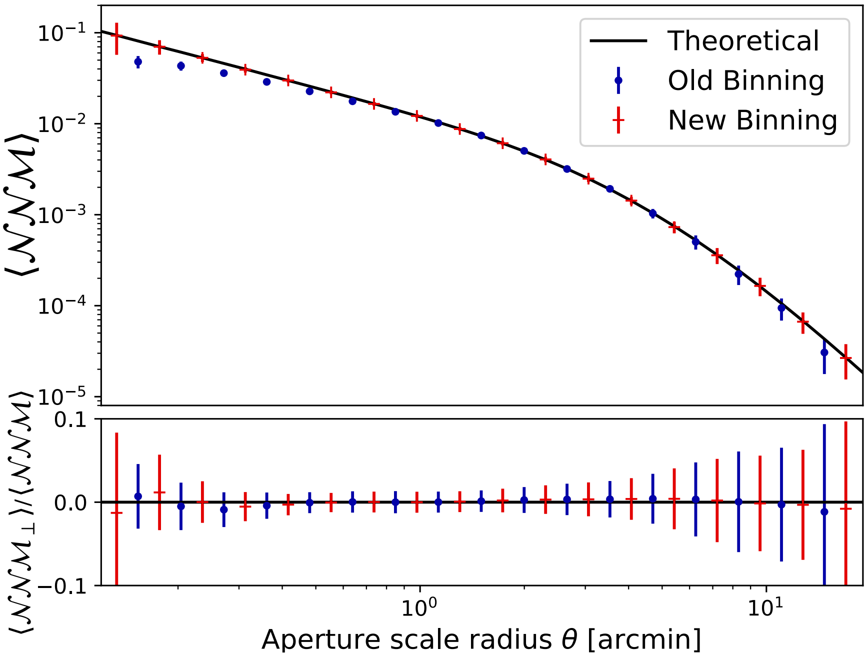

Figure 3.4: Aperture statistics measured in the simple mock data with the old binning scheme (blue dots) and the new binning scheme (red crosses), as well as the theoretical expectation (black line) given by Eq. (3.33). The upper plot shows the E mode $\langle \mathcal{NNM} \rangle$, and the lower plot shows the ratio of the B mode $\langle \mathcal{NNM}_\perp \rangle$ and the E mode. Uncertainties are the statistical error estimated with jackknifing.

at $\theta = 0\farcm1$. The new binning scheme does not show this behaviour. Instead, the bias of the $\langle \mathcal{NNM} \rangle$ measured with the new method is consistent with zero at all considered scales.

3.4.2 Effect of lens magnification

As outlined in Sect. 3.2.4, the redshift weighting enables us to measure the impact of lens magnification on G3L. We estimated this effect in the data based on the MR with the two different methods outlined in Sect 3.2.4. In the following, the terms “first” and “second” lens plane refer to the redshift plane in which the lens galaxy lies closer to the observer and closer to the source, respectively.

The result for the first method, using the step function weighting in the estimation of $\tilde{\mathcal{G}}_Z$, is shown in Figs. 3.6 and 3.7 for $\langle \mathcal{NNM} \rangle$ and $\langle \mathcal{NNM} \rangle_{\mathrm{phys}}$, respectively. The figures show the aperture statistics measured for lens pairs with redshift differences larger than 0.01. If there were no lens magnification, this signal should vanish. The figures also show the aperture statistics measured with all lens pairs, as well as the intrinsic aperture statistics. These were“corrected” for the effect of lens magnification by subtracting the signal of physically distant lens pairs from the total measured aperture statistics.

For both $\langle \mathcal{NNM} \rangle$ and $\langle \mathcal{NNM} \rangle_{\mathrm{phys}}$, the signal of physically separated lens pairs is non-zero. We attribute this signal to the three magnification terms in Eq. (3.24). For $\langle \mathcal{NNM} \rangle$ this signal

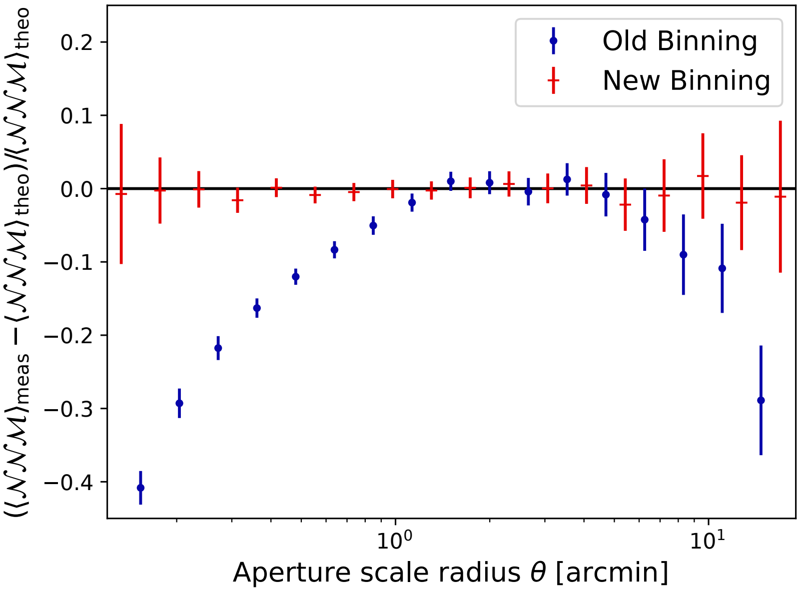

Figure 3.5: Fractional difference of the measured $\langle\mathcal{NNM}\rangle$ relative to the theoretical prediction in the simple mock data. Blue dots show the measurement with the old binning scheme; red crosses show the measurement with the new binning scheme.

is approximately 10 % of the signal of all lens pairs. For $\langle\mathcal{NNM}\rangle_{\mathrm{phys}}$, the magnification leads to a slightly weaker additional signal at scales below $0.1h^{-1}$ Mpc and approximately 10 % at larger scales.

At angular scales smaller than $0\farcm2$, the signal due to lens magnification for $\langle\mathcal{NNM}\rangle$ decreases. This decrease is probably due to smoothing in the simulation, which is no longer accurate at these small angular scales. Smoothing flattens the centre of halo convergence profiles in the simulation. If we measure the aperture statistics at scale radii smaller than the smoothing lengths, the flattening leads to a lower measured signal.

To verify that the signal for separated lens pairs is related to lens magnification, Fig. 3.8 shows the magnification terms estimated with the second method from Sect. 3.2.4. For comparison, the figure also shows the measured $\langle\mathcal{NNM}\rangle$ from the first method.

The figure shows that $L_{\mathcal{NMM}}(\theta)$, which is due to the correlation of the number density of galaxies at smaller redshift to the convergence measured at higher redshifts, is the dominating term. It is higher than $L_{\mathcal{MMM}}$ and $L_{\mathcal{MNM}}$ by three orders of magnitude. Furthermore, the correlation of three convergence maps $L_{\mathcal{MMM}}$, and the foreground convergence to background galaxies $L_{\mathcal{MNM}}$ are almost identical. Consequently, the total lens magnification signal is approximately $L_{\mathcal{NMM}}$.

This finding implies that the lens magnification signal is driven mainly by the correlation of matter and the galaxy distribution at the first lens plane. This matter affects the convergence at the second lens and the source plane and thereby causes a significant $L_{\mathcal{NMM}}$. Neither $L_{\mathcal{MNM}}$

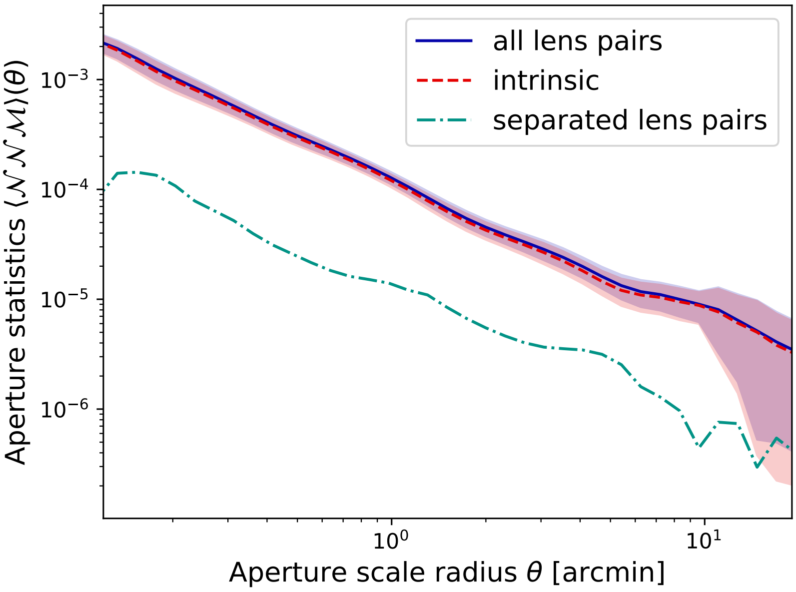

Figure 3.6: Effect of lens magnification on aperture statistics in the data based on the MR. The green dash-dotted line shows the signal measured for lens pairs with redshift differences larger than 0.01, which corresponds to the magnification terms in Eq. (3.24). The solid blue line is the aperture statistics for all lens pairs. The red dashed line is the intrinsic signal corrected for lens magnification by subtracting the signal of separated lens pairs. Shaded regions are the 1 σ uncertainties from jackknifing.

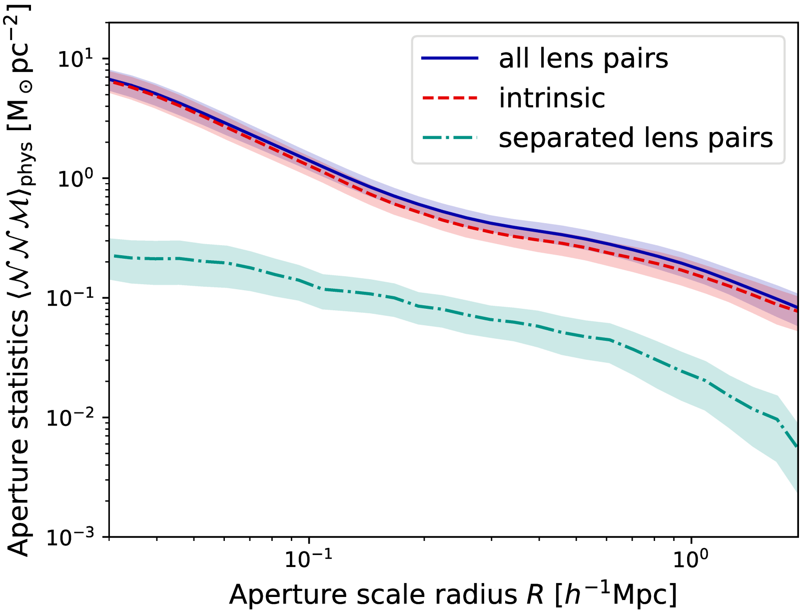

Figure 3.7: Same as Fig. 3.6, but for physical aperture statistics.

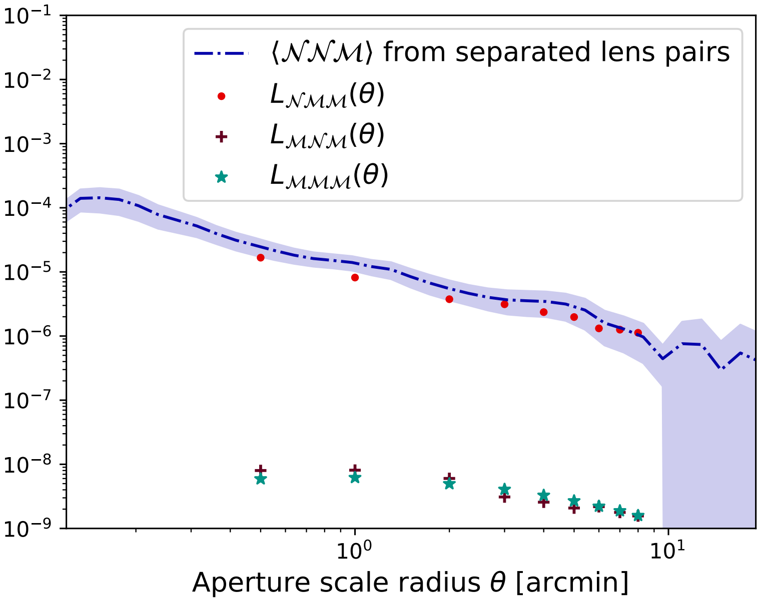

Figure 3.8: Individual lens magnification terms in the MR. Green stars depict the term due to the correlation between the convergence maps at the two lens planes and the source plane. Red dots are the term due to correlation of the galaxy number density at the first lens plane to the convergence maps at the second lens and the source plane. Brown crosses are the term due to correlation of the convergence maps at the first lens and the source plane to the galaxy number density at the second lens plane. The blue line is the measured $\langle\mathcal{N}\mathcal{N}\mathcal{M}\rangle$ for separated lens pairs, which should correspond to the total lens magnification signal.

nor $L_{\mathcal{MMM}}$ depend on the correlation between matter and galaxies at the same plane. Instead, they are mainly due to the LSS in front of the first lens plane. This LSS influences $\mathcal{N}_\theta$ and $\mathcal{M}_\theta$ at the lens planes and the source plane and thereby induces the non-zero $L_{\mathcal{MNM}}$ and $L_{\mathcal{MMM}}$. However, as shown in Fig. 3.8, this effect is secondary. The LSS in front of the lenses does not have a strong effect on the overall signal.

The total lens magnification signal is of the same order of magnitude as the $\langle \mathcal{NNM} \rangle$ measured with separated lens pairs. At scales above $1'$, it indeed agrees with the measured $\langle \mathcal{NNM} \rangle$ for separated lens pairs within its statistical uncertainty. At smaller scales, the difference between the two quantities is still smaller than twice the statistical uncertainty. According to Eq. (3.28), the intrinsic aperture statistics are

$$\begin{aligned}&\left\langle \mathcal{N}_{0,\theta}(\boldsymbol{\vartheta}, z_1)\, \mathcal{N}_{0,\theta}(\boldsymbol{\vartheta}, z_2)\, \mathcal{M}_\theta(\boldsymbol{\vartheta})\right\rangle \\ &= \langle \mathcal{NNM} \rangle\,(\theta) - L_{\mathcal{NMM}}(\theta) - L_{\mathcal{MNM}}(\theta) - L_{\mathcal{MMM}}(\theta)\ ,\end{aligned} \tag{3.35}$$

where $\langle \mathcal{NNM} \rangle$ are the measured aperture statistics for separated lens pairs. Therefore, the intrinsic aperture statistics for separated lens pairs vanishes, as expected.

3.4.3 Effect of redshift weighting

We show the results for $\langle \mathcal{NNM} \rangle$ for the data based on the MR with and without redshift weighting in Fig. 3.9a. The measured $\langle \mathcal{NNM}_\perp \rangle$ is consistent with zero, both with and without redshift weighting. This result signifies that no indication of parity violation exists in the simulation.

Redshift-weighting increases the S/N, (indicated by the decreasing error region in Fig. 3.9a). Simultaneously, the measured $\langle \mathcal{NNM} \rangle$ increases by a factor of approximately two. This increase occurs because redshift weighting is assumed to increase both signal and S/N, as discussed in Sect. 3.2.1. The lower plot in Fig. 3.9a shows the S/N of $\langle \mathcal{NNM} \rangle$ with and without redshift weighting. Redshift weighting increases the S/N on all scales. On average, the S/N of $\langle \mathcal{NNM} \rangle$ with redshift weighting is 1.35 times the S/N of $\langle \mathcal{NNM} \rangle$ without redshift weighting.

The measured physical aperture statistics $\langle \mathcal{NNM} \rangle_{\mathrm{phys}}$ are displayed in Fig. 3.9b. Again, the B mode is consistent with zero at all scales. Redshift weighting increases the signal by a factor of two, similar to the increase of $\langle \mathcal{NNM} \rangle$, whereas the error region decreases. The increase of the S/N of $\langle \mathcal{NNM} \rangle_{\mathrm{phys}}$, shown in the lower plot of Fig. 3.9b, is at the same level as for $\langle \mathcal{NNM} \rangle$. On average, the S/N increases by 34 %. In Fig. 3.9 the S/N of $\langle \mathcal{NNM} \rangle_{\mathrm{phys}}$ is higher than the S/N of $\langle \mathcal{NNM} \rangle$, both with and without redshift weighting.

3.5 Discussion

We proposed three improvements to the measurement of the G3L signal: Using a redshift weighting of lens galaxies to improve the precision, removing biases on the estimator with a

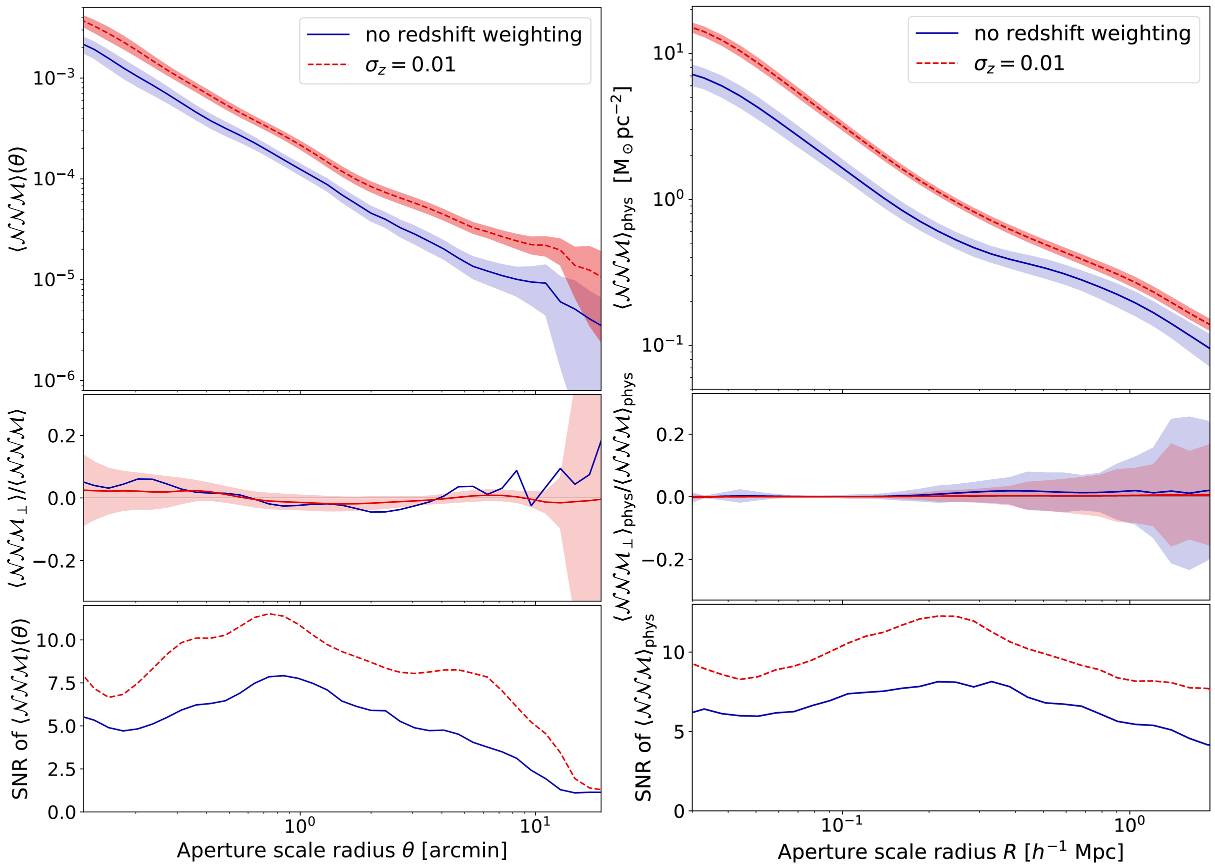

(a) $\langle \mathcal{NNM} \rangle$ in the MR.

(b) $\langle \mathcal{NNM} \rangle_{\rm phys}$ in the MR.

Figure 3.9: Aperture statistics measured in the mock data based on the MR, in (a) with angular and in (b) with physical units. The upper plots show the E modes $\langle \mathcal{NNM} \rangle$ and $\langle \mathcal{NNM} \rangle_{\rm phys}$, and the middle plot shows the ratio of the B modes $\langle \mathcal{NNM}_\perp \rangle$ and $\langle \mathcal{NNM}_\perp \rangle_{\rm phys}$ to $\langle \mathcal{NNM} \rangle$ and $\langle \mathcal{NNM} \rangle_{\rm phys}$. The lower plots give the S/N of $\langle \mathcal{NNM} \rangle$ and $\langle \mathcal{NNM} \rangle_{\rm phys}$. The red dashed line depicts $\langle \mathcal{NNM} \rangle$ taken with a redshift weighting function with width $\sigma_z = 0.01$. Shaded regions show the 1σ uncertainties from jackknifing. The blue solid line denotes the measurements without redshift weighting.

new binning scheme, and accounting for the impact of lens magnification. Furthermore, we showed how to measure the G3L signal in physical units.

The effect of the improved binning scheme becomes apparent when comparing our results for the simple mock data with the theoretical expectation. The original binning causes discrepancies between the theoretical expectation and the measurement for aperture scale radii below $1'$ and above $5'$. The aperture statistics measured with the improved binning agree with the expectation at all scales. At $\theta = 0\farcm1$, the original binning underestimates $\langle \mathcal{N}\mathcal{N}\mathcal{M} \rangle$ by 40 %, whereas the result of the new binning scheme agrees with the theoretical expectation. Thus, our new method extends the reliability of the measurement, due to the tessellation.

The signal due to the magnification of lens galaxies is approximately 10 % of the total G3L signal. Theoretical modelling of the G3L signal, therefore, needs to account for it. Previous studies (Simon et al., 2008, 2013) neglected lens magnification. Nonetheless, even though it has a significant effect on the measured G3L signal, the conclusions of Saghiha et al. (2017) are not impaired because the observational data and the simulations both included lens magnification.

We also demonstrated how to correct for the effect of lens magnification. The additional signal due to this effect can be measured by considering only lens pairs sufficiently far separated along the line of sight. The resulting signal matches the expectation for lens magnification from the convergence and number density maps at different redshift slices. We, therefore, conclude that we can measure the lens magnification signal with physically separated lens pairs without any inherent correlation.

We found that the dominating effect is the correlation of galaxies at the first lens plane with the convergence at the second lens and the source plane. In contrast, the other terms are three orders of magnitude smaller. This finding explains why we measure a significant signal due to lens magnification, even though previous studies (e.g. Simon et al., 2013) expected that this effect is negligible. These evaluations considered only the $\langle \mathcal{M}\,\mathcal{M}\,\mathcal{M} \rangle$ term, which is indeed much smaller than any $\langle \mathcal{N}\mathcal{N}\mathcal{M} \rangle$ signal. However, as we have shown here, it is not the dominant term for lens magnification.

The magnification signal is mainly due to the correlation of galaxies with the matter at the first lens plane, which influences the convergence at the second lens and the source plane. Matter in front of both lenses also contributes to the magnification signal. However, its measured contribution is minor. The effect of foreground matter might be more substantial for lens samples at higher redshifts because our lens sample has a low median redshift of 0.2.

Using redshift weighting, we increased the S/N of both $\langle \mathcal{N}\mathcal{N}\mathcal{M} \rangle$ and $\langle \mathcal{N}\mathcal{N}\mathcal{M} \rangle_{\rm phys}$ by approximately 35 % between $0\farcm1$ and $10'$ and $0.1h^{-1}$Mpc and $2h^{-1}$Mpc. Simultaneously, the signal was increased by a factor of approximately two. This meets our expectation that the signal increases by the square of the increase in S/N.

Our choice of σ_z was motivated by the correlation length between galaxies, the redshift distribution of galaxy pairs, and the typical peculiar velocities of galaxies in clusters. Choosing a different σ_z will lead to a different measured signal and increase in S/N. However, σ_z does not affect the interpretation of the aperture statistics as long as the theoretical modelling uses the same σ_z. Moreover, for each survey, we can assume different values of σ_z, and choose the one that provides the highest S/N.

For the redshift-weighting scheme in the MR, we could use the true redshifts for all lens galaxies. However, precise redshifts are generally not available for observations. We expect that redshift weighting is most useful for data sets that include spectroscopic redshifts. Nevertheless, redshift weighting with a broad weighting function might be possible for lens galaxies with photometric redshift estimates. The uncertainties of spectroscopic redshifts are much smaller than of those photometric redshifts so a narrow weighting function can be used.

At first glance, the measurement of the aperture statistics in physical units $\langle \mathcal{N}\mathcal{N}\mathcal{M}\rangle_{\mathrm{phys}}$ does not appear to provide additional information to the aperture statistics in angular units. However, in contrast to $\langle \mathcal{N}\mathcal{N}\mathcal{M}\rangle$, $\langle \mathcal{N}\mathcal{N}\mathcal{M}\rangle_{\mathrm{phys}}$ is independent of the source redshift distribution. Direct comparisons of $\langle \mathcal{N}\mathcal{N}\mathcal{M}\rangle_{\mathrm{phys}}$ between surveys with different galaxy distributions are possible. Furthermore, the S/N of $\langle \mathcal{N}\mathcal{N}\mathcal{M}\rangle_{\mathrm{phys}}$ is slightly higher than for $\langle \mathcal{N}\mathcal{N}\mathcal{M}\rangle$, independent of the redshift weighting. $\langle \mathcal{N}\mathcal{N}\mathcal{M}\rangle_{\mathrm{phys}}$ is more precise because its estimator weighs triplets according to their lensing efficiency.

We only applied our improvements on the lens-lens-shear correlation function and the aperture statistics $\langle \mathcal{N}\mathcal{N}\mathcal{M}\rangle$ here. However, measurements of the lens-shear-shear correlation and $\langle \mathcal{N}\,\mathcal{M}\,\mathcal{M}\rangle$ can also use the new binning scheme. We expect that this might extend the accuracy of measurement of this aperture statistics to scales below $1'$, which were not taken into account in previous measurements (Simon et al., 2013). The transformation into physical units can also be applied to $\langle \mathcal{N}\,\mathcal{M}\,\mathcal{M}\rangle$.

4

Testing semi-analytic galaxy models with galaxy-galaxy-galaxy lensing

This chapter is based on Linke et al. (2020), published in Astronomy & Astrophysics.

In this chapter, we use the improved estimator presented in the last chapter and apply it to galaxy surveys. We compare these measurements to the predictions by two different SAMs. This comparison allows us to evaluate the SAMs and discuss their assumptions on baryonic physics. We motivate our measurement set-up in the Sect. 4.1. Sect. 4.2 describes the details of the application of the G3L estimator and the uncertainty estimation. We introduce our observational and simulated data sets in Sect. 4.3 The aperture statistics measured in the observation and predicted by the SAMs are presented in Sect. 4.4 and discussed in Sect. 4.5.

4.1 Motivation

In the previous chapter, we demonstrated that the S/N of G3L measurements could be improved substantially by weighting each lens galaxy pair according to the line-of-sight separation between its galaxies to reduce the impact of chance pairs. In this chapter, we use this improved estimator to test the H15 and the L12 SAMs with state-of-the-art observational data, consisting of the photometric KiDS and VIKING, and the spectroscopic GAMA. We use the shapes of galaxies observed by KiDS as shear estimates, while GAMA provides lens galaxies with precise spectroscopic redshifts. These spectroscopic redshifts allow us to employ the redshift weighting (see Sect. 3.2.1). Furthermore, we extend the angular range at which we measure the G3L signal to lower scales with the adaptive binning scheme for the G3L three-point correlation function proposed in Sect. 3.2.2. Thereby, we can assess the SAMs deeper inside dark-matter halos.

As of now, the lens-lens-shear correlation has only been measured for lens pairs with galaxies from the same colour or stellar-mass sample (unmixed lens pairs) and not for lens pairs with galaxies from different samples (mixed lens pairs). However, comparing the measurements for G3L with mixed pairs is a compelling new test of SAMs, because this signal depends on the correlation of different galaxy populations inside halos. For example, the G3L signal for mixed pairs is higher for fully correlated galaxy populations than for uncorrelated populations, while the GGL signal stays the same. Therefore, we can assess the predictions of SAMs for the correlation between different galaxy populations with the G3L of mixed lens pairs. Accordingly, we measure not only the G3L signal for lens pairs from the same population but also the signal for mixed lens pairs, with galaxies from different colour- or stellar-mass samples.

4.2 Methods

4.2.1 Estimating the three-point correlation function

For measuring $\tilde{\mathcal{G}}_Z$ and $\tilde{\mathcal{G}}_{\rm phys}$, we use the estimators from Eqs (3.4) and (3.20). However, as we are also considering lens pairs with galaxies from different populations, we use a generalization of Eq. (3.5) to obtain the lens two-point correlation function ω_Z, which is (Szapudi and Szalay, 1998)

$$\omega_Z(\theta) = \frac{N_{\rm r_1}\,N_{\rm r_2}}{N_{\rm d_1}\,N_{\rm d_2}}\frac{D_1D_{2Z}(\theta)}{R_1R_{2Z}(\theta)} - \frac{N_{\rm r_1}}{N_{\rm d_1}}\frac{D_1R_{2Z}(\theta)}{R_1R_{2Z}(\theta)} - \frac{N_{\rm r_2}}{N_{\rm d_2}}\frac{D_2R_{1Z}(\theta)}{R_1R_{2Z}(\theta)} + 1\;. \tag{4.1}$$

for two different observed lens samples with $N_{\rm d_1}$ and $N_{\rm d_2}$ galaxies and two *random samples*. These random samples contain $N_{\rm r_1}$ and $N_{\rm r_2}$ unclustered galaxies following the same selection function as the observed galaxies.

The D_1D_{2Z}, D_1R_{2Z}, D_2R_{1Z}, and R_1R_{2Z} are the pair counts of observed and random galaxies. For two equal lens samples and $DD = D_1D_2$, $DR = D_1R_2 = D_2R_1$, and $RR = R_1R_2$, the estimator in Eq. (4.1) reduces to the usual Landy-Szalay estimator in Eq. (3.5). Again, we use redshift-weighted pair counts to account for the stronger clustering of true lens pairs due to the redshift weighting function Z. These are defined in Eqs (3.6) and (3.8).

Following the reasoning in Sect. 3.2.1, we choose a Gaussian weighting function,

$$Z(\Delta z_{12}) = \exp\left(-\frac{\Delta z_{12}^2}{2\sigma_z^2}\right)\,, \tag{4.2}$$

with width $\sigma_z = 0.01$. Choosing a different σ_z influences the magnitude of the measured aperture statistics as well as the S/N of the measurement. Nonetheless, as long as the same width is chosen for the observation and the simulation, their G3L signals can be compared.

We measure $\tilde{\mathcal{G}}_Z$ and $\tilde{\mathcal{G}}_{\rm phys}$ initially for 128 × 128 × 128 bins, which are linearly spaced along ϕ and logarithmically spaced along $\vartheta_{1,2}$ and $r_{1,2}$. For $\tilde{\mathcal{G}}_Z$, the $\vartheta_{1,2}$ are between $0\farcm15$ and $200'$ for the observed and between $0\farcm15$ and $320'$ for the simulated data. For $\tilde{\mathcal{G}}_{\rm phys}$, we choose $r_{1,2}$ between 0.02 Mpc and 40 Mpc. We then apply the adaptive binning scheme of Sect. 3.2.2, by which the parameter space is tessellated to remove bins for which no galaxy triplet is in the data.

The correlation function is measured individually for 24 tiles of the observational data of size 2.5° × 3° and 64 fields-of-view of the MR of size 4° × 4°, leading to estimates $\tilde{\mathcal{G}}^i_{Z,\rm est}$ and $\tilde{\mathcal{G}}^i_{\rm est,\,phys}$ for each tile and field-of-view, respectively. The division into small patches allows us to project the observational measurements to Cartesian coordinates and to estimate the uncertainty of the measurement with jackknife resampling. For each data set, the individual estimates are combined to form the total correlation functions. This combination takes the form of a weighted average over all tiles, so the angular correlation function $\tilde{\mathcal{G}}_Z$ is estimated by

$$\tilde{\mathcal{G}}_{Z,\mathrm{est}}(B) = \frac{\sum_{i=1}^N \tilde{\mathcal{G}}^i_{Z,\mathrm{est}}(B)\, W^i(B)}{\sum_{i=1}^N W^i(B)}\;, \tag{4.3}$$

and the physical correlation function $\tilde{\mathcal{G}}_\mathrm{phys}$ by

$$\tilde{\mathcal{G}}_{\mathrm{est,\ phys}}(B) = \frac{\sum_{i=1}^N \tilde{\mathcal{G}}^i_{\mathrm{est,\ phys}}(B)\, W^i_\mathrm{phys}(B)}{\sum_{i=1}^N W^i_\mathrm{phys}(B)}\;, \tag{4.4}$$

where $W^i(B)$ and $W^i_\mathrm{phys}(B)$ are the angular and physical weights of tile i in bin B. These weights are the sum over the weights of each triple in the respective tile and bin. The weight of the triplet with lenses i and j and source k consists of the measurement weight w_k, the redshift weight $Z(\Delta z_{ij})$, and, for the physical correlation function, the inverse square of the average critical surface mass density $\bar{\Sigma}^{-2}_\mathrm{crit}$ at the center between the lenses. The total weights of each tile are therefore

$$W^i(B) = \sum_{ijk} w_k\, Z(\Delta z_{ij})\ \Delta_{ijk}(B)\;, \tag{4.5}$$

and

$$W^i_\mathrm{phys}(B) = \sum_{ijk} w_k\, \bar{\Sigma}^{-2}_\mathrm{crit}(z_{ij})\, Z(\Delta z_{ij})\ \Delta^\mathrm{phys}_{ijk}(B)\;. \tag{4.6}$$

4.2.2 Computing aperture statistics

To compute $\langle\mathcal{N}\mathcal{N}\mathcal{M}\rangle$ and $\langle\mathcal{N}\mathcal{N}\mathcal{M}\rangle_\mathrm{phys}$, we integrate over $\tilde{\mathcal{G}}_Z$ using Eq. (2.143) and (3.21). We numerically approximate the integrals by summing over all N_bins of $\tilde{\mathcal{G}}_Z$ after tessellation with

$$\begin{aligned}&\langle\mathcal{N}\mathcal{N}\mathcal{M}\rangle\,(\theta) \\ &= \mathrm{Re}\Big[\sum_{i=1}^{N_\mathrm{bin}} V(B_i)\, \tilde{\mathcal{G}}_{Z,\mathrm{est}}(B_i)\, \mathcal{A}_{NNM}(B_i\,|\,\theta)\Big]\;,\end{aligned} \tag{4.7}$$

and

$$\begin{aligned}&\langle\mathcal{N}\mathcal{N}\mathcal{M}\rangle_\mathrm{phys}\,(r) + \mathrm{i}\ \langle\mathcal{N}\mathcal{N}\mathcal{M}_\perp\rangle_\mathrm{phys}\,(r) \\ &= \sum_{i=1}^{N_\mathrm{bin}} V(B_i)\, \tilde{\mathcal{G}}_{\mathrm{est,\ phys}}(B_i)\, \mathcal{A}_{NNM}(B_i\,|\,r)\;.\end{aligned} \tag{4.8}$$

Here, B_i is the ith bin, which has the volume $V(B_i)$, and $\mathcal{A}_{\mathcal{N}\mathcal{N}\mathcal{M}}$ is the kernel function evaluated at the tessellation seed of bin B_i.

We estimate the statistical uncertainty of the aperture statistics in the observational data with jackknife resampling. For this, we assume that the 24 tiles are statistically independent.

Although this assumption is not correct for noise due to sample variance, we expect our noise to be dominated by shape noise which is independent for each tile. In the jackknife resampling, we combine the $\tilde{\mathcal{G}}^i_Z$ of all N tiles to the total $\tilde{\mathcal{G}}_Z$. Additionally, we create N jackknife samples by combining all but one tile. The aperture statistics $\langle \mathcal{NNM} \rangle (\theta)$ are calculated for the total $\tilde{\mathcal{G}}_Z$, as well as for each of the N jackknife samples to get N $\langle \mathcal{NNM} \rangle_k (\theta)$. The covariance matrix $\tilde{C}$ of $\langle \mathcal{NNM} \rangle (\theta)$ is then estimated with Eq. (3.31) as $\tilde{C}_{ij} = C(\theta_i, \theta_j)$.

As discussed by Hartlap et al. (2007) and Anderson (2003), the inverse of this estimate of the covariance matrix is not an unbiased estimate of the inverse covariance matrix. Following their suggestion, we instead estimate the inverse covariance matrix with

$$C^{-1}_{ij} = \frac{N-p-2}{N-1} \left(\tilde{C}_{ij}\right)^{-1} , \tag{4.9}$$

where p is the number of data points. This gives an unbiased estimate of the inverse covariance matrix if the realisations are statistically independent and have Gaussian errors.

With this estimate of the inverse covariance matrix, we calculate the S/N of our observational measurement with

$$S/N = \left[\sum_{i,j=1}^{p} \langle \mathcal{NNM} \rangle (\theta_i)\, C^{-1}_{ij}\, \langle \mathcal{NNM} \rangle (\theta_j) \right]^{1/2} . \tag{4.10}$$

We also use C^{-1}_{ij} to perform a χ^2-test, evaluating the agreement of the observational measurement $\langle \mathcal{NNM} \rangle_{\mathrm{obs}}$ with the SAMs prediction $\langle \mathcal{NNM} \rangle_{\mathrm{sim}}$. For this, we calculate the reduced χ^2_{redu} as

$$\begin{aligned} \chi^2_{\mathrm{redu}} = \frac{1}{p} \sum_{i,j=1}^{p} & \left(\langle \mathcal{NNM} \rangle_{\mathrm{obs}} (\theta_i) - \langle \mathcal{NNM} \rangle_{\mathrm{sim}} (\theta_i) \right) \\ & \times C^{-1}_{ij} \left(\langle \mathcal{NNM} \rangle_{\mathrm{obs}} (\theta_j) - \langle \mathcal{NNM} \rangle_{\mathrm{sim}} (\theta_j) \right) . \end{aligned} \tag{4.11}$$

4.3 Data

4.3.1 Observational data

Our observational data is overlap of the KiDS, VIKING, and GAMA (KV450 × GAMA). This overlap encompasses approximately 180 deg^2, divided into the three patches G9, G12 and G15, each with dimensions of $12 \times 5\,\mathrm{deg}^2$.

VIKING (Edge et al., 2013; Venemans et al., 2015) is a photometric survey in five near-infrared bands, conducted at the Visible and Infrared Survey Telescope for Astronomy (VISTA) telescope in Paranal, Chile and covering approximately 1350 deg^2. It covers the same area as KiDS (Kuijken et al., 2015; de Jong et al., 2015), an optical photometric survey conducted with the OmegaCAM at the Very Large Telescope (VLT) Survey Telescope. The data of KiDS and VIKING were combined to form the KV450 data set, which we use in the following. This data set described in detail in Wright et al. (2019). KV450 has the same footprint as the third data release of KiDS (de Jong et al., 2017) and was processed by the same data reduction pipelines, described in detail in Hildebrandt et al. (2017). Data are processed by THELI (Erben et al., 2005; Schirmer, 2013) and Astro-WISE (de Jong et al., 2015). Shears are measured with *lens*fit (Miller et al., 2013; Kannawadi et al., 2019). Photometric redshifts are obtained from PSF-matched photometry (Wright et al., 2019) and calibrated using external overlapping spectroscopic surveys (Hildebrandt et al., 2020).

We use the galaxies observed by KV450 with photometric redshift between 0.5 and 1.2 as source galaxies. We exclude galaxies with a photometric redshift less than 0.5 because most of them are in front of our lens galaxies and therefore dilute and bias the lensing signal. The averaged inverse critical surface mass density $\bar{\Sigma}_{\mathrm{crit}}^{-1}$ is calculated as described in Sect. 4.2 by using the weighted direct calibration redshift distributions (DIR distributions) of the KV450 galaxies as the source distribution. These DIR distributions were obtained with in-depth spectroscopic surveys overlapping with KiDS and VIKING. The spectroscopic redshift distributions from these surveys were weighted according to the photometric data in KV450 to estimate the redshift distribution of KV450 galaxies. Hildebrandt et al. (2017, 2020) describe details of this procedure. We neglect the uncertainties on the redshift distribution and the multiplicative bias of the shear estimate. However, as these uncertainties are small, we do not expect them to impact our conclusions.

GAMA (Driver et al., 2009, 2011; Liske et al., 2015) is a spectroscopic survey carried out at the Anglo Australian Telescope with the AAOmega spectrograph. We use the Data Management Unit (DMU) *distanceFramesv14*, which contains positions and spectroscopic redshifts z of galaxies with a Petrosian observer-frame r-band magnitude brighter than 19.8 mag. The spectroscopic redshifts were flow-corrected to account for the proper motion of the Milky Way. This correction used the model by Tonry et al. (2000) and the procedure described in Baldry et al. (2012). We include all galaxies with a spectroscopic redshift lower than 0.5 and redshift quality flag N_Q≥3. For the calculation of the angular two-point correlation function of lenses, we use randoms from the DMU *randomsv02* (Farrow et al., 2015), which incorporates the galaxy selection function of GAMA while maintaining an unclustered galaxy distribution. From the GAMA galaxies, we select lens samples according to their colour and stellar mass. Restframe photometry and stellar masses were obtained from the DMU *stellarMassesLambdarv20*. An overview of our samples is given in Table 4.1.

We select a ‘red’ and ‘blue’ lens sample, defined according to the galaxies’ rest-frame $(g-r)_0$ colour. We use the colour cut by Farrow et al. (2015), according to which a galaxy is red if its rest-frame colour $(g-r)_0$ and its absolute Petrosian magnitude M_r in the r-band fulfil

$$(g-r)_0 + 0.03\,(M_r - 5\log_{10} h + 20.6) > 0.6135\ . \tag{4.12}$$

Otherwise, the galaxy is considered blue. We chose this colour cut so that approximately equal numbers of red and blue galaxies (93 524 red and 93 702 blue galaxies). Using a hard colour cut does not automatically produce two physically distinct galaxy populations (Taylor et al., 2015). However, as we apply the same cuts in the observational and simulated data, we expect to obtain comparable ‘red’ and ‘blue’ galaxy samples.

Table 4.1: Selection criteria for lens samples and number density N of selected galaxies per sample. Lenses are selected either according to their stellar mass M^* or to their rest-frame $(g-r)_0$ colour and absolute r-band magnitude M_r and need to have $r < 19.8\,\mathrm{mag}$.

Sample	**Selection Criterion**	**N, GAMA** arcmin^{-2}	**N, H15** arcmin^{-2}	**N, L12** arcmin^{-2}
red	$(g-r)_0 + 0.03\,(M_r - 5\log_{10}h\ \ 20.6) > 0.6135$	0.143	0.140	0.152
blue	$(g-r)_0 + 0.03\,(M_r - 5\log_{10}h\ \ 20.6) \leq 0.6135$	0.144	0.142	0.139
m1	$8.5 < \log_{10}(M^*\,\mathrm{M}_\odot^{-1}\,h^{-2}) \leq 9.5$	0.037	0.040	0.059
m2	$9.5 < \log_{10}(M^*\,\mathrm{M}_\odot^{-1}\,h^{-2}) \leq 10$	0.058	0.059	0.064
m3	$10 < \log_{10}(M^*\,\mathrm{M}_\odot^{-1}\,h^{-2}) \leq 10.5$	0.099	0.096	0.095
m4	$10.5 < \log_{10}(M^*\,\mathrm{M}_\odot^{-1}\,h^{-2}) \leq 11$	0.080	0.076	0.058
m5	$11 < \log_{10}(M^*\,\mathrm{M}_\odot^{-1}\,h^{-2}) \leq 11.5$	0.014	0.011	0.009

Absolute magnitudes and rest-frame colours of the GAMA galaxies were obtained by Wright et al. (2016) using matched aperture photometry and the LAMBDAR code. These magnitudes were aperture corrected, using

$$M_{r,\mathrm{tot}} = M_{r,\mathrm{meas}} - 2.5\log_{10} f + 5\log_{10} h\ , \tag{4.13}$$

where f is the flux scale, which is the ratio between the measured r-band flux and the total r-band flux inferred from fitting a Sérsic-profile to the galaxies photometry.

We define five stellar mass bins with the same cuts as Farrow et al. (2015), with M^* between $10^{8.5}\,h^{-2}\,\mathrm{M}_\odot$ and $10^{11.5}\,h^{-2}\,\mathrm{M}_\odot$. The stellar masses of GAMA galaxies were obtained by Wright et al. (2017), assuming the IMF by Chabrier (2003), stellar population synthesis according to Bruzual and Charlot (2003), and dust extinction according to Calzetti et al. (2000).

The estimator for $\tilde{\mathcal{G}}_Z$ and $\tilde{\mathcal{G}}_{\mathrm{phys}}$ are defined in terms of Cartesian coordinates. Therefore, we project the right ascension α and the declination δ of the galaxies onto a tangential plane on the sky. For this, we divide the source and the lens galaxy catalogues into 24 tiles with a size of $2.5 \times 3\,\mathrm{deg}^2$, which are also used for the jackknife resampling. We use the tile centres (α_0, δ_0) as projection points and find the Cartesian coordinates (x, y) with the orthographic projection

$$x = \cos(\delta)\sin(\alpha - \alpha_0)\ , \tag{4.14}$$

$$y = \cos(\delta_0)\sin(\delta) - \sin(\delta_0)\cos(\delta)\cos(\alpha - \alpha_0)\ . \tag{4.15}$$

4.3.2 Simulated data

We compare the results for the aperture statistics in KV450 × GAMA to measurements in the MR (see Sect. 2.2.1) with two different SAMs.

We use the same simulated shear maps as in the last chapter, whose creation we described in Sect. 3.3.1. These shear maps have the same source galaxy distribution as the observational data. However, here, we do not add any shape noise.

We obtain simulated lens galaxies from two SAMs implemented in the MR, the SAM by H15 and the SAM by L12 (see Sect. 2.2.2). The principal differences between these SAMs are listed in Table 2.2. These are primarily the choice of IMF and stellar population model. Furthermore, the magnitudes of the H15 SAM are given in AB-magnitudes, whereas the magnitudes of the L12 SAM are originally in the Vega magnitude system. We convert the Vega magnitudes to the AB-system with the conversion suggested by Blanton and Roweis (2007),

$$g_{\mathrm{AB}} = g_{\mathrm{Vega}} - 0.08\ , \tag{4.16}$$

$$r_{\mathrm{AB}} = r_{\mathrm{Vega}} + 0.16\ . \tag{4.17}$$

The lens galaxies are selected in the same way as the lenses in GAMA. We use all galaxies with redshifts less than 0.5 and brighter than $r = 19.8$ mag, which is the limiting magnitude of GAMA. With this criterion, we aim to mimic the selection function of GAMA galaxies and expect to obtain samples of similar lenses as in the observation. Systematic errors in the galaxy fluxes, for example, due to the dust modelling, of either GAMA or the SAM galaxies could invalidate this expectation, as we would sample different galaxies. However, as shown in Fig. 4.1, the redshift distribution of selected simulated and observed lens galaxies agree well. This likely would not be the case if there were fundamental differences in the selection function for simulated and observed galaxies. The number density of simulated lenses $0.282\,\mathrm{arcmin}^{-2}$ for the H15 SAM and $0.291\,\mathrm{arcmin}^{-2}$ for the L12 SAM, which are both close to the GAMA number density of $0.287\,\mathrm{arcmin}^{-2}$. Consequently, we expect the lens samples in the simulated and observational data to be comparable.

We split the simulated lens galaxies into colour and stellar-mass samples by applying the same cuts as to the GAMA galaxies (Table 4.1). Figures 4.2 and 4.3 show the colour- and stellar mass distribution of observed and simulated galaxies. The colour distributions of GAMA and SAM galaxies have similar modes, however, the blue mode of the L12 SAM is more concentrated. The H15 SAM also predicts stellar mass distributions similar to the observation, while the L12 SAM predicts more galaxies with stellar masses below $9.5 \times 10^{10}\mathrm{M}_{\odot}$ and fewer galaxies with stellar masses above $11 \times 10^{10}\mathrm{M}_{\odot}$.

4.4 Results

In this section, we present our results for the physical aperture statistics $\langle \mathcal{N}\mathcal{N}\mathcal{M}\rangle_{\mathrm{phys}}$, defined in Eq. (3.21). The measured angular aperture statistics $\langle \mathcal{N}\mathcal{N}\mathcal{M}\rangle$, which exhibit similar trends, are given in Appendix B.1.

The upper plot of Fig. 4.4 presents $\langle \mathcal{N}\mathcal{N}\mathcal{M}\rangle_{\mathrm{phys}}$ for red-red, red-blue, and blue-blue lens pairs. For the observed and both simulated data sets, the signal for red-red lens pairs is larger than

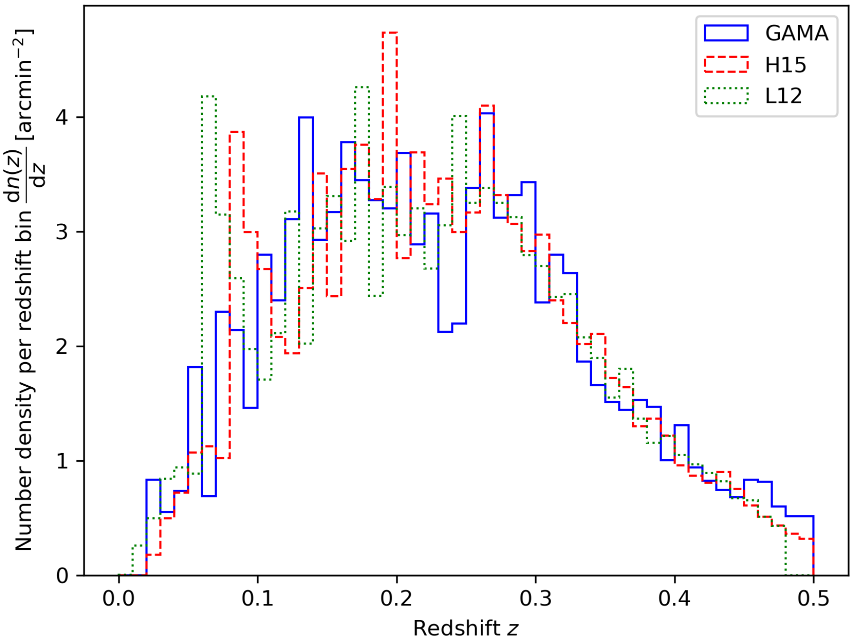

Figure 4.1: Number density per redshift bin of GAMA (solid blue), H15 galaxies (dashed red), and L12 galaxies (dotted green) for the limiting magnitude of $r < 19.8$. The bin size is $\Delta z = 0.01$.

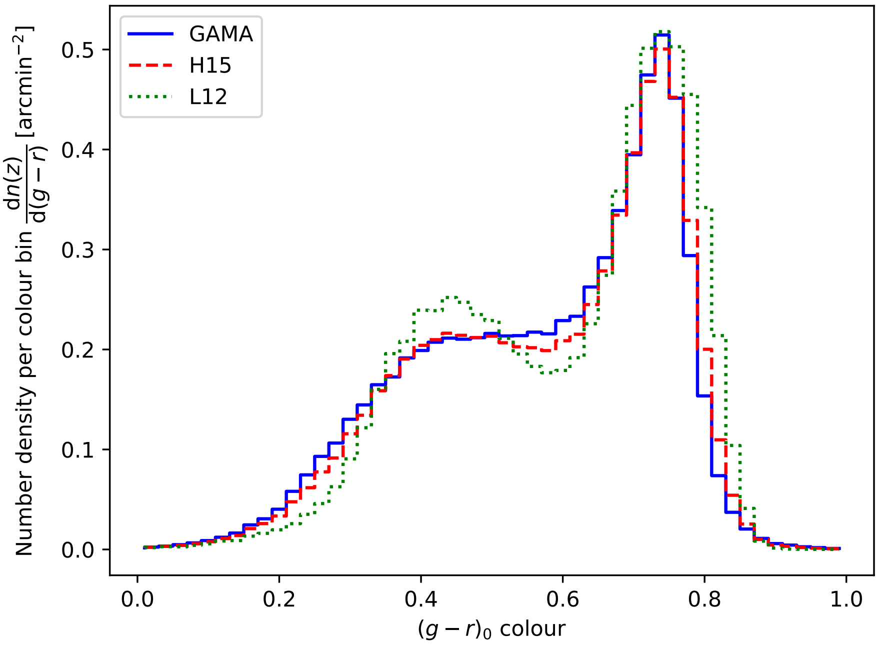

Figure 4.2: Number density per colour bin of GAMA (solid blue), H15 (dashed red), and L12 galaxies (dotted green) for the limiting magnitude of $r < 19.8$. The bin size is $\Delta(g_0 - r_0)$= 0.01.

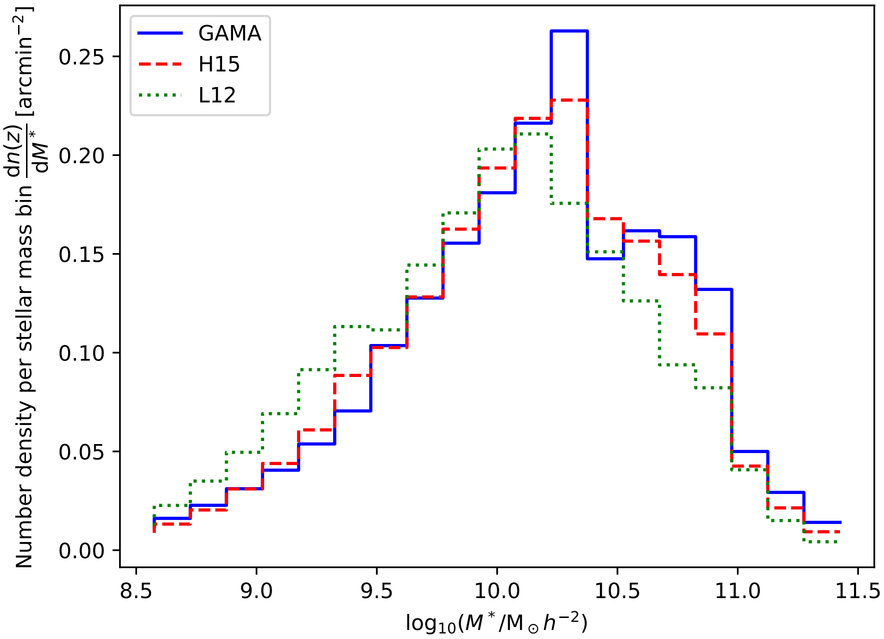

Figure 4.3: Number density per stellar mass bin of GAMA (solid blue), H15 (dashed red), and L12 galaxies (dotted green) for the limiting magnitude of $r < 19.8$. The bin size is $\Delta \log\left(M^* \mathrm{M}_\odot^{-1} h^{-2}\right) = 0.15$.

for red-blue and blue-blue lens pairs. Consequently, the linear deterministic bias model of Eq. (2.42) suggests that the bias factor b_{red} of red galaxies is larger than the bias factor b_{blue} of blue galaxies.

The linear deterministic bias model predicts that the aperture statistics for mixed red-blue lens pairs are the geometric mean of the aperture statistics for red-red and blue-blue lens pairs (see Eq. 2.147). To test this prediction, we show R in the lower plot of Fig. 4.4. For the observed galaxies, R is consistent with unity, supporting the linear deterministic bias model. However, for scales below $0.2\,h^{-1}$ Mpc, the noise of the observed R is more than three times larger than R itself, which inhibits any meaningful deductions on the bias model at small scales. For the H15 model, the prediction by the linear bias model is fulfilled , while for the L12 model R is slightly larger than unity at scales below $0.2\,h^{-1}$ Mpc.

The SAMs give different predictions for the aperture statistics. While the $\langle \mathcal{N}\mathcal{N}\mathcal{M}\rangle_{\mathrm{phys}}$ of the H15 SAM agrees well with the observations, the signals for red-red and blue-blue lens pairs of the L12 model differ markedly. The L12 SAM predicts much larger aperture statistics for red-red pairs than the observation and significantly smaller aperture statistics for blue-blue pairs. For red-blue pairs, the signal from the L12 SAM is similar to the observed one at small scales, but too high for $r > 0.3\,h^{-1}$ Mpc .

The difference between the SAMs is also visible in Table 4.2, whose upper part shows the χ^2_{redu} values for the different colour-selected lens pairs. We consider here $p = 12$ data points and

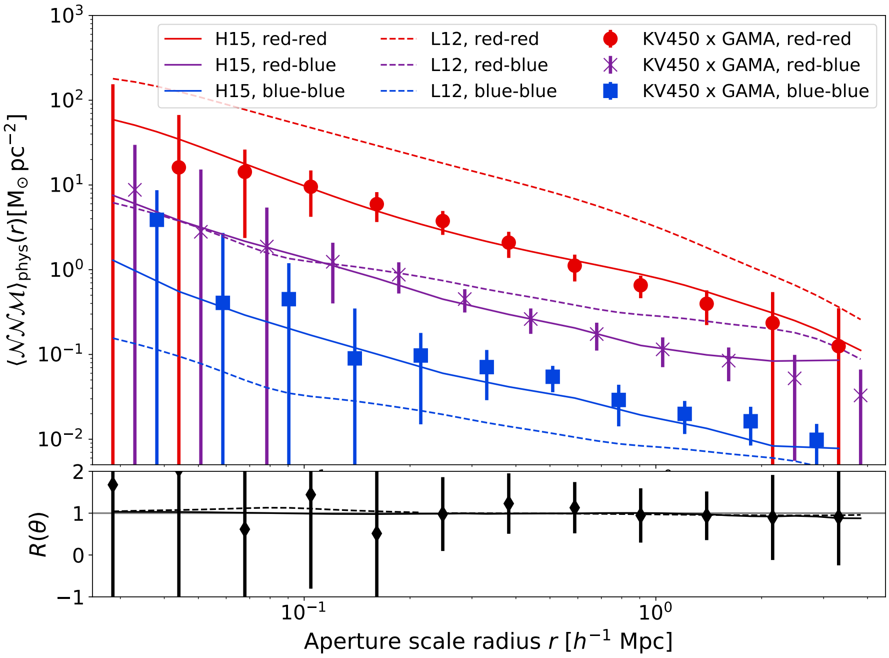

Figure 4.4: *Upper panel:* $\langle \mathcal{N}\mathcal{N}\mathcal{M}\rangle_{\rm phys}$ for colour-selected lens samples of the H15 galaxies (solid lines), L12 galaxies (dashed lines) and KV450 × GAMA (points). The signal is shown for red-red lens pairs (red lines and filled circles), red-blue lens pairs (purple lines and crosses), and blue-blue lens pairs (blue lines and squares). Error bars on the observational measurements are the standard deviation from jackknifing. *Lower panel:* Ratio statistics R as given by Eq. (2.147) for the red and blue lens samples of KV450 × GAMA (points), the H15 SAM (solid line) and the L12 SAM (dashed line).

Table 4.2: The reduced χ^2_{redu} of $\langle\mathcal{NNM}\rangle_{\mathrm{phys}}$ for the H15 and L12 SAMs. Samples are selected according to Table 4.1. Bold values indicate a tension at the 95% confidence level (CL).

lens pairs	χ^2_{redu} **for H15**	χ^2_{redu} **for L12**
red – red	1.08	**55.12**
red – blue	0.95	**3.13**
blue – blue	1.10	**2.19**
m1 – m1	1.44	**32.72**
m1 – m2	1.75	**42.96**
m1 – m3	1.54	**46.83**
m1 – m4	**2.84**	**45.33**
m1 – m5	1.75	**64.22**
m2 – m2	1.58	**16.04**
m2 – m3	0.80	**17.11**
m2 – m4	0.97	**10.04**
m2 – m5	0.85	**47.10**
m3 – m3	1.31	**51.21**
m3 – m4	1.17	**41.01**
m3 – m5	1.10	**8.60**
m4 – m4	1.62	**2.56**
m4 – m5	0.97	**8.54**
m5 – m5	0.73	**6.93**

define a tension between observation and simulation at the 95% CL if $\chi^2_{\mathrm{redu}} > 1.75$. For the H15 SAM, χ^2_{redu} is smaller than this threshold for red-red, red-blue, and blue-blue lens pairs, so there is no tension between the observation and this model. The χ^2_{redu} for the L12 SAM, though, are notably higher than the threshold. Consequently, the predictions by the L12 SAM do not agree with the observations for these.

Figure 4.5 shows the measured $\langle\mathcal{NNM}\rangle_{\mathrm{phys}}$ for lenses split by their stellar mass. The amplitude of the aperture statistics increases with the stellar mass of galaxies in a pair. Consequently, the bias factor increases with stellar mass. This trend exists for observed and both kinds of simulated lenses. Nevertheless, the predictions of the SAMs differ notably, with the aperture statistics obtained from the L12 SAM being substantially higher than those from the H15 SAM. The L12 SAM also deviates strongly from the observational measurements in KV450×GAMA, that agree better with the H15 SAM. The deviation of the L12 SAM from the observations is strongest for lenses with $M^* \leq 10^{9.5}\,h^{-2}\mathrm{M}_\odot$ and decreases for larger stellar masses.

To quantify the deviation, we list the χ^2_{redu} of the aperture statistics measured in the H15 and L12 SAM in the lower part of Table 4.3. Again, a $\chi^2_{\mathrm{redu}} > 1.75$ indicates a tension at the 95% CL. The L12 SAM disagrees with the observation for all lens samples. The χ^2_{redu} of the H15 SAM, though, are smaller than 1.75 for all but one correlation. The only tension exists for the correlation of lenses from stellar-mass samples m1 and m4, driven by differences at $r \lesssim 0.2\,h^{-1}\,\mathrm{Mpc}$, where the H15 SAM underestimates $\langle\mathcal{NNM}\rangle_{\mathrm{phys}}$.

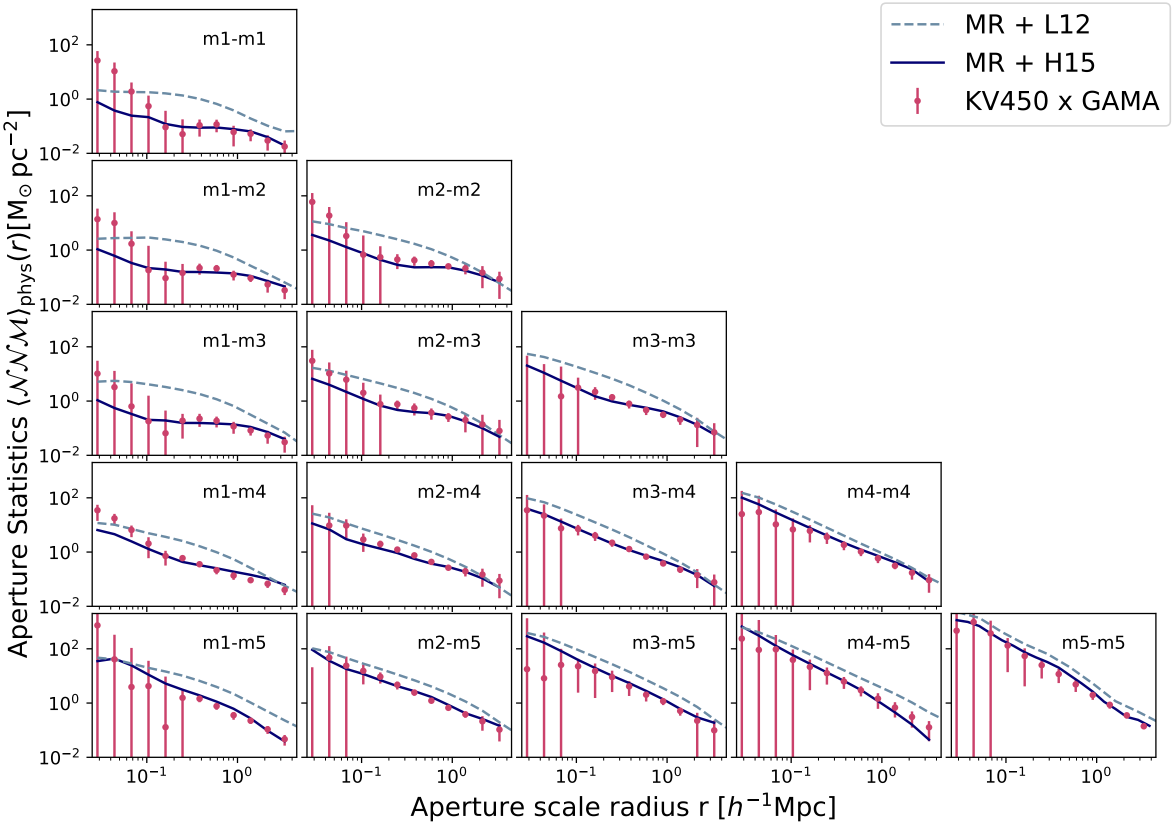

Figure 4.5: $\langle\mathcal{NNM}\rangle_{\mathrm{phys}}$ for stellar mass-selected lens samples in the MR with the H15 SAM (solid blue lines), the L12 SAM (dashed grey lines), and in GAMA with KV450 sources (pink points), using the mass bins defined in Table 4.1. Plots on the diagonal show the signal for unmixed lens pairs, while the other plots show the signal for mixed lens pairs. Error bars are the standard deviation from jackknife resampling.

Table 4.3: S/N of observed aperture statistics for the E-mode in the middle column and the B-mode in the right column. Samples are selected according to Table 4.1. B-mode is consistent with zero.

lens pairs	S/N of $\langle\mathcal{N}\mathcal{N}\mathcal{M}\rangle_{\mathrm{phys}}$	S/N of $\langle\mathcal{N}\mathcal{N}\mathcal{M}_\perp\rangle_{\mathrm{phys}}$
red – red	7.3	1.7
red – blue	5.1	1.4
blue – blue	4.7	0.6
m1 – m1	3.9	1.7
m1 – m2	4.1	1.4
m1 – m3	3.7	0.7
m1 – m4	5.6	0.8
m1 – m5	9.2	0.7
m2 – m2	8.6	1.2
m2 – m3	3.3	1.8
m2 – m4	5.3	1.5
m2 – m5	3.4	0.9
m3 – m3	4.7	0.8
m3 – m4	5.7	0.9
m3 – m5	6.2	1.3
m4 – m4	7.1	0.7
m4 – m5	9.8	1.1
m5 – m5	9.1	0.4

Finally, we test for systematic effects by considering the B-mode $\langle\mathcal{N}\mathcal{N}\mathcal{M}_\perp\rangle_{\mathrm{phys}}$. Table 4.3 compares the S/Ns, defined by Eq. (4.10), of $\langle\mathcal{N}\mathcal{N}\mathcal{M}\rangle_{\mathrm{phys}}$ with those of the B-modes $\langle\mathcal{N}\mathcal{N}\mathcal{M}_\perp\rangle_{\mathrm{phys}}$ for all observed lens pairs. The S/Ns of $\langle\mathcal{N}\mathcal{N}\mathcal{M}_\perp\rangle_{\mathrm{phys}}$ are considerably smaller than the S/Ns of the $\langle\mathcal{N}\mathcal{N}\mathcal{M}\rangle_{\mathrm{phys}}$, and they are consistent with a vanishing B-mode.

4.5 Discussion

We evaluated the SAM by H15 and the SAM by L12 by comparing their G3L predictions to measurements with KiDS, VIKING and GAMA. For this, we applied the improved estimator for the G3L three-point correlation function by L20 and measured aperture statistics for mixed and unmixed lens galaxy pairs from colour- or stellar-mass-selected lens samples.

Our measurements show a higher S/N than previous studies of G3L, due to the use of the improved estimator for G3L, proposed in Chapter 3 and new data. We also extended the considered scales. Thereby, we could probe the predictions of the SAMs well inside of dark matter halos at lengths below 1 h^{-1}Mpc. These ranges are particularly interesting for testing galaxy formation models because the principal variations between different SAMs are the assumptions on phenomena, whose effects are most substantial at small scales, such as star-formation, stellar and AGN feedback and environmental processes (Guo et al., 2016).

The aperture statistics are larger for red-red lens pairs than for red-blue or blue-blue lens pairs, which indicates that red galaxies have higher bias factors than blue galaxies. We also found that the bias factor increases with stellar mass. These results support the general expectation that redder and more massive galaxies have higher bias factors, as confirmed by multiple studies (e.g. Zehavi et al., 2002; Sheldon et al., 2004; Simon and Hilbert, 2018; Saghiha et al., 2017).

The predictions by the H15 SAM for aperture statistics of colour-selected lens samples agree with the observations at the 95% CL. The signal predicted by the L12 SAM, though, deviates significantly from the observed G3L signal, being too high for red-red and red-blue, and too low for blue-blue pairs.

This deviation could be due to an overproduction of red galaxies in massive halos by the L12 SAM. As shown by Watts and Schneider (2005), the G3L signal increases if more lens pairs reside in massive halos, so the relatively high $\langle \mathcal{N}\mathcal{N}\mathcal{M} \rangle_{\mathrm{phys}}$ indicates that in the L12 SAM massive halos contain too many pairs of red galaxies. This interpretation is supported by studies by Baldry et al. (2006) of the Bower et al. (2006) SAM, on which the L12 SAM is based. They compared the fraction of red galaxies in the SAM with observations by the SDSS and found that the SAM predicts too many red galaxies, especially in regions of high surface mass density.

Font et al. (2008) accredited the overproduction of red satellite galaxies to excessive tidal interactions and ram pressure stripping in the L12 SAM. This process decreases the amount of gas in satellite galaxies inside halos and thereby inhibits their star-formation. Consequently, the stripped galaxies become redder, so the fraction of red galaxies increases, while the number of blue galaxies decreases. This effect could explain the low aperture statistics for blue-blue lens pairs in the Lagos et al. (2012) SAM, as fewer blue galaxies remain inside massive halos.

The aperture statistics for the stellar-mass-selected samples measured in the observation agree with the H15 SAM at the 95% CL except for one sample. This finding is consistent with the conclusion by Saghiha et al. (2017), although their study was limited to angular scales between $1'$ and $10'$, did not consider mixed lens pairs and had a lower S/N due to the effect of chance lens pairs.

The H15 SAM agrees with the observations at the 95% CL for all but the correlation of m1 and m4 lens galaxies. This difference is driven mainly by a low signal by the SAM at scales below $0.2\,h^{-1}$Mpc. At these scales, the SAM also gives lower predictions for $\langle \mathcal{N}\mathcal{N}\mathcal{M} \rangle$ than the observations for m1-m2, m1-m3, and m2-m2 lens pairs. This trend could indicate that the SAM underpredicts G3L at small scales for low stellar masses. A possible reason is the limited resolution of the MR. The MRs softening length is $5\,h^{-1}$kpc, so its spatial resolution is in the order of tens of kpc (Vogelsberger et al., 2020). Therefore, the limited resolution might cause the difference between the aperture statistics in the H15 SAM and the observation at small scales.

The L12 SAM disagrees with the observations for all considered stellar-mass samples at the 95% CL, and its predicted signal is significantly larger. The tension increases for lenses with lower stellar mass and is more prominent at smaller scales.

This tension might be due to inaccurate stellar masses of the simulated lens galaxies. If the SAM assigns too low stellar masses, galaxies from a higher stellar mass bin are incorrectly assigned to a lower mass bin, for example into m2 instead of m3. The SAM then overestimates the aperture statistics, because the bias factors of galaxies with larger stellar masses are higher. The choice of IMF could cause different stellar-mass assignments by the SAMs. While the H15 SAM used the same IMF (Chabrier, 2003) as assumed for the stellar masses of GAMA galaxies, the L12 SAM assumes the IMF by Kennicutt (1983). Therefore, the stellar masses of the observation and the L12 might be inconsistent with each other.

Another cause for the tension of the L12 SAM with the observation could be an overproduction of satellite galaxies inside massive halos. This interpretation agrees with Saghiha et al. (2017), who found that the satellite fraction and mean halo masses for the L12 SAM is higher than for the H15 SAM. The tension between the L12 SAM and the observation increases for lower stellar masses and smaller scales, indicating that especially galaxies with low stellar mass are overproduced by the SAM and that their fraction rises closer to the centre of their dark matter halo. An excess of galaxies with small stellar masses would be consistent with excessive galaxy interactions inside halos. This finding, therefore, fits with the interpretation of the high G3L signal for red-red lens pairs in the SAM as caused by excessive ram pressure stripping.

We presented the first measurements of G3L for mixed lens pairs and used the aperture statistics for red-blue lens pairs to test the linear deterministic bias model. This bias model predicts that the aperture statistics for mixed lens pairs is the geometric mean of the signals for equal lens pairs. Our observational measurements are consistent with this prediction, although the signal is too noisy at scales below $0.2\,h^{-1}$ Mpc for meaningful constraints on the bias model.

The aperture statistics for mixed lens pairs are also useful for constraining the correlations of different galaxy populations inside the same dark matter halos. For example, the measured aperture statistics for red-blue lens pairs indicate that lens galaxies of different samples co-populate the same halos, as the signal would decrease at sub-Mpc scales due to a vanishing 1-halo term. Modelling of mixed-pair G3L in the context of the halo model will provide further insights into the correlation of galaxy populations inside halos. In contrast, GGL, which is only sensitive to the mean number of lenses inside halos and hence blind to the way mixed lens pairs populate halos, cannot yield the same information.

A compelling future study would be investigating whether full hydrodynamical simulations predict G3L with the same accuracy as the H15 SAM. Such a study would complement previous comparisons of GGL in hydrodynamical simulations to observations, for example by Velliscig et al. (2017) for the EAGLE simulation to KiDS and GAMA data, or Gouin et al. (2019) for the Horizon-AGN simulation to CFHTLenS and the Baryon Oscillation Spectroscopic Survey (BOSS). While these studies concluded that the GGL predictions of these simulations agree with the observations, the same is not necessarily true for G3L, which depends on the correlation of matter and galaxy pairs.

5

Modelling galaxy-galaxy-galaxy lensing with the halo model

In this chapter, we present an analytical model for G3L. We then extract the best-fitting parameters of the G3L model from the observations in KV450 × GAMA described in the last chapter. In Sect. 5.1, we explain our motivation for developing a G3L model based on the halo model. We derive our model in Sect. 5.2. Sect. 5.3 outlines how we obtain the best-fitting model parameters for the observations in KV450 × GAMA. We explore the sensitivity of G3L to the model parameters in Sect. 5.4.1 and present our results for the best fitting values in Sect. 5.4.2. A discussion of our model and the parameter values found follows in Sect. 5.5.

5.1 Motivation

After improving the estimator for G3L in Chapter 3 and measuring it with high precision in Chapter 4, we are now interested in theoretically modelling the effect. We propose an analytic model based on the halo model (Cooray and Sheth, 2002; Zheng et al., 2005, 2007), whose ingredients we presented in Sect. 2.3. Analytically describing G3L has two purposes. First, successful modelling of G3L would support the halo model as an accurate description of the LSS. Consequently, the assumptions of the halo model would be sufficient for three-point statistics of the galaxy and matter correlations. Second, with an analytical model, we can determine the free parameters of the halo model with G3L measurements. Therefore, G3L could complement other observables such as GGL or galaxy clustering when constraining the halo model parameters.

The halo model is a useful tool for describing galaxy-matter correlations since it is valid in the non-linear regime, flexible enough to represent a range of observables and computationally simple enough to be quickly calculated. It has been applied to model galaxy clustering (Simon et al., 2009), GGL (Mandelbaum et al., 2006), as well as the Sunyaev-Zel'dovich effect (Mead et al., 2020). Rödinger (2009) and Martin (2019) adopted it also to G3L and modelled the galaxy-galaxy-matter bispectrum and $\langle \mathcal{N}\mathcal{N}\mathcal{M}\rangle$ for unmixed lens pairs with galaxies from a single population.

We build on their work and propose a model for G3L which can describe the effect both for unmixed and mixed lens pairs. Our model includes several free parameters, which control the spatial distribution of galaxies, their HODs, and the cross-correlation of different populations. We analyze the impact of the parameters on the predicted G3L signal by varying them. Afterwards, we use a multidimensional optimization routine to extract the best-fitting model parameters for the observations in the KV450 × GAMA for red and blue galaxies.

5.2 Derivation of the halo model for galaxy-galaxy-galaxy-lensing

To model the G3L aperture statistics, we use a three-step approach. First, we model the first and second moments of the HODs of galaxies from two different populations. These moments give the expected numbers of each galaxy population in a halo of a given mass. Second, we use the HODs to calculate the three-dimensional galaxy-galaxy-matter bispectrum $B_{\mathrm{gg}\delta}$. Third, we project this bispectrum to the two-dimensional bispectrum $B_{\mathrm{gg}\kappa}$ with the Limber equation and convert it to the aperture statistics $\langle \mathcal{N}\mathcal{N}\mathcal{M} \rangle$ by convolving it with the suitable filter function.

The derivation in this section is valid for lens galaxies from two populations a and b defined by any arbitrary galaxy property, such as stellar mass, SFR, or colour. In Sect. 5.3, we identify a with 'red' and b with 'blue', to extract the best-fitting model for the observations. However, the model proposed in this section is fully general.

5.2.1 Moments of the joint halo occupation distribution

As outlined in Sect. 2.3.4, the halo model depends on the expected number of galaxies in a halo of given mass, $\langle N|m \rangle$. A useful approach to model the number of galaxies per halo is splitting their distribution into centrals and satellites (Kravtsov et al., 2004), each with their own expected number per halo, such that

$$\langle N|m \rangle = \left\langle N_{\mathrm{cen}}|m \right\rangle + \left\langle N_{\mathrm{sat}}|m \right\rangle \ . \tag{5.1}$$

Each halo hosts at most one central galaxy situated at the halo centre and can contain several satellite galaxies, distributed with the halo galaxy profile u_{g}.

Since we want to model G3L both for mixed and unmixed lens pairs, we need to model the following moments of the joint halo occupation distribution (JHOD) of population a and b galaxies, using $p \in \{a, b\}$:

- The expected number $\left\langle N_{\mathrm{cen}}^{(p)}|m \right\rangle$ of central galaxies for each population,
- The expected number $\left\langle N_{\mathrm{sat}}^{(p)}|m \right\rangle$ of satellite galaxies for each population,
- The expected number $\left\langle N_{\mathrm{sat}}^{(p)} \left(N_{\mathrm{sat}}^{(p)} - 1\right) |m \right\rangle$ of satellite galaxy pairs,

- The correlation $\left\langle N_\mathrm{cen}^{(p)}\, N_\mathrm{sat}^{(p)} | m \right\rangle$ of central galaxies with satellite galaxies of the same population,
- The correlation $\left\langle N_\mathrm{cen}^{(a)}\, N_\mathrm{cen}^{(b)} | m \right\rangle$ of central galaxies from different populations,
- The correlation $\left\langle N_\mathrm{sat}^{(a)}\, N_\mathrm{sat}^{(b)} | m \right\rangle$ of satellite galaxies from different populations,
- The correlation $\left\langle N_\mathrm{cen}^{(a)}\, N_\mathrm{sat}^{(b)} | m \right\rangle$ of satellite galaxies with central galaxies from different populations.

The number $N_\mathrm{cen}^{(p)}$ of central galaxies depends sensitively on the halo mass. For small halo masses no galaxy formation occurs, so $N_\mathrm{cen}^{(p)} = 0$. Halos with masses above a certain threshold, though, will contain central galaxies. Following Martin (2019), we assume

$$\left\langle N_\mathrm{cen}^{(p)} | m \right\rangle = \frac{\alpha^{(p)}}{2} \left\{ 1 + \mathrm{erf}\left[\frac{\log(m) - \log\left(M_\mathrm{th}^{(p)}\right)}{\sigma^{(p)}} \right] \right\} , \tag{5.2}$$

with the free parameters $\alpha^{(p)}$, $M_\mathrm{th}^{(p)}$, and $\sigma^{(p)}$. The parameter $\alpha^{(p)}$ gives the fraction of massive halos ($m \gg M_\mathrm{th}$) with a central galaxy of population p. The mass M_th is the halo mass at which a fraction of $\alpha^{(p)}/2$ halos have a central galaxy of population p. The parameter $\sigma^{(p)}$ determines the steepness of $\langle N_\mathrm{cen}^{p} | m \rangle$. If $\sigma^{(p)}$ is small, the transition from $\left\langle N_\mathrm{cen}^{(p)|m} \right\rangle = 0$ to $\left\langle N_\mathrm{cen}^{(p)|m} \right\rangle = \alpha^{(p)}$ occurs quickly, whereas the transition is smoother for larger $\sigma^{(p)}$.

The number $N_\mathrm{sat}^{(p)}$ of satellite galaxies is also zero for small halo masses, but follows a power law at higher halo masses. We assume therefore, with the free parameters $M'^{(p)}$ and $\beta^{(p)}$,

$$\left\langle N_\mathrm{sat}^{(p)} | m \right\rangle = \left\{ 1 + \mathrm{erf}\left[\frac{\log(m) - \log\left(M_\mathrm{th}^{(p)}\right)}{\sigma^{(p)}} \right] \right\} \left(\frac{m}{M'^{(p)}} \right)^{\beta^{(p)}} . \tag{5.3}$$

Figure 5.1 shows the expected number of satellite and central galaxies per halo mass with these models and the fiducial parameters in Table 5.1. For low-mass halos, the total number of galaxies is strongly influenced by the central galaxy distribution. Satellite galaxies predominate in massive halos.

The central galaxies are defined such that there can be either one or zero centrals of each population in a halo. Therefore,

$$\left\langle N_\mathrm{cen}^{(p)} \left(N_\mathrm{cen}^{(p)} - 1 \right) | m \right\rangle = 0 , \tag{5.4}$$

and

$$\left\langle N_\mathrm{cen}^{(a)}\, N_\mathrm{cen}^{(b)} | m \right\rangle = 0 . \tag{5.5}$$

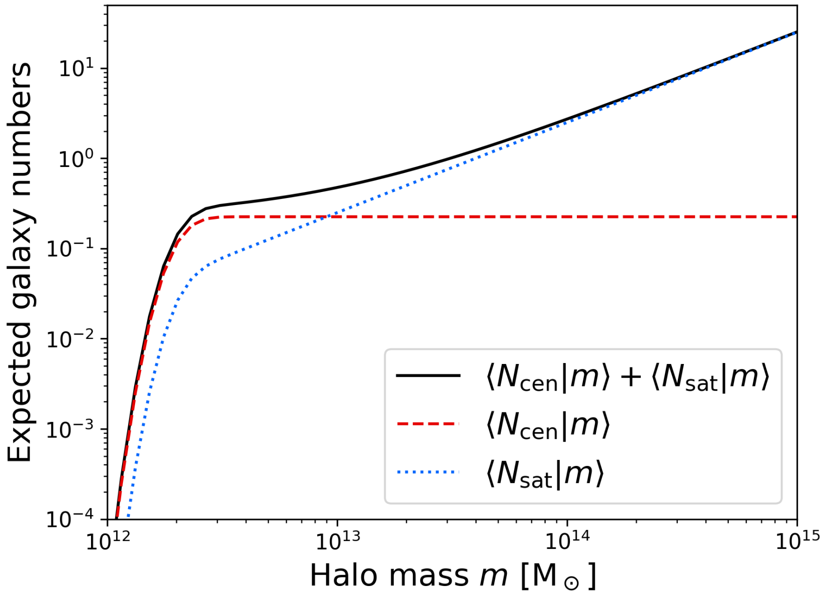

Figure 5.1: Halo occupation distribution for fiducial parameters in Table 5.1. The solid black line shows the total galaxy number per halo, the dashed red line shows the fraction of halos with central galaxies, and the dotted blue line shows the number of satellite galaxies per halo.

We assume that satellite galaxies are distributed Poissonian, following Kravtsov et al. (2004). Therefore,

$$\left\langle N^{(p)}_{\mathrm{sat}} \left(N^{(p)}_{\mathrm{sat}} - 1\right) |m \right\rangle = \left\langle N^{(p)}_{\mathrm{sat}} |m \right\rangle^2 \; . \tag{5.6}$$

Furthermore, we assume that the distributions of centrals and satellites are independent, so

$$\left\langle N^{(a)}_{\mathrm{cen}}\, N^{(b)}_{\mathrm{sat}} |m \right\rangle = \left\langle N^{(a)}_{\mathrm{cen}} |m \right\rangle \left\langle N^{(b)}_{\mathrm{sat}} |m \right\rangle \; , \tag{5.7}$$

and

$$\left\langle N^{(p)}_{\mathrm{cen}}\, N^{(p)}_{\mathrm{sat}} |m \right\rangle = \left\langle N^{(p)}_{\mathrm{cen}} |m \right\rangle \left\langle N^{(p)}_{\mathrm{sat}} |m \right\rangle \; . \tag{5.8}$$

Finally, we require the correlation of satellite galaxies from different populations. For this, we introduce the cross-correlation parameter r with

$$\left\langle N^{(a)}_{\mathrm{sat}}\, N^{(b)}_{\mathrm{sat}} |m \right\rangle = \left\langle N^{(a)}_{\mathrm{sat}} \right\rangle \left\langle N^{(b)}_{\mathrm{sat}} \right\rangle + r\, \sigma(N^{(a)}_{\mathrm{sat}} |m)\, \sigma(N^{(b)}_{\mathrm{sat}} |m) \; , \tag{5.9}$$

where $\sigma^2(N^{(p)}_{\mathrm{sat}} |m) = \left\langle N^{(p)}_{\mathrm{sat}} \left(N^{(p)}_{\mathrm{sat}} - 1\right) |m \right\rangle$. The parameter r is negative, if a and b galaxies are anticorrelated, zero, if a and b galaxies are independent, and positive, if the galaxies are positively correlated.

With these moments of the HODs, along with the NFW-profile for the dark matter distribution (Sect. 2.3.1), the Sheth-Tormen HMF (Sect. 2.3.2) and the linear halo bias (Sect. 2.3.3), the model

Table 5.1: Fiducial values and priors of the halo model parameters, motivated by Clampitt et al. (2017).

Parameter	Fiducial Value	Prior Range
$\alpha^{(p)}$	0.225	[0,0.45]
$\sigma^{(p)}$	0.255	[0.01,0.5]
$M_{\mathrm{th}}{}^{(p)}$	2×10^{12} M$_\odot$	$[0.1,50]\times10^{12}$ M$_\odot$
$\beta^{(p)}$	1	[0.6,1.4]
$M'^{(p)}$	8×10^{13} M$_\odot$	$[3,20]\times10^{13}$ M$_\odot$
$f^{(p)}$	1	[0,2]
r	1	[-1,1]

is specified and predicts the galaxy-matter two and three point statistics. This model has five free parameters per galaxy population and an additional parameter r constraining the cross-correlation of the two populations. Additionally, as explained in Sect. 2.3.4, we adopt the free parameters $f^{(a)}$ and $f^{(b)}$, which control the concentration of the spatial galaxy distribution with respect to the dark matter profile in a halo. Therefore, galaxies of population p are distributed with an NFW profile of concentration $f^{(p)}\,c$. We collect these parameters in the parameter vector $\boldsymbol{p}$, defined as

$$\boldsymbol{p}^{\mathrm{T}} = \begin{pmatrix}\alpha^{(a)} & \sigma^{(a)} & M_{\mathrm{th}}^{(a)} & \beta^{(a)} & f^{(a)} & \alpha^{(b)} & \sigma^{(b)} & M_{\mathrm{th}}^{(b)} & \beta^{(b)} & f^{(b)} & r\end{pmatrix} \;. \tag{5.10}$$

We use priors and fiducial values on $\boldsymbol{p}$ motivated by Clampitt et al. (2017) and given in Table 5.1.

5.2.2 Modelling the galaxy-galaxy-matter bispectrum

In the halo model the cosmic density field consists of H halos with masses $\{m_1,\dots,m_H\}$ at positions $\{\boldsymbol{x}_1,\dots,\boldsymbol{x}_H\}$. With the normalized density profile u defined in Sect. 2.3.1, the total density is

$$\rho(\boldsymbol{x},t) = \sum_{i=1}^{H} m_i\, u(\boldsymbol{x}-\boldsymbol{x}_i|m_i) \;. \tag{5.11}$$

The Fourier transform of the density is therefore

$$\hat{\rho}(\boldsymbol{k},t) = \sum_{i=1}^{H} \frac{m_i}{\bar{\rho}} \hat{u}(\boldsymbol{k}|m_i)\, \exp(-\mathrm{i}\boldsymbol{k}\cdot\boldsymbol{x}_i) \;. \tag{5.12}$$

Galaxies are treated as point particles. Each satellite galaxy belongs to a halo centred at $\boldsymbol{x}_i$ and is at separation $\Delta\boldsymbol{x}_{ij}$ to the halo centre, while centrals are exactly at the centre. The number density of population p galaxies is therefore

$$n_p(\boldsymbol{x},t) = \sum_{i=1}^{H}\left[\sum_{j=1}^{N_{\mathrm{sat},i}^{(p)}} \delta_{\mathrm{D}}(\boldsymbol{x}-\boldsymbol{x}_i-\Delta\boldsymbol{x}_{ij}) + N_{\mathrm{cen},i}^{(p)}\,\delta_{\mathrm{D}}(\boldsymbol{x}-\boldsymbol{x}_i)\right] \;, \tag{5.13}$$

where $N^{(p)}_{\mathrm{sat},i}$ is the number of population p satellite galaxies and $N^{(p)}_{\mathrm{cen},i}$ is the number of population p central galaxies in halo i. The Fourier transform of the number density is

$$\hat{n}_p(\boldsymbol{k},t) = \sum_{i=1}^{H} \left\{ \sum_{j=1}^{N^{(p)}_{\mathrm{sat},i}} \exp\Big[-\mathrm{i}\boldsymbol{k}\cdot(\boldsymbol{x}_i + \Delta\boldsymbol{x}_{ij}) + N^{(p)}_{\mathrm{cen},i}\, \exp(-\mathrm{i}\boldsymbol{k}\cdot\boldsymbol{x}_i)\Big] \right\} . \tag{5.14}$$

The galaxy-galaxy-matter bispectrum can now be inferred, using

$$\begin{aligned}(2\pi)^3 B^{p_1 p_2}_{\mathrm{gg}\delta}(\boldsymbol{k}_1,\boldsymbol{k}_2,\boldsymbol{k}_3,t)\delta_{\mathrm{D}}(\boldsymbol{k}_1+\boldsymbol{k}_2+\boldsymbol{k}_3) &= \frac{1}{\bar{n}_{p_1}\,\bar{n}_{p_2}} \left\langle \hat{n}_{p_1}(\boldsymbol{k}_1,t)\,\hat{n}_{p_2}(\boldsymbol{k}_2,t)\,\hat{\delta}(\boldsymbol{k}_3,t)\right\rangle \\ &= \frac{1}{\bar{n}_{p_1}\,\bar{n}_{p_2}\,\bar{\rho}} \left\langle \hat{n}_{p_1}(\boldsymbol{k}_1,t)\,\hat{n}_{p_2}(\boldsymbol{k}_2,t)\,\hat{\rho}(\boldsymbol{k}_3,t)\right\rangle ,\end{aligned} \tag{5.15}$$

where $p_1, p_2 \in \{a, b\}$ and n_p is the number density of population p galaxies. The bispectrum can be divided into three terms, the 1-halo term $B^{1-\mathrm{h}}_{\mathrm{gg}\delta}(\boldsymbol{k}_1,\boldsymbol{k}_2,-\boldsymbol{k}_1-\boldsymbol{k}_2,t)$, the 2-halo term $B^{2-\mathrm{h}}_{\mathrm{gg}\delta}(\boldsymbol{k}_1,\boldsymbol{k}_2,-\boldsymbol{k}_1-\boldsymbol{k}_2,t)$, and the 3-halo term $B^{3-\mathrm{h}}_{\mathrm{gg}\delta}(\boldsymbol{k}_1,\boldsymbol{k}_2,-\boldsymbol{k}_1-\boldsymbol{k}_2,t)$,

$$\begin{aligned}B_{\mathrm{gg}\delta}(\boldsymbol{k}_1,\boldsymbol{k}_2,-\boldsymbol{k}_1-\boldsymbol{k}_2,t) = B^{1-\mathrm{h}}_{\mathrm{gg}\delta}(\boldsymbol{k}_1,\boldsymbol{k}_2,-\boldsymbol{k}_1-\boldsymbol{k}_2,t) + B^{2-\mathrm{h}}_{\mathrm{gg}\delta}(\boldsymbol{k}_1,\boldsymbol{k}_2,-\boldsymbol{k}_1-\boldsymbol{k}_2,t) \\ + B^{3-\mathrm{h}}_{\mathrm{gg}\delta}(\boldsymbol{k}_1,\boldsymbol{k}_2,-\boldsymbol{k}_1-\boldsymbol{k}_2,t) .\end{aligned} \tag{5.16}$$

The 1-halo term contains the correlation of galaxies and matter in the same halo. The 2-halo term is caused by galaxies in one halo correlated with matter in a different halo, as well as galaxies and matter in one halo correlated with galaxies in a different halo. Correlations between matter and galaxies in three different halos cause the 3-halo term. For galaxies from the same population with number density $\bar{n}$, we find with the derivation in Appendix C.1,

$$\begin{aligned}&B^{1-\mathrm{h}}_{\mathrm{gg}\delta}(\boldsymbol{k}_1,\boldsymbol{k}_2,-\boldsymbol{k}_1-\boldsymbol{k}_2,t) \\ &= \frac{1}{\bar{\rho}\,\bar{n}^2}\int \mathrm{d}m\;\; n(m)\, m\, \hat{u}(-\boldsymbol{k}_1-\boldsymbol{k}_2|m) \Big\{ \big\langle N_{\mathrm{cen}}(N_{\mathrm{cen}}-1)|m\big\rangle \\ &\quad + \big\langle N_{\mathrm{cen}}\, N_{\mathrm{sat}}\big\rangle \left[\hat{u}_{\mathrm{g}}(\boldsymbol{k}_1|m) + \hat{u}_{\mathrm{g}}(\boldsymbol{k}_2|m)\right] + \big\langle N_{\mathrm{sat}}(N_{\mathrm{sat}}-1)|m\big\rangle\; \hat{u}_{\mathrm{g}}(\boldsymbol{k}_1|m)\,\hat{u}_{\mathrm{g}}(\boldsymbol{k}_2|m)\Big\} ,\end{aligned} \tag{5.17}$$

$$\begin{aligned}&B^{2-\mathrm{h}}_{\mathrm{gg}\delta}(\boldsymbol{k}_1,\boldsymbol{k}_2,-\boldsymbol{k}_1-\boldsymbol{k}_2,t) \\ &= \frac{1}{\bar{\rho}\,\bar{n}^2}\int \mathrm{d}m_1 \int \mathrm{d}m_2\;\; n(m_1)\, n(m_2) \\ &\times \Big\{ \big[m_1\, \hat{u}(-\boldsymbol{k}_1-\boldsymbol{k}_2|m_1)\, P_{\mathrm{H}}(\boldsymbol{k}_2,-\boldsymbol{k}_2,t|m_1,m_2) + m_2\, \hat{u}(-\boldsymbol{k}_1-\boldsymbol{k}_2|m_2)\, P_{\mathrm{H}}(\boldsymbol{k}_1,-\boldsymbol{k}_1,t|m_1,m_2)\big] \\ &\quad\times \left[\big\langle N_{\mathrm{cen}}|m_1\big\rangle + \big\langle N_{\mathrm{sat}}|m_1\big\rangle\; \hat{u}_{\mathrm{g}}(\boldsymbol{k}_1|m_1)\right]\; \left[\big\langle N_{\mathrm{cen}}|m_2\big\rangle + \big\langle N_{\mathrm{sat}}|m_2\big\rangle\; \hat{u}_{\mathrm{g}}(\boldsymbol{k}_2|m_2)\right] \\ &+ m_2\, \hat{u}(-\boldsymbol{k}_1-\boldsymbol{k}_2|m_2)\, P_{\mathrm{H}}(-\boldsymbol{k}_1-\boldsymbol{k}_2,+\boldsymbol{k}_1+\boldsymbol{k}_2,t|m_1,m_2) \\ &\quad\times \Big[\big\langle N_{\mathrm{cen}}(N_{\mathrm{cen}}-1)|m_1\big\rangle + \big\langle N_{\mathrm{cen}}\, N_{\mathrm{sat}}|m_1\big\rangle\; \big(\hat{u}_{\mathrm{g}}(\boldsymbol{k}_1|m_1) + \hat{u}_{\mathrm{g}}(\boldsymbol{k}_2|m_1)\big) \\ &\qquad + \big\langle N_{\mathrm{sat}}(N_{\mathrm{sat}}-1)|m_1\big\rangle\; \hat{u}_{\mathrm{g}}(\boldsymbol{k}_1|m_1)\,\hat{u}_{\mathrm{g}}(\boldsymbol{k}_2|m_2)\Big] \Big\} ,\end{aligned} \tag{5.18}$$

and

$$\begin{aligned}
&B^{3-\mathrm{h}}_{\mathrm{gg}\delta}(\boldsymbol{k}_1,\boldsymbol{k}_2,-\boldsymbol{k}_1-\boldsymbol{k}_2,t)\\
&=\frac{1}{\bar{\rho}\,\bar{n}^2}\int \mathrm{d}m_1 \int \mathrm{d}m_2 \int \mathrm{d}m_3 \;\; n(m_1)\,n(m_2)\,n(m_3)\,m_3\,\hat{u}(-\boldsymbol{k}_1-\boldsymbol{k}_2|m_3)\\
&\quad\times B_{\mathrm{H}}(\boldsymbol{k}_1,\boldsymbol{k}_2,-\boldsymbol{k}_1-\boldsymbol{k}_2,t)\,\left[\left\langle N_{\mathrm{cen}}|m_1\right\rangle+\left\langle N_{\mathrm{sat}}|m_1\right\rangle\,\hat{u}_{\mathrm{g}}(\boldsymbol{k}_1|m_1)\right]\\
&\quad\times\left[\left\langle N_{\mathrm{cen}}|m_2\right\rangle+\left\langle N_{\mathrm{sat}}|m_2\right\rangle\,\hat{u}_{\mathrm{g}}(\boldsymbol{k}_2|m_2)\right]\;.
\end{aligned}\tag{5.19}$$

Here $n(m)$ is the HMF in Eq. (2.82) and $\hat{u}$ is the Fourier transform of the NFW profile in Eq. (2.76). The P_{H} and B_{H} are the halo power- and bispectrum, which can be approximated with Eq. (2.85) and Eq. (2.86).

For two different galaxy populations a and b, the calculation in Appendix C.2 leads to

$$\begin{aligned}
&B^{1-\mathrm{h}}_{\mathrm{gg}\delta}(\boldsymbol{k}_1,\boldsymbol{k}_2,-\boldsymbol{k}_1-\boldsymbol{k}_2,t)\\
&=\frac{1}{\bar{\rho}\,\bar{n}_a\,\bar{n}_b}\int \mathrm{d}m\;\; n(m)\,m\,\hat{u}(-\boldsymbol{k}_1-\boldsymbol{k}_2|m)\\
&\quad\times\left[\left\langle N^{(a)}_{\mathrm{cen}}\,N^{(b)}_{\mathrm{cen}}|m\right\rangle+\left\langle N^{(a)}_{\mathrm{cen}}\,N^{(b)}_{\mathrm{sat}}\right\rangle\,\hat{u}^{(b)}_{\mathrm{g}}(\boldsymbol{k}_2|m)+\left\langle N^{(b)}_{\mathrm{cen}}\,N^{(a)}_{\mathrm{sat}}\right\rangle\,\hat{u}^{(a)}_{\mathrm{g}}(\boldsymbol{k}_1|m)\right.\\
&\qquad\left.+\left\langle N^{(a)}_{\mathrm{sat}}\,N^{(b)}_{\mathrm{sat}}|m\right\rangle\,\hat{u}^{(a)}_{\mathrm{g}}(\boldsymbol{k}_1|m)\,\hat{u}^{(b)}_{\mathrm{g}}(\boldsymbol{k}_2|m)\right]\;,
\end{aligned}\tag{5.20}$$

$$\begin{aligned}
&B^{2-\mathrm{h}}_{\mathrm{gg}\delta}(\boldsymbol{k}_1,\boldsymbol{k}_2,-\boldsymbol{k}_1-\boldsymbol{k}_2,t)\\
&=\frac{1}{\bar{\rho}\,\bar{n}_a\,\bar{n}_b}\int \mathrm{d}m_1 \int \mathrm{d}m_2\;\; n(m_1)\,n(m_2)\\
&\quad\times\Big\{\left[m_1\,\hat{u}(-\boldsymbol{k}_1-\boldsymbol{k}_2|m_1)\,P_{\mathrm{H}}(\boldsymbol{k}_2,-\boldsymbol{k}_2,t|m_1,m_2)+m_2\,\hat{u}(-\boldsymbol{k}_1-\boldsymbol{k}_2|m_2)\,P_{\mathrm{H}}(\boldsymbol{k}_1,-\boldsymbol{k}_1,t|m_1,m_2)\right]\\
&\quad\times\left[\left\langle N^{(a)}_{\mathrm{cen}}|m_1\right\rangle+\left\langle N^{(a)}_{\mathrm{sat}}|m_1\right\rangle\,\hat{u}^{(a)}_{\mathrm{g}}(\boldsymbol{k}_1|m_1)\right]\;\left[\left\langle N^{(b)}_{\mathrm{cen}}|m_2\right\rangle+\left\langle N^{(b)}_{\mathrm{sat}}|m_2\right\rangle\,\hat{u}^{(b)}_{\mathrm{g}}(\boldsymbol{k}_2|m_2)\right]\\
&\quad+m_2\,\hat{u}(-\boldsymbol{k}_1-\boldsymbol{k}_2|m_2)\,P_{\mathrm{H}}(-\boldsymbol{k}_1-\boldsymbol{k}_2,\boldsymbol{k}_1+\boldsymbol{k}_2,t|m_1,m_2)\\
&\quad\times\left[\left\langle N^{(a)}_{\mathrm{cen}}\,N^{(b)}_{\mathrm{cen}}|m_1\right\rangle+\left\langle N^{(a)}_{\mathrm{cen}}\,N^{(b)}_{\mathrm{sat}}|m_1\right\rangle\,\hat{u}^{(b)}_{\mathrm{g}}(\boldsymbol{k}_2|m_1)\;+\left\langle N^{(b)}_{\mathrm{cen}}\,N^{(a)}_{\mathrm{sat}}|m_1\right\rangle\,\hat{u}^{(a)}_{\mathrm{g}}(\boldsymbol{k}_1|m_1)\right.\\
&\qquad\left.+\left\langle N^{(a)}_{\mathrm{sat}}\,N^{(b)}_{\mathrm{sat}}|m_1\right\rangle\,\hat{u}^{(a)}_{\mathrm{g}}(\boldsymbol{k}_1|m_1)\,\hat{u}^{(b)}_{\mathrm{g}}(\boldsymbol{k}_2|m_2)\right]\Big\}\;,
\end{aligned}\tag{5.21}$$

and

$$\begin{aligned}
&B^{3-\mathrm{h}}_{\mathrm{gg}\delta}(\boldsymbol{k}_1,\boldsymbol{k}_2,-\boldsymbol{k}_1-\boldsymbol{k}_2,t)\\
&=\frac{1}{\bar{\rho}\,\bar{n}_a\,\bar{n}_b}\int \mathrm{d}m_1 \int \mathrm{d}m_2 \int \mathrm{d}m_3\;\; n(m_1)\,n(m_2)\,n(m_3)\,m_3\,\hat{u}(-\boldsymbol{k}_1-\boldsymbol{k}_2|m_3)\\
&\quad\times B_{\mathrm{H}}(\boldsymbol{k}_1,\boldsymbol{k}_2,-\boldsymbol{k}_1-\boldsymbol{k}_2,t)\,\left[\left\langle N^{(a)}_{\mathrm{cen}}|m_1\right\rangle+\left\langle N^{(a)}_{\mathrm{sat}}|m_1\right\rangle\,\hat{u}^{(a)}_{\mathrm{g}}(\boldsymbol{k}_1|m_1)\right]\\
&\quad\times\left[\left\langle N^{(b)}_{\mathrm{cen}}|m_2\right\rangle+\left\langle N^{(b)}_{\mathrm{sat}}|m_2\right\rangle\,\hat{u}^{(b)}_{\mathrm{g}}(\boldsymbol{k}_2|m_2)\right]\;.
\end{aligned}\tag{5.22}$$

With the assumptions on the moments of the HOD outlined in Sect. 5.4.1 the galaxy-matter bispectrum is fully specified.

5.2.3 Projecting the bispectrum and obtaining the aperture statistics

To obtain $B_{\mathrm{gg}\kappa}$, we use the Limber approximation in Eq. (2.114). The projected bispectrum depends on the distribution of lens and source galaxies with co-moving distance w. We use the redshift distribution of KiDS galaxies, shown in Fig. 3.3, as source distribution and the distribution of GAMA galaxies, shown in Fig. 4.1, as lens distribution. To convert these redshift distributions $p_z(z)$ to the distributions with co-moving distance, we use

$$p(w)\,\mathrm{d}w = p_z(z)\,\mathrm{d}z \Rightarrow p(w) = p_z(z)\left(\frac{\mathrm{d}w}{\mathrm{d}z}\right)^{-1} \tag{5.23}$$

From the projected bispectrum, we obtain $\langle \mathcal{N}\mathcal{N}\mathcal{M}\rangle$ with Eq. (2.141).

The computation of the aperture statistics with the halo model is computationally involved. Any calculation of $\langle \mathcal{N}\mathcal{N}\mathcal{M}\rangle$ requires the evaluation of at least one mass integral, one integral along the line-of-sight, and three integrals over the parameters of the projected bispectrum. To speed-up the computation, we use the processing power of a GPU to evaluate the integrals. We compute the aperture statistics with Monte-Carlo integration, with several thousand simultaneous function evaluations on the GPU. This method enables a quick computation of the model (approximately 1 minute for 30 values of $\langle \mathcal{N}\mathcal{N}\mathcal{M}\rangle$).

5.3 Fitting procedure

5.3.1 Estimation of best-fitting parameters

We constrain the parameters of the G3L halo model by fitting it to observations. For this, we use the KV450 × GAMA data described in Sect. 4.3.1. We again divide the lens galaxies into ‘red’ and ‘blue’ with the criterion in Eq. (4.12). However, we do not use the measurements described in Sect. 4.4 but rather estimate $\tilde{\mathcal{G}}$ without redshift weighting with Eq. (2.126). We choose this approach because the assumptions for the Limber approximation break down if lens galaxy pairs are redshift weighted. In particular, the assumption that the lens redshift distribution varies only slowly is no longer true. The other improvements of the G3L estimator detailed in Sect. 3.2, such as the adaptive binning scheme and the calculation on a GPU, are still employed. The covariance matrix C is estimated as in Sect. 4.2 with Eq. (3.31).

We measure $\langle \mathcal{NNM} \rangle$ for 30 scale radii θ between $0\overset{\prime}{.}1$ and $20'$ for red-red, red-blue and blue-blue lens pairs. These measurements are summarized to the data vector $\boldsymbol{d}$, given as

$$\boldsymbol{d} = \begin{pmatrix} \langle \mathcal{NNM} \rangle_{\text{red-red}}\,(\theta_1) \\ \vdots \\ \langle \mathcal{NNM} \rangle_{\text{red-red}}\,(\theta_{30}) \\ \langle \mathcal{NNM} \rangle_{\text{blue-blue}}\,(\theta_1) \\ \vdots \\ \langle \mathcal{NNM} \rangle_{\text{blue-blue}}\,(\theta_{30}) \\ \langle \mathcal{NNM} \rangle_{\text{red-blue}}\,(\theta_1) \\ \vdots \\ \langle \mathcal{NNM} \rangle_{\text{red-blue}}\,(\theta_{30}) \end{pmatrix} . \tag{5.24}$$

Analogously, we define the model vector $\boldsymbol{m}(\boldsymbol{p})$ for each parameter set $\boldsymbol{p}$ as composed of the halo model predictions $\langle \mathcal{NNM} \rangle^{\text{model}}$ for the aperture statistics of red-red, blue-blue, and red-blue galaxy pairs,

$$\boldsymbol{m} = \begin{pmatrix} \langle \mathcal{NNM} \rangle^{\text{model}}_{\text{red-red}}\,(\theta_1|\boldsymbol{p}) \\ \vdots \\ \langle \mathcal{NNM} \rangle^{\text{model}}_{\text{red-red}}\,(\theta_{30}|\boldsymbol{p}) \\ \langle \mathcal{NNM} \rangle^{\text{model}}_{\text{blue-blue}}\,(\theta_1|\boldsymbol{p}) \\ \vdots \\ \langle \mathcal{NNM} \rangle^{\text{model}}_{\text{blue-blue}}\,(\theta_{30}|\boldsymbol{p}) \\ \langle \mathcal{NNM} \rangle^{\text{model}}_{\text{red-blue}}\,(\theta_1|\boldsymbol{p}) \\ \vdots \\ \langle \mathcal{NNM} \rangle^{\text{model}}_{\text{red-blue}}\,(\theta_{30}) \end{pmatrix} . \tag{5.25}$$

To find the optimal parameters $\boldsymbol{p}_{\text{opt}}$ of the halo model, we apply a χ^2-minimization. We find $\boldsymbol{p}_{\text{opt}}$ by minimizing

$$\chi^2(\boldsymbol{p}) = [\boldsymbol{d} - \boldsymbol{m}(\boldsymbol{p})]^{\mathrm{T}}\; C^{-1}\; [\boldsymbol{d} - \boldsymbol{m}(\boldsymbol{p})]\ , \tag{5.26}$$

where C^{-1} is the inverse covariance matrix of the observations defined by Eq. (4.9). We minimize χ^2 with the Nelder-Mead algorithm (Nelder and Mead, 1965) as implemented in the GSL (Gough, 2009). To avoid local minima, the algorithm is restarted multiple times at different, randomly chosen, initial parameter values. Evaluations of χ^2 are performed on a GPU for computational speed.

5.3.2 Estimation of parameter uncertainty

To estimate the uncertainties on the best-fitting halo parameters $\boldsymbol{p}_{\text{opt}}$, we estimate the parameter covariance C_{p},

$$C_{\text{p}} = \int \mathrm{d}^{13}p\ \ (\boldsymbol{p} - \boldsymbol{p}_{\text{opt}})\,(\boldsymbol{p} - \boldsymbol{p}_{\text{opt}})^{\mathrm{T}}\, post(\boldsymbol{p}|\boldsymbol{d})\ , \tag{5.27}$$

with the posterior distribution $post(\boldsymbol{p}|\boldsymbol{d})$, which gives the probability of the parameters $\boldsymbol{p}$ given the data $\boldsymbol{d}$. Following Bayes theorem, the posterior can be expressed as

$$post(\boldsymbol{p}|\boldsymbol{d}) \propto \mathcal{L}(\boldsymbol{d}|\boldsymbol{p})\, \mathcal{P}(\boldsymbol{p})\;, \tag{5.28}$$

where $\mathcal{P}(\boldsymbol{p})$ is the prior on the parameters and $\mathcal{L}(\boldsymbol{d}|\boldsymbol{p})$ is the likelihood of the data given the parameters $\boldsymbol{p}$. Assuming that the likelihood $\mathcal{L}$ is Gaussian in the data, it is

$$\mathcal{L}(\boldsymbol{d}|\boldsymbol{p}) = \exp\left\{-\frac{1}{2}\;[\boldsymbol{d} - \boldsymbol{m}(\boldsymbol{p})]^{\mathrm{T}}\; C^{-1}\; [\boldsymbol{d} - \boldsymbol{m}(\boldsymbol{p})]\right\} = \exp\left[-\frac{1}{2}\chi^2(\boldsymbol{p})\right]\;, \tag{5.29}$$

with the covariance matrix C of the data and χ as defined in Eq. (5.26).

In principle, C_p could be estimated by drawing N_p parameter sets $\tilde{\boldsymbol{p}}_i$ from the posterior and estimating

$$C_\mathrm{p} = \frac{1}{N_\mathrm{p} - 1} \sum_{i=0}^{N_\mathrm{p}} (\tilde{\boldsymbol{p}}_i - \boldsymbol{p}_\mathbf{opt})\, (\tilde{\boldsymbol{p}}_i - \boldsymbol{p}_\mathbf{opt})^{\mathrm{T}}\;. \tag{5.30}$$

However, this would require many, computationally expensive, evaluations of the posterior. Therefore, we instead use importance sampling. For this, we find a distribution $q(\boldsymbol{p}|\boldsymbol{d})$ which is similar to $post(\boldsymbol{p}|\boldsymbol{d})$. Then, we draw N_p parameter sets $\boldsymbol{p}_i$ from q and assign them weights $w(\boldsymbol{p}_i|\boldsymbol{d})$, which are

$$w(\boldsymbol{p}_i|\boldsymbol{d}) = \frac{post(\boldsymbol{p}_i|\boldsymbol{d})}{q(\boldsymbol{p}_i|\boldsymbol{d})}\;. \tag{5.31}$$

The parameter covariance matrix is then estimated with

$$C_\mathrm{p} = \frac{1}{N_\mathrm{p} - 1} \sum_{i=0}^{N_\mathrm{p}} w^2(\boldsymbol{p}_i|\boldsymbol{d})(\boldsymbol{p}_i - \boldsymbol{p}_\mathbf{opt})\, (\boldsymbol{p}_i - \boldsymbol{p}_\mathbf{opt})^{\mathrm{T}}\;. \tag{5.32}$$

The uncertainty σ_i of parameter p_i is then given by

$$\sigma_i = \sqrt{C_{\mathrm{p}ii}}\;. \tag{5.33}$$

We find the importance sampling function q by approximating the likelihood $\mathcal{L}(\boldsymbol{d}|\boldsymbol{p})$ in the proximity of the optimal parameters $\boldsymbol{p}_\mathrm{opt}$ with a Gaussian $\tilde{\mathcal{L}}(\boldsymbol{d}|\boldsymbol{p})$,

$$\tilde{\mathcal{L}}(\boldsymbol{d}|\boldsymbol{p}) \simeq \exp\left[-\frac{1}{2}\left(\boldsymbol{p} - \boldsymbol{p}_\mathrm{opt}\right)^{\mathrm{T}} \mathcal{F}(\boldsymbol{p}_\mathrm{opt}) \left(\boldsymbol{p} - \boldsymbol{p}_\mathrm{opt}\right)\right]. \tag{5.34}$$

The matrix $\mathcal{F}$ is the Fisher information matrix, which is defined as

$$\mathcal{F}_{ij}(\boldsymbol{p}) = \frac{\partial \boldsymbol{m}(\boldsymbol{p})}{\partial p_i}\, C^{-1}\, \frac{\partial \boldsymbol{m}(\boldsymbol{p})}{\partial p_j}\;. \tag{5.35}$$

With this approximated likelihood, a good choice for q is

$$q(\boldsymbol{p}|\boldsymbol{d}) = \tilde{\mathcal{L}}(\boldsymbol{d}|\boldsymbol{p})\, \mathcal{P}(\boldsymbol{p})\;, \tag{5.36}$$

so the weights w are

$$w(\boldsymbol{p}_i|\boldsymbol{d}) = \frac{\mathcal{L}(\boldsymbol{d}|\boldsymbol{p}_i)}{\tilde{\mathcal{L}}(\boldsymbol{d}|\boldsymbol{p}_i)} = \exp\left[-\frac{1}{2}\chi^2(\boldsymbol{p}) + \frac{1}{2}\left(\boldsymbol{p} - \boldsymbol{p}_\mathrm{opt}\right)^{\mathrm{T}} \mathcal{F}(\boldsymbol{p}_\mathrm{opt}) \left(\boldsymbol{p} - \boldsymbol{p}_\mathrm{opt}\right)\right]. \tag{5.37}$$

5.4 Results

5.4.1 Impact of model parameters

Before fitting the halo model for G3L to the observations, we qualitatively study the impact of the halo model parameters on the G3L signal. For this, we set each parameter inside the prior range to three different values, while keeping the other parameters fixed to their fiducial values.

Figure 5.2 shows the predicted $\langle \mathcal{N}\mathcal{N}\mathcal{M} \rangle$ for unmixed lens pairs, when varying the parameters by ±25%. All parameters impact the 1- and 2-halo term, except for σ (see Fig. 5.2a). This parameter has no noticeable effect on the aperture statistics and can consequently not be constrained with G3L measurements. The 3-halo term is only weakly affected by all parameters and fully independent of σ and f.

The slope β of the satellite galaxy distribution has the largest effect on $\langle \mathcal{N}\mathcal{N}\mathcal{M} \rangle$ (see Fig. 5.2b). Larger β increase the signal, especially the 1-halo term, on scales above $0\overset{\prime}{.}2$. This behaviour is expected, as larger β lead to more satellite galaxies in massive halos. Therefore, the correlation between satellite galaxies, which impacts the 1- and 2-halo terms, increases on scales above $0\overset{\prime}{.}2$. The 3-halo term is less sensitive to β because this term does not depend on the correlation of galaxies in the same halo. Therefore, the total aperture statistics at large scales are the same for all values of β.

The mass scale M' of satellite galaxies also impacts the 1- and 2-halo terms the strongest (see Fig. 5.2e). These terms increase at all scales for decreasing M', with the strongest increase on scales between $1'$ and $10'$. This increase with decreasing M' occurs, because halos contain more satellite galaxies if the mass scale is lower. Therefore, the correlation of satellite galaxies as well as the correlation of central galaxies with satellites increases.

The parameters α and M_th, which determine the central galaxy distribution, affect the signal almost equally with the largest effect on scales between $1'$ and $5'$ (see Figs. 5.2d and 5.2c). A decrease of α, as well as an increase of M_th lead to a smaller $\langle \mathcal{N}\mathcal{N}\mathcal{M} \rangle$. This is because both a smaller α and a higher M_th lead to more halos containing only satellite galaxies. Consequently, the correlation between satellite galaxies increases, which causes larger 1- and 2-halo terms of $\langle \mathcal{N}\mathcal{N}\mathcal{M} \rangle$.

The concentration of the galaxy distribution per halo also affects the aperture statistics (see Fig. 5.2f). $\langle \mathcal{N}\mathcal{N}\mathcal{M} \rangle$ increases on scales below $2'$ for galaxy profiles more concentrated than the matter distribution ($f > 1$). The aperture statistics decrease for $f < 1$. This behaviour is expected as a more concentrated galaxy profile leads to more galaxies in the dense inner regions of the halo. Therefore, the galaxy-matter three-point correlation function increases at small scales. The concentration affects only the 1- and 2-halo term because it is only relevant when correlating the galaxy and matter distribution in the same halo. Consequently, the three-halo term, which considers only galaxies and matter from different halos, is independent of f.

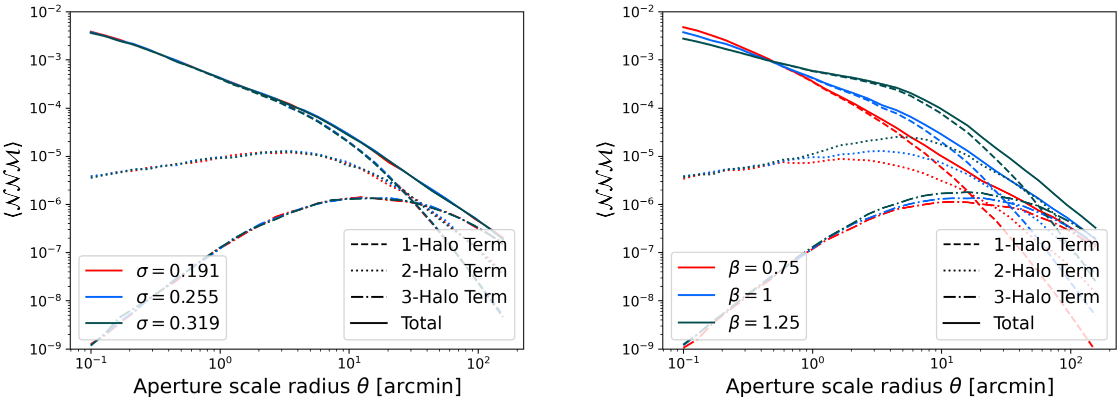

(a) Impact of σ **(b)** Impact of β

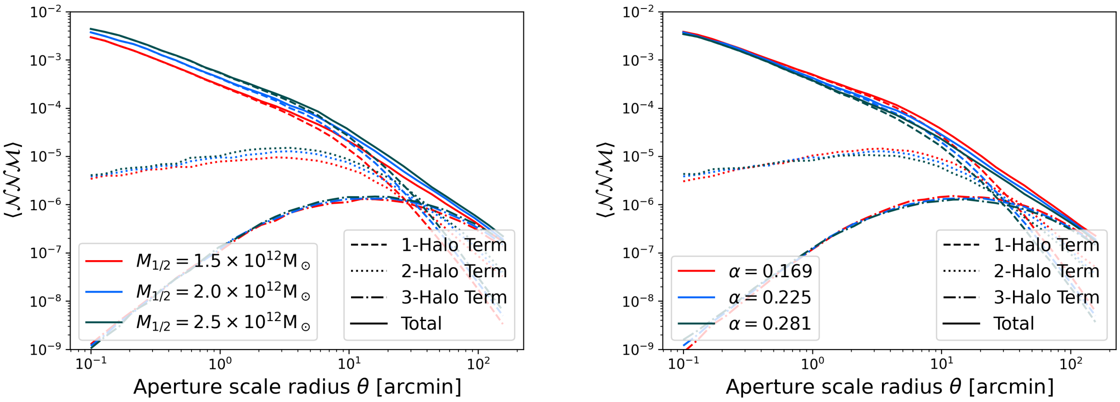

(c) Impact of $M_{\rm th}$ **(d)** Impact of α

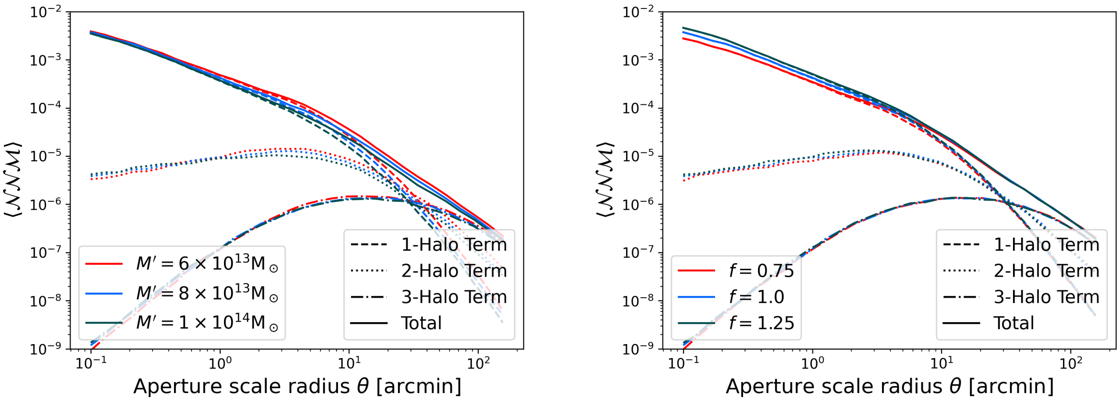

(e) Impact of M' **(f)** Impact of f

Figure 5.2: Impact of halo model parameters on $\langle\mathcal{NNM}\rangle$ for unmixed lens pairs. In each subfigure, one parameter is varied by adding/subtracting 25% of its fiducial value from Table 5.1, while keeping all other parameters fixed. Solid lines indicate the total $\langle\mathcal{NNM}\rangle$, while dashed lines show the 1-halo, dotted lines the 2-halo, and dash-dotted lines the 3-halo term.

To estimate the sensitivity of G3L to the cross-correlation of lens populations, we show in Fig. 5.3 the predicted $\langle \mathcal{N}\mathcal{N}\mathcal{M} \rangle$ for two different lens populations which are fully correlated ($r = 1$), not correlated ($r = 0$) or anticorrelated ($r = -1$). We have set one parameter for each population to a value either higher or lower than the fiducial one while keeping the other parameters to the fiducial model. For comparison, we also show the auto-correlation signal for both populations.

The figure shows that the $\langle \mathcal{N}\mathcal{N}\mathcal{M} \rangle$ for independent populations is at the geometric mean of the auto-correlations. This finding is independent of which parameter we vary between the populations. Consequently, for $r = 0$, the halo model prediction coincides with those of a linear deterministic galaxy bias (see Sect. 2.4.4 and Sect. 4.4).

Furthermore, the aperture statistics for $r = -1, 0$, and 1 coincide at large scales but differ below that for all parameters. The signal for anti-correlated lens populations is consistently smaller than for uncorrelated and positively correlated lenses. The amount of variation between the $\langle \mathcal{N}\mathcal{N}\mathcal{M} \rangle$ is almost independent of the varied parameter and is detectable even for different σ.

A more detailed look at Fig. 5.3 reveals that r impacts small, but not large scales because it primarily affects the 1-halo term. The 2-halo term is less dependent on r, and the 3-halo term is entirely independent of it. This observation is not surprising, as the 3-halo term only depends on galaxies from different halos and is therefore not sensitive to the correlation of galaxies in the same halo. For the same reason, the 2-halo term is less affected than the 1-halo term.

Another reason for the stronger dependence of $\langle \mathcal{N}\mathcal{N}\mathcal{M} \rangle$ on r at smaller scales is that smaller halos with lower masses dominate these scales. Therefore, the ratio $\sigma_\mathrm{sat}/\langle N_\mathrm{sat}|m \rangle$ is large and the term proportional to r in Eq. (5.9) contributes significantly. At larger scales, the 1-halo term is dominated by halos with larger masses and higher $\left\langle N_\mathrm{sat}|m \right\rangle$. Therefore, the correlation term loses importance, which explains why the 1-halo terms for different values of r converge for large scales.

5.4.2 Results of fitting halo model to observations

Next, we give the results of fitting our halo model to the observations in the KV450 × GAMA data. Figure 5.4 shows the measured G3L aperture statistics. The measurement has a lower S/N than the measurement in Sect. 4.4 because we did not weigh lens galaxy pairs according to their redshift differences. Consequently, the signal is lower by a factor of approximately 2, while the noise is lower by only 40%, compared to Fig. B.1. Nevertheless, a clear, non-zero signal can be detected, in particular for the red-red lens pairs in Fig. 5.4a.

The best fit of our halo model is also shown in Fig. 5.4, together with its decomposition into the 1-, 2-, and 3-halo terms. In all three cases, the fit agrees well with the measurement. For

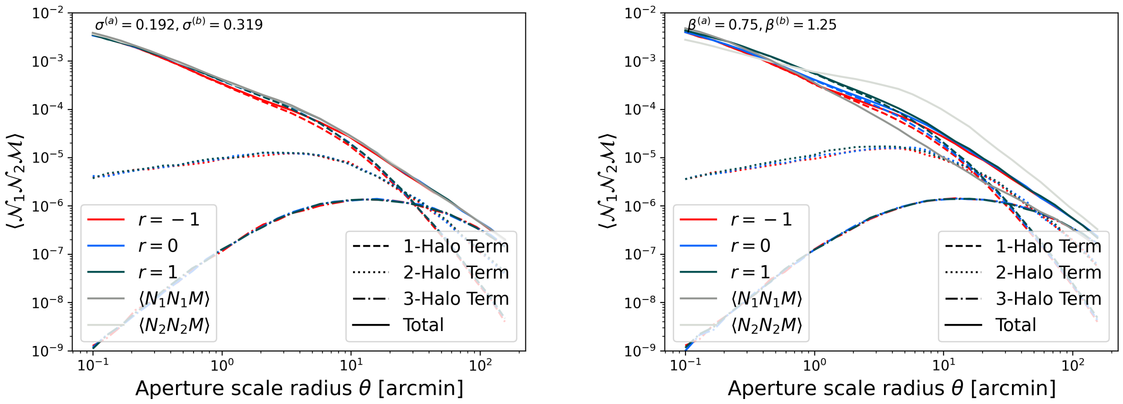

(a) Impact of σ

(b) Impact of β

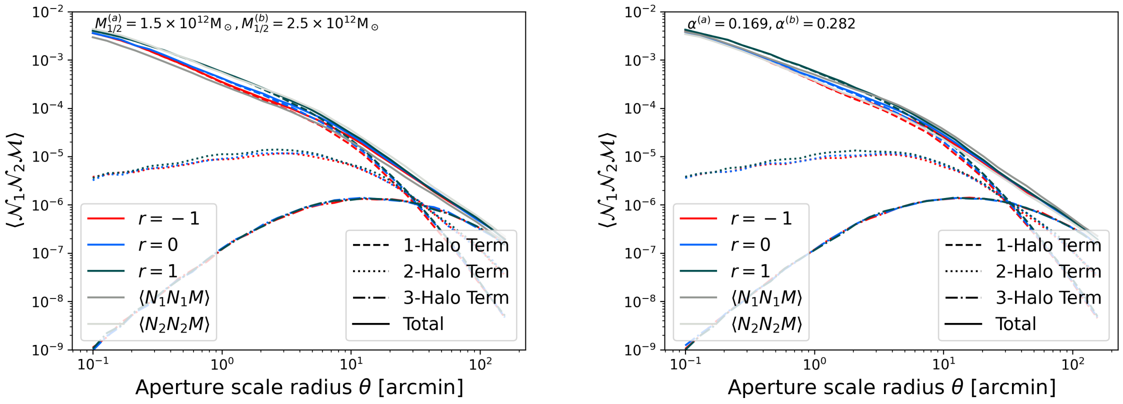

(c) Impact of M_{th}

(d) Impact of α

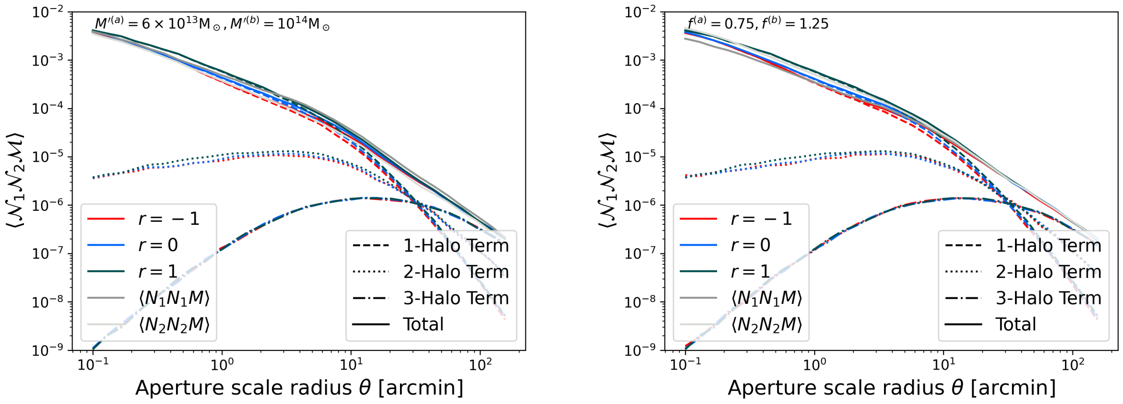

(e) Impact of M'

(f) Impact of f

Figure 5.3: Impact of halo model parameters on $\langle \mathcal{N}\mathcal{N}\mathcal{M} \rangle$ for mixed lens pairs. In each subfigure, one parameter is varied, while keeping the others at the fiducial values from Table 5.1. Lenses are either correlated ($r = 1$, green lines), uncorrelated ($r = 0$, blue lines) or anti-correlated ($r = -1$, red lines). Also shown are the auto-correlations in grey. Solid lines indicate the total aperture statistics, dashed lines the 1-halo, dotted lines the 2-halo, and dash-dotted lines the 3-halo term.

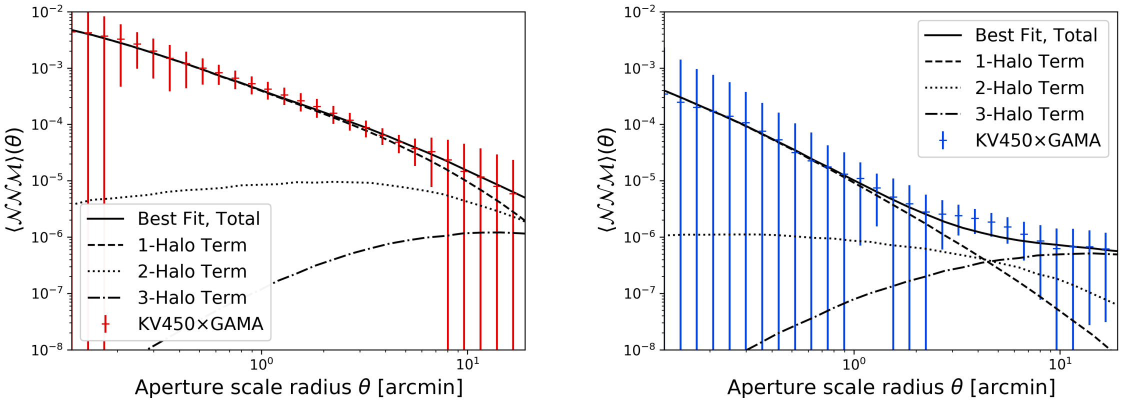

(a) Red-red lens pairs

(b) Blue-blue lens pairs

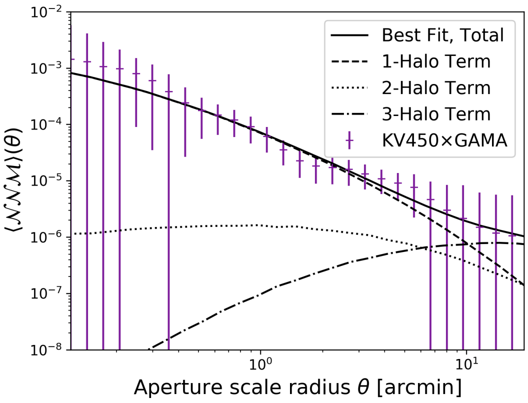

(c) Red-blue lens pairs

Figure 5.4: G3L measurement in KV450 $\times$ GAMA (points) and best fitting halo model (lines). Solid lines indicate the total aperture statistics, dashed lines the 1-halo, dotted lines the 2-halo, and dash-dotted lines the 3-halo term of the fit. 5.4a shows the result for red-red galaxy pairs, 5.4b shows the result for blue-blue galaxy pairs, and 5.4c shows the result for red-blue mixed pairs.

Table 5.2: Best fitting values for halo model parameters for KV450 × GAMA.

Parameter	Best fitting value	Parameter	Best fitting value
$\alpha^{(\mathrm{red})}$	0.389 ± 0.057	$\alpha^{(\mathrm{blue})}$	0.138 ± 0.032
$\sigma^{(\mathrm{red})}$	0.24 ± 0.31	$\sigma^{(\mathrm{blue})}$	0.25 ± 0.33
$M_{\mathrm{th}}{}^{(\mathrm{red})}$	$(1.66 \pm 0.59) \times 10^{12}\ \mathrm{M}_\odot$	$M_{\mathrm{th}}{}^{(\mathrm{blue})}$	$(1.25 \pm 0.64) \times 10^{11}\ \mathrm{M}_\odot$
$\beta^{(\mathrm{red})}$	0.85 ± 0.18	$\beta^{(\mathrm{blue})}$	0.51 ± 0.15
$M'^{(\mathrm{red})}$	$(3.50 \pm 0.63) \times 10^{13}\ \mathrm{M}_\odot$	$M'^{(\mathrm{blue})}$	$(1.82 \pm 0.73) \times 10^{14}\ \mathrm{M}_\odot$
$f^{(\mathrm{red})}$	1.35 ± 0.52	$f^{(\mathrm{blue})}$	0.83 ± 0.32
r	0.88 ± 0.47		

this fit, the χ^2, as defined by Eq. (5.26) is $\chi^2 = 61.5859$. Since the fit has $90 - 13 = 77$ degrees of freedom, the reduced χ^2 is

$$\chi^2_{\mathrm{redu}} = \frac{\chi^2}{\mathrm{d.o.f}} = 0.799 \; . \tag{5.38}$$

This indicates that the best-fit halo model agrees with the measurement at the 95% CL.

The aperture statistics for red-red lenses are dominated by the 1-halo term in the whole range from $[0\overset{\prime}{.}1 : 20']$. For blue-blue lens pairs, though, the signal is dominated by the 3-halo term for $\theta > 3\overset{\prime}{.}7$. For mixed lens pairs, the 3-halo term dominates for $\theta > 10'$.

The best-fitting parameter values are shown in Table 5.2. They indicate that red and blue galaxies need to be described by different HODs, as $M_{\mathrm{th}}^{(\mathrm{red})}$ and $M_{\mathrm{th}}^{(\mathrm{blue})}$, $M'^{(\mathrm{red})}$ and $M'^{(\mathrm{blue})}$, as well as $\beta^{(\mathrm{red})}$ and $\beta^{(\mathrm{blue})}$ differ significantly. The threshold halo mass for red galaxies is $M_{\mathrm{th}}^{(\mathrm{red})} = (1.66 \pm 0.59) \times 10^{12}\,\mathrm{M}_\odot$, while for blue galaxies $M_{\mathrm{th}}^{(\mathrm{blue})} = (1.24 \pm 0.64) \times 10^{11}\,\mathrm{M}_\odot$. Consequently, halos need to be ten times as massive to host red than blue galaxies. However, because $M'^{(\mathrm{red})} < M'^{(\mathrm{blue})}$ and $\beta^{(\mathrm{red})} > \beta^{(\mathrm{blue})}$, as soon as the mass of a halo exceeds the threshold for red galaxies, it contains more red than blue galaxies.

The spatial distribution of galaxies inside a halo is consistent with unity for both red and blue galaxies, which indicates that their distribution follows the dark matter density profile. The parameter $f^{(\mathrm{red})}$ for red galaxies is larger than for blue galaxies, but this difference is not significant.

We find that the cross-correlation of red and blue galaxies is positive ($r = 0.88 \pm 0.47$). Consequently, red and blue galaxies are positively correlated.

As expected, we could not constrain the parameter σ with G3L. The 1σ interval for this parameter corresponds to the whole prior range, both for red and blue galaxies.

5.5 Discussion

In this chapter, we proposed a theoretical model for G3L both by mixed and unmixed lens pairs, based on the halo model. Our model can predict the expected G3L signal, given the moments of the HODs of the lens galaxy populations and their correlation. It is valid for lens populations defined by any galaxy property, such as stellar mass, SFR, or colour. In our analysis, we concentrate on galaxy samples divided according to their colour in ‘red’ and ‘blue’ galaxies.

We qualitatively studied the impact of the halo model parameters. The G3L signal is sensitive to all parameters except for the steepness σ of the central galaxy HOD. Consequently, G3L cannot constrain σ. This finding agrees with Martin (2019), who came to a similar conclusion. Future studies could dispense with this parameter altogether and model $\langle N_{\mathrm{cen}}|m\rangle$ with a step function.

Furthermore, we found that varying the concentration of the spatial galaxy distribution has only a small effect, predominantly at small scales. Consequently, the assumption in Martin (2019) and Rödinger (2009) that the galaxy distribution perfectly traces dark matter should not be critical to their analysis.

The G3L signal depends stronger on the distribution of satellite galaxies than centrals. The reason for this behaviour is that satellite galaxies are more numerous and are primarily responsible for G3L, in particular, the 1- and 2-halo term.

The cross-correlation of satellite galaxies primarily affects the 1-halo term at small scales, because the correlations of galaxies inside low mass halos dominate these scales. Low-mass halos have fewer satellite galaxies than high mass halos, so the cross-correlations of satellite populations have a more notable effect. As expected, the 2-halo term depends only weakly, and the 3-halo term not at all, on the correlation of galaxy populations in the same halo.

We obtained the best-fitting parameter values for the KV450 × GAMA measurements of G3L with a multidimensional optimization. We simultaneously fit the signal for mixed red-blue lens pairs and unmixed red-red and blue-blue lens pairs. Our best fit agrees with the measurements at the 95% CL. Thus, the halo model can explain the observed signal.

The threshold halo mass M_{th} to contain galaxies is larger for red than for blue galaxies. Therefore red galaxies populate more massive halos than blue galaxies. If the halo mass exceeds M_{th}, red galaxies are more numerous than blue galaxies. This observation fits the general expectation that red galaxies dominate dense dark matter environments. In contrast, blue galaxies are predominantly ‘field galaxies’ in smaller mass halos (see Sect. 2.1.3). Similar conclusions are drawn by Martin (2019) and Simon et al. (2009).

The tendency of red galaxies to cluster in denser environments also explains why the 1-halo term of red-red lens pairs stretches to larger scales than for blue-blue lens pairs. Red galaxies exist in more massive and therefore larger halos than blue galaxies. So, pairs of red galaxies in the same halo can have wider separations than pairs of blue galaxies. Accordingly, the 1-halo term extends to larger scales for red-red lens pairs than for blue-blue lens pairs. Mixed red-blue pairs exist in intermediate halos, which are large enough to have red galaxies but small enough to contain a significant fraction of blue galaxies. Consequently, the ’cross-over’ between the domination of the 1-halo and the 3-halo term occurs at larger scales than for blue-blue lens pairs.

Surprisingly, the sum of the fraction of central galaxies $\alpha^{(\mathrm{red})}$ and $\alpha^{(\mathrm{blue})}$ is less than unity, $\alpha^{(\mathrm{red})} + \alpha^{(\mathrm{blue})} = 0.53 \pm 0.34$. This indicates that some halos have neither a red nor a blue central galaxy, which contradicts our expectation that all halos have a central galaxy. To validate this unexpected finding, additional studies of the central galaxy population, for example with simulated galaxy catalogues, need to be conducted. Nevertheless, it fits the results by Martin (2019), who fitted a similar halo model to the GGL in CFHTLenS. The sum of their α values for early- and late-type-galaxies is also significantly smaller than unity.

Even though the best-fitting parameter values agree with the trends in previous works, the measurements could be improved in two ways. First, the uncertainties of the G3L observation could be reduced with the lens pair redshift weighting discussed in Sect. 3.2.1. The measurements in Sect. 4.4 which include the redshift weighting show a 40% higher S/N and could therefore better constrain the halo model parameters. However, this would require abandoning the Limber approximation in Eq. (2.114), because it is no longer valid. Accordingly, computing the model would become more complex.

Second, parameter degeneracies could be broken by modelling other observables, such as the mean galaxy number, the GGL signal or the galaxy clustering correlation function. Observations of other three-point statistics, such as $\langle \mathcal{NMM} \rangle$, $\langle \mathcal{MMM} \rangle$, or $\langle \mathcal{NNN} \rangle$, could also help in this aspect.

There are also limitations to the proposed model. One is the assumption that the number of satellite galaxies follows a Poissonian. Even though this assumption agrees with simulations by Kravtsov et al. (2004), recent studies found that the satellite number might be super-Poissonian (Dvornik et al., 2018; Gruen et al., 2018). Additional parameters could be inserted into the model to describe a super-Poissonian satellite distribution.

Another limitation of the proposed halo model is its treatment of halos itself. We chose halos to be spherical and without any substructure. A more realistic halo model would incorporate both the ellipticity of halos and the possibility of subhalos. In particular, ellipticity might be studied with G3L, as the axis connecting the lens galaxies introduces a preferred direction. This direction can act as a reference frame for the halo elongation. Accordingly, further studies of the correlation of halo ellipticity and G3L would be interesting.

Furthermore, the halo model ignores all dependence of the halo properties on its environment and assembly history. However, simulations (Gao and White, 2007; Mao et al., 2018) showed that the so-called assembly bias due to these influences might play an important role. Incorporating it into the halo model is difficult, as the fundamental assumption of independent dark matter halos has to be questioned.

Nevertheless, the agreement of our best-fitting model with the measurements shows that the halo model can describe G3L. This conclusion is sustained by the observation in Martin (2019) that the halo model can predict the G3L signal of unmixed lens pairs. Our extended model can also represent G3L with mixed lens pairs. Concludingly, despite its simple assumptions, the halo model provides valid predictions for galaxy-matter correlations.

Conclusion

6

"I may not have gone where I intended to go, but I think I have ended up where I needed to be."

– Douglas Adams, The long dark tea-time of the soul (Adams, 1990).

In this thesis, we explored different models of galaxy formation and evolution by studying their prediction for G3L. For this, we improved the measurement scheme for G3L, compared the predictions of SAMs with observations and presented a theoretical model for G3L based on the halo model. In this final chapter, we summarize our results and conclusions before giving a short outlook to the future of G3L and galaxy models

6.1 Summary

Our first step to answering the overall question were several improvements to the estimator of the G3L correlation function $\tilde{\mathcal{G}}$, which we proposed and tested in Chapter 3. These improvements entailed

- adaptive binning of $\tilde{\mathcal{G}}$, designed to remove biases at small scales,
- weighing lens galaxy pairs according to the redshift difference between their members to enhance the S/N,
- and accounting for biases due to magnification of lens galaxies by the matter distribution between them and the observer.

We tested these improvements on mock galaxy catalogues and shear maps. The first improvement, the adaptive binning scheme, was tested by applying the original and improved estimator to simple mock data, for which we could estimate the G3L signal analytically. Then, we compared the results of both estimators to the analytical expectation. The second and third improvement were tested on more realistic data from the MR with galaxies from the SAM by Henriques et al. (2015). We selected these realistic mock data such that the redshift distributions of lens- and source galaxies were similar to galaxies in KV450 × GAMA.

Our results from these tests were the following:

- The adaptive binning scheme significantly improves the accuracy of the measured G3L aperture statistics at small scales. For scales below $1'$, the estimate with the original estimator deviates by several percent from the analytical expectation and is 40% too low for $\theta = 0.'1$. The result with the new estimator agrees with the analytical aperture statistics in the whole considered range from $0.'1$ to $20'$. Therefore, adaptive binning successfully removes small-scale biasing, which impeded previous measurements of G3L (Simon et al., 2008, 2013).
- Weighing lens pairs according to the redshift difference between the galaxies lessens the impact of uncorrelated pairs and significantly improves the S/N. In our test, the S/N of the aperture statistics between $0.'1$ and $10'$ increased by approximately 35%. Consequently, redshift weighting enhances G3L measurements.
- Magnification of lens galaxies plays a significant role in G3L. This effect is primarily due to matter at the plane of the first lens galaxy (closer to the observer). This matter magnifies galaxies at the plane of the second lens galaxy and affects the observed shear of sources. It, therefore, changes the aperture number count $\mathcal{N}_2$ at the second lens plane and the aperture mass $\mathcal{M}$. If the matter at the first lens plane is correlated to the aperture number count $\mathcal{N}_1$ at the first lens plane, the G3L aperture statistics $\langle \mathcal{N}\mathcal{N}\mathcal{M} \rangle$ get an additional component due to the magnification. In our simulated data, this additional signal is roughly 10% of the signal without magnification. Magnification by matter between the observer and the first lens plane or between the second lens plane and the source is negligible for G3L.

After improving the estimator for G3L, we used the new measurement method to test the predictions by two SAMs in Chapter 4. We measured the G3L signal in galaxy catalogues based on the SAMs by Henriques et al. (2015, H15) and Lagos et al. (2012, L12) and compared the result to observations in KV450 × GAMA. For a more detailed analysis, we divided the lens galaxies into two colour- and five stellar mass-selected samples and measured the G3L signal separately for each of these samples. In this measurement, we considered both unmixed lens pairs, with two galaxies from the same sample and mixed lens pairs with galaxies from different samples. For the latter G3L has not been measured before.

In these measurements, we found the following:

- The L12 SAM does not agree with the observations, regardless of whether we select lenses by colour or stellar mass. For lens pairs with two blue galaxies, the L12 SAM underpredicts the signal. At the same time, it overpredicts G3L for pairs with at least one red galaxy. This deviation could be due to an overproduction of red galaxies by strong environmental effects. Excessive tidal interaction could cause galaxies to lose their gas and stop star-formation too quickly. Therefore, they appear redder than they would in a more realistic scenario. This finding agrees with previous studies (Baldry et al., 2006; Font et al., 2008) of the L12 SAM and its predecessor by Bower et al. (2006).
- For stellar mass-selected lens galaxies, the L12 SAM predicts a too high G3L signal. This overprediction could be due to the chosen IMF or too many satellite galaxies. A high satellite fraction for massive halos could be due to strong environmental effects or excessive galaxy interactions.

- The H15 agrees well with the observed G3L signal. This finding is consistent with the previous study by Saghiha et al. (2017). We conclude that the H15 SAM describes galaxy formation and evolution accurately.
- The G3L of mixed lens pairs with one red and one blue galaxy is consistent with a linear deterministic model for the galaxy bias. In this bias model, we would expect the G3L of mixed pairs to be at the geometric mean of the G3L signals for red-red and blue-blue lens pairs. This expectation is met, both in the observation and the H15 SAM for scales above $0.2\,h^{-1}$ Mpc.

Finally, in Chapter 5, we presented an analytical model for G3L based on the halo model. We qualitatively studied the effect of different parameters on the predicted G3L aperture statistics and obtained the best-fitting parameter values for KV450 × GAMA. We found:

- The cross-correlation of satellite galaxies affects mainly the 1-halo term at small scales. At small scales, lower mass halos dominate the signal. These lower mass halos contain fewer galaxies in total, so the correlation of satellites has a bigger effect.
- The best-fitting halo model agrees with the measurement in KV450 × GAMA at the 95% CL. The parameter values indicate that red galaxies form in more massive halos than blue galaxies and that these two populations are positively correlated.

In conclusion, we can now answer the question posed in the introduction: *How well do the different models for galaxy formation, evolution and distribution reproduce the observed correlation of dark matter and galaxy pairs?* We find that not all galaxy models accurately predict the correlation of matter and galaxy pairs. SAMs, when tuned to the right level of galaxy interaction and star formation (like the H15 SAM), can agree very well with observations of G3L. However, this is not automatically the case for every SAM, as demonstrated by the failure of the L12 SAM to match observations. A careful setting of models for baryon physics is required to predict the correlation of the galaxy and matter distributions correctly. Analytical models based on the halo model can, despite its simple assumptions, reproduce the observed G3L, with plausible values for its parameters, a notable success for the halo model.

6.2 Outlook

Higher-order statistics are complicated. They take longer to compute and measure than two-point correlations, and the signal-to-noise ratio is worse. Moreover, modelling higher-order statistics requires more terms with higher-dimensional integrations. However, we have shown how to remedy some of these difficulties. The S/N improves with an appropriate weighting of galaxies, and the computational time reduces with highly parallelized routines on GPUs. Modelling, while still complicated, is possible with the halo model. Therefore, we should not be scared of third-order correlations and continue measuring its properties to test models of galaxy evolution, as well as cosmological models.

G3L is especially interesting in light of upcoming stage IV [1] surveys such as Euclid (Laureijs et al., 2011) or the Legacy Survey of Space and Time (LSST; Ivezić et al., 2019)[2]. These surveys will observe large areas of the sky with extraordinary resolution. Euclid, a space telescope expected to launch in late 2022, will observe an area of approximately 15 000 deg^2 over six years. LSST is a ground-based survey, which will be conducted at the Vera C. Rubin observatory in northern Chile with first light expected in 2022. It will cover approximately 18 000 deg^2. Both surveys aim at observing 30 galaxies per arcmin^2, so due to their unprecedented size and resolution, shapes and positions of billions of galaxies will be available. Applying our estimators to these data sets will lead to precise measurements of G3L.

These precise measurements are essential for another exciting development: the progress of cosmological simulations. Cosmological structure formation is simulated in increasingly larger and better resolved N-body simulations, such as the Euclid flagship simulation (Potter et al., 2017) or the 'Last Journey' simulation (Heitmann et al., 2020). Both of these have boxes with side lengths larger than 5 Gpc while retaining a mass resolution of approximately $10^9\,\mathrm{M}_\odot$. These dark-matter-only simulations will be populated with billions of galaxies according to SAMs so that they can predict G3L with high statistical precision. These predictions can then be compared to the measurements of the stage IV surveys.

G3L measurements can also be compared to full hydrodynamical simulations, like IllustrisTNG (Springel et al., 2018), EAGLE (Schaye et al., 2015), or Horizon-AGN (Dubois et al., 2014). These simulations represent a different approach to galaxy formation than SAMs, as they directly solve the hydrodynamical equations for baryonic gases. Therefore, it would be interesting to test whether their predictions for G3L are as accurate as of the SAMs. However, hydrodynamical simulations are more complex than dark-matter-only simulations. Accordingly, they have smaller box sizes with less galaxies. Larger simulations might become achievable with new numerical techniques, so estimates of G3L may be possible soon.

New G3L measurements and predictions by large cosmological simulations, will allow us to constrain galaxy formation models with increasing precision. Deviations between the simulations and measurements indicate problems with current models for small-scale baryonic effects. Agreement shows that the models are 'on the right track'. With more precise observations, increasingly stringent tests of existing galaxy formation models can be performed, and better models developed. Thus, comparing predictions and measurements of galaxy-matter statistics will lead to a full understanding of galaxies and, ultimately, our Universe.

---

[1] The 'Dark Energy Task Force Report' by Albrecht et al. (2006) classifies present and planned cosmological surveys into four different stages, with stage I being small surveys already completed at the time of the report and stage IV being the largest surveys planned. KiDS is a stage II survey.

[2] Formerly known as Large Synoptic Space Telescope.

Bibliography

Abbott, T. M. C., Abdalla, F. B., Alarcon, A., et al., 2018. *Dark Energy Survey year 1 results: Cosmological constraints from galaxy clustering and weak lensing.* Physical Review D, 98, 4:043526. doi:10.1103/PhysRevD.98.043526

Adams, D., *The Restaurant at the End of the Universe.* Hitchhiker's Guide to the Galaxy Series (Harmony Books, 1981). ISBN 9780517545355

Adams, D., *Long Dark Tea-Time of the Soul.* Dirk Gently trilogy (Pocket Books, 1990). ISBN 9780671742515

Agrawal, P., Cyr-Racine, F.-Y., Pinner, D., and Randall, L., 2019. *Rock 'n' Roll Solutions to the Hubble Tension.* arXiv e-prints:arXiv:1904.01016

Albrecht, A., Bernstein, G., Cahn, R., et al., 2006. *Report of the Dark Energy Task Force.* arXiv e-prints:astro-ph/0609591

Anderson, T. W., *An introduction to multivariate statistical analysis* (Wiley-Interscience, 2003). ISBN 9780471360919

Baldry, I. K., Balogh, M. L., Bower, R. G., et al., 2006. *Galaxy bimodality versus stellar mass and environment.* Monthly Notices of the Royal Astronomical Society, 373, 2:469. doi:10.1111/j.1365-2966.2006.11081.x

Baldry, I. K., Driver, S. P., Loveday, J., et al., 2012. *Galaxy And Mass Assembly (GAMA): the galaxy stellar mass function at $z < 0.06$.* Monthly Notices of the Royal Astronomical Society, 421, 1:621. doi:10.1111/j.1365-2966.2012.20340.x

Bard, D., Bellis, M., Allen, M. T., Yepremyan, H., and Kratochvil, J. M., 2013. *Cosmological calculations on the GPU.* Astronomy and Computing, 1:17. doi:10.1016/j.ascom.2012.11.001

Barreira, A., Llinares, C., Bose, S., and Li, B., 2016. *RAY-RAMSES: a code for ray tracing on the fly in N-body simulations.* Journal of Cosmology and Astropartical Physics, 2016, 5:001. doi:10.1088/1475-7516/2016/05/001

Bartelmann, M., 2010. *Gravitational lensing.* Classical and Quantum Gravity, 27, 23:233001. doi:10.1088/0264-9381/27/23/233001

Bartelmann, M., *Theoretical Astrophysics: An Introduction* (Wiley, 2013). ISBN 9783527410040

Bartelmann, M., Kozlikin, E., Lilow, R., et al., 2019. *Cosmic Structure Formation with Kinetic Field Theory.* Annalen der Physik, 531, 11:1800446. doi:10.1002/andp.201800446

Bartelmann, M. and Schneider, P., 2001. *Weak gravitational lensing.* Physics Reports, 340:291. doi:10.1016/S0370-1573(00)00082-X

Baugh, C. M., 2006. *A primer on hierarchical galaxy formation: the semi-analytical approach.* Reports on Progress in Physics, 69, 12:3101. doi:10.1088/0034-4885/69/12/R02

Benson, A. J., 2010. *Galaxy formation theory.* Physics Reports, 495, 2-3:33. doi:10.1016/j.physrep.2010.06.001

Bernardeau, F., Colombi, S., Gaztañaga, E., and Scoccimarro, R., 2002. *Large-scale structure of the Universe and cosmological perturbation theory.* Physics Reports, 367, 1-3:1. doi:10.1016/S0370-1573(02)00135-7

Bernardeau, F. and Valageas, P., 2008. *Propagators in Lagrangian space.* Physical Review D, 78, 8:083503. doi:10.1103/PhysRevD.78.083503

Blanton, M. and SDSS, 2014. *SDSS galaxy map.* https://www.sdss.org/science/orangepie. Accessed: 23.08.2019

Blanton, M. R. and Roweis, S., 2007. *K-Corrections and Filter Transformation in the Ultraviolet, Optical and Near-Infrared.* Astronomical Journal, 133, 2:734. doi:10.1086/510127

Bond, J. R., Cole, S., Efstathiou, G., and Kaiser, N., 1991. *Excursion Set Mass Functions for Hierarchical Gaussian Fluctuations.* Astrophysical Journal, 379:440. doi:10.1086/170520

Bower, R. G., Benson, A. J., Malbon, R., et al., 2006. *Breaking the hierarchy of galaxy formation.* Monthly Notices of the Royal Astronomical Society, 370:645. doi:10.1111/j.1365-2966.2006.10519.x

Bower, R. G., Vernon, I., Goldstein, M., et al., 2010. *The parameter space of galaxy formation.* Monthly Notices of the Royal Astronomical Society, 407, 4:2017. doi:10.1111/j.1365-2966.2010.16991.x

Brainerd, T. G., Blandford, R. D., and Smail, I., 1996. *Weak Gravitational Lensing by Galaxies.* Astrophysical Journal, 466:623. doi:10.1086/177537

Bruzual, G. and Charlot, S., 2003. *Stellar population synthesis at the resolution of 2003.* Monthly Notices of the Royal Astronomical Society, 344, 4:1000. doi:10.1046/j.1365-8711.2003.06897.x

Buchert, T., 1992. *Lagrangian theory of gravitational instability of Friedman-Lemaitre cosmologies and the 'Zel'dovich approximation'.* Monthly Notices of the Royal Astronomical Society, 254:729. doi:10.1093/mnras/254.4.729

Buchert, T., Melott, A. L., and Weiss, A. G., 1994. *Testing higher-order Lagrangian perturbation theory against numerical simulations I. Pancake models.* Astronomy & Astrophysics, 288:349

Bullock, J. S., Kolatt, T. S., Sigad, Y., et al., 2001. *Profiles of dark haloes: evolution, scatter and environment.* Monthly Notices of the Royal Astronomical Society, 321, 3:559. doi:10.1046/j.1365-8711.2001.04068.x

Burchett, J. N., Elek, O., Tejos, N., et al., 2020. *Revealing the Dark Threads of the Cosmic Web.* Astrophysical Journal Letters, 891, 2:L35. doi:10.3847/2041-8213/ab700c

Calzetti, D., Armus, L., Bohlin, R. C., et al., 2000. *The Dust Content and Opacity of Actively Star-forming Galaxies.* Astrophysical Journal, 533, 2:682. doi:10.1086/308692

Cárdenas-Montes, M., Rodríguez-Vázquez, J. J., Vega-Rodríguez, M. A., Sevilla-Noarbe, I., and Alvaro, E. S., 2014. *Performance and precision of histogram calculation on GPUs: Cosmological analysis as a case study.* Computer Physics Communications, 185, 10:2558. doi:10.1016/j.cpc.2014.06.002

Carrasco, J. J. M., Foreman, S., Green, D., and Senatore, L., 2014. *The Effective Field Theory of Large Scale Structures at two loops.* Journal of Cosmology and Astropartical Physics, 2014, 7:057. doi:10.1088/1475-7516/2014/07/057

Chabrier, G., 2003. *Galactic Stellar and Substellar Initial Mass Function.* Publications of the Astronomical Society of the Pacific, 115, 809:763. doi:10.1086/376392

Clampitt, J., Miyatake, H., Jain, B., and Takada, M., 2016. *Detection of stacked filament lensing between SDSS luminous red galaxies.* Monthly Notices of the Royal Astronomical Society, 457, 3:2391. doi:10.1093/mnras/stw142

Clampitt, J., Sánchez, C., Kwan, J., et al., 2017. *Galaxy-galaxy lensing in the Dark Energy Survey Science Verification data.* Monthly Notices of the Royal Astronomical Society, 465, 4:4204. doi:10.1093/mnras/stw2988

Cole, S., Lacey, C. G., Baugh, C. M., and Frenk, C. S., 2000. *Hierarchical galaxy formation.* Monthly Notices of the Royal Astronomical Society, 319, 1:168. doi:10.1046/j.1365-8711.2000.03879.x

Coles, P. and Lucchin, F., *Cosmology: The Origin and Evolution of Cosmic Structure, Second Edition* (Wiley, 2002). ISBN 9780471489093

Cooray, A. and Sheth, R., 2002. *Halo models of large scale structure.* Physics Reports, 372, 1:1. doi:10.1016/S0370-1573(02)00276-4

d'Amico, G., Gleyzes, J., Kokron, N., et al., 2020. *The cosmological analysis of the SDSS/BOSS data from the Effective Field Theory of Large-Scale Structure.* Journal of Cosmology and Astropartical Physics, 2020, 5:005. doi:10.1088/1475-7516/2020/05/005

Davis, M., Efstathiou, G., Frenk, C. S., and White, S. D. M., 1985. *The evolution of large-scale structure in a universe dominated by cold dark matter.* Astrophysical Journal, 292:371. doi:10.1086/163168

de Jong, J. T. A., Verdoes Kleijn, G. A., Boxhoorn, D. R., et al., 2015. *The first and second data releases of the Kilo-Degree Survey.* Astronomy & Astrophysics, 582:A62. doi:10.1051/0004-6361/201526601

de Jong, J. T. A., Verdoes Kleijn, G. A., Erben, T., et al., 2017. *The third data release of the Kilo-Degree Survey and associated data products.* Astronomy & Astrophysics, 604:A134. doi:10.1051/0004-6361/201730747

De Lucia, G. and Blaizot, J., 2007. *The hierarchical formation of the brightest cluster galaxies.* Monthly Notices of the Royal Astronomical Society, 375, 1:2. doi:10.1111/j.1365-2966.2006.11287.x

Dehnen, W., 2000. *A Very Fast and Momentum-conserving Tree Code.* Astrophysical Journal Letters, 536, 1:L39. doi:10.1086/312724

Dolag, K., Bartelmann, M., Perrotta, F., et al., 2004. *Numerical study of halo concentrations in dark-energy cosmologies.* Astronomy & Astrophysics, 416:853. doi:10.1051/0004-6361:20031757

Driver, S. P., Hill, D. T., Kelvin, L. S., et al., 2011. *Galaxy and Mass Assembly (GAMA): survey diagnostics and core data release.* Monthly Notices of the Royal Astronomical Society, 413:971. doi:10.1111/j.1365-2966.2010.18188.x

Driver, S. P., Norberg, P., Baldry, I. K., et al., 2009. *GAMA: towards a physical understanding of galaxy formation.* Astronomy and Geophysics, 50, 5:5.12. doi:10.1111/j.1468-4004.2009.50512.x

Dubois, Y., Pichon, C., Welker, C., et al., 2014. *Dancing in the dark: galactic properties trace spin swings along the cosmic web.* Monthly Notices of the Royal Astronomical Society, 444, 2:1453. doi:10.1093/mnras/stu1227

Dvornik, A., Hoekstra, H., Kuijken, K., et al., 2018. *Unveiling galaxy bias via the halo model, KiDS, and GAMA.* Monthly Notices of the Royal Astronomical Society, 479, 1:1240. doi:10.1093/mnras/sty1502

Dyson, F. W., Eddington, A. S., and Davidson, C., 1920. *A Determination of the Deflection of Light by the Sun's Gravitational Field, from Observations Made at the Total Eclipse of May 29, 1919.* Philosophical Transactions of the Royal Society of London Series A, 220:291. doi:10.1098/rsta.1920.0009

Edge, A., Sutherland, W., Kuijken, K., et al., 2013. *The VISTA Kilo-degree Infrared Galaxy (VIKING) Survey: Bridging the Gap between Low and High Redshift.* The Messenger, 154:32

Einstein, A., 1915. *Die Feldgleichungen der Gravitation.* Sitzungsberichte der Königlich Preußischen Akademie der Wissenschaften (Berlin), 2:844

Einstein, A., 1917. *Kosmologische Betrachtungen zur allgemeinen Relativitätstheorie.* Sitzungsberichte der Königlich Preußischen Akademie der Wissenschaften (Berlin), 1:142

Einstein, A., 1936. *Lens-Like Action of a Star by the Deviation of Light in the Gravitational Field.* Science, 84, 2188:506. doi:10.1126/science.84.2188.506

Eisenstein, D. J. and Hu, W., 1998. *Baryonic Features in the Matter Transfer Function.* Astrophysical Journal, 496, 2:605. doi:10.1086/305424

Eisenstein, D. J., Weinberg, D. H., Agol, E., et al., 2011. *SDSS-III: Massive Spectroscopic Surveys of the Distant Universe, the Milky Way, and Extra-Solar Planetary Systems.* Astronomical Journal, 142, 3:72. doi:10.1088/0004-6256/142/3/72

Eke, V. R., Cole, S., Frenk, C. S., and Navarro, J. F., 1996. *Cluster correlation functions in N-body simulations.* Monthly Notices of the Royal Astronomical Society, 281:703. doi: 10.1093/mnras/281.2.703

Epps, S. D. and Hudson, M. J., 2017. *The Weak Lensing Masses of Filaments between Luminous Red Galaxies.* Monthly Notices of the Royal Astronomical Society, 468, 3:2605. doi:10.1093/mnras/stx517

Erben, T., Schirmer, M., Dietrich, J. P., et al., 2005. *GaBoDS: The Garching-Bonn Deep Survey. IV. Methods for the image reduction of multi-chip cameras demonstrated on data from the ESO Wide-Field Imager.* Astronomische Nachrichten, 326:432. doi:10.1002/asna.200510396

Fabbian, G., Calabrese, M., and Carbone, C., 2018. *CMB weak-lensing beyond the Born approximation: a numerical approach.* Journal of Cosmology and Astropartical Physics, 2018, 2:050. doi:10.1088/1475-7516/2018/02/050

Farouki, R. and Shapiro, S. L., 1981. *Computer simulations of environmental influences on galaxy evolution in dense clusters. II - Rapid tidal encounters.* Astrophysical Journal, 243:32. doi:10.1086/158563

Farrow, D. J., Cole, S., Norberg, P., et al., 2015. *Galaxy and mass assembly (GAMA): projected galaxy clustering.* Monthly Notices of the Royal Astronomical Society, 454:2120. doi:10.1093/mnras/stv2075

Font, A. S., Bower, R. G., McCarthy, I. G., et al., 2008. *The colours of satellite galaxies in groups and clusters.* Monthly Notices of the Royal Astronomical Society, 389, 4:1619. doi: 10.1111/j.1365-2966.2008.13698.x

Fosalba, P., Gaztañaga, E., Castand er, F. J., and Manera, M., 2008. *The onion universe: all sky lightcone simulations in spherical shells.* Monthly Notices of the Royal Astronomical Society, 391, 1:435. doi:10.1111/j.1365-2966.2008.13910.x

Friedmann, A., 1922. *Über die Krümmung des Raumes.* Zeitschrift fur Physik, 10:377. doi: 10.1007/BF01332580

Gao, L. and White, S. D. M., 2007. *Assembly bias in the clustering of dark matter haloes.* Monthly Notices of the Royal Astronomical Society, 377, 1:L5. doi:10.1111/j.1745-3933.2007.00292.x

Giocoli, C., Jullo, E., Metcalf, R. B., et al., 2016. *Multi Dark Lens Simulations: weak lensing light-cones and data base presentation.* Monthly Notices of the Royal Astronomical Society, 461, 1:209. doi:10.1093/mnras/stw1336

Gladders, M. D. and Yee, H. K. C., 2005. *The Red-Sequence Cluster Survey. I. The Survey and Cluster Catalogs for Patches RCS 0926+37 and RCS 1327+29.* Astrophysical Journal Supplement, 157, 1:1. doi:10.1086/427327

Gough, B., *GNU Scientific Library Reference Manual - Third Edition* (Network Theory Ltd., 2009). ISBN 9780954612078

Gouin, C., Gavazzi, R., Pichon, C., et al., 2019. *Weak lensing in the Horizon-AGN simulation lightcone. Small-scale baryonic effects.* Astronomy & Astrophysics, 626:A72. doi:10.1051/0004-6361/201834199

Gruen, D., Friedrich, O., Krause, E., et al., 2018. *Density split statistics: Cosmological constraints from counts and lensing in cells in DES Y1 and SDSS data.* Physical Review D, 98, 2:023507. doi:10.1103/PhysRevD.98.023507

Gunn, J. E. and Gott, I., J. Richard, 1972. *On the Infall of Matter Into Clusters of Galaxies and Some Effects on Their Evolution.* Astrophysical Journal, 176:1. doi:10.1086/151605

Guo, Q., Gonzalez-Perez, V., Guo, Q., et al., 2016. *Galaxies in the EAGLE hydrodynamical simulation and in the Durham and Munich semi-analytical models.* Monthly Notices of the Royal Astronomical Society, 461, 4:3457. doi:10.1093/mnras/stw1525

Guo, Q., White, S., Boylan-Kolchin, M., et al., 2011. *From dwarf spheroidals to cD galaxies: simulating the galaxy population in a ΛCDM cosmology.* Monthly Notices of the Royal Astronomical Society, 413:101. doi:10.1111/j.1365-2966.2010.18114.x

Guth, A. H., 1981. *Inflationary universe: A possible solution to the horizon and flatness problems.* Physical Review D, 23, 2:347. doi:10.1103/PhysRevD.23.347

Hamilton, A. J. S. and Tegmark, M., 2002. *The real-space power spectrum of the PSCz survey from 0.01 to 300h* Mpc^{-1}. Monthly Notices of the Royal Astronomical Society, 330, 3:506. doi:10.1046/j.1365-8711.2002.05033.x

Harrison, E. R., 1970. *Fluctuations at the Threshold of Classical Cosmology.* Physical Review D, 1, 10:2726. doi:10.1103/PhysRevD.1.2726

Hartlap, J., Simon, P., and Schneider, P., 2007. *Why your model parameter confidences might be too optimistic. Unbiased estimation of the inverse covariance matrix.* Astronomy & Astrophysics, 464, 1:399. doi:10.1051/0004-6361:20066170

Heitmann, K., Frontiere, N., Rangel, E., et al., 2020. *The Last Journey. I. An Extreme-Scale Simulation on the Mira Supercomputer.* arXiv e-prints:arXiv:2006.01697

Henriques, B. M. B., Thomas, P. A., Oliver, S., and Roseboom, I., 2009. *Monte Carlo Markov Chain parameter estimation in semi-analytic models of galaxy formation.* Monthly Notices of the Royal Astronomical Society, 396, 1:535. doi:10.1111/j.1365-2966.2009.14730.x

Henriques, B. M. B., White, S. D. M., Thomas, P. A., et al., 2015. *Galaxy formation in the Planck cosmology - I. Matching the observed evolution of star formation rates, colours and stellar masses.* Monthly Notices of the Royal Astronomical Society, 451:2663. doi:10.1093/mnras/stv705

Heymans, C., Van Waerbeke, L., Miller, L., et al., 2012. *CFHTLenS: the Canada-France-Hawaii Telescope Lensing Survey.* Monthly Notices of the Royal Astronomical Society, 427, 1:146. doi:10.1111/j.1365-2966.2012.21952.x

Heymans, C., White, M., Heavens, A., Vale, C., and van Waerbeke, L., 2006. *Potential sources of contamination to weak lensing measurements: constraints from N-body simulations.* Monthly Notices of the Royal Astronomical Society, 371, 2:750. doi:10.1111/j.1365-2966.2006.10705.x

Hilbert, S., Barreira, A., Fabbian, G., et al., 2020. *The accuracy of weak lensing simulations.* Monthly Notices of the Royal Astronomical Society, 493, 1:305. doi:10.1093/mnras/staa281

Hilbert, S., Hartlap, J., White, S. D. M., and Schneider, P., 2009. *Ray-tracing through the Millennium Simulation: Born corrections and lens-lens coupling in cosmic shear and galaxy-galaxy lensing.* Astronomy & Astrophysics, 499:31. doi:10.1051/0004-6361/200811054

Hildebrandt, H., Köhlinger, F., van den Busch, J. L., et al., 2020. *KiDS+VIKING-450: Cosmic shear tomography with optical and infrared data.* Astronomy & Astrophysics, 633:A69. doi:10.1051/0004-6361/201834878

Hildebrandt, H., Viola, M., Heymans, C., et al., 2017. *KiDS-450: cosmological parameter constraints from tomographic weak gravitational lensing.* Monthly Notices of the Royal Astronomical Society, 465:1454. doi:10.1093/mnras/stw2805

Hockney, R. W. and Eastwood, J. W., *Computer Simulation Using Particles* (McGraw-Hill, 1981). ISBN 9780852743928

Hubble, E., 1929. *A Relation between Distance and Radial Velocity among Extra-Galactic Nebulae.* Proceedings of the National Academy of Science, 15, 3:168. doi:10.1073/pnas.15.3.168

Ivezić, Ž., Kahn, S. M., Tyson, J. A., et al., 2019. *LSST: From Science Drivers to Reference Design and Anticipated Data Products.* Astrophysical Journal, 873, 2:111. doi:10.3847/1538-4357/ab042c

Jenkins, A., Frenk, C. S., White, S. D. M., et al., 2001. *The mass function of dark matter haloes.* Monthly Notices of the Royal Astronomical Society, 321, 2:372. doi:10.1046/j.1365-8711.2001.04029.x

Joudaki, S., Hildebrandt, H., Traykova, D., et al., 2020. *KiDS+VIKING-450 and DES-Y1 combined: Cosmology with cosmic shear.* Astronomy & Astrophysics, 638:L1. doi:10.1051/0004-6361/201936154

Kaiser, N., 1984. *On the spatial correlations of Abell clusters.* Astrophysical Journal Letters, 284:L9. doi:10.1086/184341

Kaiser, N., 1992. *Weak Gravitational Lensing of Distant Galaxies.* Astrophysical Journal, 388:272. doi:10.1086/171151

Kaiser, N. and Squires, G., 1993. *Mapping the dark matter with weak gravitational lensing.* Astrophysical Journal, 404:441. doi:10.1086/172297

Kannawadi, A., Hoekstra, H., Miller, L., et al., 2019. *Towards emulating cosmic shear data: revisiting the calibration of the shear measurements for the Kilo-Degree Survey.* Astronomy & Astrophysics, 624:A92. doi:10.1051/0004-6361/201834819

Kauffmann, G., White, S. D. M., and Guiderdoni, B., 1993. *The formation and evolution of galaxies within merging dark matter haloes.* Monthly Notices of the Royal Astronomical Society, 264:201. doi:10.1093/mnras/264.1.201

Kauffmann, G., White, S. D. M., Heckman, T. M., et al., 2004. *The environmental dependence of the relations between stellar mass, structure, star formation and nuclear activity in galaxies.* Monthly Notices of the Royal Astronomical Society, 353, 3:713. doi:10.1111/j.1365-2966.2004.08117.x

Kennicutt, J., R. C., 1983. *The rate of star formation in normal disk galaxies.* Astrophysical Journal, 272:54. doi:10.1086/161261

Klypin, A. A., Trujillo-Gomez, S., and Primack, J., 2011. *Dark Matter Halos in the Standard Cosmological Model: Results from the Bolshoi Simulation.* Astrophysical Journal, 740, 2:102. doi:10.1088/0004-637X/740/2/102

Knox, L. and Millea, M., 2020. *Hubble constant hunter's guide.* Physical Review D, 101, 4:043533. doi:10.1103/PhysRevD.101.043533

Kravtsov, A. V., Berlind, A. A., Wechsler, R. H., et al., 2004. *The Dark Side of the Halo Occupation Distribution.* Astrophysical Journal, 609, 1:35. doi:10.1086/420959

Kreisch, C. D., Cyr-Racine, F.-Y., and Doré, O., 2020. *Neutrino puzzle: Anomalies, interactions, and cosmological tensions.* Physical Review D, 101, 12:123505. doi:10.1103/PhysRevD.101.123505

Kuijken, K., Heymans, C., Hildebrandt, H., et al., 2015. *Gravitational lensing analysis of the Kilo-Degree Survey.* Monthly Notices of the Royal Astronomical Society, 454:3500. doi: 10.1093/mnras/stv2140

Lacey, C. and Cole, S., 1993. *Merger rates in hierarchical models of galaxy formation.* Monthly Notices of the Royal Astronomical Society, 262, 3:627. doi:10.1093/mnras/262.3.627

Lacey, C. and Cole, S., 1994. *Merger Rates in Hierarchical Models of Galaxy Formation - Part Two - Comparison with N-Body Simulations.* Monthly Notices of the Royal Astronomical Society, 271:676. doi:10.1093/mnras/271.3.676

Lagos, C. d. P., Bayet, E., Baugh, C. M., et al., 2012. *Predictions for the CO emission of galaxies from a coupled simulation of galaxy formation and photon-dominated regions.* Monthly Notices of the Royal Astronomical Society, 426, 3:2142. doi:10.1111/j.1365-2966.2012.21905.x

Landy, S. D. and Szalay, A. S., 1993. *Bias and Variance of Angular Correlation Functions.* Astrophysical Journal, 412:64. doi:10.1086/172900

Laureijs, R., Amiaux, J., Arduini, S., et al., 2011. *Euclid Definition Study Report.* arXiv e-prints:arXiv:1110.3193

Lemaître, G., 1931. *Expansion of the universe, A homogeneous universe of constant mass and increasing radius accounting for the radial velocity of extra-galactic nebulae.* Monthly Notices of the Royal Astronomical Society, 91:483. doi:10.1093/mnras/91.5.483

Linke, L., Simon, P., Schneider, P., and Hilbert, S., 2020a. *Measuring galaxy-galaxy-galaxy-lensing with higher precision and accuracy.* Astronomy & Astrophysics, 634:A13. doi:10.1051/0004-6361/201936693

Linke, L., Simon, P., Schneider, P., et al., 2020. *KiDS+VIKING+GAMA: Testing semi-analytic models of galaxy evolution with galaxy-galaxy-galaxy lensing.* Astronomy & Astrophysics, 640:A59. doi:10.1051/0004-6361/202038355

Liske, J., Baldry, I. K., Driver, S. P., et al., 2015. *Galaxy And Mass Assembly (GAMA): end of survey report and data release 2.* Monthly Notices of the Royal Astronomical Society, 452:2087. doi:10.1093/mnras/stv1436

Mandelbaum, R., Hirata, C. M., Broderick, T., Seljak, U., and Brinkmann, J., 2006. *Ellipticity of dark matter haloes with galaxy-galaxy weak lensing.* Monthly Notices of the Royal Astronomical Society, 370:1008. doi:10.1111/j.1365-2966.2006.10539.x

Mandelbaum, R., Hirata, C. M., Seljak, U., et al., 2005. *Systematic errors in weak lensing: application to SDSS galaxy-galaxy weak lensing.* Monthly Notices of the Royal Astronomical Society, 361, 4:1287. doi:10.1111/j.1365-2966.2005.09282.x

Mao, Y.-Y., Zentner, A. R., and Wechsler, R. H., 2018. *Beyond assembly bias: exploring secondary halo biases for cluster-size haloes.* Monthly Notices of the Royal Astronomical Society, 474, 4:5143. doi:10.1093/mnras/stx3111

Maraston, C., 2005. *Evolutionary population synthesis: models, analysis of the ingredients and application to high-z galaxies.* Monthly Notices of the Royal Astronomical Society, 362, 3:799. doi:10.1111/j.1365-2966.2005.09270.x

Martin, S., 2019. *Can the halo model describe 2nd- and 3rd- order correlation functions of gravitational lensing consistently?* Ph.D. thesis, Rheinische Friedrich-Wilhelms Universität Bonn

Mathews, W. G. and Brighenti, F., 2003. *Stellar Orbits and the Interstellar Gas Temperature in Elliptical Galaxies.* Astrophysical Journal, 599, 2:992. doi:10.1086/379537

Mead, A. J., Tröster, T., Heymans, C., Van Waerbeke, L., and McCarthy, I. G., 2020. *A hydrodynamical halo model for weak-lensing cross correlations.* arXiv e-prints:arXiv:2005.00009

Mead, J. M. G., King, L. J., and McCarthy, I. G., 2010. *Probing the cosmic web: intercluster filament detection using gravitational lensing.* Monthly Notices of the Royal Astronomical Society, 401, 4:2257. doi:10.1111/j.1365-2966.2009.15840.x

Melott, A. L., Buchert, T., and Weiss, A. G., 1995. *Testing higher-order Lagrangian perturbation theory against numerical simulations. II. Hierarchical models.* Astronomy & Astrophysics, 294:345

Meszaros, P., 1974. *The behaviour of point masses in an expanding cosmological substratum.* Astronomy & Astrophysics, 37, 2:225

Miller, L., Heymans, C., Kitching, T. D., et al., 2013. *Bayesian galaxy shape measurement for weak lensing surveys - III. Application to the Canada-France-Hawaii Telescope Lensing Survey.* Monthly Notices of the Royal Astronomical Society, 429, 4:2858. doi:10.1093/mnras/sts454

Mo, H. J., Jing, Y. P., and White, S. D. M., 1997. *High-order correlations of peaks and haloes: a step towards understanding galaxy biasing.* Monthly Notices of the Royal Astronomical Society, 284, 1:189. doi:10.1093/mnras/284.1.189

Mo, H. J., van den Bosch, F., and White, S. D. M., *Galaxy Formation and Evolution* (Cambridge University Press, 2010). ISBN 9780521857932

Mukhanov, V. F. and Chibisov, G. V., 1981. *Quantum fluctuations and a nonsingular universe.* Soviet Journal of Experimental and Theoretical Physics Letters, 33:532

Navarro, J. F., Frenk, C. S., and White, S. D. M., 1996. *The Structure of Cold Dark Matter Halos.* Astrophysical Journal, 462:563. doi:10.1086/177173

Nelder, J. A. and Mead, R., 1965. *A Simplex Method for Function Minimization.* The Computer Journal, 7, 4:308. ISSN 0010-4620. doi:10.1093/comjnl/7.4.308

Peebles, P. J. E., 1970. *Structure of the Coma Cluster of Galaxies.* Astronomical Journal, 75:13. doi:10.1086/110933

Peebles, P. J. E., *The large-scale structure of the universe* (Princeton University Press, 1980). ISBN 9780691082400

Perlmutter, S., Aldering, G., Goldhaber, G., et al., 1999. *Measurements of Ω and Λ from 42 High-Redshift Supernovae.* Astrophysical Journal, 517, 2:565. doi:10.1086/307221

Planck Collaboration: Aghanim, N., Akrami, Y., Arroja, F., et al., 2019. *Planck 2018 results. I. Overview and the cosmological legacy of Planck.* Astronomy & Astrophysics. doi:10.1051/0004-6361/201833880

Potter, D., Stadel, J., and Teyssier, R., 2017. *PKDGRAV3: beyond trillion particle cosmological simulations for the next era of galaxy surveys.* Computational Astrophysics and Cosmology, 4, 1:2. doi:10.1186/s40668-017-0021-1

Poulin, V., Smith, T. L., Karwal, T., and Kamionkowski, M., 2019. *Early Dark Energy can Resolve the Hubble Tension.* Physical Review Letters, 122, 22:221301. doi:10.1103/PhysRevLett.122.221301

Press, W. H. and Schechter, P., 1974. *Formation of Galaxies and Clusters of Galaxies by Self-Similar Gravitational Condensation.* Astrophysical Journal, 187:425. doi:10.1086/152650

Reid, B. A. and White, M., 2011. *Towards an accurate model of the redshift-space clustering of haloes in the quasi-linear regime.* Monthly Notices of the Royal Astronomical Society, 417, 3:1913. doi:10.1111/j.1365-2966.2011.19379.x

Renneby, M., Henriques, B. M. B., Hilbert, S., et al., 2020. *Joint galaxy-galaxy lensing and clustering constraints on galaxy formation.* Monthly Notices of the Royal Astronomical Society. doi:10.1093/mnras/staa2675

Richard, J., Kneib, J.-P., Ebeling, H., et al., 2011. *Discovery of a possibly old galaxy at z= 6.027, multiply imaged by the massive cluster Abell 383.* Monthly Notices of the Royal Astronomical Society, 414, 1:L31. doi:10.1111/j.1745-3933.2011.01050.x

Riess, A. G., 2019. *The expansion of the Universe is faster than expected.* Nature Reviews Physics, 2, 1:10. doi:10.1038/s42254-019-0137-0

Riess, A. G., Casertano, S., Yuan, W., Macri, L. M., and Scolnic, D., 2019. *Large Magellanic Cloud Cepheid Standards Provide a 1% Foundation for the Determination of the Hubble Constant and Stronger Evidence for Physics beyond ΛCDM.* Astrophysical Journal, 876, 1:85. doi:10.3847/1538-4357/ab1422

Riess, A. G., Filippenko, A. V., Challis, P., et al., 1998. *Observational Evidence from Supernovae for an Accelerating Universe and a Cosmological Constant.* Astronomical Journal, 116, 3:1009. doi:10.1086/300499

Roberts, M. S., Hogg, D. E., Bregman, J. N., Forman, W. R., and Jones, C., 1991. *Interstellar Matter in Early-Type Galaxies. I. The Catalog.* Astrophysical Journal Supplement, 75:751. doi:10.1086/191548

Robertson, H. P., 1935. *Kinematics and World-Structure.* Astrophysical Journal, 82:284. doi:10.1086/143681

Rödinger, J., 2009. *Studying Galaxy-Galaxy Lensing and Higher-Order Galaxy-Mass Correlations Using the Halo Model.* Ph.D. thesis, Rheinische Friedrich-Wilhelms Universität Bonn

Rubin, V. C., Ford, J., W. K., and Thonnard, N., 1980. *Rotational properties of 21 SC galaxies with a large range of luminosities and radii, from NGC 4605 (R=4kpc) to UGC 2885 (R=122kpc).* Astrophysical Journal, 238:471. doi:10.1086/158003

Rycroft, C. H., 2009. *VORO++: A three-dimensional Voronoi cell library in C++.* Chaos, 19, 4:041111. doi:10.1063/1.3215722

Saghiha, H., Simon, P., Schneider, P., and Hilbert, S., 2017. *Confronting semi-analytic galaxy models with galaxy-matter correlations observed by CFHTLenS.* Astronomy & Astrophysics, 601:A98. doi:10.1051/0004-6361/201629608

Schaye, J., Crain, R. A., Bower, R. G., et al., 2015. *The EAGLE project: simulating the evolution and assembly of galaxies and their environments.* Monthly Notices of the Royal Astronomical Society, 446, 1:521. doi:10.1093/mnras/stu2058

Schirmer, M., 2013. *THELI: Convenient Reduction of Optical, Near-infrared, and Mid-infrared Imaging Data.* Astrophysical Journal Supplement, 209:21. doi:10.1088/0067-0049/209/2/21

Schmidt, K. B., Huang, K. H., Treu, T., et al., 2017. *The Grism Lens-Amplified Survey from Space (GLASS). XI. Detection of C IV in Multiple Images of the z = 6.11 Lyα Emitter behind RXC J2248.7-4431.* Astrophysical Journal, 839, 1:17. doi:10.3847/1538-4357/aa68a3

Schneider, P., *Weak gravitational lensing.* In Meylan, G., Jetzer, P., and North, P. (eds.), *Gravitational Lensing: Strong, Weak & Micro. Lecture Notes of the 33rd Saas-Fee Advanced Course* (Springer-Verlag, 2005). ISBN 9783540303107, p. 273 ff.

Schneider, P., van Waerbeke, L., Jain, B., and Kruse, G., 1998. *A new measure for cosmic shear.* Monthly Notices of the Royal Astronomical Society, 296, 4:873. doi:10.1046/j.1365-8711.1998.01422.x

Schneider, P., van Waerbeke, L., and Mellier, Y., 2002. *B-modes in cosmic shear from source redshift clustering.* Astronomy & Astrophysics, 389:729. doi:10.1051/0004-6361:20020626

Schneider, P. and Watts, P., 2005. *Galaxy-galaxy-galaxy lensing: Third-order correlations between the galaxy and mass distributions in the Universe.* Astronomy & Astrophysics, 432:783. doi:10.1051/0004-6361:20041923

Scoccimarro, R., Sheth, R. K., Hui, L., and Jain, B., 2001. *How Many Galaxies Fit in a Halo? Constraints on Galaxy Formation Efficiency from Spatial Clustering.* Astrophysical Journal, 546, 1:20. doi:10.1086/318261

Sheldon, E. S., Johnston, D. E., Frieman, J. A., et al., 2004. *The Galaxy-Mass Correlation Function Measured from Weak Lensing in the Sloan Digital Sky Survey.* Astronomical Journal, 127, 5:2544. doi:10.1086/383293

Sheth, R. K., Mo, H. J., and Tormen, G., 2001. *Ellipsoidal collapse and an improved model for the number and spatial distribution of dark matter haloes.* Monthly Notices of the Royal Astronomical Society, 323, 1:1. doi:10.1046/j.1365-8711.2001.04006.x

Sheth, R. K. and Tormen, G., 1999. *Large-scale bias and the peak background split.* Monthly Notices of the Royal Astronomical Society, 308, 1:119. doi:10.1046/j.1365-8711.1999.02692.x

Simon, P., 2005. *Time evolution of the stochastic linear bias of interacting galaxies on linear scales.* Astronomy & Astrophysics, 430:827. doi:10.1051/0004-6361:20041450

Simon, P., 2007. *How accurate is Limber's equation?* Astronomy & Astrophysics, 473, 3:711. doi:10.1051/0004-6361:20066352

Simon, P., Erben, T., Schneider, P., et al., 2013. *CFHTLenS: higher order galaxy-mass correlations probed by galaxy-galaxy- galaxy lensing.* Monthly Notices of the Royal Astronomical Society, 430:2476. doi:10.1093/mnras/stt069

Simon, P., Hetterscheidt, M., Wolf, C., et al., 2009. *Relative clustering and the joint halo occupation distribution of red sequence and blue-cloud galaxies in COMBO-17.* Monthly Notices of the Royal Astronomical Society, 398, 2:807. doi:10.1111/j.1365-2966.2009.14973.x

Simon, P. and Hilbert, S., 2018. *Scale dependence of galaxy biasing investigated by weak gravitational lensing: An assessment using semi-analytic galaxies and simulated lensing data.* Astronomy & Astrophysics, 613:A15. doi:10.1051/0004-6361/201732248

Simon, P., Saghiha, H., Hilbert, S., et al., 2019. *Comparison of the excess mass around CFHTLenS galaxy-pairs to predictions from a semi-analytic model using galaxy-galaxy-galaxy lensing.* Astronomy & Astrophysics, 622:A104. doi:10.1051/0004-6361/201732179

Simon, P., Watts, P., Schneider, P., et al., 2008. *First detection of galaxy-galaxy-galaxy lensing in RCS. A new tool for studying the matter environment of galaxy pairs.* Astronomy & Astrophysics, 479:655. doi:10.1051/0004-6361:20078197

Singh, S., Mandelbaum, R., Seljak, U., Slosar, A., and Vazquez Gonzalez, J., 2017. *Galaxy-galaxy lensing estimators and their covariance properties.* Monthly Notices of the Royal Astronomical Society, 471, 4:3827. doi:10.1093/mnras/stx1828

Sokol, J., 2017. *Hubble trouble.* Science, 355, 6329:1010. doi:10.1126/science.355.6329.1010

Spergel, D. N., Verde, L., Peiris, H. V., et al., 2003. *First-Year Wilkinson Microwave Anisotropy Probe (WMAP) Observations: Determination of Cosmological Parameters.* Astrophysical Journal Supplement, 148, 1:175. doi:10.1086/377226

Springel, V., 2005. *The cosmological simulation code GADGET-2.* Monthly Notices of the Royal Astronomical Society, 364, 4:1105. doi:10.1111/j.1365-2966.2005.09655.x

Springel, V., 2010. *E pur si muove: Galilean-invariant cosmological hydrodynamical simulations on a moving mesh.* Monthly Notices of the Royal Astronomical Society, 401, 2:791. doi:10.1111/j.1365-2966.2009.15715.x

Springel, V., Pakmor, R., Pillepich, A., et al., 2018. *First results from the IllustrisTNG simulations: matter and galaxy clustering.* Monthly Notices of the Royal Astronomical Society, 475, 1:676. doi:10.1093/mnras/stx3304

Springel, V., Wang, J., Vogelsberger, M., et al., 2008. *The Aquarius Project: the subhaloes of galactic haloes.* Monthly Notices of the Royal Astronomical Society, 391, 4:1685. doi:10.1111/j.1365-2966.2008.14066.x

Springel, V., White, S. D. M., Jenkins, A., et al., 2005. *Simulations of the formation, evolution and clustering of galaxies and quasars.* Nature, 435, 7042:629. doi:10.1038/nature03597

Stadel, J., Potter, D., Moore, B., et al., 2009. *Quantifying the heart of darkness with GHALO - a multibillion particle simulation of a galactic halo.* Monthly Notices of the Royal Astronomical Society, 398, 1:L21. doi:10.1111/j.1745-3933.2009.00699.x

Szapudi, I. and Szalay, A. S., 1998. *A New Class of Estimators for the N-Point Correlations.* Astrophysical Journal Letters, 494, 1:L41. doi:10.1086/311146

Taylor, E. N., Hopkins, A. M., Baldry, I. K., et al., 2015. *Galaxy And Mass Assembly (GAMA): deconstructing bimodality - I. Red ones and blue ones.* Monthly Notices of the Royal Astronomical Society, 446, 2:2144. doi:10.1093/mnras/stu1900

Tinker, J., Kravtsov, A. V., Klypin, A., et al., 2008. *Toward a Halo Mass Function for Precision Cosmology: The Limits of Universality.* Astrophysical Journal, 688, 2:709. doi:10.1086/591439

Tolkien, J., *The Return of the King.* The Lord of the Rings trilogy (Ballantine Books, 1955). ISBN 9780345339737

Tonry, J. L., Blakeslee, J. P., Ajhar, E. A., and Dressler, A., 2000. *The Surface Brightness Fluctuation Survey of Galaxy Distances. II. Local and Large-Scale Flows.* Astrophysical Journal, 530, 2:625. doi:10.1086/308409

Unruh, S., Schneider, P., and Hilbert, S., 2019. *Magnification bias in the shear-ratio test: a viable mitigation strategy.* Astronomy & Astrophysics, 623:A94. doi:10.1051/0004-6361/201834151

Unruh, S., Schneider, P., Hilbert, S., et al., 2020. *The importance of magnification effects in galaxy-galaxy lensing.* Astronomy & Astrophysics, 638:A96. doi:10.1051/0004-6361/201936915

van Uitert, E., Joachimi, B., Joudaki, S., et al., 2018. *KiDS+GAMA: cosmology constraints from a joint analysis of cosmic shear, galaxy-galaxy lensing, and angular clustering.* Monthly Notices of the Royal Astronomical Society, 476, 4:4662. doi:10.1093/mnras/sty551

Velliscig, M., Cacciato, M., Hoekstra, H., et al., 2017. *Galaxy-galaxy lensing in EAGLE: comparison with data from 180 deg*^{2} *of the KiDS and GAMA surveys.* Monthly Notices of the Royal Astronomical Society, 471, 3:2856. doi:10.1093/mnras/stx1789

Venemans, B. P., Verdoes Kleijn, G. A., Mwebaze, J., et al., 2015. *First discoveries of z=6 quasars with the Kilo-Degree Survey and VISTA Kilo-Degree Infrared Galaxy survey.* Monthly Notices of the Royal Astronomical Society, 453:2259. doi:10.1093/mnras/stv1774

Verde, L., Treu, T., and Riess, A. G., 2019. *Tensions between the early and late Universe.* Nature Astronomy, 3:891. doi:10.1038/s41550-019-0902-0

Vikhlinin, A., Kravtsov, A. V., Burenin, R. A., et al., 2009. *Chandra Cluster Cosmology Project III: Cosmological Parameter Constraints.* Astrophysical Journal, 692, 2:1060. doi:10.1088/0004-637X/692/2/1060

Vogelsberger, M., Genel, S., Springel, V., et al., 2014. *Introducing the Illustris Project: simulating the coevolution of dark and visible matter in the Universe.* Monthly Notices of the Royal Astronomical Society, 444:1518. doi:10.1093/mnras/stu1536

Vogelsberger, M., Marinacci, F., Torrey, P., and Puchwein, E., 2020. *Cosmological simulations of galaxy formation.* Nature Reviews Physics, 2, 1:42. doi:10.1038/s42254-019-0127-2

Walker, A. G., 1937. *On Milne's Theory of World-Structure.* Proceedings of the London Mathematical Society, 42:90. doi:10.1112/plms/s2-42.1.90

Watts, P. and Schneider, P., *Higher Order Cross-Correlation Functions from Galaxy-Galaxy-Galaxy Lensing.* In Mellier, Y. and Meylan, G. (eds.), *Gravitational Lensing Impact on Cosmology*, volume 225 of *IAU Symposium* (2005), pp. 243–248. doi:10.1017/S1743921305002048

White, M., Zheng, Z., Brown, M. J. I., Dey, A., and Jannuzi, B. T., 2007. *Evidence for Merging or Disruption of Red Galaxies from the Evolution of Their Clustering.* Astrophysical Journal Letters, 655, 2:L69. doi:10.1086/512015

White, S. D. M. and Rees, M. J., 1978. *Core condensation in heavy halos: a two-stage theory for galaxy formation and clustering.* Monthly Notices of the Royal Astronomical Society, 183:341. doi:10.1093/mnras/183.3.341

Wright, A. H., Hildebrandt, H., Kuijken, K., et al., 2019. *KiDS+VIKING-450: A new combined optical and near-infrared dataset for cosmology and astrophysics.* Astronomy & Astrophysics, 632:A34. doi:10.1051/0004-6361/201834879

Wright, A. H., Robotham, A. S. G., Bourne, N., et al., 2016. *Galaxy And Mass Assembly: accurate panchromatic photometry from optical priors using LAMBDAR.* Monthly Notices of the Royal Astronomical Society, 460, 1:765. doi:10.1093/mnras/stw832

Wright, A. H., Robotham, A. S. G., Driver, S. P., et al., 2017. *Galaxy And Mass Assembly (GAMA): the galaxy stellar mass function to z = 0.1 from the r-band selected equatorial regions.* Monthly Notices of the Royal Astronomical Society, 470, 1:283. doi:10.1093/mnras/stx1149

Xia, Q., Robertson, N., Heymans, C., et al., 2020. *A gravitational lensing detection of filamentary structures connecting luminous red galaxies.* Astronomy & Astrophysics, 633:A89. doi:10.1051/0004-6361/201936678

Zehavi, I., Blanton, M. R., Frieman, J. A., et al., 2002. *Galaxy Clustering in Early Sloan Digital Sky Survey Redshift Data.* Astrophysical Journal, 571, 1:172. doi:10.1086/339893

Zehavi, I., Zheng, Z., Weinberg, D. H., et al., 2005. *The Luminosity and Color Dependence of the Galaxy Correlation Function.* Astrophysical Journal, 630, 1:1. doi:10.1086/431891

Zehavi, I., Zheng, Z., Weinberg, D. H., et al., 2011. *Galaxy Clustering in the Completed SDSS Redshift Survey: The Dependence on Color and Luminosity.* Astrophysical Journal, 736:59. doi:10.1088/0004-637X/736/1/59

Zeldovich, Y. B., 1972. *A hypothesis, unifying the structure and the entropy of the Universe.* Monthly Notices of the Royal Astronomical Society, 160:1P. doi:10.1093/mnras/160.1.1P

Zheng, Z., Berlind, A. A., Weinberg, D. H., et al., 2005. *Theoretical Models of the Halo Occupation Distribution: Separating Central and Satellite Galaxies.* Astrophysical Journal, 633, 2:791. doi:10.1086/466510

Zheng, Z., Coil, A. L., and Zehavi, I., 2007. *Galaxy Evolution from Halo Occupation Distribution Modeling of DEEP2 and SDSS Galaxy Clustering.* Astrophysical Journal, 667, 2:760. doi:10.1086/521074

Zwicky, F., 1933. *Die Rotverschiebung von extragalaktischen Nebeln.* Helvetica Physica Acta, 6:110

Zwicky, F., 1937a. *Nebulae as Gravitational Lenses.* Physical Review, 51, 4:290. doi:10.1103/PhysRev.51.290

Zwicky, F., 1937b. *On the Probability of Detecting Nebulae Which Act as Gravitational Lenses.* Physical Review, 51, 8:679. doi:10.1103/PhysRev.51.679

Appendix to Chapter 3

A

A.1 Calculation of aperture statistics for mock data

Averages in the halo model are given by

$$
\begin{aligned}
\langle f \rangle = \int \mathrm{d}m_1 \dots \mathrm{d}m_H \; & \underbrace{P_\mathrm{m}(m_1, \dots, m_H)}_{\substack{\text{Probability that haloes} \\ \text{have masses } m_1,\dots,m_2}} \\
\times \int \mathrm{d}^3x_1 \dots \mathrm{d}^3x_H \quad & \underbrace{P_\mathrm{h}(\boldsymbol{x}_1, \dots, \boldsymbol{x}_H \mid m_1, \dots, m_H)}_{\text{Probability that halo centres are at } \boldsymbol{x}_1,\dots,\boldsymbol{x}_H} \\
\times \int \mathrm{d}^3\Delta\boldsymbol{x}_{11} \cdots \int \mathrm{d}^3\Delta\boldsymbol{x}_{HN_\mathrm{gal}} & \\
\underbrace{P_\mathrm{gal}(\Delta\boldsymbol{x}_{11}, \dots, \Delta\boldsymbol{x}_{HN_\mathrm{gal}} \mid \boldsymbol{x}_1, \dots, \boldsymbol{x}_H, m_1, \dots, m_H)}_{\substack{\text{Probability that galaxies are at } \Delta\boldsymbol{x}_{11},\dots,\Delta\boldsymbol{x}_{HN_\mathrm{gal}} \\ \text{if the halos are at } \boldsymbol{\vartheta}_1,\dots,\boldsymbol{\vartheta}_H}} & \; f \; .
\end{aligned}
\tag{A.1}
$$

Using assumption B in Sect. 3.3.2, we can reduce this integration to two spatial dimensions and use the projected halo centres $\boldsymbol{\vartheta}_i$ and the projected separation $\Delta\boldsymbol{\vartheta}_{ij}$ of the jth galaxy to the ith halo centre instead of $\boldsymbol{x}_i$ and $\Delta\boldsymbol{x}_{ij}$. Furthermore, due to assumption C, the mass integrals are trivial. Assumption D leads to

$$
\begin{aligned}
& P_\mathrm{gal}(\Delta\vartheta_{11}, \dots, \Delta\vartheta_{HN_\mathrm{gal}} \mid \boldsymbol{\vartheta}_1, \dots, \boldsymbol{\vartheta}_H, m_1, \dots, m_H) \\
& = u(\Delta\vartheta_{11}) \dots u(\Delta\vartheta_{HN_\mathrm{gal}}) \; .
\end{aligned}
\tag{A.2}
$$

Assumption E means that

$$
P_\mathrm{h}(\boldsymbol{\vartheta}_1, \dots, \boldsymbol{\vartheta}_H) = \begin{cases} A^{-H} & \text{for } (\boldsymbol{\vartheta}_1, \dots, \boldsymbol{\vartheta}_H) \in A \\ 0 & \text{else} \end{cases} \; , \tag{A.3}
$$

so that the average of a quantity is given by

$$\begin{aligned}\langle f\rangle = A^{-H} &\int_A \mathrm{d}^2\vartheta_1 \dots \mathrm{d}^2\vartheta_H \\ &\times \int \mathrm{d}^2\Delta\vartheta_{11} \dots \mathrm{d}^2\Delta\vartheta_{HN_{\mathrm{gal}}}\; u_1(\Delta\vartheta_{11}) \dots u_H(\Delta\vartheta_{HN_{\mathrm{gal}}})\, f\ .\end{aligned} \tag{A.4}$$

Consequently, the correlation function $\langle N(\boldsymbol{\theta}_1)\, N(\boldsymbol{\theta}_2)\, \kappa(\boldsymbol{\theta}_3)\rangle$ of the galaxy number density $N(\boldsymbol{\theta})$ and the projected matter density κ is

$$\begin{aligned}&\langle N(\boldsymbol{\theta}_1)\, N(\boldsymbol{\theta}_2)\, \kappa(\boldsymbol{\theta}_3)\rangle \\ &= A^{-H} \int_A \mathrm{d}^2\vartheta_1 \dots \mathrm{d}^2\vartheta_H \\ &\quad\times \int \mathrm{d}^2\Delta\vartheta_{11} \dots \mathrm{d}^2\Delta\vartheta_{HN_{\mathrm{gal}}}\; u_1(\Delta\vartheta_{11}) \dots u_H(\Delta\vartheta_{HN_{\mathrm{gal}}}) \\ &\quad\times N(\boldsymbol{\theta}_1)\, N(\boldsymbol{\theta}_2)\, \kappa(\boldsymbol{\theta}_3)\ .\end{aligned} \tag{A.5}$$

The matter density κ is the sum of the convergence profiles of all halos,

$$\kappa(\boldsymbol{\theta}) = K \sum_{i=1}^{H} u\left(|\boldsymbol{\theta} - \boldsymbol{\vartheta}_i|\right)\ . \tag{A.6}$$

We treat galaxies as discrete objects, therefore their number density is

$$N(\boldsymbol{\theta}) = \sum_{i=1}^{H} \sum_{j=1}^{N_{\mathrm{gal}}} \delta_{\mathrm{D}}(\boldsymbol{\theta} - \boldsymbol{\vartheta}_i - \Delta\boldsymbol{\vartheta}_{ij})\ . \tag{A.7}$$

Inserting Eq. (A.6) and Eq. (A.7) into Eq. (A.5) leads to

$$\begin{aligned}&\langle N(\boldsymbol{\theta}_1)\, N(\boldsymbol{\theta}_2)\, \kappa(\boldsymbol{\theta}_3)\rangle \\ &= A^{-H}\, K \int_A \mathrm{d}^2\vartheta_1 \dots \mathrm{d}^2\vartheta_H \\ &\quad\times \int \mathrm{d}^2\Delta\vartheta_{11} \dots \mathrm{d}^2\Delta\vartheta_{HN_{\mathrm{gal}}}\; u_1(\Delta\vartheta_{11}) \dots u_H(\Delta\vartheta_{HN_{\mathrm{gal}}}) \\ &\quad\times \sum_{i=1}^{H} \sum_{j=1}^{H} \sum_{k=1}^{H} u(|\boldsymbol{\theta}_1 - \boldsymbol{\vartheta}_i|) \sum_{l=1}^{N_{\mathrm{gal}}} \delta_{\mathrm{D}}(\boldsymbol{\theta}_2 - \boldsymbol{\vartheta}_j - \Delta\boldsymbol{\vartheta}_{jl}) \\ &\quad\times \sum_{m=1}^{N_{\mathrm{gal}}} \delta_{\mathrm{D}}(\boldsymbol{\theta}_3 - \boldsymbol{\vartheta}_k - \Delta\boldsymbol{\vartheta}_{km})\,.\end{aligned} \tag{A.8}$$

The delta ‘functions’ reduce the integrals, therefore the expression simplifies to

$$
\begin{aligned}
&\langle N(\boldsymbol{\theta}_1)\, N(\boldsymbol{\theta}_2)\, \kappa(\boldsymbol{\theta}_3)\rangle \\
&= A^{-H}\, K \int_A \mathrm{d}^2\vartheta_1 \dots \mathrm{d}^2\vartheta_H \qquad (\mathrm{A}.9)\\
&\quad \sum_{i=1}^{H} \sum_{j=1}^{H} \sum_{k=1}^{H} \sum_{l=1}^{N_\mathrm{gal}} \sum_{m=1}^{N_\mathrm{gal}} u(|\boldsymbol{\theta}_1 - \boldsymbol{\vartheta}_i|)\, u(|\boldsymbol{\theta}_2 - \boldsymbol{\vartheta}_j|)\, u(|\boldsymbol{\theta}_3 - \boldsymbol{\vartheta}_k|) \\
&= A^{-H}\, K\, N_\mathrm{gal}^2 \int_A \mathrm{d}^2\vartheta_1 \dots \mathrm{d}^2\vartheta_H \qquad (\mathrm{A}.10)\\
&\quad \sum_{i=1}^{H} \sum_{j=1}^{H} \sum_{k=1}^{H} u(|\boldsymbol{\theta}_1 - \boldsymbol{\vartheta}_i|)\, u(|\boldsymbol{\theta}_2 - \boldsymbol{\vartheta}_j|)\, u(|\boldsymbol{\theta}_3 - \boldsymbol{\vartheta}_k|).
\end{aligned}
$$

We can split this triple sum into a one-halo term with $i = j = k$, three two-halo terms with $i = j \neq k$, $i = k \neq k$ and $j = k \neq i$, and a three-halo term with $i \neq j \neq k$. When we use $\int_A \mathrm{d}^2\vartheta = A$ and $\int \mathrm{d}^2\vartheta\, u(\vartheta) = 1$, this leads to

$$
\begin{aligned}
&\langle N(\boldsymbol{\theta}_1)\, N(\boldsymbol{\theta}_2)\, \kappa(\boldsymbol{\theta}_3)\rangle \\
&= A^{-H}\, K\, N_\mathrm{gal}^2 \sum_{i=1}^{H} A^{H-1} \qquad (\mathrm{A}.11)\\
&\quad \times \int \mathrm{d}^2\vartheta\;\, u\,(|\boldsymbol{\theta}_1 - \boldsymbol{\vartheta}|)\;\, u\,(|\boldsymbol{\theta}_2 - \boldsymbol{\vartheta}|)\;\, u\,(|\boldsymbol{\theta}_3 - \boldsymbol{\vartheta}|) \\
&\quad + A^{-H}\, K\, N_\mathrm{gal}^2 \sum_{i=1}^{H} \sum_{j \neq i} A^{H-2} \int \mathrm{d}^2\vartheta\;\, u\,|\boldsymbol{\theta}_1 - \boldsymbol{\vartheta}|)\;\, u\,(|\boldsymbol{\theta}_3 - \boldsymbol{\vartheta}|) \\
&\quad + A^{-H}\, K\, N_\mathrm{gal}^2 \sum_{i=1}^{H} \sum_{j \neq i} A^{H-2} \int \mathrm{d}^2\vartheta\;\, u\,|\boldsymbol{\theta}_1 - \boldsymbol{\vartheta}|)\;\, u\,(|\boldsymbol{\theta}_2 - \boldsymbol{\vartheta}|) \\
&\quad + A^{-H}\, K\, N_\mathrm{gal}^2 \sum_{i=1}^{H} \sum_{j \neq i} A^{H-2} \int \mathrm{d}^2\vartheta\;\, u\,|\boldsymbol{\theta}_2 - \boldsymbol{\vartheta}|)\;\, u\,(|\boldsymbol{\theta}_3 - \boldsymbol{\vartheta}|) \\
&\quad + A^{-H}\, K\, N_\mathrm{gal}^2 \sum_{i=1}^{H} \sum_{j \neq i} \sum_{k \neq i, k \neq j} A^{H-3}
\end{aligned}
$$

$$
\begin{aligned}
&= \frac{H\,K\,N_{\mathrm{gal}}^2}{A} \int \mathrm{d}^2\vartheta \;\; u\left(|\boldsymbol{\vartheta}_1 - \boldsymbol{\vartheta}|\right)\, u\left(|\boldsymbol{\vartheta}_2 - \boldsymbol{\vartheta}|\right)\, u\left(|\boldsymbol{\vartheta}_3 - \boldsymbol{\vartheta}|\right) \qquad \text{(A.12)}\\
&+ \frac{H\,(H-1)\,K\,N_{\mathrm{gal}}^2}{A^2} \int \mathrm{d}^2\vartheta \;\; u_i\, |\boldsymbol{\vartheta}_1 - \boldsymbol{\vartheta}|)\; u_i\left(|\boldsymbol{\vartheta}_3 - \boldsymbol{\vartheta}|\right)\\
&+ \frac{H\,(H-1)\,K\,N_{\mathrm{gal}}^2}{A^2} \int \mathrm{d}^2\vartheta \;\; u\left(|\boldsymbol{\vartheta}_1 - \boldsymbol{\vartheta}|\right)\, u\left(|\boldsymbol{\vartheta}_2 - \boldsymbol{\vartheta}|\right)\\
&+ \frac{H\,(H-1)\,K\,N_{\mathrm{gal}}^2}{A^2} \int \mathrm{d}^2\vartheta \;\; u\left(|\boldsymbol{\vartheta}_2 - \boldsymbol{\vartheta}|\right)\, u\left(|\boldsymbol{\vartheta}_3 - \boldsymbol{\vartheta}|\right)\\
&+ \frac{H\,(H-1)\,(H-2)\,K\,N_{\mathrm{gal}}^2}{A^3}\;.
\end{aligned}
$$

From this, we can infer $\langle \mathcal{N}\mathcal{N}\mathcal{M}\rangle$ with Eq. (2.138). Because the filter function U_θ is compensated, the integrals over constant terms vanish and only the first term in the sum remains. Therefore, with he exponential filter function from Eq. (2.142) and $\overline{N} = H\,N_{\mathrm{gal}}/A$, Eq. (2.138) leads to

$$
\begin{aligned}
&\langle \mathcal{N}\mathcal{N}\mathcal{M}\rangle\,(\theta_1, \theta_2, \theta_3)\\
&= \frac{A\,K}{H(2\pi)^3} \int_0^\infty \mathrm{d}^2\vartheta \prod_{i=1}^{3} \frac{1}{\theta_i^2} \qquad \text{(A.13)}\\
&\times \int \mathrm{d}^2\vartheta_i\, u\left(|\boldsymbol{\vartheta}_i - \boldsymbol{\vartheta}|\right) \left(1 - \frac{\vartheta_i^2}{2\theta_i^2}\right) \exp\left(-\frac{\vartheta_i^2}{2\theta_i^2}\right)\\
&= \frac{A\,K}{H(2\pi)^2} \int_0^\infty \mathrm{d}^2\vartheta \prod_{i=1}^{3} \frac{1}{\theta_i^2} \int_0^{2\pi} \mathrm{d}\phi_i \int_0^\infty \mathrm{d}y_i \;\; y_i\, u(y_i) \qquad \text{(A.14)}\\
&\times \exp\left(-\frac{y_i^2 + \vartheta^2}{2\theta_i^2}\right) \left(1 - \frac{y_i^2 + \vartheta^2}{2\theta_i^2} - \frac{y_i\,\vartheta\,\cos(\phi_i)}{\theta_i^2}\right)\;.
\end{aligned}
$$

We can now use that

$$
\int_0^{2\pi} \mathrm{d}x \;\; \cos(x)\;\exp(-a\;\cos(x)) = -2\pi\, I_1(a)\,, \qquad \text{(A.15)}
$$

$$
\int_0^{2\pi} \mathrm{d}x \;\; \exp(-a\;\cos(x)) = 2\pi\, I_0(a)\;, \qquad \text{(A.16)}
$$

with the modified Bessel functions of the first kind I_n. We also introduce the scaled Bessel functions $f_n(x) = I_n(x)\exp(-x)$, so that the aperture statistics are finally

$$
\begin{aligned}
&\langle \mathcal{N}\mathcal{N}\mathcal{M}\rangle\,(\theta_1, \theta_2, \theta_3) \qquad \text{(A.17)}\\
&= \frac{2\pi\,A\,K}{H} \int_0^\infty \mathrm{d}\vartheta \;\; \vartheta \prod_{i=1}^{3} \int_0^\infty \mathrm{d}y_i \;\; \frac{y_i\,u(y_i)}{\theta_i^2}\; \exp\left[-\frac{(y_i - \vartheta)^2}{2\theta_i^2}\right]\\
&\times \left[\left(1 - \frac{y_i^2 + \vartheta^2}{2\theta_i^2}\right) f_0\left(\frac{y_i\,\vartheta}{\theta_i^2}\right) + \frac{y_i\vartheta}{\theta_i^2} f_1\left(\frac{y_i\,\vartheta}{\theta_i^2}\right)\right]\;.
\end{aligned}
$$

A.2 Computational implementation with graphics processing units

Our estimates of $\tilde{\mathcal{G}}$ are computed by calculating the sums in Eqs. (2.126), (3.4) and (3.20) brute-force on a GPU. Our algorithm (see Algorithm 1) for the estimation of $\tilde{\mathcal{G}}$ works similar to the procedures proposed by Bard et al. (2013) for the calculation of the galaxy two-point correlation and by Cárdenas-Montes et al. (2014) for the calculation of the galaxy two- and three-point function and the shear-shear correlation. It can be used for calculating the correlation between lenses from the same and different samples.

Algorithm 1 Algorithm for computing $\tilde{\mathcal{G}}$

```
Read in lens and source galaxy positions and source ellipticities into main memory (RAM)
Copy galaxy positions and ellipticities from RAM to the GPU
Initialize container for $\tilde{\mathcal{G}}$ with $N_\mathrm{bins}$ bins on RAM
Initialize container for $\tilde{\mathcal{G}}$ with $N_\mathrm{bins}$ bins on GPU
Initialize $N_\mathrm{th}$ threads on GPU
In each thread $i$ do
    for all sources $j$ with $j \in [i, i + N_\mathrm{th}, i + 2N_\mathrm{th}, \dots, N_s]$ do
        for all lenses do
            for all lenses do
                Get index of $\tilde{\mathcal{G}}$ bin for this galaxy triplet
                Add contribution of this triplet to $\tilde{\mathcal{G}}$ on GPU
            end for
        end for
    end for
end thread
Copy $\tilde{\mathcal{G}}$ from GPU to RAM
Write $\tilde{\mathcal{G}}$ to file
```

This algorithm is implemented in CUDA 10 using double floating-point precision. For the calculation, we used an NVIDIA RTX 2080 Ti GPU, which has CUDA capability 7.5 and 4352 cores. Data were read from and written to ASCII files on an SSD hard drive, enabling fast data transfer.

Appendix to Chapter 4

B

B.1 Results for aperture statistics in angular units

For completeness, we show here our results for the angular aperture statistics $\langle \mathcal{N}\mathcal{N}\mathcal{M} \rangle$, for colour-selected lens samples (Fig. B.1) and stellar-mass-selected lens samples (Fig. B.2). The $\langle \mathcal{N}\mathcal{N}\mathcal{M} \rangle$ exhibit similar trends to the $\langle \mathcal{N}\mathcal{N}\mathcal{M} \rangle_{\text{phys}}$ (see Sect 4.4). In particular, $\langle \mathcal{N}\mathcal{N}\mathcal{M} \rangle$ also increases with the lenses stellar masses and is larger for red-red than for red-blue or blue-blue lens galaxies. Furthermore, the predictions by the H15 SAM agrees well with the observed $\langle \mathcal{N}\mathcal{N}\mathcal{M} \rangle$, while the L12 SAM expects too large aperture statistics, especially for low stellar-mass galaxies.

The agreement of the H15 SAM and the discrepancy of the L12 SAM with the observations is supported by the χ^2_{redu} of the SAMs predictions for $\langle \mathcal{N}\mathcal{N}\mathcal{M} \rangle$, presented in Table B.1. The H15 SAM disagrees with the observations only for the correlation of m1 and m4 galaxies at the 95% CL, while the L12 SAM is in tension with the observation for all samples.

Note, that while the measurements of $\langle \mathcal{N}\mathcal{N}\mathcal{M} \rangle$ do not depend on the choice of cosmology, they change with the lens redshift distribution. Comparing $\langle \mathcal{N}\mathcal{N}\mathcal{M} \rangle$ measured in different observational surveys requires, therefore, careful consideration of the survey's selection functions.

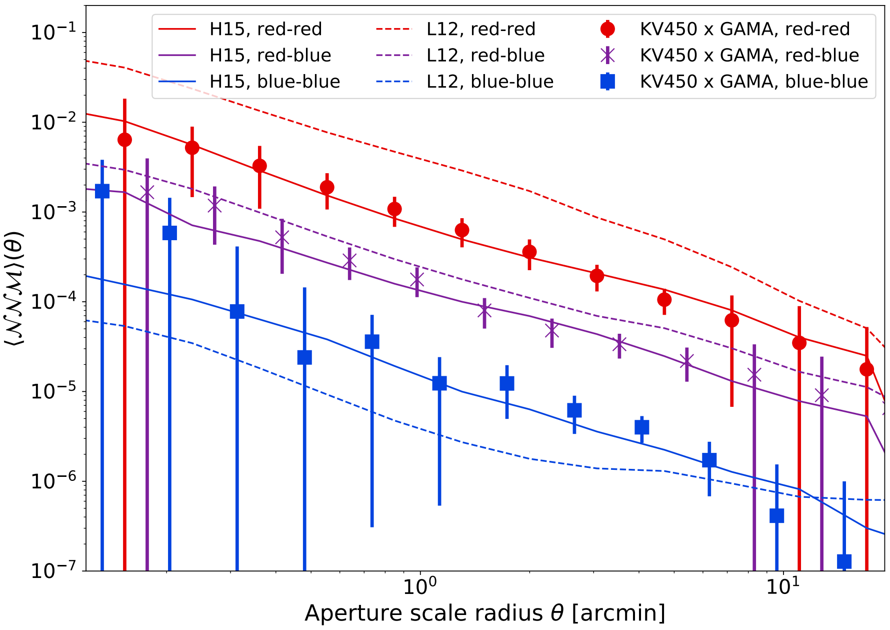

Figure B.1: $\langle\mathcal{NNM}\rangle$ for colour-selected lens samples of the H15 galaxies (solid lines), L12 galaxies (dashed lines) and KV450 × GAMA (points). The signal is shown for red-red lens pairs (red lines and filled circles), red-blue lens pairs (purple lines and crosses), and blue-blue lens pairs (blue lines and squares). Error bars on the observational measurements are the standard deviation from jackknifing.

Table B.1: χ^2_{redu} of $\langle\mathcal{NNM}\rangle$ for H15 and L12 SAMs. Bold values indicate a tension at the 95% CL.

lens pairs	χ^2_{redu} **for H15**	χ^2_{redu} **for L12**
red – red	1.33	**32.4**
red – blue	0.39	**1.92**
blue – blue	0.85	**2.31**
m1 – m1	0.95	**27.0**
m1 – m2	0.81	**28.9**
m1 – m3	1.27	**50.3**
m1 – m4	**3.69**	**22.13**
m1 – m5	1.18	**5.29**
m2 – m2	1.29	**10.28**
m2 – m3	0.74	**17.13**
m2 – m4	0.45	**7.90**
m2 – m5	1.37	**21.66**
m3 – m3	0.40	**60.61**
m3 – m4	0.56	**18.57**
m3 – m5	0.90	**27.14**
m4 – m4	0.66	**3.15**
m4 – m5	1.36	**11.43**

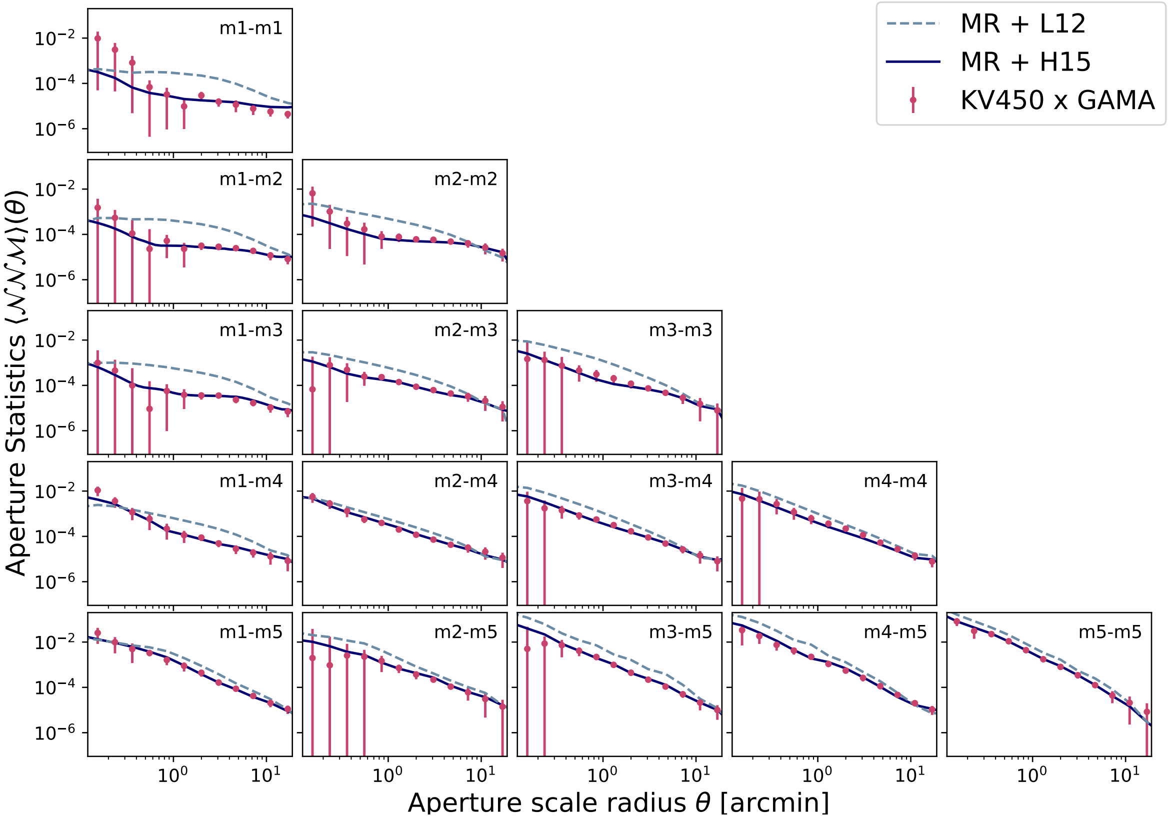

Figure B.2: Angular aperture statistics for stellar mass-selected lens samples in the MR with the H15 SAM (solid blue lines), the L12 SAM (dashed grey lines), and in GAMA with KV450 sources (pink points), using the mass bins defined in Table 4.1. Plots on the diagonal show the signal for unmixed lens pairs, while the other plots show the signal for mixed lens pairs. Error bars are the standard deviation from jackknife resampling.

C

Appendix to Chapter 5

C.1 Calculation of galaxy-galaxy-matter bispectrum for galaxies from the same population

Averages in the halo model are calculated by averaging over the probability distributions of the halos masses, positions, galaxy numbers and galaxy positions. Since we distinguish between central and satellite galaxies, separate averages are needed for these two galaxy types. So, the average of an arbitrary quantity f is

$$\begin{aligned}\langle f \rangle = \int \mathrm{d}m_1 \dots \mathrm{d}m_H \; & \underbrace{P_\mathrm{m}(m_1, \dots, m_H)}_{\substack{\text{Probability that haloes}\\ \text{have masses } m_1,\dots,m_2}} \\ & \times \int \mathrm{d}N_{\mathrm{cen},1} \dots \mathrm{d}N_{\mathrm{cen},H} \int \mathrm{d}N_{\mathrm{sat},1} \dots \mathrm{d}N_{\mathrm{sat},H} \\ & \times \underbrace{P_N(N_{\mathrm{cen},1}\, N_{\mathrm{sat},1} | m_1) \dots P_N(N_{\mathrm{cen},H}\, N_{\mathrm{sat},H} | m_H)}_{\text{Probability that halo } i \text{ has } N_{\mathrm{cen},i} \text{ centrals and } N_{\mathrm{sat},i} \text{ satellites}} \\ & \times \int \mathrm{d}^3 x_1 \dots \mathrm{d}^3 x_H \quad \underbrace{P_\mathrm{c}(\boldsymbol{x}_1, \dots, \boldsymbol{x}_H \mid m_1, \dots, m_H)}_{\text{Probability that halo centres are at } \boldsymbol{x}_1,\dots,\boldsymbol{x}_H} \\ & \times \int \mathrm{d}^3 \Delta \boldsymbol{x}_{11} \cdots \int \mathrm{d}^3 \Delta \boldsymbol{x}_{HN_{\mathrm{sat},H}} \; \underbrace{P_\mathrm{gal}(\Delta \boldsymbol{x}_{11}, \dots, \Delta \boldsymbol{x}_{HN_{\mathrm{sat},H}} \mid m_1, \dots, m_H)}_{\text{Probability that satellites are at } \Delta\boldsymbol{x}_{11},\dots,\Delta\boldsymbol{x}_{HN_{\mathrm{sat},H}}} \; f \, .\end{aligned} \tag{C.1}$$

The probability P_m is a product of the HMF,

$$P_\mathrm{m}(m_1 \dots m_H) = \bar{n}_\mathrm{H}^{-H} \, n(m_1) \dots n(m_H) \, , \tag{C.2}$$

where $\bar{n}_\mathrm{H} = H/V$ is the halo number density. The probability P_gal is a product of the spatial distributions of satellites in each halo,

$$P_\mathrm{gal}(\Delta \boldsymbol{x}_{11}, \dots, \Delta \boldsymbol{x}_{HN_{\mathrm{sat},H}} | m_1, \dots, m_H) = u_\mathrm{g}(\boldsymbol{x}_{11} | m_1) \; \dots \; u_\mathrm{g}(\Delta \boldsymbol{x}_{HN_{\mathrm{sat},H}} | m_H) \, . \tag{C.3}$$

Using Eqs (5.12), (5.2.2), and (5.15), the bispectrum $B_{\mathrm{gg}\delta}$ is given by

$$\begin{aligned}
&(2\pi)^3\,\delta_{\mathrm{D}}(\boldsymbol{k}_1+\boldsymbol{k}_2+\boldsymbol{k}_3)\,B_{\mathrm{gg}\delta}(\boldsymbol{k}_1,\boldsymbol{k}_2,\boldsymbol{k}_3,t)\\
&=\frac{1}{\bar{n}_{\mathrm{H}}^{H}\,\bar{\rho}\,\bar{n}^2}\int \mathrm{d}m_1\ldots\mathrm{d}m_H\;\;n(m_1)\;\ldots\;n(m_H) \qquad\qquad (\mathrm{C.4})\\
&\quad\times\int \mathrm{d}N_{\mathrm{cen},1}\ldots\mathrm{d}N_{\mathrm{cen},H}\int \mathrm{d}N_{\mathrm{sat},1}\ldots\mathrm{d}N_{\mathrm{sat},H}\,P_N(N_{\mathrm{cen},1}\,N_{\mathrm{sat},1}|m_1)\ldots P_N(N_{\mathrm{cen},H}\,N_{\mathrm{sat},H}|m_H)\\
&\quad\times\int \mathrm{d}^3x_1\ldots\mathrm{d}^3x_H\;\;P_{\mathrm{c}}(\boldsymbol{x}_1,\ldots,\boldsymbol{x}_H\mid m_1,\ldots,m_H)\\
&\quad\times\int \mathrm{d}^3\Delta\boldsymbol{x}_{11}\ldots\mathrm{d}^3\Delta\boldsymbol{x}_{HN_{\mathrm{sat},H}}\;\;u_{\mathrm{g}}(\Delta\boldsymbol{x}_{11}|m_1)\;\ldots\;u_{\mathrm{g}}(\Delta\boldsymbol{x}_{HN_{\mathrm{sat},H}}|m_H)\\
&\quad\times\sum_{i=0}^{H}\sum_{j=0}^{H}\sum_{k=0}^{H}\;m_k\,\hat{u}(\boldsymbol{k}_3|m_k)\\
&\qquad\times\left[\exp(-\mathrm{i}\,\boldsymbol{k}_1\cdot\boldsymbol{x}_i)+\sum_{l=1}^{N_{\mathrm{sat},i}}\exp(-\mathrm{i}\,\boldsymbol{k}_1\cdot\boldsymbol{x}_i-\mathrm{i}\,\boldsymbol{k}_1\cdot\Delta\boldsymbol{x}_{il})\right]\\
&\qquad\times\left[\exp\big(-\mathrm{i}\,\boldsymbol{k}_2\cdot\boldsymbol{x}_j\big)+\sum_{m=1}^{N_{\mathrm{sat},j}}\exp\big(-\mathrm{i}\,\boldsymbol{k}_2\cdot\boldsymbol{x}_j-\mathrm{i}\,\boldsymbol{k}_2\cdot\Delta\boldsymbol{x}_{jm}\big)\right]\;.
\end{aligned}$$

We split up the triple sum over i, j and k into three separate terms: the 1-halo term $B_{\mathrm{gg}\delta}^{1-\mathrm{h}}$ with $i=j=k$, the 2-halo term $B_{\mathrm{gg}\delta}^{2-\mathrm{h}}$ with $i=j\neq k, i=k\neq j$, and $j=k\neq i$, and the 3-halo term $B_{\mathrm{gg}\delta}^{3-\mathrm{h}}$ with $i\neq j\neq k$.

The 1-halo term is given by

$$\begin{aligned}
&(2\pi)^3\,\delta_{\mathrm{D}}(\boldsymbol{k}_1+\boldsymbol{k}_2+\boldsymbol{k}_3)\,B_{\mathrm{gg}\delta}^{1-\mathrm{h}}(\boldsymbol{k}_1,\boldsymbol{k}_2,\boldsymbol{k}_3,t)\\
&=\frac{1}{\bar{n}_{\mathrm{H}}\,\bar{\rho}\,\bar{n}^2}\sum_{i=1}^{H}\int \mathrm{d}m_i\;\;n(m_i)\int \mathrm{d}N_{\mathrm{cen},i}\int \mathrm{d}N_{\mathrm{sat},i}\;\;P_N(N_{\mathrm{cen},i},N_{\mathrm{sat},i}|m_i)\,m_i\,\hat{u}(\boldsymbol{k}_3|m_i) \qquad (\mathrm{C.5})\\
&\quad\times\int \mathrm{d}^3x_1\ldots\mathrm{d}^3x_H\;\;P_{\mathrm{c}}(\boldsymbol{x}_1,\ldots,\boldsymbol{x}_H\mid m_1,\ldots,m_H)\;\exp\big[-\mathrm{i}\,(\boldsymbol{k}_1+\boldsymbol{k}_2+\boldsymbol{k}_3)\cdot\boldsymbol{x}_i\big]\\
&\quad\times\Big\{N_{\mathrm{cen},i}(N_{\mathrm{cen},i}-1)+N_{\mathrm{cen},i}\,N_{\mathrm{sat},i}\big[\hat{u}_{\mathrm{g}}(\boldsymbol{k}_1|m_i)+\hat{u}_{\mathrm{g}}(\boldsymbol{k}_2|m_i)\big]\\
&\qquad+N_{\mathrm{sat},i}(N_{\mathrm{sat},i}-1)\,\hat{u}_{\mathrm{g}}(\boldsymbol{k}_1|m_i)\,\hat{u}_{\mathrm{g}}(\boldsymbol{k}_2|m_i)\Big\} \qquad (\mathrm{C.6})\\
&=(2\pi)^3\,\delta_{\mathrm{D}}(\boldsymbol{k}_1+\boldsymbol{k}_2+\boldsymbol{k}_3)\,\frac{1}{\bar{\rho}\,\bar{n}^2}\int \mathrm{d}m\;\;n(m)\,m\,\hat{u}(\boldsymbol{k}_3|m) \qquad (\mathrm{C.7})\\
&\quad\times\Big\{\big\langle N_{\mathrm{cen}}(N_{\mathrm{cen}}-1)|m\big\rangle+\big\langle N_{\mathrm{cen}}\,N_{\mathrm{sat}}\big\rangle\,\big[\hat{u}_{\mathrm{g}}(\boldsymbol{k}_1|m)+\hat{u}_{\mathrm{g}}(\boldsymbol{k}_2|m)\big]\\
&\qquad+\big\langle N_{\mathrm{sat}}(N_{\mathrm{sat}}-1)|m\big\rangle\;\hat{u}_{\mathrm{g}}(\boldsymbol{k}_1|m)\,\hat{u}_{\mathrm{g}}(\boldsymbol{k}_2|m)\Big\}\;, \qquad (\mathrm{C.8})
\end{aligned}$$

where we used that

$$
\begin{aligned}
&\int_V \mathrm{d}^3x_1 \,\dots\, \mathrm{d}^3x_H \;\; P_\mathrm{c}(\boldsymbol{x}_1,\dots,\boldsymbol{x}_H \mid m_1,\dots,m_H)\; \exp\big[-\mathrm{i}\,(\boldsymbol{k}_1+\boldsymbol{k}_2+\boldsymbol{k}_3)\cdot\boldsymbol{x}_i\big] \\
&= \frac{V^{H-1}}{V^H}\int_V \mathrm{d}^3x_i\;\frac{1}{V}\;\exp\big[-\mathrm{i}\,(\boldsymbol{k}_1+\boldsymbol{k}_2+\boldsymbol{k}_3)\cdot\boldsymbol{x}_i\big] && \text{(C.9)}\\
&= \frac{1}{V}\,(2\pi)^3\,\delta_\mathrm{D}(\boldsymbol{k}_1+\boldsymbol{k}_2+\boldsymbol{k}_3)\;. && \text{(C.10)}
\end{aligned}
$$

The 2-halo term is given by

$$
\begin{aligned}
&(2\pi)^3\,\delta_\mathrm{D}(\boldsymbol{k}_1+\boldsymbol{k}_2+\boldsymbol{k}_3)\,B^{2-\mathrm{h}}_{\mathrm{gg}\delta}(\boldsymbol{k}_1,\boldsymbol{k}_2,\boldsymbol{k}_3,t)\\
&= \frac{1}{\bar{n}_\mathrm{H}^2\,\bar{\rho}\,\bar{n}^2}\sum_{i=1}^{H}\sum_{j\neq i}\int \mathrm{d}m_i\int \mathrm{d}m_j\;\; n(m_i)\,n(m_j) && \text{(C.11)}\\
&\times\int \mathrm{d}N_{\mathrm{cen},i}\int \mathrm{d}N_{\mathrm{sat},i}\;\; P_N(N_{\mathrm{cen},i},N_{\mathrm{sat},i}|m_i)\int \mathrm{d}N_{\mathrm{cen},j}\int \mathrm{d}N_{\mathrm{sat},j}\;\; P_N(N_{\mathrm{cen},j},N_{\mathrm{sat},j}|m_j)\\
&\times\int \mathrm{d}^3x_1\dots\mathrm{d}^3x_H\;\; P_\mathrm{c}(\boldsymbol{x}_1,\dots,\boldsymbol{x}_H \mid m_1,\dots,m_H)\\
&\times\Big\{m_i\,\hat{u}(\boldsymbol{k}_3|m_i)\;\exp\big[-\mathrm{i}\,(\boldsymbol{k}_1+\boldsymbol{k}_3)\cdot\boldsymbol{x}_i-\mathrm{i}\,\boldsymbol{k}_2\cdot\boldsymbol{x}_j\big]\\
&\quad\times\big[N_{\mathrm{cen},i}+N_{\mathrm{sat},i}\,\hat{u}_\mathrm{g}(\boldsymbol{k}_1|m_i)\big]\,\big[N_{\mathrm{cen},j}+N_{\mathrm{sat},j}\,\hat{u}_\mathrm{g}(\boldsymbol{k}_2|m_j)\big]\\
&\quad+m_j\,\hat{u}(\boldsymbol{k}_3|m_j)\;\exp\big[-\mathrm{i}\,(\boldsymbol{k}_2+\boldsymbol{k}_3)\cdot\boldsymbol{x}_j-\mathrm{i}\,\boldsymbol{k}_1\cdot\boldsymbol{x}_i\big]\\
&\qquad\times\big[N_{\mathrm{cen},i}+N_{\mathrm{sat},i}\,\hat{u}_\mathrm{g}(\boldsymbol{k}_1|m_i)\big]\,\big[N_{\mathrm{cen},j}+N_{\mathrm{sat},j}\,\hat{u}_\mathrm{g}(\boldsymbol{k}_2|m_j)\big]\\
&\quad+m_j\,\hat{u}(\boldsymbol{k}_3|m_j)\;\exp\big[-\mathrm{i}\,(\boldsymbol{k}_1+\boldsymbol{k}_2)\cdot\boldsymbol{x}_i-\mathrm{i}\,\boldsymbol{k}_3\cdot\boldsymbol{x}_j\big]\\
&\qquad\times\big[N_{\mathrm{cen},i}(N_{\mathrm{cen},i}-1)+N_{\mathrm{cen},i}\,N_{\mathrm{sat},i}\big(\hat{u}_\mathrm{g}(\boldsymbol{k}_1|m_i)+\hat{u}_\mathrm{g}(\boldsymbol{k}_2|m_i)\big)\\
&\qquad\quad+N_{\mathrm{sat},i}(N_{\mathrm{sat},i}-1)\hat{u}_\mathrm{g}(\boldsymbol{k}_1|m_i)\hat{u}_\mathrm{g}(\boldsymbol{k}_2|m_i)\big]\Big\}\\
&= (2\pi)^3\,\delta_\mathrm{D}(\boldsymbol{k}_1+\boldsymbol{k}_2+\boldsymbol{k}_3)\,\frac{1}{\bar{\rho}\,\bar{n}^2}\int \mathrm{d}m_1\int \mathrm{d}m_2\;\; n(m_1)\,n(m_2) && \text{(C.12)}\\
&\times\Big\{\,[m_1\,\hat{u}(\boldsymbol{k}_3|m_1)\,P_\mathrm{H}(\boldsymbol{k}_2,-\boldsymbol{k}_2|m_1,m_2)+m_2\,\hat{u}(\boldsymbol{k}_3|m_2)\,P_\mathrm{H}(\boldsymbol{k}_1,-\boldsymbol{k}_1|m_1,m_2)]\\
&\quad\times\big[\big\langle N_\mathrm{cen}|m_1\big\rangle+\big\langle N_\mathrm{sat}|m_1\big\rangle\;\hat{u}_\mathrm{g}(\boldsymbol{k}_1|m_1)\big]\;\big[\big\langle N_\mathrm{cen}|m_2\big\rangle+\big\langle N_\mathrm{sat}|m_2\big\rangle\;\hat{u}_\mathrm{g}(\boldsymbol{k}_2|m_2)\big]\\
&+m_2\,\hat{u}(\boldsymbol{k}_3|m_2)\,P_\mathrm{H}(\boldsymbol{k}_3,-\boldsymbol{k}_3|m_1,m_2)\\
&\quad\times\big[\big\langle N_\mathrm{cen}(N_\mathrm{cen}-1)|m_1\big\rangle+\big\langle N_\mathrm{cen}\,N_\mathrm{sat}|m_1\big\rangle\;\big(\hat{u}_\mathrm{g}(\boldsymbol{k}_1|m_1)+\hat{u}_\mathrm{g}(\boldsymbol{k}_2|m_1)\big)\\
&\qquad+\big\langle N_\mathrm{sat}(N_\mathrm{sat}-1)|m_1\big\rangle\;\hat{u}_\mathrm{g}(\boldsymbol{k}_1|m_1)\,\hat{u}_\mathrm{g}(\boldsymbol{k}_2|m_2)\big]\,\Big\}\;,
\end{aligned}
$$

where P_H is the halo power spectrum. Here we used

$$\int_V \mathrm{d}^3x_1 \,\dots\, \mathrm{d}^3x_H \;\; P_\mathrm{c}(\boldsymbol{x}_1,\dots,\boldsymbol{x}_H \mid m_1,\dots,m_H)\; \exp\left[-\mathrm{i}\,\boldsymbol{k}_1\boldsymbol{x}_i - \mathrm{i}\,\boldsymbol{k}_2\cdot\boldsymbol{x}_j\right]$$

$$= \frac{V^{H-2}}{V^H}\int_V \mathrm{d}^3x_i \int_V \mathrm{d}^3x_j \;\frac{1}{V^2}\left[1+\xi_\mathrm{H}(\boldsymbol{x}_i,\boldsymbol{x}_j)\right]\;\exp\left[-\mathrm{i}\,\boldsymbol{k}_1\boldsymbol{x}_i - \mathrm{i}\,\boldsymbol{k}_2\cdot\boldsymbol{x}_j\right] \tag{C.13}$$

$$= \frac{1}{V^2}\;\left[(2\pi)^6\,\delta_\mathrm{D}(\boldsymbol{k}_1)\,\delta_\mathrm{D}(\boldsymbol{k}_2) + (2\pi)^3\,\delta_\mathrm{D}(\boldsymbol{k}_1+\boldsymbol{k}_2)\,P_\mathrm{H}(\boldsymbol{k}_1,\boldsymbol{k}_2,t)\right]\;, \tag{C.14}$$

with the halo two-point correlation function ξ_H. The terms proportional to $\delta_\mathrm{D}(\boldsymbol{k})$ can be ignored, as the bispectrum only depends on the terms proportional to $\delta_\mathrm{D}(\boldsymbol{k}_1+\boldsymbol{k}_2+\boldsymbol{k}_3)$.

The 3-halo term is given by

$$(2\pi)^3\,\delta_\mathrm{D}(\boldsymbol{k}_1+\boldsymbol{k}_2+\boldsymbol{k}_3)\,B^{3-\mathrm{h}}_{\mathrm{gg}\delta}(\boldsymbol{k}_1,\boldsymbol{k}_2,\boldsymbol{k}_3,t)$$

$$= \frac{1}{\bar{n}_\mathrm{H}^2\,\bar{\rho}\,\bar{n}^2}\sum_{i=1}^{H}\sum_{j\neq i}\sum_{k\neq i,j}\int \mathrm{d}m_i\int \mathrm{d}m_j\int \mathrm{d}m_k\;\; n(m_i)\,n(m_j)\,n(m_k) \tag{C.15}$$

$$\times\int \mathrm{d}N_{\mathrm{cen},i}\int \mathrm{d}N_{\mathrm{sat},i}\;\;P_N(N_{\mathrm{cen},i},N_{\mathrm{sat},i}|m_i)\;\int \mathrm{d}N_{\mathrm{cen},j}\int \mathrm{d}N_{\mathrm{sat},j}\;\;P_N(N_{\mathrm{cen},j},N_{\mathrm{sat},j}|m_j)$$

$$\times\int \mathrm{d}^3x_1\dots\mathrm{d}^3x_H\;\;P_\mathrm{c}(\boldsymbol{x}_1,\dots,\boldsymbol{x}_H \mid m_1,\dots,m_H)$$

$$\times\, m_k\,\hat{u}(\boldsymbol{k}_3|m_k)\;\exp\left[-\mathrm{i}\,\boldsymbol{k}_1\cdot\boldsymbol{x}_i - \mathrm{i}\,\boldsymbol{k}_2\cdot\boldsymbol{x}_j - \mathrm{i}\,\boldsymbol{k}_3\cdot\boldsymbol{x}_k\right]$$

$$\times\left[N_{\mathrm{cen},i} + N_{\mathrm{sat},i}\,\hat{u}_\mathrm{g}(\boldsymbol{k}_1|m_i)\right]\;\left[N_{\mathrm{cen},j} + N_{\mathrm{sat},j}\,\hat{u}_\mathrm{g}(\boldsymbol{k}_2|m_j)\right]$$

$$= (2\pi)^3\,\delta_\mathrm{D}(\boldsymbol{k}_1+\boldsymbol{k}_2+\boldsymbol{k}_3)\,\frac{1}{\bar{\rho}\,\bar{n}^2}\int \mathrm{d}m_1\int \mathrm{d}m_2\int \mathrm{d}m_3\;\; n(m_1)\,n(m_2)\,n(m_3)\,m_3\,\hat{u}(\boldsymbol{k}_3|m_3) \tag{C.16}$$

$$\times\, B_\mathrm{H}(\boldsymbol{k}_1,\boldsymbol{k}_2,-\boldsymbol{k}_1-\boldsymbol{k}_2,t)\,\left[\left\langle N_\mathrm{cen}|m_1\right\rangle + \left\langle N_\mathrm{sat}|m_1\right\rangle\;\hat{u}_\mathrm{g}(\boldsymbol{k}_1|m_1)\right]$$

$$\times\left[\left\langle N_\mathrm{cen}|m_2\right\rangle + \left\langle N_\mathrm{sat}|m_2\right\rangle\;\hat{u}_\mathrm{g}(\boldsymbol{k}_2|m_2)\right]\;.$$

Here we used

$$\int_V \mathrm{d}^3x_1 \,\dots\, \mathrm{d}^3x_H \;\; P_\mathrm{c}(\boldsymbol{x}_1,\dots,\boldsymbol{x}_H \mid m_1,\dots,m_H)\; \exp\left[-\mathrm{i}\,\boldsymbol{k}_1\boldsymbol{x}_i - \mathrm{i}\,\boldsymbol{k}_2\cdot\boldsymbol{x}_j - \mathrm{i}\,\boldsymbol{k}_3\cdot\boldsymbol{x}_k\right]$$

$$= \frac{V^{H-3}}{V^H}\int_V \mathrm{d}^3x_i\int_V \mathrm{d}^3x_j\int_V \mathrm{d}^3x_k\;\frac{1}{V^3}\left[1+\xi_\mathrm{H}(\boldsymbol{x}_i,\boldsymbol{x}_j)+\xi_\mathrm{H}(\boldsymbol{x}_i,\boldsymbol{x}_k)+\xi_\mathrm{H}(\boldsymbol{x}_j,\boldsymbol{x}_k)+\zeta_\mathrm{H}(\boldsymbol{x}_i,\boldsymbol{x}_j,\boldsymbol{x}_k)\right] \tag{C.17}$$

$$\times\exp\left[-\mathrm{i}\,\boldsymbol{k}_1\boldsymbol{x}_i - \mathrm{i}\,\boldsymbol{k}_2\cdot\boldsymbol{x}_j - I\,\boldsymbol{k}_3\right]$$

$$= \frac{1}{V^3}\left[(2\pi)^9\,\delta_\mathrm{D}(\boldsymbol{k}_1)\,\delta_\mathrm{D}(\boldsymbol{k}_2)\,\delta_\mathrm{D}(\boldsymbol{k}_3) + (2\pi)^6\,\delta_\mathrm{D}(\boldsymbol{k}_3)\,\delta_\mathrm{D}(\boldsymbol{k}_1+\boldsymbol{k}_2)\,P_\mathrm{H}(\boldsymbol{k}_1,\boldsymbol{k}_2,t)\right. \tag{C.18}$$

$$+\,(2\pi)^6\,\delta_\mathrm{D}(\boldsymbol{k}_2)\,\delta_\mathrm{D}(\boldsymbol{k}_1+\boldsymbol{k}_3)\,P_\mathrm{H}(\boldsymbol{k}_1,\boldsymbol{k}_3,t) + (2\pi)^6\,\delta_\mathrm{D}(\boldsymbol{k}_1)\,\delta_\mathrm{D}(\boldsymbol{k}_2+\boldsymbol{k}_3)\,P_\mathrm{H}(\boldsymbol{k}_2,\boldsymbol{k}_3,t)$$

$$\left.+\,(2\pi)^3\,\delta_\mathrm{D}(\boldsymbol{k}_1+\boldsymbol{k}_2+\boldsymbol{k}_3)\,B_\mathrm{H}(\boldsymbol{k}_1,\boldsymbol{k}_2,\boldsymbol{k}_3,t)\right]\;,$$

with the halo three-point correlation function ζ_H.

C.2 Calculation of galaxy-galaxy-matter bispectrum for different galaxy populations

For two different galaxy populations Eq. (C.1) needs to be extended to include averages over central and satellite galaxies from populations a and b. Therefore the average of an arbitrary quantity f is

$$
\begin{aligned}
\langle f \rangle = \int & \mathrm{d}m_1 \dots \mathrm{d}m_H \;\; P_\mathrm{m}(m_1, \dots, m_H) \\
\times & \int \mathrm{d}N^{(a)}_{\mathrm{cen},1} \dots \mathrm{d}N^{(a)}_{\mathrm{cen},H} \int \mathrm{d}N^{(a)}_{\mathrm{sat},1} \dots \mathrm{d}N^{(a)}_{\mathrm{sat},H} \\
\times & \int \mathrm{d}N^{(b)}_{\mathrm{cen},1} \dots \mathrm{d}N^{(b)}_{\mathrm{cen},H} \int \mathrm{d}N^{(b)}_{\mathrm{sat},1} \dots \mathrm{d}N^{(b)}_{\mathrm{sat},H} \\
\times & \underbrace{P_N(N^{(a)}_{\mathrm{cen},1}\, N^{(a)}_{\mathrm{sat},1}\, N^{(b)}_{\mathrm{cen},1}\, N^{(b)}_{\mathrm{sat},1} | m_1) \dots P_N(N^{(a)}_{\mathrm{cen},H}\, N^{(a)}_{\mathrm{sat},H}\, N^{(b)}_{\mathrm{cen},H}\, N^{(b)}_{\mathrm{sat},H} | m_H)}_{\substack{\text{Probability that halo } i \text{ has } N^{(a)}_{\mathrm{cen},i} \text{ centrals and } N^{(a)}_{\mathrm{sat},i} \text{ satellites of population } a \\ \text{and } N^{(b)}_{\mathrm{cen},i} \text{ centrals and } N^{(b)}_{\mathrm{sat},i} \text{ satellites of population } b}} \\
\times & \int \mathrm{d}^3x_1 \dots \mathrm{d}^3x_H \;\; P_\mathrm{c}(\boldsymbol{x}_1, \dots, \boldsymbol{x}_H \mid m_1, \dots, m_H) \\
\times & \int \mathrm{d}^3\Delta\boldsymbol{x}^{(a)}_{11} \cdots \int \mathrm{d}^3\Delta\boldsymbol{x}^{(a)}_{HN^{(a)}_{\mathrm{sat},H}} \int \mathrm{d}^3\Delta\boldsymbol{x}^{(b)}_{11} \cdots \int \mathrm{d}^3\Delta\boldsymbol{x}^{(b)}_{HN^{(b)}_{\mathrm{sat},H}} \\
\times & \underbrace{P_\mathrm{gal}(\Delta\boldsymbol{x}^{(a)}_{11}, \dots, \Delta\boldsymbol{x}^{(a)}_{HN^{(a)}_{\mathrm{sat},H}}, \Delta\boldsymbol{x}^{(b)}_{11}, \dots, \Delta\boldsymbol{x}^{(b)}_{HN^{(b)}_{\mathrm{sat},H}} \mid m_1, \dots, m_H)}_{\substack{\text{Probability that population } a \text{ satellites are at } \Delta\boldsymbol{x}^{(a)}_{11}, \dots, \Delta\boldsymbol{x}^{(a)}_{HN^{(a)}_{\mathrm{sat},H}} \\ \text{and population } b \text{ satellites are at } \Delta\boldsymbol{x}^{(b)}_{11}, \dots, \Delta\boldsymbol{x}^{(b)}_{HN^{(b)}_{\mathrm{sat},H}}}} \; f \; .
\end{aligned}
\tag{C.19}
$$

Again we split the triple sum into a 1-halo, 2-halo, and 3-halo term. The 1-halo term is given by

$$
\begin{aligned}
&(2\pi)^3\,\delta_{\mathrm{D}}(\boldsymbol{k}_1+\boldsymbol{k}_2+\boldsymbol{k}_3)\,B^{1-\mathrm{h}}_{\mathrm{gg}\delta}(\boldsymbol{k}_1,\boldsymbol{k}_2,\boldsymbol{k}_3,t)\\
&=\frac{1}{\bar{n}_{\mathrm{H}}\,\bar{\rho}\,\bar{n}_a\,\bar{n}_b}\sum_{i=1}^{H}\int \mathrm{d}m_i\;\; n(m_i) \qquad\qquad\qquad\qquad\qquad\qquad\qquad\qquad \text{(C.20)}\\
&\times\int \mathrm{d}N^{(a)}_{\mathrm{cen},i}\int \mathrm{d}N^{(a)}_{\mathrm{sat},i}\int \mathrm{d}N^{(b)}_{\mathrm{cen},i}\int \mathrm{d}N^{(b)}_{\mathrm{sat},i}\;\; P_N(N^{(a)}_{\mathrm{cen},i},N^{(a)}_{\mathrm{sat},i},N^{(b)}_{\mathrm{cen},i},N^{(b)}_{\mathrm{sat},i}|m_i)\\
&\times\int \mathrm{d}^3x_1\dots\mathrm{d}^3x_H\;\; P_{\mathrm{c}}(\boldsymbol{x}_1,\dots,\boldsymbol{x}_H\mid m_1,\dots,m_H)\;\exp\big[-\mathrm{i}\,(\boldsymbol{k}_1+\boldsymbol{k}_2+\boldsymbol{k}_3)\cdot\boldsymbol{x}_i\big]m_i\,\hat{u}(\boldsymbol{k}_3|m_i)\\
&\times\Big[N^{(a)}_{\mathrm{cen},i}\,N^{(b)}_{\mathrm{cen},i}+N^{(a)}_{\mathrm{cen},i}\,N^{(b)}_{\mathrm{sat},i}\,\hat{u}^{(b)}_{\mathrm{g}}(\boldsymbol{k}_2|m_i)\\
&\quad+N^{(b)}_{\mathrm{cen},i}\,N^{(a)}_{\mathrm{sat},i}\,\hat{u}^{(a)}_{\mathrm{g}}(\boldsymbol{k}_1|m_i)+N^{(a)}_{\mathrm{sat},i}\,N^{(b)}_{\mathrm{sat},i}\,\hat{u}^{(a)}_{\mathrm{g}}(\boldsymbol{k}_1|m_i)\,\hat{u}^{(b)}_{\mathrm{g}}(\boldsymbol{k}_2|m_i)\Big]
\end{aligned}
$$

$$
\begin{aligned}
&=(2\pi)^3\,\delta_{\mathrm{D}}(\boldsymbol{k}_1+\boldsymbol{k}_2+\boldsymbol{k}_3)\,\frac{1}{\bar{\rho}\,\bar{n}_a\,\bar{n}_b}\int \mathrm{d}m\;\; n(m)\,m\,\hat{u}(\boldsymbol{k}_3|m) \qquad\qquad\qquad \text{(C.21)}\\
&\times\Big[\Big\langle N^{(a)}_{\mathrm{cen}}\,N^{(b)}_{\mathrm{cen}}|m\Big\rangle+\Big\langle N^{(a)}_{\mathrm{cen}}\,N^{(b)}_{\mathrm{sat}}\Big\rangle\;\hat{u}^{(b)}_{\mathrm{g}}(\boldsymbol{k}_2|m)+\Big\langle N^{(b)}_{\mathrm{cen}}\,N^{(a)}_{\mathrm{sat}}\Big\rangle\;\hat{u}^{(a)}_{\mathrm{g}}(\boldsymbol{k}_1|m)\\
&\quad+\Big\langle N^{(a)}_{\mathrm{sat}}\,N^{(b)}_{\mathrm{sat}}\,|m\Big\rangle\;\hat{u}^{(a)}_{\mathrm{g}}(\boldsymbol{k}_1|m)\,\hat{u}^{(b)}_{\mathrm{g}}(\boldsymbol{k}_2|m)\Big]\;\;,
\end{aligned}
$$

The 2-halo term is given by

$$
\begin{aligned}
&(2\pi)^3\,\delta_\mathrm{D}(\boldsymbol{k}_1+\boldsymbol{k}_2+\boldsymbol{k}_3)\,B^{2\mathrm{-h}}_{\mathrm{gg}\delta}(\boldsymbol{k}_1,\boldsymbol{k}_2,\boldsymbol{k}_3,t)\\
&=\frac{1}{\bar{n}_\mathrm{H}^2\,\bar{\rho}\,\bar{n}_a\,\bar{n}_b}\sum_{i=1}^{H}\sum_{j\neq i}\int\mathrm{d}m_i\int\mathrm{d}m_j\;\;n(m_i)\,n(m_j) \qquad\qquad (\mathrm{C}.22)\\
&\quad\times\int\mathrm{d}N^{(a)}_{\mathrm{cen},i}\int\mathrm{d}N^{(a)}_{\mathrm{sat},i}\int\mathrm{d}N^{(b)}_{\mathrm{cen},i}\int\mathrm{d}N^{(b)}_{\mathrm{sat},i}\\
&\quad\times\int\mathrm{d}N^{(a)}_{\mathrm{cen},j}\int\mathrm{d}N^{(a)}_{\mathrm{sat},j}\int\mathrm{d}N^{(b)}_{\mathrm{cen},j}\int\mathrm{d}N^{(b)}_{\mathrm{sat},j}\\
&\quad\times P_N(N^{(a)}_{\mathrm{cen},i},N^{(a)}_{\mathrm{sat},i}\,N^{(b)}_{\mathrm{cen},i},N^{(b)}_{\mathrm{sat},i}|m_i)\,P_N(N^{(a)}_{\mathrm{cen},j},N^{(a)}_{\mathrm{sat},j}\,N^{(b)}_{\mathrm{cen},j},N^{(b)}_{\mathrm{sat},j}|m_j)\\
&\quad\times\int\mathrm{d}^3x_1\ldots\mathrm{d}^3x_H\;\;P_\mathrm{c}(\boldsymbol{x}_1,\ldots,\boldsymbol{x}_H\mid m_1,\ldots,m_H)\,\exp\left[-\mathrm{i}\,(\boldsymbol{k}_1+\boldsymbol{k}_2+\boldsymbol{k}_3)\cdot\boldsymbol{x}_i\right]\\
&\quad\times\Big\{m_i\,\hat{u}(\boldsymbol{k}_3|m_i)\,\exp\big[-\mathrm{i}\,(\boldsymbol{k}_1+\boldsymbol{k}_3)\cdot\boldsymbol{x}_i-\mathrm{i}\,\boldsymbol{k}_2\cdot\boldsymbol{x}_j\big]\\
&\qquad\times\left[N^{(a)}_{\mathrm{cen},i}+N^{(a)}_{\mathrm{sat},i}\,\hat{u}^{(a)}_\mathrm{g}(\boldsymbol{k}_1|m_i)\right]\left[N^{(b)}_{\mathrm{cen},j}+N^{(b)}_{\mathrm{sat},j}\,\hat{u}^{(b)}_\mathrm{g}(\boldsymbol{k}_2|m_j)\right]\\
&\qquad+m_j\,\hat{u}(\boldsymbol{k}_3|m_j)\,\exp\big[-\mathrm{i}\,(\boldsymbol{k}_2+\boldsymbol{k}_3)\cdot\boldsymbol{x}_j-\mathrm{i}\,\boldsymbol{k}_1\cdot\boldsymbol{x}_i\big]\\
&\qquad\quad\times\left[N^{(a)}_{\mathrm{cen},i}+N^{(a)}_{\mathrm{sat},i}\,\hat{u}^{(a)}_\mathrm{g}(\boldsymbol{k}_1|m_i)\right]\left[N^{(b)}_{\mathrm{cen},j}+N^{(b)}_{\mathrm{sat},j}\,\hat{u}^{(b)}_\mathrm{g}(\boldsymbol{k}_2|m_j)\right]\\
&\qquad+m_j\,\hat{u}(\boldsymbol{k}_3|m_j)\,\exp\big[-\mathrm{i}\,(\boldsymbol{k}_1+\boldsymbol{k}_2)\cdot\boldsymbol{x}_i-\mathrm{i}\,\boldsymbol{k}_3\cdot\boldsymbol{x}_j\big]\\
&\qquad\quad\times\Big[N^{(a)}_{\mathrm{cen},i}\,N^{(b)}_{\mathrm{cen},i}+N^{(a)}_{\mathrm{cen},i}\,N^{(b)}_{\mathrm{sat},i}\,\hat{u}^{(b)}_\mathrm{g}(\boldsymbol{k}_2|m_i)+N^{(b)}_{\mathrm{cen},i}\,N^{(a)}_{\mathrm{sat},i}\,\hat{u}^{(a)}_\mathrm{g}(\boldsymbol{k}_1|m_i)\\
&\qquad\qquad+N^{(a)}_{\mathrm{sat},i}\,N^{(b)}_{\mathrm{sat},i}\,\hat{u}^{(a)}_\mathrm{g}(\boldsymbol{k}_1|m_i)\hat{u}^{(b)}_\mathrm{g}(\boldsymbol{k}_2|m_i)\Big]\Big\}\\
&=(2\pi)^3\,\delta_\mathrm{D}(\boldsymbol{k}_1+\boldsymbol{k}_2+\boldsymbol{k}_3)\,\frac{1}{\bar{\rho}\,\bar{n}_a\,\bar{n}_b}\int\mathrm{d}m_1\int\mathrm{d}m_2\;\;n(m_1)\,n(m_2) \qquad\qquad (\mathrm{C}.23)\\
&\quad\times\Big\{\left[m_1\,\hat{u}(\boldsymbol{k}_3|m_1)\,P_\mathrm{H}(\boldsymbol{k}_2,-\boldsymbol{k}_2|m_1,m_2)+m_2\,\hat{u}(\boldsymbol{k}_3|m_2)\,P_\mathrm{H}(\boldsymbol{k}_1,-\boldsymbol{k}_1|m_1,m_2)\right]\\
&\qquad\times\left[\left\langle N^{(a)}_\mathrm{cen}|m_1\right\rangle+\left\langle N^{(a)}_\mathrm{sat}|m_1\right\rangle\,\hat{u}^{(a)}_\mathrm{g}(\boldsymbol{k}_1|m_1)\right]\left[\left\langle N^{(b)}_\mathrm{cen}|m_2\right\rangle+\left\langle N^{(b)}_\mathrm{sat}|m_2\right\rangle\,\hat{u}^{(b)}_\mathrm{g}(\boldsymbol{k}_2|m_2)\right]\\
&\quad+m_2\,\hat{u}(\boldsymbol{k}_3|m_2)\,P_\mathrm{H}(\boldsymbol{k}_3,-\boldsymbol{k}_3|m_1,m_2)\\
&\qquad\times\Big[\left\langle N^{(a)}_\mathrm{cen}\,N^{(b)}_\mathrm{cen}|m_1\right\rangle+\left\langle N^{(a)}_\mathrm{cen}\,N^{(b)}_\mathrm{sat}|m_1\right\rangle\,\hat{u}^{(b)}_\mathrm{g}(\boldsymbol{k}_2|m_1)\\
&\qquad\quad+\left\langle N^{(b)}_\mathrm{cen}\,N^{(a)}_\mathrm{sat}|m_1\right\rangle\,\hat{u}^{(a)}_\mathrm{g}(\boldsymbol{k}_1|m_1)+\left\langle N^{(a)}_\mathrm{sat}\,N^{(b)}_\mathrm{sat}|m_1\right\rangle\,\hat{u}^{(a)}_\mathrm{g}(\boldsymbol{k}_1|m_1)\,\hat{u}^{(b)}_\mathrm{g}(\boldsymbol{k}_2|m_2)\Big]\Big\}\;.
\end{aligned}
$$

The 3-halo term is given by

$$
\begin{aligned}
&(2\pi)^3\,\delta_{\mathrm{D}}(\boldsymbol{k}_1+\boldsymbol{k}_2+\boldsymbol{k}_3)\,B^{3\text{-h}}_{\mathrm{gg}\delta}(\boldsymbol{k}_1,\boldsymbol{k}_2,\boldsymbol{k}_3,t)\\
&=\frac{1}{\bar{n}_{\mathrm{H}}^2\,\bar{\rho}\,\bar{n}_a\,\bar{n}_b}\sum_{i=1}^{H}\sum_{j\neq i}\sum_{k\neq i,j}\int\mathrm{d}m_i\int\mathrm{d}m_j\int\mathrm{d}m_k\;\;n(m_i)\,n(m_j)\,n(m_k) \qquad\qquad (\mathrm{C.24})\\
&\quad\times\int\mathrm{d}N^{(a)}_{\mathrm{cen},i}\int\mathrm{d}N^{(a)}_{\mathrm{sat},i}\int\mathrm{d}N^{(b)}_{\mathrm{cen},i}\int\mathrm{d}N^{(b)}_{\mathrm{sat},i}\\
&\quad\times\int\mathrm{d}N^{(a)}_{\mathrm{cen},j}\int\mathrm{d}N^{(a)}_{\mathrm{sat},j}\int\mathrm{d}N^{(b)}_{\mathrm{cen},j}\int\mathrm{d}N^{(b)}_{\mathrm{sat},j}\\
&\quad\times P_N(N^{(a)}_{\mathrm{cen},i},N^{(a)}_{\mathrm{sat},i}\,N^{(b)}_{\mathrm{cen},i},N^{(b)}_{\mathrm{sat},i}|m_i)\,P_N(N^{(a)}_{\mathrm{cen},j},N^{(a)}_{\mathrm{sat},j}\,N^{(b)}_{\mathrm{cen},j},N^{(b)}_{\mathrm{sat},j}|m_j)\\
&\quad\times\int\mathrm{d}^3x_1\ldots\mathrm{d}^3x_H\;\;P_{\mathrm{c}}(\boldsymbol{x}_1,\ldots,\boldsymbol{x}_H\mid m_1,\ldots,m_H)\;\exp\left[-\mathrm{i}\,(\boldsymbol{k}_1+\boldsymbol{k}_2+\boldsymbol{k}_3)\cdot\boldsymbol{x}_i\right]\\
&\quad\times m_k\,\hat{u}(\boldsymbol{k}_3|m_k)\;\exp\!\left[-\mathrm{i}\,\boldsymbol{k}_1\cdot\boldsymbol{x}_i-\mathrm{i}\,\boldsymbol{k}_2\cdot\boldsymbol{x}_j-\mathrm{i}\,\boldsymbol{k}_3\cdot\boldsymbol{x}_k\right]\\
&\quad\times\left[N^{(a)}_{\mathrm{cen},i}+N^{(a)}_{\mathrm{sat},i}\,\hat{u}^{(a)}_{\mathrm{g}}(\boldsymbol{k}_1|m_i)\right]\;\left[N^{(b)}_{\mathrm{cen},j}+N^{(b)}_{\mathrm{sat},j}\,\hat{u}^{(b)}_{\mathrm{g}}(\boldsymbol{k}_2|m_j)\right]\\
&=(2\pi)^3\,\delta_{\mathrm{D}}(\boldsymbol{k}_1+\boldsymbol{k}_2+\boldsymbol{k}_3)\,\frac{1}{\bar{\rho}\,\bar{n}_a\,\bar{n}_b}\int\mathrm{d}m_1\int\mathrm{d}m_2 \qquad\qquad (\mathrm{C.25})\\
&\quad\times\int\mathrm{d}m_3\;\;n(m_1)\,n(m_2)\,n(m_3)\,m_3\,\hat{u}(\boldsymbol{k}_3|m_3)\\
&\quad\times B_{\mathrm{H}}(\boldsymbol{k}_1,\boldsymbol{k}_2,-\boldsymbol{k}_1-\boldsymbol{k}_2,t)\,\left[\left\langle N^{(a)}_{\mathrm{cen}}|m_1\right\rangle+\left\langle N^{(a)}_{\mathrm{sat}}|m_1\right\rangle\,\hat{u}^{(a)}_{\mathrm{g}}(\boldsymbol{k}_1|m_1)\right]\\
&\quad\times\left[\left\langle N^{(b)}_{\mathrm{cen}}|m_2\right\rangle+\left\langle N^{(b)}_{\mathrm{sat}}|m_2\right\rangle\,\hat{u}^{(b)}_{\mathrm{g}}(\boldsymbol{k}_2|m_2)\right]\;.
\end{aligned}
$$

List of Figures

2.1 SDSS galaxy map . . . 11
2.2 Measured and linear power spectrum . . . 19
2.3 Sketch of dark matter halo merger tree . . . 22
2.4 Gravitational lensing system . . . 32
2.5 G3L configuration . . . 38

3.1 Weighted redshift distribution of lens galaxy pairs in the MR . . . 47
3.2 Illustration of the old and new binning scheme for $\tilde{\mathcal{G}}$ . . . 48
3.3 Assumed source redshift distribution . . . 54
3.4 $\langle\mathcal{N}\mathcal{N}\mathcal{M}\rangle$ measured in simple mock data and theoretical expectation . . . 57
3.5 Fractional difference of measured $\langle\mathcal{N}\mathcal{N}\mathcal{M}\rangle$ to theoretical prediction . . . 58
3.6 Effect of lens magnification in the MR in angular units . . . 59
3.7 Effect of lens magnification in the MR in physical units . . . 59
3.8 Individual lens magnification terms in the MR . . . 60
3.9 Aperture statistics measured in the MR. . . . 62

4.1 Redshift distribution of GAMA and SAM galaxies . . . 72
4.2 Colour distribution of GAMA and SAM galaxies . . . 72
4.3 Stellar mass distribution of GAMA and SAM galaxies . . . 73
4.4 $\langle\mathcal{N}\mathcal{N}\mathcal{M}\rangle_{\mathrm{phys}}$ for colour-selected lenses in observation and simulation . . . 74
4.5 $\langle\mathcal{N}\mathcal{N}\mathcal{M}\rangle_{\mathrm{phys}}$ for stellar mass-selected lenses in observation and simulation . 76

5.1 Halo occupation distribution for fiducial parameters . . . 84
5.2 Impact of halo model parameters on $\langle\mathcal{N}\mathcal{N}\mathcal{M}\rangle$ for unmixed lens pairs . . . 92
5.3 Impact of halo model parameters on $\langle\mathcal{N}\mathcal{N}\mathcal{M}\rangle$ for mixed lens pairs . . . 94
5.4 Best fitting halo model for KV450 × GAMA . . . 95

B.1 $\langle\mathcal{N}\mathcal{N}\mathcal{M}\rangle$ for colour-selected lenses in observation and simulation . . . 126
B.2 $\langle\mathcal{N}\mathcal{N}\mathcal{M}\rangle$ for stellar-mass selected lenses in observation and simulations . . 127

List of Tables

2.1 Cosmological parameters 10
2.2 Differences of used SAMs 25

3.1 Slopes of the galaxy luminosity function in the MR 53

4.1 Selection criteria for lens samples 70
4.2 χ^2_{redu} of $\langle\mathcal{N}\mathcal{N}\mathcal{M}\rangle_{\mathrm{phys}}$ for both SAMs 75
4.3 S/N of observed $\langle\mathcal{N}\mathcal{N}\mathcal{M}\rangle_{\mathrm{phys}}$ and $\langle\mathcal{N}\mathcal{N}\mathcal{M}_\perp\rangle_{\mathrm{phys}}$ 77

5.1 Halo model parameters 85
5.2 Best fitting halo model parameters 96

B.1 χ^2_{redu} of $\langle\mathcal{N}\mathcal{N}\mathcal{M}\rangle$ for both SAMs. 126

List of Acronyms

AGN Active Galactic Nuclei

BBS Brainerd-Blandford-Smail

BOSS Baryon Oscillation Spectroscopic Survey

CFHTLenS Canada-France-Hawaii Telescope Lensing Survey

CMB cosmic microwave background

CL confidence level

DMU Data Management Unit

EAGLE Evolution and Assembly of GaLaxies and their Environments

FOF friends-of-friends

G3L galaxy-galaxy-galaxy lensing

GAMA Galaxy And Mass Assembly survey

GGL galaxy-galaxy lensing

GPU graphics processing unit

GR general relativity

GSL GNU Scientific Library

HMF halo mass function

HOD halo occupation distribution

IMF initial mass function

ISM interstellar medium

JHOD joint halo occupation distribution

KiDS Kilo-Degree Survey

KV450 × GAMA overlap of the KiDS, VIKING, and GAMA

LSS cosmic large-scale structure

LSST Legacy Survey of Space and Time

MR Millennium Run

NFW Navarro-Frenk-White

PM particle-mesh

P^{3}M particle-particle particle-mesh

SAM semi-analytic model of galaxy formation and evolution

RCS Red-sequence Cluster Survey

SDSS Sloan Digital Sky Survey

SFR star-formation rate

SIS singular isothermal sphere

S/N signal-to-noise ratio

SNIa supernovae type Ia

SO spherical-overdensity

VIKING VISTA Kilodegree Infrared Galaxy survey

VISTA Visible and Infrared Survey Telescope for Astronomy

VLT Very Large Telescope

WMAP Wilkinson Microwave Anisotropy Probe

Acknowledgements

In the third volume of the *Lord of the Rings* by Tolkien (1955), one of the main heroes Aragorn consoles the Rohirrim princess Eowyn by explaining that "*...[D]eeds will not be less valiant because they are unpraised.*" Nevertheless, I want to praise here the 'deeds' of several people who helped with the completion of this thesis in countless ways. I am deeply grateful to each one of them.

First of all, I would like to thank my supervisor, Peter Schneider, for bringing me to Bonn by offering this fascinating research project and supporting me during it. Thank you so much for all the time you took, to discuss ideas, carefully read manuscript drafts, and give general guidance. This applies in particular to the last months, when even during work-from-home, lock-down and homeschooling fruitful meetings and discussions were possible.

Likewise, I am immensely grateful to Patrick Simon, who acted as my day-to-day advisor. Thank you for helping me understand galaxy-galaxy-galaxy-lensing and thank you for regularly discussing my work and clarifying a million subtleties, that I completely missed at first glance.

I would also like to thank the other two members of my Thesis Advisory Committee, Cristiano Porciani and Norbert Wex. Thank you for offering advice during our meetings and helping me 'stay on track'. Thank you, Cristiano, for accepting to be my second thesis referee.

No work is ever achieved alone. I want to thank the co-authors of the two papers from which this thesis arose. These are Thomas Erben, Daniel Farrow, Catherine Heymans, Stefan Hilbert, Hendrik Hildebrandt, Andrew Hopkins, Arun Kannawadi, Nicola Napolitano, Cristobal Sifón and Angus Wright. In particular, I am thankful to Stefan. He not only provided the galaxy and shear catalogues from the Millennium Run but also answered all my questions and misunderstandings on this data. Thank you very much!

I am also very thankful for the KiDS collaboration, whose member I became in the process of this thesis. Thank you very much for accepting me with open arms, the scientific discussions during the regular telecons and the very memorable 'busy weeks' - even though the last one had to happen in a Zoom call.

My work was not only supported scientifically. Thanks to some key members of the AIfA, I could fully concentrate on science, as they took care of other issues. Accordingly, I would like to thank Sabine Derdau and Ellen Fuhrmann for their administrative support and the IT infrastructure team for support even during difficult times. Many thanks also to Rainer Mauersberger and Simone Pott, for the management of the IMPRS, the help they offered, and for organizing some very memorable IMPRS retreats.

My time in Bonn would have been only half as fun without the team of Astronomy On Tap Bonn. Many thanks to Aarti, Ana, Angus, Eleni, Enrico, Toma, Felix, Florian, Kevin, Manali, Maude, Sandra and Sven. I had a great time organizing events with you, in Fiddlers or virtual and loved the time in the pub.

I am also very grateful to the young PhD researches at the AIfA, in particular Hannah, Luis, Maude, Rongchuan, Sandra, Sven, and Pierre. Discussing papers with you every week in a relaxed atmosphere was great fun, and I can safely say that I am not sorry to have joined :).

My deepest gratitude belongs to my family. I thank my parents for awakening my curiosity in the Universe, supporting me all my life, both physically and emotionally, and giving me strength even in difficult times. And, thank you, Arwen for being the extraordinary kind, compassionate and intelligent person you are. If you are a representative example of your generation, I have the highest hopes for the future of humanity.

Finally, I would like to thank Allan. There are a million reasons why this thesis would not exist without you. Thank you for pushing me to learn GPU computing. Thank you for countless hours reviewing my manuscripts. And thank you for keeping me sane.